Theoretical Models of Gamma-Ray Burst Central Engines

by

Brian David Metzger

B.S. (University of Iowa) 2003
M.A. (University of California, Berkeley) 2005

A dissertation submitted in partial satisfaction of the
requirements for the degree of
Doctor of Philosophy

in

Physics

in the

GRADUATE DIVISION
of the
UNIVERSITY OF CALIFORNIA, BERKELEY

Committee in charge:
Professor Eliot Quataert, Co-chair
Professor Jonathan Arons, Co-chair
Professor Steven Boggs
Professor Joshua Bloom

Spring 2009

The dissertation of Brian David Metzger is approved:

Co-chair Date

Co-chair Date

Date

Date

University of California, Berkeley

Spring 2009

Theoretical Models of Gamma-Ray Burst Central Engines

Abstract

Theoretical Models of Gamma-Ray Burst Central Engines

by

Brian David Metzger

Doctor of Philosophy in Physics

University of California, Berkeley

Professor Eliot Quataert, Co-chair
Professor Jonathan Arons, Co-chair

The rapid variability and large energies that characterize Gamma-Ray Bursts (GRBs) strongly implicate neutron stars or stellar-mass black holes as their central engines. In this thesis, I develop theoretical models of both accretion powered and spin-down-powered central engines and apply them to long- and short-duration GRBs. This research covers several topics, including:

(1) The effects of strong magnetic fields and rapid rotation on winds from newly-formed neutron stars (NSs). I describe the evolution of the wind through the Kelvin-Helmholtz cooling epoch of the NS, emphasizing the transition between (i) thermal neutrino-driven, (ii) non-relativistic magnetically-dominated, and (iii) relativistic magnetically-dominated outflows. NSs with millisecond rotation periods and $\sim 10^{15}$ G magnetic fields drive relativistic winds with luminosities, energies, and Lorentz factors consistent with those required to produce long GRBs.

Evidence is growing for a class of short GRBs that are followed by an epoch of extended X-ray emission lasting $\sim 10 - 100$ s. I propose that these events are produced by the formation of a magnetar following the accretion-induced collapse (AIC) of a white dwarf. The GRB is powered by accretion onto the NS from a small disk that is formed during AIC. The extended emission is produced by a relativistic wind that extracts the rotational energy of the proto-magnetar on a timescale $\sim 10-100$ s. I successfully model the light curve of the extended emission of GRB 060614 using spin-down calculations of a cooling proto-magnetar.

(2) A calculation of the nuclear composition of neutrino-heated magnetized winds from the surface of proto-magnetars and from the midplane of hyper-accreting disks in order to evaluate the conditions necessary for neutron-rich GRB outflows. Although the base of the wind is neutron-rich, weak interactions typically raise the neutron-to-proton ratio to ~ 1 just above the disk or PNS surface. Neutron-rich accretion disk winds possess a minimum mass-loss rate that precludes simultaneously ultra-relativistic winds from accompanying a substantial accretion power.

(3) Time-dependent models of the accretion disks created during compact object (CO) mergers. At early times the disk is cooled by neutrinos; neutrino irradiation of the disk produces a wind that synthesizes up to $\sim 10^{-3} M_\odot$ of ^{56}Ni, resulting in a short-lived ($\sim$ 1 day) optical/infrared transient. At later times, neutrino cooling becomes inefficient, alpha-particles form, and powerful outflows blow away the remaining mass of the disk. Since the disk is neutron rich and weak interactions freeze out when it becomes advective, these outflows robustly synthesize neutron-rich isotopes. The abundances of these rare isotopes strongly constrain the CO merger rate and the beaming fraction of short GRBs.

The accretion disks formed during AIC undergo a similar evolution. However, because the disk is irradiated by electron neutrinos from the central NS, the neutron-to-proton ratio increases to ~ 1 by the point of freeze out. As a result, outflows from the disk synthesize up to $\sim 10^{-2} M_\odot$ in ^{56}Ni. Thus, AIC will be accompanied by a spectroscopically-distinct SN-like transient that should be detectable with upcoming optical transient surveys.

Professor Eliot Quataert
Dissertation Committee Co-chair

Professor Jonathan Arons
Dissertation Committee Co-Chair

To Mom and Dad

Contents

List of Figures

List of Tables

Acknowledgments

Many people have shaped my life in positive ways and have provided me with support as I have pursued academic study and research. I owe each of these individuals a debt of gratitude.

First and foremost, my advisor Eliot Quataert. It has been an honor to learn theoretical astrophysics from one of the best. Your steadfast patience and tutelage has helped transform me into a researcher and a more effective communicator. I hope that even a small fraction of your unique ability to hone in on interesting problems has rubbed off on me. I cannot thank you enough.

To my colleague Todd Thompson, for your friendship and informal guidance. Your enthusiasm, creativity, and boldness has inspired my approach to research. To Jon Arons, for your wisdom and for providing an independent perspective on each problem. To Josh Bloom, for encouraging my research, supporting travel to my first GRB conference, and for carefully reading through my thesis. To my colleagues Niccolo Bucciantini, Tony Piro, and Prateek Sharma, for your friendship, mentorship, and many helpful conversations.

To my friend, officemate, and colleague Dan Perley: our numerous conversations on GRBs (sometimes late-night and caffeine-loaded) were enormously helpful. To my close friend and classmate Tommy O'Donnell: our coffee walks and trips to the pub kept me sane and gave me perspective on my time at Berkeley. To Melanie Colburn, for your friendship, love, and support during my first few years at Berkeley. To my "Net Force" basketball teammates, including Henry Fu, Willie Klemm, Brian Kessler, Joel Moore, Adam Bryant, Jordan Carlson, Jeremy Mardon, Craig Hetherington, and, especially, fellow organizer Marc Pulupa - yes, even physicists

can 'ball'! To my colleague and classmate Mark Bandstra, for your friendship and unique perspective on GRB research. To my fellow graduate students and friends, especially Katie Alatalo, Charles Hansen, Eric Huff, Stella Offner, Linda Strubbe, Andrew Wetzel, and Diane Wong, for your support and friendship. To Anne Takizawa, for providing the glue that holds Berkeley Physics together.

I also owe a debt of gratitude to individuals that shaped my life and education prior to Berkeley. To Professor Craig Kletzing, for giving me the opportunity to begin hands-on research as a completely inexperienced undergrad. To Professors Steve Spangler and Jack Scudder, for your mentorship during my undergraduate years at Iowa. To my senior undergraduate research advisor Ben Chandran, for introducing me to the addictive properties of research and for guiding me to Berkeley. To my high school physics teacher, Keith Summerson, for always holding me to a high standard and for never witholding your opinion.

Finally, to my family - grandparents, aunts, uncles, and cousins, for providing me steadfast support and love. To my parents David and Inez, for always encouraging me to pursue my interests. To my brother Bjorn, for instilling in me a competitive drive and for always keeping my life interesting. To my grandma Ruth, for writing me every week and keeping me in your prayers, through good times and bad. And last, but not least, to my love, Ms. Stacey Thomas, for exploring California with me and having patience with the sometimes all-consuming lifestyle of a graduate student.

I appreciate the financial support that I received from a National Aeronautics and Space Administration (NASA) Graduate Student Research Fellowship. I also gratefully acknowledge support through my advisor Eliot Quataert: NSF grant AST 0206006; NSF-DOE Grant PHY-0812811; NASA grants NAG5-12043, NNG05GO22H, and NNG06GI68G; an Alfred P. Sloan Fellowship; and the David and Lucile Packard Foundation.

Chapter 1

Introduction and Outline

1.1 Preface

Despite being discovered over forty years ago, Gamma-Ray Bursts (GRBs) remain one of the forefront mysteries in astrophysics. The past decade of observations has, however, revealed much about the properties of these enigmatic events. In particular, with the advent of NASA's *Swift* satellite and extensive ground-based, multi-wavelength follow-up observations, the field of GRB observations has reached a certain level of maturity. Although these new observations have helped to answer many questions, new phenomenology has been uncovered, previous assumptions have been challenged, and many new questions have emerged. Furthermore, a number of basic questions remain unanswered, such as: *"What emission mechanism creates the gamma-rays? (e.g., synchrotron or inverse-Compton?),"* *"What is the composition of the outflows that produce GRBs? (e.g., baryons or e^-/e^+ pairs?),"* *"In what form is the outflow's energy stored (e.g., kinetic energy or Poynting flux?),"* *"How is this ordered energy 'randomized' and how are the radiating charges accelerated?,"* *"How are the magnetic fields that appear necessary for the prompt and afterglow emission produced? (e.g., are they generated by shocks or carried out from the outflow's source?)."*

Perhaps the key question associated with GRBs is the nature of the astrophysical agent (or agents) that ultimately powers them: the "central engine." Soon after

their discovery, there were almost as many theories for GRBs as there were theorists (Ruderman 1975). The presently appreciated requirements of supernova-scale energies, short timescales (down to milliseconds), and relativistic speeds (Lorentz factors $\gtrsim 100$) have, however, significantly narrowed the possibilities: GRBs are almost certainly the result of stellar-mass black holes (BHs) or neutron stars (NSs) being formed or undergoing catastrophic rearrangement (e.g., Katz 1997). All plausible central engines are powered by either accretion or rotation, which makes a deep gravitational potential and a reservoir of significant angular momentum the key ingredients of any model. A full understanding of GRBs may ultimately require comprehending the interplay between the physics of relativistic fluid dynamics, ultra-strong gravity, strong electromagnetic fields, nuclear/weak interactions, and plasma processes such as collisionless shock formation, non-thermal particle acceleration, and magnetic reconnection. The ways in which these nominally disparate physical processes conspire to produce a GRB makes studying the central engine both exciting and uniquely challenging.

In this thesis, I develop simple theoretical models of GRB central engines in order to obtain a better understanding of both the *abilities* and the *limitations* of these prime movers. Fundamental questions about GRBs (such as those raised in the first paragraph) are typically addressed by taking an agnostic approach towards the nature of the central engine. Pursued in the spirit of "model independence," this approach also often allows the central engine undue freedom, making it "a flexible source of power whose properties are only limited by its total mass and the referees of theoretical papers" (Blandford 2002). One of the important themes of this work is that rather stringent constraints can be placed on GRB models by employing a self-consistent physical model for the central engine. It is certainly true, for instance, that the formation, collimation, and stability of ultra-relativistic jets remains a formidable unsolved theoretical problem. However, other characteristics of the central engine (such as the mass loading of the jet and energy budget) can, in some cases, be evaluated with more confidence. These aspects of the problem are more theoretically tractable largely because the immediate vicinity of the central engine is highly collisional and (local) kinetic equilibrium is assured; in this sense,

the "extreme" environment of the central engine is a blessing. For example, the mass loading and nuclear composition of GRB jets in the "millisecond magnetar" model is largely set by thermal physics at the surface of the NS (see Chapter 2). Similarly, the viscous expansion of accretion disks created during compact-object mergers is quite similar to the expansion during the Big Bang (perhaps the best case of thermal equilibrium known! See Chapter 6).

Another recurring theme of this thesis is that any central engine capable of producing an ultra-relativistic jet will almost certainly also produce a comparably energetic non-relativistic outflow. Although not as immediately conspicuous as the GRB itself, this slower ejecta may lead to other observable consequences, such as the synthesis and ejection of unusual and/or radioactive isotopes (Chapters 5, 6, and 7). Such secondary diagnostics are important because they often can be calculated with more confidence; just as measurements of elemental abundances strongly constrain the nucleosynthesis that occured well before light left the last scattering surface, these unique fingerprints could inform the nature of the central engine much better than the GRB itself.[1]

Deciphering the origin of GRBs is also important because GRB science has a significant impact on other fields in astrophysics. Perhaps most directly, GRB research complements studies of other known systems powered by relativistic outflows from compact-objects, such as pulsars, magnetars, micro-quasars, and active galactic nuclei. Due to their close connection to core-collapse supernovae and (possibly) merging compact-objects, the study of GRB progenitors is also closely tied to the fields of stellar structure and evolution, both of single stars and binary systems. As an unambiguous site of high energy particle acceleration, GRBs are a promising target for detection with the troika of "nascent cosmic windows" probing the frontiers of high-energy astrophysics: $\sim$ GeV-TeV photons (Hurley et al. 1994), ultra high-energy cosmic rays (Waxman 1995; Vietri 1995), and TeV-PeV neutrinos (Waxman & Bahcall 2000). Many GRB central engines are also

[1]Evidence is strong, for instance, that the stellar progenitors of long and short-duration GRBs are distinct (e.g., Bloom et al. 2006; Berger et al. 2005), despite overall similarities in the properties of their prompt GRB emission (e.g., Ghirlanda et al. 2009). This alone suggests that information about the central engine encoded in the prompt emission may be limited.

expected to be strong ∼kHz gravitational wave (GW) sources (e.g., Hughes 2003), perhaps detectable with upcoming km-scale GW interferometers such as Advanced LIGO (Abramovici et al. 1992). GRBs and their afterglows could be used as beacons to such sources, which would lower the signal-to-noise required for a confident detection (Kochanek & Piran 1993) and break several of the degeneracies required to extract important information from the GW signal (Hughes & Holz 2003; Nissanke et al. 2009). Many GRB central engines are also expected to be accompanied by longer-wavelength (e.g., optical) transient emission, which could be detected independent of a high energy trigger, such as off-axis or "orphan" afterglows (e.g., Totani & Panaitescu 2002) and SN-like transients powered by radioactive ejecta (see Chapters 5 and 7). Although rare, these events are important targets for upcoming optical transient surveys such as Pan-STARRS (Kaiser et al. 2002), Palomar Transient Factory (Rau et al. 2008), and the Large Synoptic Survey Telescope (LSST; LSST collaboration 2007). Furthermore, since the radioactive material ejected from the central engine is often highly neutron-rich, GRB progenitors are a likely site for the nucleosynthesis of rare heavy elements (e.g., Eichler et al. 1989; see Chapters 5 and 6), whose abundances in metal poor stars in the Galactic halo and in surrounding satellite galaxies can be used to probe the formation of our Galaxy (e.g., Sneden et al. 2008). Finally, as the most luminous known electromagnetic events, GRBs provide a unique probe of the high redshift Universe. GRBs can be used to constrain the global star formation rate (e.g., Yüksel et al. 2008) as well as the local properties of star formation regions (e.g., Prochaska et al. 2007) in high-redshift galaxies. In addition, since GRBs may accompany the deaths of the first generations of stars at redshift $z \sim 10$, they may someday be used to probe of the epoch of reionization (e.g., Barkana & Loeb 2001; McQuinn et al. 2009).

The remainder of this introductory section is summarized as follow. I begin in §1.2 with a discussion of the historical background of GRBs that blends the observational and theoretical advances. This discussion offers a different perspective from other extant GRB reviews (e.g., Piran 2005; Zhang & Mészáros 2004; Nakar 2007) since I shall focus on issues that are directly relevant to deciphering

the central engine and use them to motivate the research described in subsequent Chapters. I conclude in §1.3 with an outline of the remainder of the thesis.

1.2 Historical Background

1.2.1 Early Developments

GRBs were discovered using the Vela satellites in the late 1960s[2], but they were not announced until 1973 (Klebesadel et al. 1973). GRBs manifest as a deluge of high-energy emissions with characteristic durations of $\sim$ milliseconds to minutes; the light curves display rapid variability (down to $\sim$ milliseconds) and a non-thermal (broken power-law) spectrum that peaks in the sub-MeV energy range but that often possesses a high-energy tail with significant power above ~ 1 MeV (see Fishman & Meegan 1995 for a review).

Determining distances to astronomical objects is always challenging. With GRBs, one hope was to identify a coincident optical counterpart. Unfortunately, inherent limitations of the NaI(Tl) scintillators used in early gamma-ray detectors made GRBs extremely difficult to localize with single satellites. In some cases multiple satellites detecting a common burst employed time-delay techniques to achieve arcminute localizations (e.g., Atteia et al. 1987). However, these positions were only available to astronomers following a delay of $\sim$months. As discussed further below, we now appreciate that GRBs are in fact accompanied by fading "afterglow" emission at longer wavelengths. However, due to the ephemeral nature of the afterglow, it is unsurprising that no bone fide optical counterparts were detected in these early days.

During the 1970s and 1980s, GRBs were generally believed to originate from the surfaces of Galactic NSs. This was considered a reasonable hypothesis given phenomenological similarities between GRBs and X-ray bursts on NSs, the GRB-like giant flare from a Soft Gamma-Ray Repeater (SGR) on March 5, 1979 (which *did* originate from a Galactic NS), and theoretical "compactness" arguments (Ru-

[2]The first observed GRB was 670702.

derman 1975; Cavallo & Rees 1978; see below for further discussion). Other observations (e.g., X-ray cyclotron lines and recurring optical counterparts on archival photographs) also appeared to support a Galactic origin, but later proved to be unsubstantiated and likely spurious.

Usov and Chibisov (1975) first argued that GRBs might originate from cosmological distances. This viewpoint was developed in the influential works of Paczyński (1986) and Goodman (1986). The Burst and Transient Source Experiment (BATSE) experiment on the Compton Gamma-Ray Obsevatory (CGRO; launched in 1991) provided strong support for the cosmological hypothesis by showing that GRBs are distributed isotropically on the sky (Meegan et al. 1992). A "watershed moment" occurred in 1997 when the Italian-Dutch satellite Beppo-Sax first detected a fading GRB X-ray "afterglow" (Costa et al. 1997). With precise X-ray positions available rapidly to ground-based observers, afterglow emission was soon discovered in the optical (van Paradijs et al. 1997) and radio (Frail et al. 1997) bands. Absorptions lines detected in a GRB spectrum at redshift $z = 0.835$ provided definitive evidence that GRBs are truly a cosmological phenomena (Metzger et al. 1997).

As cosmological sources, the implied energies of GRBs became enormous, sometimes exceeding $\sim 10^{54}$ ergs $\sim M_\odot c^2$ for an assumed isotropic emission (e.g., Kulkarni et al. 1999). If such a huge energy flux truly originated from a region with a size ~ 100 km (typical of that inferred from the observed millisecond variability), the opacity to pair-production in the high-energy photon power-law tail would be enormous (since the optical depth for photon-photon and photon-electron interactions was $\tau_{\gamma-\gamma}, \tau_{e-\gamma} \sim 10^{15}$ for typical parameters). This requires the formation of a thermal pair photosphere, which is inconsistent with the observed non-thermal spectrum. In order to overcome this "compactness problem," the GRB-producing region must be expanding towards the observer ultra-relativistically, with a bulk Lorentz factor $\Gamma \gtrsim 100$ (e.g., Lithwick & Sari 2001). Relativistic bulk motion allows high-energy gamma-rays to escape because (1) observed photons are blueshifted from the rest frame of the emitting region, thus reducing the true number of photon pairs with energies above the pair-production threshold (2) by

naively inferring the size of the emitting region from the variability, the observer is tricked by relativistic effects into believing that the emitting region is more compact than its true physical dimensions (indeed, as discussed below, current models place the location of GRB emission at radii ranging from $10^{12} - 10^{18}$ cm, *not* 100 km). Relativistic speeds in GRB outflows have been confirmed observationally by the angular expansion rate inferred from the quenching of scintillation in a radio afterglow (Frail et al. 1997) and by direct VLBI imaging of an expanding GRB blast wave (Taylor et al. 2004).

1.2.2 Emission Models

Although it is established that GRBs are produced by relativistic outflows, the composition of the outflow and the means by which electrons are accelerated to produce gamma-rays remain areas of heated debate. Broadly speaking, GRB emission models can be classified by (1) their dominant energy source: kinetic energy or Poynting flux, and (2) the reason this ordered energy is dissipated — in particular, whether the GRB is triggered by processes "internal" or "external" to the outflow itself.

"External" Prompt and Afterglow Emission

The most popular kinetic/external emission model is the "external shock" scenario (Mészáros & Rees 1993), which posits that GRBs are produced when the relativistic outflow is decelerated by its interaction with the surrounding "circumburst medium" (CBM), in analogy with the way that supernova (SN) ejecta slows upon interacting with its interstellar surroundings. Although a SN may take hundreds of years to enter its adiabatic phase, an ultra-relativistic outflow transfers a significant fraction of its energy to the CBM much quicker, in a matter of seconds according to an external observer. This accelerated evolution occurs because: (1) a relativistic outflow sweeps up surrounding material more quickly; (2) relativistic ejecta transfers $\sim$ half of its energy to the CBM after sweeping up only a fraction $\sim 1/\Gamma$ of its rest mass (3) due to travel-time effects, photons from the

ultra-relativistic GRB shock arrive at an external observer "scrunched together" in time by a factor $\sim 1/\Gamma^2$. If GRBs are indeed produced by external shocks, emission occurs at the relativistic analog of the Sedov radius, which is $\sim 10^{17} - 10^{18}$ cm for typical CBM and GRB parameters.

One criticism of the external shock model for prompt emission is that highly variable light curves are difficult to produce while simultaneously maintaining a high radiative efficiency (Sari & Piran 1997). Random relativistic motions ("turbulence") of the emitting material in the co-moving frame (or any other form of highly anisotropic emission) may overcome this difficulty (Lyutikov & Blandford 2002; Narayan & Kumar 2008). Such relativistic motions are in fact predicted by the "electromagnetic" model of Lyutikov & Blandford (2002). This model is classified as Poynting/external because interaction with the CBM ultimately triggers instabilities in the magnetically-dominated outflow that leads to the GRB.

A more serious problem for all "external" GRB models is emerging from studies of a newly identified subclass of GRBs, "Short-Duration GRBs with Extended Emission" (or SGRBEEs; see Chapter 3 for a detailed discussion). As discussed below, GRB afterglow emission should be a reliable diagnostic of the CBM. Although SGRBEEs have remarkably similar prompt emission light curves[3], their afterglow luminosities can vary tremendously between bursts (e.g., compare GRB050724 [Malesani et al. 2007] with GRB080503 [Perley et al. 2008]). This suggests that the prompt emission of SGRBEEs (and, by reasonable extension, of all GRBs) is relatively independent of the external environment.

Regardless of its merits as the mechanism for prompt GRB emission, the external shock model has enjoyed considerable success in explaining the observed broad-band afterglow emission (e.g., Sari et al. 1998). The decelerating ultra-relativistic blast wave is generally modeled using the Blandford-McKee (1976) self-similar solution, and synchrotron radiation is generally invoked as the emission process. A major recent theoretical breakthrough is the first principles demonstration that unmagnetized (Weibel-mediated) relativistic shocks indeed efficiently

[3]The wide diversity in GRB light curves is often summarized by the quip "when you've seen one GRB, you've seen one GRB." This is emphatically *not* true for SGRBEEs.

accelerate a population of high energy non-thermal electrons (Spitkovsky 2008a,b). Whether the magnetic fields required to produce the afterglow radiation can be generated and sustained behind the shock is, however, much less clear (e.g., Chang, Spitkovsky, & Arons 2008). Given this uncertainty, it has recently been proposed that the requisite fields are instead generated by large-scale vorticity generated if the shock is curved due to inhomogeneities in the upstream plasma (Goodman & MacFadyen 2007), perhaps generated by a clumpy CBM (Sironi & Goodman 2007) or self-generated by a variant on the Bell (Bell 2004) cosmic ray current-driven instability (Couch et al. 2008).

The standard afterglow picture has grown murkier because of the unexpectedly complex early-time ($t \lesssim 10^4$ s) X-ray afterglow light curve behavior discovered using *Swift* (Nousek et al. 2006). This new data has led some to abandon the forward shock as the emission site altogether, positing instead that all afterglow emission originates from the reverse shock (Genet et al. 2007; Uhm & Beloborodov 2007). In this case the afterglow light curve sensitively tracks the energy and density profile of the ejecta, thus providing a natural explanation for the deviations from power-law behavior (e.g., bumps, steepenings, and wiggles) observed in some well-studied GRBs (e.g., Berger et al. 2003). This model has the additional virtue that the magnetic fields required for the synchrotron emission can be carried out in the ejecta from the central engine and do not have to be generated (or greatly amplified) locally. Others, however, have argued that the new observations remain consistent with the forward shock model, provided that it is supplemented with additional effects (see Zhang 2007 for a review). Powering the X-ray "plateau" phase observed at $t \sim 10^3 - 10^4$ s, in particular, requires the forward shock to be continually replenished with substantial energy (e.g., Granot & Kumar 2006). Perhaps the most interesting new discovery are powerful late-time X-ray flares (Burrows et al. 2005), which strongly suggest that the central engine is active long after the initial GRB (e.g., Lazzati & Perna 2007).

"Internal" Prompt Emission

For reasons discussed above, internal models are generally favored to explain the prompt GRB emission. One important restriction in this case is that the GRB must originate between the photosphere[4] at $\sim 10^{12} - 10^{13}$ cm and the deceleration radius at $\sim 10^{17} - 10^{18}$ cm. The most popular kinetic/internal model is the "internal shock" model (Rees & Mészáros 1994; Sari & Piran 1997), which posits that GRBs are produced by shocks between "shells" of material ejected from the central engine with large relative velocities. This model overcomes some of the difficulties of the external shock model because the observed rapid variability is now pinned on the central engine. Indeed, in internal shock emission models the GRB light curve roughly tracks the energy release from the central engine (see Figures 3.1 and 3.2 for an explicit example). Such a one-to-one mapping is often implicitly assumed when connecting central engine models to observations (e.g., Kumar, Narayan, & Johnson 2008). Despite its successes, internal shock models may have difficulties explaining the very high radiative efficiencies of GRBs (since only *relative* kinetic energy can be tapped) and the relatively narrow peak energy E_p distribution (in synchrotron internal shock models, $E_p \propto \Gamma^{-2}$ at fixed burst luminosity; Zhang & Mészáros 2002).

Even if GRB outflows are dominated by kinetic energy at the emission site, this energy is unlikely to have begun in kinetic form at the base of the outflow. In internal shock models, the outflow acceleration to relativistic speeds is typically envisioned to result from adiabatic expansion following the formation of an ultra-high entropy "fireball," analogous to the Big Bang (Goodman 1986; Shemi & Piran 1990). A photon cavity of this sort is unavoidable if GRBs are powered by neutrino annihilation along the polar axis of a BH (e.g., Rosswog et al. 2003). Most other models, however, such as magnetized jets powered by a BH or rotational energy from a magnetar, are Poynting-flux dominated at the smallest radii. If this magnetic energy is dissipated into thermal energy well below the photosphere,

[4]If the emission in fact occurred close to the photosphere, GRBs should be accompanied by a substantial thermal component, contrary to observations (see, however, Thompson 1994, 2006).

an effective "fireball" is produced and the kinetic/internal paradigm is recovered. Such a conversion of Poynting flux to kinetic energy indeed appears to occur in pulsar wind nebulae (Kennel & Coroniti 1984).

If magnetic dissipation is instead delayed until after the outflow has breached the photosphere, the GRB must be powered by magnetic dissipation itself, through, for instance, particle accleration following magnetic reconnection or other instabilities. Models powered by reconnection have the appealing property that they may naturally radiate $\sim 1/2$ of the outflow's energy and leave $\sim 1/2$ in kinetic form (Drenkhahn & Spruit 2002), as is necessary to explain afterglow observations (Berger et al. 2003; Zhang et al. 2007). The reason that internal shock models (kinetic/internal) are more popular than magnetic dissiption models (Poynting/internal) is probably sociological: shocks provide a clear theoretical framework (e.g., jump conditions and simple microphysical parameters) upon which sufficiently detailed calculations to compare with observations can readily be performed. By contrast, determining the observational signature of magnetic dissiption requires a true understanding of the relevant collisionless processes, which are much less well understood (for a heroic attempt, see Giannios & Spruit 2005). Using the early afterglow to infer the strength of the reverse shock into the ejecta has been proposed as one means to infer the magnetization of the outflow (Zhang & Kobayashi 2005). Disentangling reverse shock emission from optical emission which is directly related to the prompt GRB emission (e.g., Vestrand et al. 2006) has, however, proven difficult.

Recent attempts to model GRB prompt emission in a model-independent manner have concluded that the gamma-ray emission occurs at very large radii $\gtrsim 10^{16} - 10^{17}$ cm (Kumar & McMahon 2008; Kumar & Narayan 2008). A similar constraint has emerged from the analysis of the bright *Fermi*-detected burst GRB 080916C (Abdo et al. 2009). An emission site near the deceleration radius of the outflow would appear to support "external" emission models triggered by interaction with the CBM (Kumar & Narayan 2008). Indeed, internal models (shocks or magnetic reconnection) generally predict smaller emission radii. However, as discussed above, other considerations appear to disfavor external models. One

remaining possibility is that GRBs are indeed internally-triggered, but this dissipation does not manifest until fairly large radii. Such a situation might occur in a magnetically-dominated outflow if the GRB is triggered when the current density required to maintain the Poynting flux ($J \propto 1/r^2$) drops below the maximum current density which can be provided by the expanding relativistic volume ($J_{\rm max} \propto 1/r^3$); this would lead to the global break-down of MHD and, potentially, efficient particle acceleration (Lyutikov & Blackman 2001).

1.2.3 Central Engine Models

Since GRB outflows are ultra-relativistic, observers are only in causal contact with a small solid angle ($\sim 1/\Gamma^2$) on the surface of the outflow (as subtended by the central engine). Thus, even if GRB outflows are significantly collimated, evidence for jet-like angular structure only becomes apparent long after the main GRB event, once the flow has slowed to a Lorentz factor $\Gamma \sim 1/\theta_j$, where θ_j is the opening angle of the jet. Indeed, observational evidence such as "jet breaks" in the late-time afterglow (Rhoads 1997) and the phenomenological similarities between GRBs and outbursts from other jetted systems (e.g., the TeV-flaring blazars; Aharonian et al. 2007) strongly suggest that GRB outflows are collimated to some degree. This implies that although the isotropic-equivalent energies of GRBs are enormous, the true energy budget (after correcting for beaming) is much lower, typically comparable to the kinetic energy of a SN, $\sim 10^{51}$ ergs (Frail et al. 2001; Bloom et al. 2003). What makes the GRB central engine unique is therefore not its large energy budget, but rather its ability to place a significant fraction of this energy into material with ultra-relativistic speeds. This is an important diagnostic on the central engine because it implies that the outflow remains relatively "clean" despite originating from what is potentially a rather dense and messy environment around the central engine. A jet with energy $\sim 10^{51}$ ergs must, for instance, entrain $\lesssim 10^{-5} M_\odot$ to achieve $\Gamma \gtrsim 100$. Because all viable central engine models are surrounded by significantly more mass than this ($\sim 10^{-2} - 10 M_\odot$), one of the major challenges of any model is to produce an outflow that avoids being polluted

by too much of this surrounding material.

The first proposed cosmological central engine model was the merger of two compact-objects (COs) in either a BH-NS or NS-NS binary system (Blinnikov 1984; Paczyńskski 1986; Eichler et al. 1989; Narayan et al. 1992). In this model and related scenarios, a BH is created and/or grows rapidly from the merger. The GRB-producing jets are then produced when material tidally stripped during the merger circularizes into a disk and accretes. Chapters 5 and 6 present evolutionary models of the accretion disks formed by CO mergers. In addition to possibly powering a GRB, these disks are blown apart at late times in a hot, dense wind that synthesizes rare neutron-rich isotopes. Interestingly, neutron-rich heavy element formation was one of the main motivations for the first studies of CO mergers as GRB central engines (Eichler et al. 1989), although the disk winds discussed in Chapters 5 and 6 represent a new site of nucleosynthesis, quite unlike the cold, dynamically-ejected "NS guts" explored in earlier models (Freiburghaus et al. 1999).

The duration of central engine activity in CO merger models is the viscous timescale $t_{\rm visc}$ at a few gravitational radii, where the tidally stripped material circularizes; for typical parameters $t_{\rm acc} \sim 0.1 - 1$ s (see eq. [3.1]). BATSE demonstrated that GRBs come in two types ("long" and "short"), separated by their duration ~ 2 seconds (Mazets et al. 1981) and spectral "hardness" (Kouveliotou et al. 1993). Although CO mergers were initially envisioned as a model for all GRBs, their characteristic duration $\sim t_{\rm visc}$ is one reason that they have emerged as a popular model for short-duration GRBs. Although long-duration GRB afterglows were discovered in the late 1990s, it was not until the advent of $Swift$ and its rapid-slewing capabilities that afterglows were first detected from short bursts (Barthelmy et al. 2005). This allowed short GRB host galaxies to be identified for the first time (Bloom et al. 2006; Berger et al. 2005; Hjorth et al. 2005), revealing that short GRBs likely originate from a more evolved stellar progenitor population than long GRBs (which are instead associated with regions of massive star formation; see Bloom & Prochaska 2006 for an early review). This discovery is consistent with a CO merger origin for short GRBs because the timescale for binary inspiral through gravitational radiation can in principle exceed the evolutionary timescale

of the stellar population. Despite its successes, it should be emphasized that CO mergers are not the only central engine model that predicts an accretion disk which circularizes at a few gravitational radii and an association with an evolved stellar population (see Chapter 7).

Usov (1992) proposed that GRBs are produced by the spin-down of newly-formed, rapidly-spinning (millisecond period), highly-magnetized NSs ("magnetars"; Duncan & Thompson 1992). Since this "millisecond magnetar" model requires a NS with a surface dipole magnetic field strength $B_{\rm dip} \sim 10^{15}$ G, it was initially considered speculative because most observed radio pulsars have $B_{\rm dip} \sim 10^{12} - 10^{13}$ G (Manchester 2004). Evidence for the existence of magnetars, in particular their association with SGRs and Anamalous X-ray Pulsars (AXPs), has increased significantly in the past decade (Kouveliotou et al. 1998). Indeed, evidence now suggests that $\sim 10\%$ of Galactic NSs are born with $B_{\rm dip} \gtrsim 10^{14}$ G (Woods & Thompson 2006). In Usov's model, magnetar formation occurred via the accretion-induced collapse (AIC) of a white dwarf, rather than from the core-collapse of a massive star (which is probably the dominant birth channel of Galactic magnetars).

One thing that the Usov model and other early models (e.g., Wheeler et al. 2000) failed to account for is that magnetars, like other NSs, are born rather hot (with a surface temperature ~ 5 MeV) and emit a substantial neutrino luminosity. This drives mass-loss from the surface of the magnetar during the first $\sim 10 - 100$ seconds of its life (Thompson, Chang, & Quataert 2004; see Chapter 2), setting a baseline mass-loading for proto-magnetar outflows on top of any entrainment from the surrounding environment. This represents a strong constraint on magnetar models since it is extremely difficult for the outflow to become ultra-relativistic during the first few seconds following core bounce (although the mass-loading falls rapidly with time $\propto t^{-5/2}$ and the outflow can achieve $\Gamma \sim 100 - 1000$ by $t \sim 10 - 100$ s). By contrast, an outflow threading the event horizon of a BH can in principle be effectively baryon free (McKinney 2005). Early magnetar GRB models also assumed that force-free conditions apply in the magnetosphere and in the wind. While this approximation is often excellent when applied to (much

older) pulsars, it is not generally applicable to newly-formed magnetars (although it becomes an increasingly better approximation with time). Chapter 3 presents an updated version of Usov's model that takes these issues into account and shows how it may explain a subclass of GRBs.

Early central-engine models (e.g., CO mergers and Usov's AIC) were focused on systems that provide a relatively baryon-clean environment from which to launch a relativistic jet. In 1993 Stan Woosley made the bold suggestion that GRB jets may be produced even in the dense environment of the core-collapse of a massive star (Woosley 1993). In the model of Woosley, the GRB is powered by accretion of the stellar envelope onto a BH that forms soon after the collapse. A jet produced by the accreting BH burrows through the collapsing star, producing a channel through which the relativistic outflow can then escape (MacFadyen & Woosley 1999). In order for a centrifugally-supported disk to form, the core of the stellar progenitor must itself be rapidly rotating; since only a small fraction of all massive stars are likely to satisfy this criterion (e.g., Langer et al. 2008), this could help explain why GRBs are such a rare phenomena. In the original collapsar model, the core-collapse was considered to have "failed" as a SN and most of the star accretes onto the BH instead of becoming unbound. Ironically, definitive support for the general collapsar picture has come from the association of some long-duration GRBs with bright, energetic Type Ib/c SNe (Galama et al. 1998; Stanek et al. 2003), which originate from stellar progenitors that have lost their outer H/He envelopes (i.e., Wolf-Rayet stars).[5] The association of long GRBs with regions of massive star formation (Bloom et al. 1999; Fruchter et al. 2006) has also been key to establishing that most (and possibly all) long-duration GRBs are produced by the core-collapse of massive stars (Woosley & Bloom 2006).[6]

Although long-duration GRBs are definitively associated with the deaths of

[5]This has been called, affectionately and in reference to Einstein, "Woosley's biggest blunder" (Bloom et al. 2008).

[6]In a few cases, GRBs technically classified as "long" have not been accompanied by bright SNe (Fynbo et al. 2006; Gehrels et al. 2006). Some of these bursts, however, may actually be physically associated with the progenitors of short bursts (e.g., SGRBEEs). For these and other reasons it has been suggested that GRBs should be classified based on more than just the traditional high energy diagnostics (Bloom et al. 2008).

massive stars, this does not establish that the central engine is a BH. Single star evolutionary calculations with supernova explosions put in by hand suggest that stars with initial masses greater than $\sim 25 M_\odot$ collapse to form BHs instead of NSs (Woosley & Weaver 1995). However, our present *observational* understanding of the mapping between high mass stars, the Wolf-Rayet progenitors of GRBs, and their compact-object progeny is far from complete (e.g., Smith & Owocki 2006). Indeed, some magnetars appear to originate from very massive stars ($\gtrsim 40 M_\odot$; Muno et al. 2006). Modern SN calculations suggest that the presence of a relatively long-lived NS may be crucial to the explosion mechanism (e.g., via the neutrino mechanism; Bethe & Wilson 1985). Thus, an important implication of collapsar models that assume that BH formation occurs promptly after collapse is that the explosion mechanism associated with GRB SNe is fundamentally different than for SNe associated with the death of "normal" (slowly rotating) massive stars. MacFadyen & Woosley (1999) suggest that winds from the accretion disk blow up the star, ejecting the large quantities of ^{56}Ni and kinetic energy observed (e.g., $E_{\rm kin} \approx 2 \times 10^{52}$ ergs and $M_{\rm Ni} \approx 0.5 M_\odot$ for SN1998bw associated with GRB090425; Iwamoto et al. 1998). A disk wind is probably not the mechanism for most core-collapse SNe, however, since accretion would spin-up the NS and the inferred rotation rates of pulsars at birth are typically much too low (e.g., Kaspi & Helfand 2002). If GRB SNe are truly produced by a different mechanism than normal SNe, two distinct SN populations might be expected. Observations indicate, however, that SN energies and Ni masses appear to vary continuously from "normal" ($\sim 10^{51}$ erg) Type Ib/c SNe to the "hypernovae" ($\sim 10^{52}$ erg) associated with GRBs (see Nomoto et al. 2007, Figure 2). Furthermore, some of the "intermediate" SNe are associated with "X-ray Flashes," the softer cousins of GRBs (e.g., SN2006aj [$E_{\rm kin} \approx 2 \times 10^{51}$ ergs; $M_{\rm Ni} \approx 0.2 M_\odot$] associated with XRF060218; Pian et al. 2006). In addition, some hypernovae do not appear to be accompanied by GRBs (e.g., Soderberg et al. 2006), which also suggests that the SN and GRB-producing mechanisms are distinct. Another critical issue is whether collapsar disk winds actually produce ^{56}Ni, which depends sensitively on the electron fraction of the outflow Y_e. In particular, although $Y_e \gtrsim 0.5$ is

required for ^{56}Ni, the midplane of neutrino-cooled disks is neutron-rich with $Y_e \sim 0.1$ (Beloborodov 2003). Although the disk's electron fraction will change as it accretes and viscously evolves (Chapter 6) and the composition of the outflow may evolve as it accelerates out of the disk (Pruet et al. 2004; Chapter 4), whether $Y_e \gtrsim 0.5$ obtains and ^{56}Ni is actually produced is presently unclear.

Although "prompt" collapsar models may have difficulties explaining the properties of GRB SNe, a BH could also form after a delay following a successful SN, due to the "fallback" of material that remains bound (Woosley & Weaver 1995). In this case, the central compact-object initially goes through a NS phase (which may have an important role in the SN mechanism), but the GRB is produced later, following BH formation. One problem with this scenario is that stellar cores that collapse with sufficient angular momentum to produce an accretion disk may also produce a powerful magneto-centrifugally driven SN. This may prevent the NS from accreting sufficient mass to produce a BH in the first place (Dessart et al. 2008). Whether the NS can in fact gain enough mass to become a BH depends on the structure of the progenitor star — which is not that well understood — and on the detailed physics of the SN explosion mechanism. For example, Dessart et al. (2008)'s simulations assume that the *large scale* magnetic fields that obtain during collapse are similar in strength to the smaller-scale fields that are generated by neutrino-driven convection or the magneto-rotational instability (e.g., Akiyama et al. 2003). Whether the large-scale field structure required to produce an energetic SN can in fact be generated (e.g., via dynamo action; Thompson & Duncan 1993) is presently unclear.

If a BH is not created following the core-collapse of a massive rotating star, a rapidly spinning proto-NS remains behind in the cavity produced by the outgoing SN shock. In Chapter 2, I present calculations of the outflows from proto-NSs which show that a millisecond magnetar left in such a situation represents a promising GRB central engine model. Using multi-dimensional MHD calculations, Bucciantini et al. (2007, 2008, 2009) show how this wind may escape the overlying star and become collimated into a bipolar jet. These calculations suggest a model for the production of long GRB jets which is similar to that used to understand the

evolution and morphology of pulsar wind nebulae (e.g., Begelman & Li 1992) and which reproduces synchrotron maps of the Crab Nebula with great success (Del Zanna et al. 2006). Importantly, although the calculations presented in Chapter 2 are formally valid only for "free" proto-magnetars winds (and thus are strictly only applicable to the case of AIC), the simulations of Bucciantini et al. show that the mass and energy flux through the jet that emerges from the star closely resemble those set by the proto-NS wind at small radii *as if it were free*. Because proto-magnetar outflows reach a potential Lorentz factor $\Gamma \sim 100$ tens of seconds after core bounce, when the spin-down luminosity is still $\sim 10^{50}$ ergs s^{-1}, it is difficult to imagine that the birth of a millisecond magnetar does not produce a GRB (or some analogous high-energy transient).

Observationally distinguishing between BH and magnetar models for long-duration GRBs is a difficult task. In principle, a detailed comparison could be performed between theoretical models and the observed prompt emission. Figure 3.2 shows a prediction for the light curve expected from "naked" magnetar birth, assuming that radiation is generated as the free energy in the outflow of the proto-magnetar is dissipated through internal shocks. The qualitative shape of the light curve resembles the time-averaged "envelope" of a surprisingly large fraction of long GRBs. Another general prediction of the magnetar model is that, at $t \sim 10$ seconds after core-collapse, **outflows from higher luminosity bursts should possess higher Lorentz factors**: although the spin-down luminosity is larger for more rapidly spinning, highly magnetized NSs, the mass-loss rate at this epoch is probably similar for all NSs. Unfortunately, similar predictions are not yet available for BH models, in part because it is still not clear how the mass and energy fluxes in jets from accretion disks are determined. Furthermore, making definitive predictions, even when the initial properties of the jet are known, is hindered by our ignorance of the dissipation and radiation mechanisms in the outflow (see §1.2.2). For instance, complex light curves with multiple peaks separated by long quiescent intervals may pose a problem for magnetar models because proto-magnetars possess only a few basic timescales: the NS rotation period, the time the outflow becomes ultra-relativistic, the spin-down timescale, and the time that

the NS becomes optically thin to neutrinos. However, if the erratic nature of some GRBs is not intrinsic to the central engine but is rather a consequence of, e.g., an irregular dissipation process or modulation by the overlying stellar envelope, then definitive conclusions are difficult to reach.

The magnetar model makes another important prediction: **for the first $\sim 10-100$ s after core bounce (when the neutrino luminosity is very high), the GRB-producing outflow should be baryon-dominated**, unlike the pair-dominated outflows expected from older pulsars (Arons & Scharlemann 1979) or along flowlines that thread the event horizon of a BH. Therefore, if a baryon-rich outflow can be definitively ruled out on this early timescale (with $t = 0$ inferred from, e.g., GWs produced by the collapse; Fryer et al. 2002), the magnetar model could be refuted. Indeed, for especially close bursts (for which a GW detection might be possible), the baryon content of the outflow could be probed by ultra-high energy neutrinos (with, e.g., IceCube; Abbasi et al. 2009) since strong neutrino emission is only expected from decays following hadronic interactions.

1.3 Outline

In this section, I provide brief summaries of the Chapters in this thesis.

Chapter 2 provides a comprehensive study of the effects of magnetic fields and rotation on proto-NS winds by solving the equations of one-dimensional magneto-hydrodynamics (MHD) in the equatorial plane. I use these calculations to determine how the mass and energy-loss rates of magnetized rotating NSs evolve during the first ~ 100 seconds following their formation. These results delineate the NS birth parameters (surface magnetic field strength and initial rotation period) that are required to significantly alter the characteristics of early proto-NS evolution. I show that the energies, timescales, and magnetization (potential Lorentz factor) of outflows from millisecond "proto-magnetars" are consistent with those required to explain long-duration GRBs. The astrophysical origin of the r-process elements (which represent $\sim 1/2$ of the elements heavier than iron) remains a major unsolved mystery in nuclear astrophysics (e.g., Qian & Woosley 1996). Although

there is observational evidence that core-collapse SNe are an r-process site, theoretical studies of the winds from non-rotating unmagnetized proto-NS's fail to reproduce the necessary conditions (Thompson et al. 2001). I conclude Chapter 2 by evaluating whether magnetic fields and rotation are the missing ingredients required to make r-process nucleosynthesis successful in proto-NS winds.

Chapter 3 presents a model for Short GRBs with Extended Emission (SGRBEEs) from the accretion-induced collapse (AIC) of a white dwarf. The short GRB is powered by accretion onto the newly-formed NS from a small disk created during the collapse. If the rapidly spinning NS is strongly magnetized (a proto-magnetar), the extended emission can be produced by a magnetized outflow that extracts the NS's rotational energy. I calculate the spin-down powered light curve expected from proto-magnetar birth during AIC using the proto-NS wind calculations from Chapter 2 and assuming that the relative kinetic energy in the magnetar's outflow is dissipated by internal shocks. Using these calculations, I successfully model the extended emission from GRB 060614. I conclude by discussing the additional implications and predictions of the AIC model for SGRBEEs.

Chapter 4 presents calculations of the structure and nuclear composition of neutrino-heated MHD winds from the surface of two possible GRB central engines: proto-magnetars and hyper-accreting disks. I show, both numerically and analytically, that although the bases of GRB-producing outflows are neutron-rich (neutron-to-proton ratio $n/p \gg 1$), the outflow's composition is generally driven back to $n/p \sim 1$ by the absorption of electron neutrinos ($n + \nu_e \rightarrow p + e^-$) as it accelerates to relativistic speeds. In particular, I demonstrate that there is a correlation between n/p and the outflow's mass-loading, such that ultra-relativistic outflows are unlikely to be neutron-rich under most conditions. I conclude by summarizing the expected neutron content of outflows from various central engines, which may be used to observationally distinguish central engine models.

Chapter 5 presents a comprehensive study of the time-dependent evolution of viscously-spreading accretion disks formed from compact-object (CO) mergers. I use a one-zone model that follows the dynamics near the outer edge of the disk, where the majority of disk's mass resides and the accretion rate onto the central

BH is set. This study focuses on important transitions in the disk's thermodynamic properties and their implications for the late-time X-ray activity observed following some short GRBs. This work also addresses outflows from the disk. At early times, neutrino irradiation of the disk drives an outflow, which produces ^{56}Ni and leads to a radioactively-powered optical transient ~ 1 day following the merger. At later times, when the disk becomes radiatively-inefficient, a powerful outflow driven by viscous heating and nuclear energy released from $\alpha-$particle formation unbinds the majority of the disk's remaining mass. I conclude by discussing the implications of these results for the connection between CO mergers and short GRBs.

Chapter 6 extends the work in Chapter 5 by focusing on the nuclear composition of the late-time outflows from CO merger disks. In addition to the one-zone model developed in Chapter 5, I present one-dimensional height-integrated calculations of the viscous evolution of the disk and its nuclear composition. I show, both numerically and analytically, that weak interactions in the disk freeze-out (i.e., n/p stops evolving) at the same point that the disk thickens. As a result, CO merger disks freeze-out neutron rich ($n/p \gg 1$) and their late-time outflows synthesize rare neutron-rich isotopes. I conclude by using the measured abundances of these isotopes in our solar system to constrain the CO merger rate in our Galaxy and the beaming fraction (i.e., jet opening angles) of short GRBs.

Chapter 7 presents calculations of the evolution of accretion disks formed from AIC using the methods developed in Chapter 6. This work is connected to the AIC model presented in Chapter 3, but focuses on the more general case, when the central NS is not necessarily highly magnetized. I show that although the viscous and thermal evolution of AIC accretion disks is similar to that of disks produced in CO mergers, the disk's final nuclear composition is significantly altered by neutrino irradiation from the proto-NS. As a result, the late-time outflows from AIC disks likely produce a substantial ^{56}Ni yield (rather than highly neutron-rich elements), which creates a moderately bright optical transient lasting ~ 1 day. I conclude by discussing the detection prospects for AIC with upcoming optical transient surveys and as beacons to gravitational wave sources.

Chapter 2

Proto-Neutron Star Winds with Magnetic Fields and Rotation

B. D. Metzger, T. A. Thompson, E. Quataert, ApJ, 619, 623.[1]

Abstract

We solve the one-dimensional neutrino-heated non-relativistic magnetohydrodynamic (MHD) wind problem for conditions that range from slowly rotating (spin period $P \gtrsim 10\,\mathrm{ms}$) protoneutron stars (PNSs) with surface field strengths typical of radio pulsars ($B \lesssim 10^{13}\,\mathrm{G}$), to "proto-magnetars" with $B \approx 10^{14} - 10^{15}\,\mathrm{G}$ in their hypothesized rapidly rotating initial states ($P \approx 1\,\mathrm{ms}$). We use the relativistic axisymmetric simulations of Bucciantini et al. (2006) to map our split-monopole results onto a more physical dipole geometry and to estimate the spindown of PNSs when their winds are relativistic. We then quantify the effects of rotation and magnetic fields on the mass-loss, energy-loss, and thermodynamic structure of PNS winds. The latter is particularly important in assessing PNS winds as the astrophysical site for the r-process. We describe the evolution of PNS winds through the Kelvin-Helmholtz cooling epoch, emphasizing the transition between

[1]The Astrophysical Journal, 659:561–579, 2007 April 10

(1) thermal neutrino-driven, (2) non-relativistic magnetically-dominated, and (3) relativistic magnetically-dominated outflows. In the last of these stages, the spin-down is enhanced relative to the canonical force-free rate because of additional open magnetic flux caused by neutrino-driven mass-loss. We find that proto-magnetars with $P \approx 1$ ms and $B \gtrsim 10^{15}$ G drive relativistic winds with luminosities, energies, and Lorentz factors (magnetization $\sigma \sim 0.1 - 1000$) consistent with those required to produce long duration gamma-ray bursts and hyper-energetic supernovae (SNe). A significant fraction of the rotational energy may be extracted in only a few seconds, sufficiently rapidly to alter the asymptotic energy of the SN remnant, its morphology, and, potentially, its nucleosynthetic yield. We find that winds from PNSs with somewhat more modest rotation periods ($\approx 2 - 10$ ms) and with magnetar-strength fields produce conditions significantly more favorable for the r-process than winds from slowly rotating, non-magnetized PNSs. Lastly, we argue that energy and momentum deposition by convectively-excited waves may be important in PNS winds. We show that this further increases the likelihood of successful r-process, relatively independent of the PNS rotation rate and magnetic field strength.

2.1 Introduction

On timescales $\lesssim 1$ s following the core collapse of a massive star, neutrino emission from the resulting hot, deleptonizing protoneutron star (PNS) may play an essential role in launching the supernova (SN) shock (Herant et al. 1994; Burrows, Hayes, & Fryxell 1995; Janka & Müller 1995) or in generating large-scale anisotropies through hydrodynamical instabilities (Blondin et al. 2003; Scheck et al. 2006; Burrows et al. 2006a,b). Independent of how the explosion is initiated at early times, a small fraction of the PNS's cooling neutrino emission continues heating the surface layers of the PNS, driving a persistent thermal wind into the cavity evacuated by the rapidly-expanding SN shock (Duncan, Shapiro, & Wasserman 1986; Woosley et al. 1994); this post-explosion neutrino-driven mass-loss persists for the duration of the PNS's Kelvin-Helmholtz cooling epoch, which lasts a time

$\tau_{\rm KH} \sim 10 - 100$ s (Burrows & Lattimer 1986; Pons et al. 1999).

Once the SN shock has been launched and the PNS cooling epoch has begun, neutrino-driven winds from non-rotating non-magnetic PNSs are unlikely to be energetically important on the scale of the kinetic energy of the accompanying SN ($E_{\rm SN} \approx 10^{51}$ ergs). However, in the presence of a sufficiently strong global magnetic field the dynamics of a PNS's neutrino-heated outflow are significantly altered (e.g., Thompson 2003a,b). This point is germane because $\sim 10\%$ (Kouveliotou et al. 1994; van Paradijs et al. 1995; Lyne et al. 1998) of young Galactic neutron stars possess significantly stronger surface magnetic fields ($\sim 10^{14} - 10^{15}$ G) than those usually inferred from pulsar spin-down estimates ("magnetars"; for a recent review see Woods & Thompson 2004). While the precise origin of these large field strengths is uncertain, it has been argued that their amplification occurs via a dynamo during $\tau_{\rm KH}$ (Duncan & Thompson 1992; Thompson & Duncan 1993). The efficiency of the dynamo is determined in part by the core's initial rotation rate $\Omega_0 = 2\pi/P_0$, and analytic arguments suggest that the formation of global magnetar-strength fields might require $P_0 \sim 1$ ms rotation at birth. Such rapid rotation would also alter the dynamics of the PNS wind and provide a reservoir of rotational energy significant on the scale of the accompanying SN explosion:

$$E_{\rm rot} \simeq 2 \times 10^{52}\, M_{1.4}\, R_{10}^2\, P_{\rm ms}^{-2}\, {\rm ergs}, \tag{2.1}$$

where $M_{1.4}$ is the PNS mass in units of 1.4 $M_\odot$, R_{10} is the radius of the PNS in units of 10 km, and $P_{\rm ms}$ is the initial PNS rotation period in ms.

Previous authors have suggested that if magnetars are indeed born rapidly rotating, their rotational energy could be efficiently extracted through a magnetized wind (Usov 1992; Thompson 1994; Wheeler et al. 2000; Thompson, Chang, & Quataert 2004, henceforth TCQ). Indeed, a proto-magnetar wind's energetics, timescale, and potential for highly relativistic outflow resemble those of the central engine required to power long-duration gamma-ray bursts (LGRBs). TCQ argue that an accurate description of magnetized PNS spin-down must include the effects of neutrino-driven mass-loss. The significant mass-loss accompanying the Kelvin-Helmholtz epoch may open the otherwise closed magnetosphere into a

"split monopole"-like structure, enhancing the early spin-down rate of the PNS. In addition, the mass loading of a PNS wind, and hence its potential asymptotic Lorentz factor Γ, is largely controlled by the neutrino luminosity during the Kelvin-Helmholtz epoch. This "baryon-loading" issue is particularly important in the LGRB context, where $\Gamma \sim 10 - 1000$ are typically inferred.

Because magnetar births are relatively frequent, most cannot produce classical LGRBs, which only occur in $\sim 0.1 - 1\%$ of massive stellar deaths (e.g., Paczynski 2001, Podsiadlowski et al. 2004, Piran 2005); however, a more common observational signature of magnetar birth may include less energetic or mildly relativistic events, which could be observable as X-ray transients or unusual SNe. Under some circumstances, the asymmetric energy injection from proto-magnetar winds could produce global anisotropies in the SN remnant, as has been detected through polarization measurements of some SNe (e.g., Wang et al. 2001, 2003). In addition, if significant rotational energy can be extracted sufficiently rapidly following the launch of the SN shock, the nucleosynthetic yield of the SN could be altered (TCQ), which could explain nickel-rich, hyper-energetic SNe such as SN 1998bw (Galama et al. 1998) or SN 2003dh (Hjorth et al. 2003; Stanek et al. 2003). Lastly, LGRBs occurring without associated SNe (e.g., GRBs 060505, 060614; Fynbo et al. 2006; Gal-Yam et al. 2006; Della Valle et al. 2006) may be accommodated if a proto-magnetar results from the accretion-induced collapse (AIC) of a white dwarf (see §2.4.4 and Chapter 3).

Quite apart from the possible impact of PNS winds on the surrounding SN shock, PNS winds themselves have often been considered a promising site for the production of r-process nuclides. However, the conditions necessary for a successful third peak ($A \approx 195$) r-process have not been realized in detailed studies of non-rotating, non-magnetized PNS winds (e.g., Qian & Woosley 1996; Cardall & Fuller 1997; Otsuki et al. 2000; Thompson et al. 2001). Given the, as yet, unidentified site of Galactic r-process enrichment and the relatively large birthrate of magnetars, it is essential to consider what effects a strong magnetic field and rapid rotation might have on nucleosynthesis in PNS winds. Conversely, if the nucleosynthetic yield from rotating, magnetized PNS winds could be well-determined theoretically,

the birth period and magnetic field distribution of neutron stars could perhaps be constrained from observations of heavy elemental abundances.

2.1.1 Stages of PNS Evolution

A sufficiently-magnetized PNS wind goes through at least three distinct stages of evolution following the launch of the SN shock ($t = 0$):

(1) During the earliest phase the PNS surface temperature is so high ($\gtrsim 5$ MeV) and the radius of the PNS is so large ($R_\nu \sim 20 - 50$ km) that, even for a magnetar-strength field, the post-explosion outflow is likely to be purely thermally-driven.

(2) By $t \sim 1$ s the SN shock has propagated to well outside the sonic point of the PNS wind. The PNS will contract and cool to a point at which, if the surface field is sufficiently strong, the outflow becomes magnetically dominated. The strong magnetic field enhances angular momentum and rotational energy-loss by forcing outgoing fluid elements to effectively corotate with the PNS surface out to the Alfvén radius (R_A) at several stellar radii, in analogy with classic work on non-relativistic stellar winds and the solar wind (e.g., Schatzman 1962, Weber & Davis 1967, and Mestel 1968). For sufficiently rapidly rotating PNSs, the spin-down timescale ($\tau_{\rm J} \equiv \Omega/\dot{\Omega}$) can be comparable to $\tau_{\rm KH}$, implying that much of the rotational energy of the PNS can be extracted in a non-relativistic, but magnetically-dominated wind. The neutrino luminosity at these relatively early times is still large (e.g., $L_\nu \sim 10^{52}$ ergs s^{-1}; see Pons et al. 1999, Fig. 14), and, for sufficiently rapid rotation, mass-loss is significantly enhanced by centrifugal flinging (TCQ). The outflow during this phase will be collimated about the PNS rotation axis by magnetic stresses (e.g., Bucciantini et al. 2006; hereafter B06).

(3) As the PNS continues to cool, the luminosity and mass-loading decrease to the point at which corotation is sustained out to nearly the light cylinder ($R_{\rm L} \equiv 2\pi c/P \simeq 48\, P_{\rm ms}^{-1}$ km). The spin-down rate then becomes approximately independent of the mass-loss rate $\dot{M}$ and the flow becomes relativistic, obtaining high magnetization $\sigma \equiv \Phi_B^2 \Omega^2/\dot{M}c^3$, where Φ_B is the total open magnetic flux

per 4π steradian (Michel 1969). Although an ultra-relativistic, pulsar-like wind is inevitable soon after $\tau_{\rm KH}$ because $\dot{M}$ abates as the neutrino luminosity vanishes, relativistic outflow can begin prior to the end of the Kelvin-Helmholtz phase. Because this outflow is accompanied by significant mass-loss, it is generally only mildly relativistic. Although the energy extracted via relativistic winds is primarily concentrated at low latitudes (B06), the confining pressure of the overlying, exploding, stellar progenitor (e.g., Wheeler et. al 2000; Uzdensky & MacFadyen 2006; Bucciantini et al. 2007, 2008, 2009) or the walls of the collimated cavity carved by the preceding non-relativistic phase may channel the relativistic outflow into a bipolar, jet-like structure.

The primary focus of this paper is to delineate the magnetic field strengths and rotation rates required to significantly alter the characteristics of early PNS evolution by solving the one-dimensional (1D) non-relativistic MHD, neutrino-heated wind problem for conditions that range from normal pulsars to proto-magnetars. In particular, we quantitatively explore the transition that occurs between stages (1) and (2) above; with these results we analyze some of the immediate consequences of neutron star birth. We defer a detailed study of the transition between stages (2) and (3) to future work, but we do explicitly address the parameter space of the $\sigma = 1$ boundary. Relativistic, mass-loaded MHD winds have been studied recently by B06 in two dimensions for both a monopolar and aligned-dipolar field structure, assuming an adiabatic equation of state. While the work of B06 is critical to understanding the multi-dimensional character of PNS winds (for instance, the degree of collimation and the fraction of open magnetic flux) it does not address the neutrino microphysics necessary for a direct application to PNS environments; this work and that of B06 are thus complementary in studying PNS spin-down in the presence of rapid rotation and a large magnetic field.

2.1.2 Chapter Organization

In §2.2 we enumerate the equations of MHD (§2.2.1), discuss the relevant microphysics (§2.2.2), and elaborate on our numerical methods (§2.2.3). Section

2.3 presents the results of our calculations and examines the regimes of magnetized PNS wind evolution. Section 2.4 discusses the implications of this work, examining the time-evolution of a cooling, magnetized PNS (§2.4.1), weighing the implications for LGRBs and hyper-energetic SNe (§2.4.2), and considering the viability for third-peak r-process nucleosynthesis in magnetized, rotating PNS winds (§2.4.3). In §2.4.3 we consider the effects that wave heating have on the r-process in PNS winds and in §2.4.4 we briefly discuss other contexts in which our calculations may be applicable, including the accretion-induced collapse of white dwarfs, "collapsars," and merging neutron star binaries. Finally, section 2.5 summarizes the conclusions of our work.

2.2 PNS Wind Model

2.2.1 MHD Equations and Conserved Quantities

Making the simplifications of Weber & Davis (1967), we restrict all physical quantities to be solely functions of radius r and time t, and confine our analysis to the equatorial plane so that the magnetic field $\mathbf{B} = [B_r, B_\phi]$ and fluid velocity $\mathbf{v} = [v_r, v_\phi]$ have no θ components. We employ Newtonian gravity for a PNS of mass M acting on gas of density ρ. We also assume that the plasma is a perfect conductor with an isotropic thermal pressure P. Under these restrictions the time evolution equations of non-relativistic MHD are

$$\frac{\partial \rho}{\partial t} = -\frac{1}{r^2}\frac{\partial}{\partial r}(r^2 \rho v_r) \tag{2.2}$$

$$\frac{\partial v_r}{\partial t} = \frac{v_\phi^2}{r} - v_r\frac{\partial v_r}{\partial r} - \frac{1}{\rho}\frac{\partial \mathrm{P}}{\partial r} - \frac{GM}{r^2} - \frac{1}{4\pi\rho}\left[\frac{B_\phi^2}{r} + B_\phi\frac{\partial B_\phi}{\partial r}\right] \tag{2.3}$$

$$\frac{\partial v_\phi}{\partial t} = \frac{1}{r}\left[\frac{B_r}{4\pi\rho}\frac{\partial}{\partial r}(rB_\phi) - v_r\frac{\partial}{\partial r}(rv_\phi)\right] \tag{2.4}$$

$$\frac{\partial B_\phi}{\partial t} = \frac{1}{r}\frac{\partial}{\partial r}(r[v_r B_\phi - v_\phi B_r]) \tag{2.5}$$

We have neglected neutrino radiation pressure in equation (2.3) because the neutrino luminosity is always below the neutrino Eddington limit. In steady state,

equation (2.2) gives a radially-conserved mass flux:

$$\dot{M} = \Delta\Omega r^2 \rho v_r, \tag{2.6}$$

where $\Delta\Omega$ is the opening solid angle of the wind. While the evolution equations considered are formally valid only in the equatorial plane, quoted values for $\dot{M}$ will be normalized to $\Delta\Omega = 4\pi$, as if the solutions were valid at all latitudes. As discussed in §2.4.1, this normalization is an overestimate because the PNS's closed magnetic flux prevents mass outflow from near the equator and centrifugal flinging concentrates $\dot{M}$ at relatively low latitudes (B06).

We take the radial magnetic field structure to be that of a "split monopole": $B_r = B_\nu (R_\nu/r)^2$, where R_ν is the radius of the PNS and B_ν is the monopole surface field strength; this prescription conserves the magnetic flux $4\pi\Phi_B \equiv 4\pi r^2 B_r$. B06 show that the spin-down in dipole simulations can be expressed in terms of an equivalent monopole field, which depends on the fraction of open magnetic flux. As discussed further in §2.4.1, we can therefore relate our monopole spin-down calculations to the more realistic dipole simulations of B06.

In steady state, manipulation of equations (2.4) and (2.5) gives the conserved specific angular momentum $\mathcal{L}$ and "the consequence of induction" $\mathcal{I}$ (e.g., Lamers & Cassinelli 1999):

$$\mathcal{L} = \mathcal{L}_{\rm gas} + \mathcal{L}_{\rm mag} = r v_\phi - \frac{r B_r B_\phi}{4\pi\rho v_r} \tag{2.7}$$

$$\mathcal{I} = r(v_\phi B_r - v_r B_\phi) \tag{2.8}$$

The total rate of angular momentum-loss from the PNS is therefore $\dot{J} = \mathcal{L}\dot{M}$.

For conditions of interest, photons are trapped and advected with the wind, providing no significant energy transport on the timescales of interest (Duncan, Shapiro, & Wasserman 1986). Instead, the PNS evolution is controlled by its neutrino luminosity L_ν, which provides heating $\dot{q}_\nu^+$ (per unit mass) above the PNS surface. Including net neutrino heating ($\dot{q}_\nu = \dot{q}_\nu^+ - \dot{q}_\nu^-$; see §2.2.2) provides a source term in the wind entropy equation:

$$T\frac{dS}{dt} = \dot{q}_\nu, \tag{2.9}$$

where $d/dt \equiv \partial/\partial t + v_r(\partial/\partial r)$, S is the wind entropy per unit mass, and T is the wind temperature. The asymptotic wind entropy S^a quantifies the total net heating a parcel of gas experiences as it is carried out by the PNS wind. As discussed further in §2.2.2, when applying equation (2.9) we assume that the wind's composition (electron fraction) remains constant (see Chapter 4 for calculations that include the full evolution of the wind composition).

With net heating the Bernoulli integral $\mathcal{B}$ is not constant with radius (in steady state); instead it receives an integrated contribution from $\dot{q}_\nu$:

$$\dot{M}\Delta\mathcal{B} = \dot{M}\{\mathcal{B}(r) - \mathcal{B}(r_0)\} = \int_{r_0}^{r} \rho\dot{q}_\nu \Delta\Omega r'^2 dr', \tag{2.10}$$

where

$$\mathcal{B} \equiv \frac{1}{2}(v_r^2 + v_\phi^2) + h - \frac{GM}{r} + \mathcal{L}_{\rm mag}\Omega, \tag{2.11}$$

$h \equiv e + \mathrm{P}/\rho$ is the specific enthalpy, e is the specific internal energy, $\mathcal{L}_{\rm mag}\Omega$ is the specific magnetic energy, and Ω is the stellar rotation rate.

To assess the impact of the PNS wind on its surroundings, it is useful to define η, the ratio of the rotational power lost by the PNS, $\dot{E}_{\rm rot} = \Omega\dot{J}$, to the asymptotic wind power $\dot{E}^a = \mathcal{B}^a\dot{M}$:

$$\eta \equiv \frac{\Omega\dot{J}}{\dot{E}^a} = \frac{\Omega\mathcal{L}}{\mathcal{B}^a}, \tag{2.12}$$

where $\mathcal{B}^a$ is the Bernoulli integral evaluated at large radii. Magnetized winds are typically assumed to have $\eta \approx 1$, but we find that in some cases $\eta \gg 1$ because much of the rotational energy is used to unbind the wind from the PNS (see §2.3.2).

2.2.2 Microphysics

The local heating and cooling rates relevant to the Kelvin-Helmholtz cooling phase have been extensively evaluated in efforts to quantify unmagnetized, slowly-rotating PNS winds as an astrophysical site for r-process nucleosynthesis (e.g., Qian & Woosley 1996, Thompson et al. 2001; hereafter T01). For our calculations we adopt the heating and cooling rates used in the analytic work of Qian & Woosley (1996, hereafter QW) for $\nu/\bar{\nu}$ annihilation and for the charged-current processes

$\nu_e + n \leftrightarrow p + e^-$ and $\bar{\nu}_e + p \leftrightarrow n + e^+$. For heating and cooling from inelastic neutrino-lepton scattering we use the rates of T01. The dominant contributions to the net heating rate are the charged-current processes, but scattering and annihilation become more significant as the entropy of the wind increases and the thermal pressure becomes radiation-dominated. The scattering and charged-current rates effectively vanish once $T \rightarrow 0.5$ MeV because the e^-/e^+ pairs annihilate and the nucleons combine into α particles. We artificially take this cutoff into account by setting $\dot{q}_\nu = 0$ for $T < 0.5$ MeV.

Because the charged-current interactions modify the neutron abundance of the outflow the electron fraction Y_e should be evolved in addition to the temperature and pressure. However, the dynamics of the wind are not sensitive to the precise profile of Y_e and thus, for simplicity, we take Y_e to be fixed at a reasonable asymptotic value at all radii: $Y_e = Y_e^a = 0.4$. This is a good approximation given how rapidly in radius Y_e^a obtains in non-rotating, unmagnetized calculations (see T01, Fig. 7) and how relatively weakly the total heating and cooling rates depend on Y_e for $Y_e \lesssim 0.5$.

As in T01 we calculate local neutrino fluxes by considering a single (for all neutrino species) sharp, thermal neutrinosphere at R_ν. To the desired accuracy of our calculations this approximation is generally good, even when the density scale height (and hence nucleon-absorption optical depth) is extended by rapid rotation. For this paper we index stages of the PNS thermal evolution in terms of the anti-electron neutrino luminosity $L_{\bar{\nu}_e}$. We scale all other neutrino luminosities ($L_{\nu_e}, L_{\nu_\mu}, L_{\bar{\nu}_\mu}, L_{\nu_\tau}$, and $L_{\bar{\nu}_\tau}$) as in TCQ: $L_{\nu_e} = L_{\bar{\nu}_e}/1.3 = 1.08 L_{\nu_\mu}$, where μ denotes each of the other four neutrino/anti-neutrino species. Note that the total neutrino luminosity is then $L_\nu \simeq 4.6 L_{\bar{\nu}_e}$. Following T01, all first energy moments at the neutrinosphere ($\langle \epsilon_\nu \rangle \equiv \langle E_\nu^2 \rangle / \langle E_\nu \rangle$, where E_ν is the neutrino energy) were scaled with luminosity as $\langle \epsilon_\nu \rangle \propto L_\nu^{1/4}$, anchoring $\{\langle \epsilon_{\nu_e} \rangle, \langle \epsilon_{\bar{\nu}_e} \rangle, \langle \epsilon_{\nu_\mu} \rangle\}$ at $\{11, 14, 23\}$MeV for $L_{\bar{\nu}_e,51} = 8$, where $L_{\bar{\nu}_e,51}$ is the anti-electron neutrino luminosity in units of 10^{51} ergs s^{-1}. Higher energy moments necessary for the heating calculations ($\langle \epsilon_{\nu_e}^n \rangle, \langle \epsilon_{\bar{\nu}_e}^n \rangle$, etc.) are related to the first through appropriate integrals over the assumed Fermi-Dirac surface distribution. We should note that the relation-

ship between the neutrino luminosity and mean neutrino energy we have assumed, while a reasonable approximation, is likely to be more complicated. For example, Pons et al. (1999) find that the mean energy is roughly constant for the first ~ 10 s of cooling, despite the fact that the neutrino luminosity decreases monotonically (see their Fig. 18).

The neutrino heating and cooling rates discussed above will be modified by the presence of magnetar-strength fields in the heating region due to quantum effects restricting the electron(positron) phase space (Lai & Qian 1998; Duan & Qian 2004). We neglect the effects that high B have on $\dot{q}_\nu$ and defer study of these effects to future work. In addition, for strong surface magnetic field strengths, heating via the dissipation of convectively-excited MHD waves may become important (Suzuki & Nagataki 2005). We assess the importance of wave heating and momentum deposition in §2.4.3.

In this work we include gravitational redshifts, radial Doppler shifts, and modifications to the "effective solid angle" (and hence local neutrino flux) presented by the neutrinosphere in the curved spacetime. The latter effect is described in Salmonson & Wilson (1999), while the Doppler and redshifts can be combined into the simple, approximate prescription relevant for all neutrino species:

$$\langle \epsilon_\nu^{\ n} \rangle = (\phi_Z \phi_D)^{n+3} \langle \epsilon_\nu^{\ n} \rangle |_{r=R_\nu}, \tag{2.13}$$

where

$$\phi_Z \equiv \alpha(R_\nu)/\alpha(r) \ , \ \phi_D \equiv \gamma(1 - v_r/c), \tag{2.14}$$

$\alpha(r) \equiv \sqrt{1-(2GM/c^2 r)}$, $\gamma^{-1} \equiv \sqrt{1-(v_r^2+v_\phi^2)/c^2}$, and we have assumed that at radii where the equatorial flow becomes mildly relativistic, typical neutrinos will primarily be moving radially. We emphasize that while we include neutrino gravitational redshifts in calculating heating rates we calculate the wind dynamics in Newtonian gravity. Including the effects of the deeper general-relativistic (GR) potential of a Schwarzschild metric lowers $\dot{M}$ and increases S^a, Y_e^a, and the asymptotic wind speed v^a (Fuller & Qian 1996; Cardall & Fuller 1997).

Our model's equation of state (EOS) includes contributions from photon radiation, ideal nucleons, and relativistic, degenerate electrons and positrons. Non-

relativistic nucleons generally dominate the EOS near the PNS surface, but within a density scale height above R_ν the flow becomes radiation-dominated. As with the heating/cooling rates, high magnetic field effects on the EOS are ignored.

2.2.3 Numerical Method

In the steady-state Weber-Davis wind, three critical points occur in the radial momentum equation at radii where the outflow velocity matches the local phase speed of infinitesimal fluid disturbances. The steady-state eigenvalues $\dot{M}, \mathcal{L}$, and $\mathcal{B}$ (eqs. [2.6], [2.7], and [2.11]) are fixed by the requirement that the solution pass smoothly through the slow-magnetosonic, Alfvénic, and fast-magnetosonic points. Physically, we choose these solutions over sub-magnetosonic "breezes" because we assume the SN shock or fallback pressures at large radii are insufficient to stifle the strong ram-pressures of the wind. However, fallback at early times is not well-understood because it depends sensitively on the mechanism for launching the SN shock (Chevalier 1989; Woosley & Weaver 1995) and thus this issue deserves further attention. Although the PNS radius, rotation rate, and neutrino luminosity evolve in time, for realistic wind conditions the timescale required for any of the MHD wavemodes to traverse all critical points is always much shorter than the timescale over which the wind characteristics appreciably change (e.g., $\tau_{\rm KH}$ or the spin-down timescale $\tau_{\rm J}$). For this reason a time-series of steady-state solutions is generally sufficient to accurately model the wind during all phases of the PNS evolution. However, precisely because all physical solutions must pass through each critical point, in the time-independent formulation of this problem boundary conditions must be placed on the wind solution at these locations. To avoid this numerically complicated singularity structure, we have instead solved the more complete, time-dependent version of the problem using the 6th order space/3rd order time, "inhomogeneous" 2N-RK3 scheme of Brandenburg (2001).

Our code evolves the variables $(\rho, T, v_r, v_\phi, B_\phi)$. The value of the PNS mass M, neutrinosphere radius R_ν, magnetic flux $\Phi_B = B_\nu R_\nu^2$, stellar rotation rate Ω, and neutrino luminosity L_ν are the parameters that uniquely identify a wind solution.

We use $M = 1.4\ \mathrm{M}_\odot$ and $R_\nu = 10$ km in all of our calculations. Because our code is intrinsically non-conservative, we use the constancy of $\dot{M}$, $\mathcal{L}$, and $\mathcal{I}$ and equation (2.10)'s constraint on $\mathcal{B}$ as independent checks on the code's numerical accuracy. For numerical stability, an artificial viscosity of the form $\nu\nabla^2$ is included in the evolution of each variable, where ν is an appropriately-scaled kinematic viscosity (e.g., Brandenburg 2001).

We chose the location of the outer boundary, generally at $r \approx 1000$ km, as a compromise between the run-time to reach steady-state and the desire to minimize the effects of artificially forcing the fast point on the computational grid (see discussion in §2.2.3). We space the radial grid logarithmically, choosing the number of grid points (generally $500 - 2000$) to obtain the desired level of conservation of $\dot{M}, \mathcal{L}, \mathcal{I}$, and $\mathcal{B}$ while simultaneously maintaining large enough artificial viscosity to maintain code stability. With sufficient resolution and low enough viscosity the code shows radial conservation of all eigenvalues to $\lesssim 1\%$ across the entire grid, although we did not require this level of conservation for all solutions so that we could efficiently explore the parameter space of wind properties. The mass-loss rate was the most difficult eigenvalue to conserve yet is accurate (relative to its fully converged value) to at least $\sim 10\%$ for all solutions presented in this paper.

Boundary Conditions

The azimuthal speed v_ϕ at R_ν is set to enforce $v_{\phi,\nu} = R_\nu\Omega + v_{r,\nu}B_{\phi,\nu}/B_\nu$, where a subscript ν denotes evaluation at R_ν and where Ω is the stellar rotation rate that defines the angular speed of the rotating frame in which the surface electric field vanishes (MacGregor & Pizzo 1983). In all cases we consider, $v_{\phi,\nu} \simeq R_\nu\Omega$. The temperature at the PNS surface $T(R_\nu)$ (generally ≈ 5 MeV) is set by requiring that the net heating rate $\dot{q}_\nu$ vanish; this assumes the inner atmosphere is in LTE (Burrows & Mazurek 1982). Given our assumption that matter at the inner grid point maintains LTE, we fix the density at R_ν to be $\simeq 10^{12}$ g cm^{-3} so that the neutrino optical depth τ_ν at the PNS surface reaches $\sim 2/3$, thereby defining a neutrinosphere. For slow rotation we find that the solution outside the inner

few scale heights remains relatively insensitive to our choice for the inner density, although we find that $\dot{M}$ depends somewhat sensitively on $\rho(R_\nu)$ as the PNS rotation rate increases approaching break-up.

If all three critical points are captured on the numerical grid, the outer boundary conditions are not in causal contact with the interior wind and will have no effect on its steady-state eigenvalues. However, as the temperature of the wind declines, the fast magnetosonic point moves to very large radii; in fact, as the sound speed $c_{\rm s} \to 0$ the fast point formally approaches infinity (Michel 1969). For this reason, the fast point is difficult to keep on the computational grid. Solutions without the fast point captured on the grid are sensitive to the outer boundary condition, with different choices altering, for instance, the spin-down rate. Therefore, to artificially force the fast point on the grid we increase the outer radial velocity boundary-condition until the fast point is captured. Otherwise equivalent solutions with the fast point naturally located and artificially placed on the grid were compared in several cases; we found that although the velocity structure changes at radii far outside the Alfv́en radius, our imposed boundary condition had little effect on the eigenvalues of the problem and the correct asymptotic speed was obtained (albeit prematurely in radius). Since the eigenvalues uniquely determine the steady-state solution, this technique, when necessary, was a useful expedient to obtain the desired transmagnetosonic solution.

2.3 Results

Figure 2.1 summarizes the physical regimes of PNS winds as a function of $L_{\bar{\nu}_e}$ and rotational period P for a representative strongly magnetized PNS: $B_\nu = 2.5 \times 10^{14}$ G, $M = 1.4$ M$_\odot$, and $R_\nu = 10$ km. A cooling PNS of fixed surface field will traverse a path from high to low L_ν in this diagram, reaching $L_{\bar{\nu}_e,51} \sim 0.1$ at $t = \tau_{\rm KH}$ (see eq. [2.28]). If the spindown timescale $\tau_{\rm J}$ is less than $\tau_{\rm KH}$, the PNS evolves to higher P during $\tau_{\rm KH}$, but otherwise, the PNS evolves from higher to lower L_ν at roughly constant P (see Tables 2.1 and 2.2 for representative $\tau_{\rm J}$). The regions in Figure 2.1 correspond to the different wind phases outlined in §2.1.1: (1)

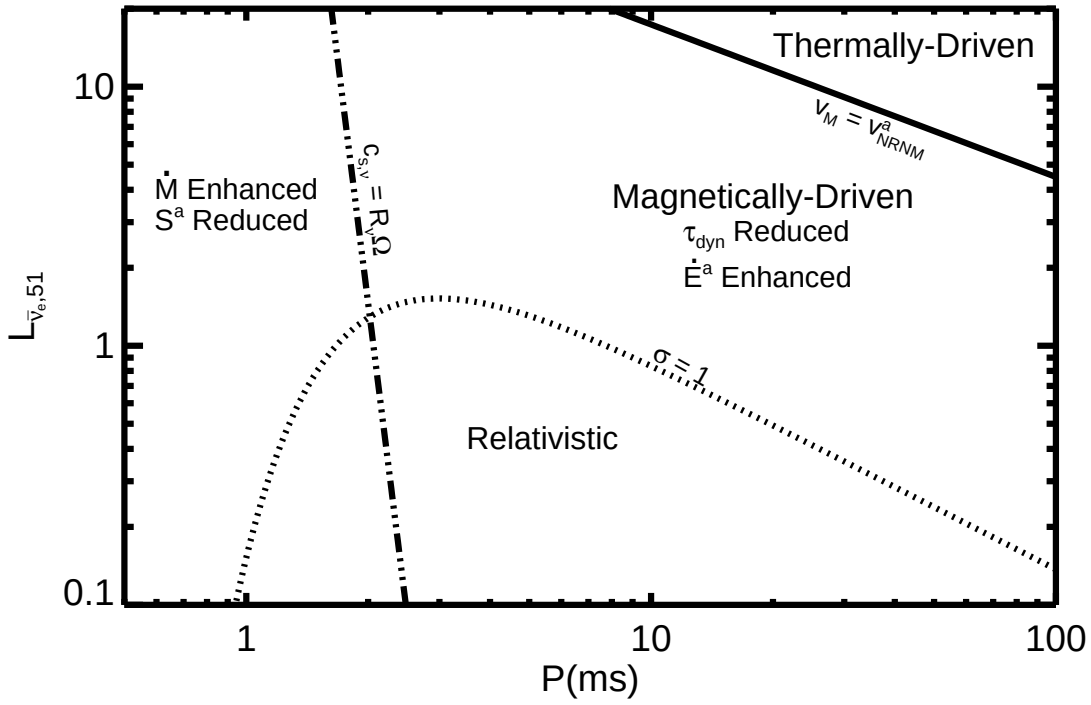

Figure 2.1: The regimes of PNS winds in the space of $L_{\bar{\nu}_e}(= L_{\bar{\nu}_e,51} \times 10^{51}$ ergs $s^{-1})$ and rotation period P for a representative strongly magnetized PNS: $B_\nu = 2.5 \times 10^{14}$ G, $R_\nu = 10$ km, and $M = 1.4$ $M_\odot$. A monopole field geometry is assumed. A cooling PNS will evolve from high $L_{\bar{\nu}_e}$ to low $L_{\bar{\nu}_e}$ in this diagram, with $L_{\bar{\nu}_e,51} \sim 10$ at a time $t_0 \sim 1$ s following the launch of the SN shock to $L_{\bar{\nu}_e,51} \sim 0.1$ by the end of the Kelvin-Helmholtz phase ($\tau_{\rm KH} \sim 10 - 100$ s after explosion). The solid line (eq. [2.18]) shows the boundary between PNS winds that are primarily thermally-driven by neutrino heating (high L_ν; slow rotation) and winds that are primarily magneto-centrifugally-driven (low L_ν; rapid rotation); for the latter, the wind power $\dot{E}^a$ is enhanced (see eq. [2.20]) and the dynamical time $\tau_{\rm dyn}$ is reduced (see Fig. 2.12). The dotted line ($\sigma = 1$; eq. [2.27]) shows the boundary between non-relativistic and relativistic magnetically-driven winds. For sufficiently rapid rotation ($P \lesssim 2 - 3$ ms; the dot-dashed line), the mass-loss from the PNS ($\dot{M}$) is enhanced because of centrifugal flinging (eq. [2.24]) and the asymptotic wind entropy S^a is reduced (eq. [2.38]) because matter moves more rapidly through the region of significant neutrino heating. The dynamical time and entropy are important for nucleosynthesis in the wind (§2.4.3). For $B_\nu \gtrsim 2.5 \times 10^{14}$ G the thermally-driven region shrinks (to longer P and higher $L_{\bar{\nu}_e}$; eq. [2.18]) and the relativistic region expands (to higher $L_{\bar{\nu}_e}$; eq. [2.27]). For $R_\nu \gtrsim$ 10 km, as will occur at early times when the PNS is still contracting, the wind is likely to be thermally-driven.

a thermally-driven wind at high L_ν and long P; (2) a non-relativistic, magnetically-driven wind at high L_ν and short P; and (3) a relativistic, magnetically-driven wind at low L_ν and short P. In addition to these different regimes, Figure 2.1 illustrates the range of rotation periods for which $\dot{M}$ is enhanced by centrifugal flinging (roughly $P \lesssim 2-3$ ms; see also Fig. 2.6) and for which $\tau_{\rm dyn}$, the dynamical time at $T = 0.5$ MeV (eq. [2.36]), and the asymptotic wind entropy S^a are altered from their non-rotating, non-magnetized values (which has important consequences for r-process nucleosynthesis; see §2.4.3). In this section, we present and discuss the properties of solutions for a range of parameters $(B_\nu, P, L_{\bar{\nu}_e})$ that span each of the non-relativistic regimes illustrated in Figure 2.1. Some of the properties of wind solutions at $L_{\bar{\nu}_e} = 8 \times 10^{51}$ ergs s^{-1}, which corresponds to a relatively early stage in the PNS cooling evolution, are given in Table 2.1. Table 2.2 compares the properties of wind solutions with $B_\nu = 2.5 \times 10^{15}$ G at two different neutrino luminosities ($L_{\bar{\nu}_e} = 8 \times 10^{51}$ and 3.5×10^{51} ergs s^{-1}).

2.3.1 Thermally-Driven Winds

The thermally-driven region in Figure 2.1 corresponds to conditions under which the PNS outflow is driven primarily by neutrino heating; the magnetic field and the rotation rate are unimportant in either accelerating or setting the mass-loss rate of the wind. Figure 2.2 shows the velocity structure of such an effectively non-rotating, non-magnetized (NRNM) solution for $L_{\bar{\nu}_e,51} = 8$, $B_\nu = 10^{13}$ G, and $\Omega = 50$ s^{-1} ($P \simeq 126$ ms). Notice that the Alfvén radius is relatively close to the PNS surface ($R_A \approx 20$ km) and that the sonic point (corresponding to the fast point in the NRNM limit) is at a much larger radius ($R_{\rm s} \approx 750$ km, approximately the "Parker radius", $R_{\rm p} \simeq GM/(v^a)^2$, of an equivalent polytropic wind, where v^a is the asymptotic wind speed). Although the magnetic field and rotation rate are low enough that they have no effect on the wind energetics, the Alfvèn radius R_A is still above the PNS surface. Angular momentum-loss is thus enhanced by a factor of $(R_A/R_\nu)^2 \approx 4$ over an unmagnetized wind. In this respect, PNS winds such as that shown in Figure 2.2 are analogous to the solar wind (which is also primarily

thermally-driven, but has $R_A \gtrsim R_\odot$).

Many of the relevant results for NRNM PNS winds (such as Fig. 2.2) are approximated analytically and verified numerically in QW. QW show that $\dot{M} \propto L_{\bar{\nu}_e}^{5/3} \langle \epsilon_{\bar{\nu}_e} \rangle^{10/3}$ (their eqs. [58a,b]); hence, if $L_\nu \propto \langle \epsilon_\nu \rangle^4$, as we have assumed, QW find that the neutrino-driven mass-loss rate is approximately given by $\dot{M}_{\rm NRNM} \simeq 3 \times 10^{-4} (L_{\bar{\nu}_e,51}/8)^{2.5} {\rm M}_\odot \ {\rm s}^{-1}$, where $L_{\bar{\nu}_e} = L_{\bar{\nu}_e,51} \times 10^{51}$ ergs s^{-1}. Our calculations find that $\dot{M}_{\rm NRNM} \propto L_\nu^{2.5}$ as well, but with a normalization lower than that of QW:

$$\dot{M}_{\rm NRNM} \simeq 1.4 \times 10^{-4} (L_{\bar{\nu}_e,51}/8)^{2.5} \, {\rm M}_\odot \, {\rm s}^{-1}, \tag{2.15}$$

primarily because we have included neutrino redshifts in our heating rates. Somewhat coincidentally, T01 found a result similar to equation (2.15) from calculations incorporating GR.

Because neutrino heating is so concentrated near the PNS surface, NRNM winds are barely unbound in comparison to the PNS escape speed (non-relativistically, $v_{\rm esc}(R_\nu) \approx 0.64$ c); indeed, from Figure 2.2 we find an asymptotic speed $v^a_{\rm NRNM} \approx 0.06$ c at $L_{\bar{\nu}_e,51} = 8$. T01 found that $v^a_{\rm NRNM} \simeq 0.1$ c $(L_{\bar{\nu}_e,51}/8)^{0.3}$ in GR at high L_ν. Although we find that $v^a_{\rm NRNM}$ scales in approximately the same way with $L_{\bar{\nu}_e}$, our asymptotic speeds are lower than those obtained by T01 primarily because we have used a more shallow, Newtonian gravitational potential. In NRNM winds the asymptotic wind power is entirely gas kinetic energy: $\dot{E}^a_{\rm NRNM} \simeq (1/2) \dot{M}_{\rm NRNM} (v^a_{\rm NRNM})^2$; hence, from our results for $\dot{M}_{\rm NRNM}$ and $v^a_{\rm NRNM}$ we find

$$\dot{E}^a_{\rm NRNM} \simeq 4 \times 10^{47} (L_{\bar{\nu}_e,51}/8)^{3.2} \, {\rm ergs \ s}^{-1}. \tag{2.16}$$

Since the time spent at $L_{\bar{\nu}_e,51} \sim 8$ is only ~ 1 s (see §2.4.1), the total energy extracted during the Kelvin-Helmholtz epoch in a NRNM wind is $\sim 10^{47} - 10^{48}$ ergs.

2.3.2 Magnetically-Driven Winds

For a PNS with a given neutrino luminosity, larger rotation rates and magnetic field strengths lead to additional acceleration in the outer, supersonic portions

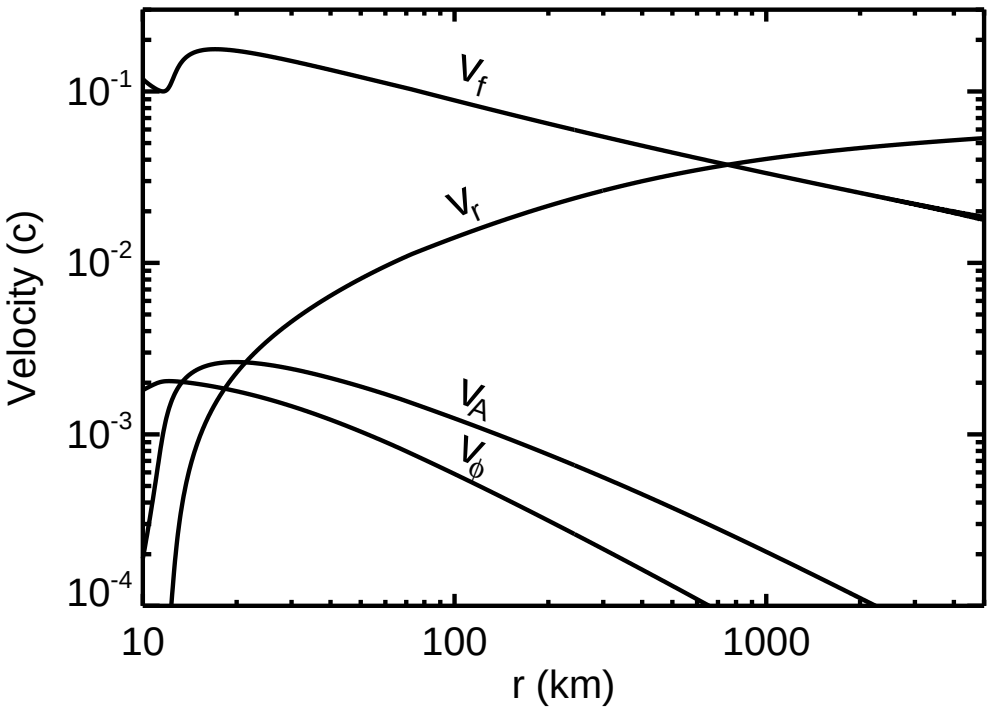

Figure 2.2: Velocity profile for a thermally-driven wind with $L_{\bar{\nu}_e,51} = 8$, $B_\nu = 10^{13}$ G, and $\Omega = 50$ s^{-1} ($P \approx 130$ ms). The variables $v_{\rm r}$, v_ϕ, $v_{\rm A}$, and $v_{\rm f}$ are the radial, azimuthal, Alfvén, and fast magnetosonic speeds, respectively; the fast(Alfvén) speed is also approximately the adiabatic sound(slow) speed for thermally-driven winds. This solution has $\dot{M} \approx 1.4 \times 10^{-4} {\rm M}_\odot$ s^{-1}, $\sigma \approx 3 \times 10^{-8}$, $\dot{E}^a \simeq 4 \times 10^{47}$ ergs s^{-1}, and $\tau_{\rm J} \sim 880$ s (see Table 2.1). The Michel speed for this solution is $v_M = \sigma^{1/3} c \simeq 0.003$ c, which is less than the thermally-driven asymptotic speed actually obtained (≈ 0.06 c); hence, the magnetic field and rotation rate have no significant effect on the acceleration of the wind.

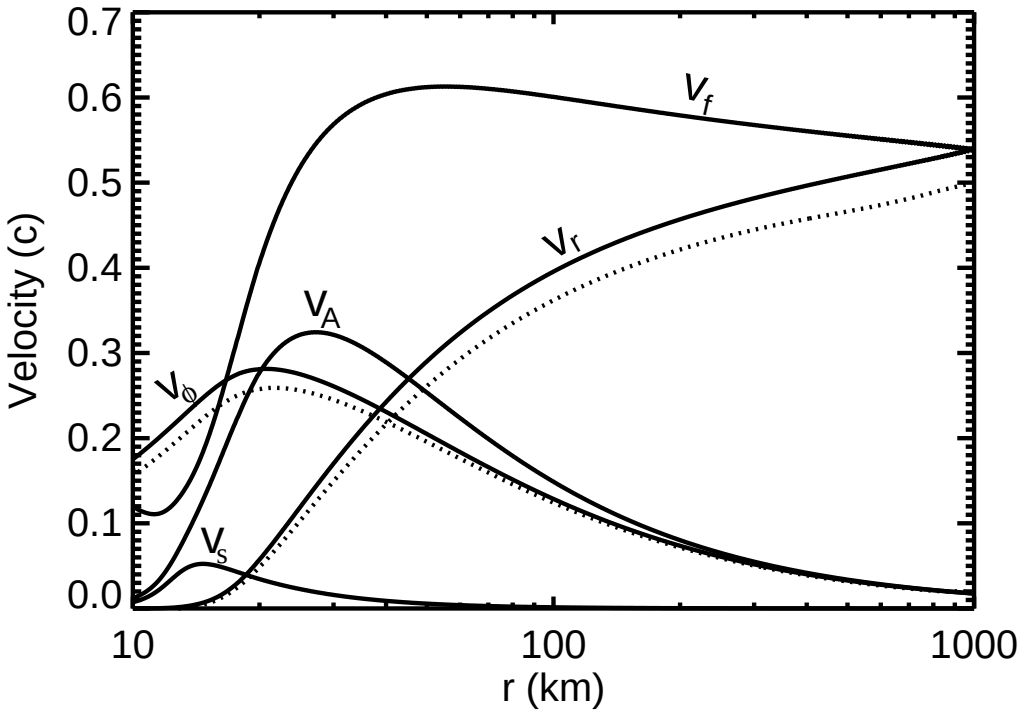

Figure 2.3: Velocity profile for a magneto-centrifugally-driven wind with $L_{\bar{\nu}_e,51} = 8$, $B_\nu = 10^{15}$ G, and $\Omega = 5000$ s^{-1} ($P \simeq 1.26$ ms); the variables $v_{\rm r}$, v_ϕ, $v_{\rm A}$, $v_{\rm f}$, and $v_{\rm s}$ are the radial, azimuthal, Alfvén, fast, and slow magnetosonic speeds, respectively. This solution has $\dot{M} \simeq 3.0 \times 10^{-3} {\rm M}_\odot$ s^{-1}, $\sigma \simeq 0.16$, $\tau_{\rm J} \simeq 9$ s, and $\dot{E}^a \simeq 2.3 \times 10^{51}$ ergs s^{-1}. Comparison plots of v_r and v_ϕ (dashed lines) are for a $\gamma = 1.15$ polytropic wind with similar $\dot{M}$, Ω, B_ν, and inner temperature. Notice that the radius of the slow point (approximately the sonic point; where $v_r = v_{\rm s}$) is very close to the value expected in the magneto-centrifugal limit: $R_{\rm s,cf} \approx 19.6$ km (eq. [2.19]).

of the wind. If the rotation rate and magnetic field are high enough, they will dominate the wind acceleration at large radii. This is the "Fast Magnetic Rotator" (FMR) limit, using the stellar-wind terminology of Belcher & MacGregor (1976); see also Lamers & Cassinelli (1999). An approximate criteria for this limit is that the magnetically-driven asymptotic speed, given roughly by the Michel speed $v_M \equiv (B_\nu^2 R_\nu^4 \Omega^2/\dot{M})^{1/3} = \sigma^{1/3} c$ (Michel 1969), exceeds the asymptotic speed obtained if the wind were entirely thermally-driven by neutrino heating ($v^a_{\rm NRNM}$). Using our result for $v^a_{\rm NRNM}$, the wind will be in the FMR limit for magnetizations

$$\sigma \gtrsim 2 \times 10^{-4} (L_{\bar{\nu}_e,51}/8)^{0.9} \equiv \sigma_{\rm FMR}. \tag{2.17}$$

Using equation (2.15) to relate $L_{\bar{\nu}_e}$ and $\dot{M}$, our calculations imply that the PNS wind is magnetically-driven below the critical rotation period

$$P_{\rm FMR} \simeq 15\,(L_{\bar{\nu}_e,51}/8)^{-1.7} B_{14}\,{\rm ms}, \tag{2.18}$$

where $B_\nu = B_n \times 10^n$ G. The $P = P_{\rm FMR}$ boundary in Figure 2.1 is marked by a solid line. The magnetically-driven regime encompasses a large range of PNS parameter space and hence generically describes most of a strongly magnetized PNS's evolution. In contrast, the wind from a relatively weakly magnetized PNS will only be dominated by magneto-centrifugal forces late in the cooling epoch. The conditions necessary for the magnetically-driven phase to dominate the total energy and mass-loss during the Kelvin-Helmholtz phase will be discussed further in §2.4.1.

Figure 2.3 shows the velocity structure of a magnetically-driven wind from a PNS with $L_{\bar{\nu}_e,51} = 8$, $B_\nu = 10^{15}$ G and $\Omega = 5000$ s^{-1} ($P \simeq 1.3$ ms). As the profile of v_ϕ in Figure 2.3 indicates, the wind corotates to ≈ 25 km, which is far inside $R_A \approx 46$ km because the magnetic field carries a significant fraction of the angular momentum. In addition, because the wind is magnetically-driven, the wind speed at large radii is almost an order of magnitude larger than in a NRNM wind: $v_r = 0.54$ c $\approx v_M$ obtains at the outer grid point. The sonic point of the wind (corresponding to the slow point in the FMR limit) is now inside R_A, less than one stellar radius off the surface; this is expected because analytic considerations show

that with increasing Ω, the location of the sonic radius $R_{\rm s}$ decreases from a value of order the Parker radius to a value independent of the local thermodynamics (see Lamers & Cassinelli 1999)[2]:

$$R_{\rm s,cf} \equiv \left(GM/\Omega^2\right)^{1/3} \simeq 17 P_{\rm ms}^{2/3}\,{\rm km}. \tag{2.19}$$

For comparison with our solution, Figure 2.3 shows the velocity structure of an adiabatic wind ($\gamma = 1.15$) with approximately the same $\dot{M}$, Ω, B_ν, and surface temperature as our neutrino-heated wind. The adiabatic solution agrees well with the neutrino-heated solution because, although $\dot{M}$ is primarily set by L_ν, once $\dot{M}$ is specified the velocity structure of the magnetically-driven wind becomes relatively independent of the details of the neutrino microphysics. This agreement implies that we can accurately map our 1D neutrino-heated calculations onto multi-dimensional polytropic calculations that employ similar boundary conditions and a similar effective adiabatic index (see §2.4.1).

For FMR winds, the Michel speed obtains at large radii and the asymptotic wind power is therefore enhanced relative to equation (2.16):

$$\begin{aligned} \dot{E}^a_{\rm FMR} = \dot{M}\mathcal{B}^a \simeq (3/2)\dot{M}v_M^2 \simeq \\ 10^{50}\, B_{14}^{4/3}\dot{M}_{-3}^{1/3}P_{\rm ms}^{-4/3}\,{\rm ergs\ s^{-1}}, \end{aligned} \tag{2.20}$$

where $\dot{M} = \dot{M}_{-3}\times 10^{-3}\ {\rm M_\odot s^{-1}}$ and $\mathcal{B}^a = \dot{E}^a/\dot{M} = (v_M^3/v^a) + (v^a)^2/2 \simeq (3/2)v_M^2$ is the Bernoulli integral at large radii in the FMR limit, and is composed of 2/3 magnetic and 1/3 kinetic energy.

To calculate the angular momentum lost by the PNS, we note that for any super-Alfvénic outflow, equation (2.7), equation (2.8), and conservation of magnetic flux require that the conserved specific angular momentum obey $\mathcal{L} = \Omega R_A^2$, where R_A is defined by the position where the radial outflow speed matches the radial Alfvén speed: $v_r(R_A) = B_r(R_A)/\sqrt{4\pi\rho(R_A)} \equiv v_A$. We estimate the location of the Alfvén point in terms of $\eta = \Omega\dot{J}/\dot{E}^a = \Omega^2 R_A^2/\mathcal{B}^a$ defined in equation (2.12):

$$R_A^2\Omega^2 \simeq (3/2)\eta v_M^2, \tag{2.21}$$

[2]The subscript "cf", here and below, stands for "centrifugal" and relates to the limit described by equation (2.25).

so that[3]

$$R_A|_{\rm FMR} \simeq 11\,\eta^{1/2}\,B_{14}^{2/3}\dot{M}_{-3}^{-1/3}P_{\rm ms}^{1/3}\,{\rm km}. \tag{2.22}$$

Figure 2.4 shows η for our wind solutions with $L_{\bar{\nu}_e,51} = 8$ for several surface magnetic field strengths (see also Table 2.1). Recall that $1/\eta$ represents the fraction of the extracted rotational energy from the PNS available to energize the surrounding environment. In the limit that $v_M \gtrsim v_{\rm esc}$, we find that $\eta \approx 1$ and almost all of the rotational energy lost by the PNS emerges as asymptotic wind power; this limit is normally assumed when considering magnetized stellar spin-down. However, as the low B_ν solutions in Figure 2.4 illustrate, winds with short rotation periods and $v^a_{\rm NRNM} < v_M < v_{\rm esc}$ can be magnetically-driven and yet have $\eta \gg 1$. The primary reason for this is that at high Ω the neutrino heating rate per unit mass is significantly reduced below its NRNM value because centrifugally-accelerated matter spends less time in the region where neutrino heating is important. Because the wind absorbs less of the neutrino energy, the magnetic field becomes more important for unbinding the matter from the PNS. Consequently, only a fraction of the rotational energy extracted at the PNS surface reaches large radii.

In the limit of thermally-driven solutions with very low B_ν (even lower than in Fig. 2.2, such that the Alfvén radius is interior to the stellar surface), R_ν is the lever arm for angular momentum-loss; thus $\mathcal{L} = \Omega R_\nu^2$ and hence $\eta = \Omega^2 R_\nu^2 \dot{M}_{\rm NRNM}/\dot{E}^a_{\rm NRNM} \approx 24(L_{\bar{\nu}_e,51}/8)^{-0.6}P_{\rm ms}^{-2}$ (using eqs. [2.15] and [2.16]). For $P \gg 1$ ms thermally-driven winds have $\eta \ll 1$, which explains why η decreases rapidly for solutions with large P in Figure 2.4. Physically, this is because for slow rotation rates the rotational power lost by the PNS is insignificant in comparison to the thermal energy supplied by neutrino heating.

The rate at which angular momentum is extracted from the PNS is $\dot{J} = I\dot{\Omega} = \Omega R_A^2 \dot{M}$, where $J = I\Omega$ is the angular momentum of the PNS and $I \simeq (2/5)MR_\nu^2$ is the PNS moment of inertia. Hence, given the Alfvén radius from equation (2.22), the spin-down time of the PNS ($\tau_J \equiv \Omega/\dot{\Omega}$) in the non-relativistic, magnetically-

[3]TCQ took $\Omega R_A = v_r(R_A) = v_M$ and assumed $\eta = 1$. We find that in some circumstances the $\eta = 1$ assumption is not applicable, even in the FMR limit (see Fig. 2.4).

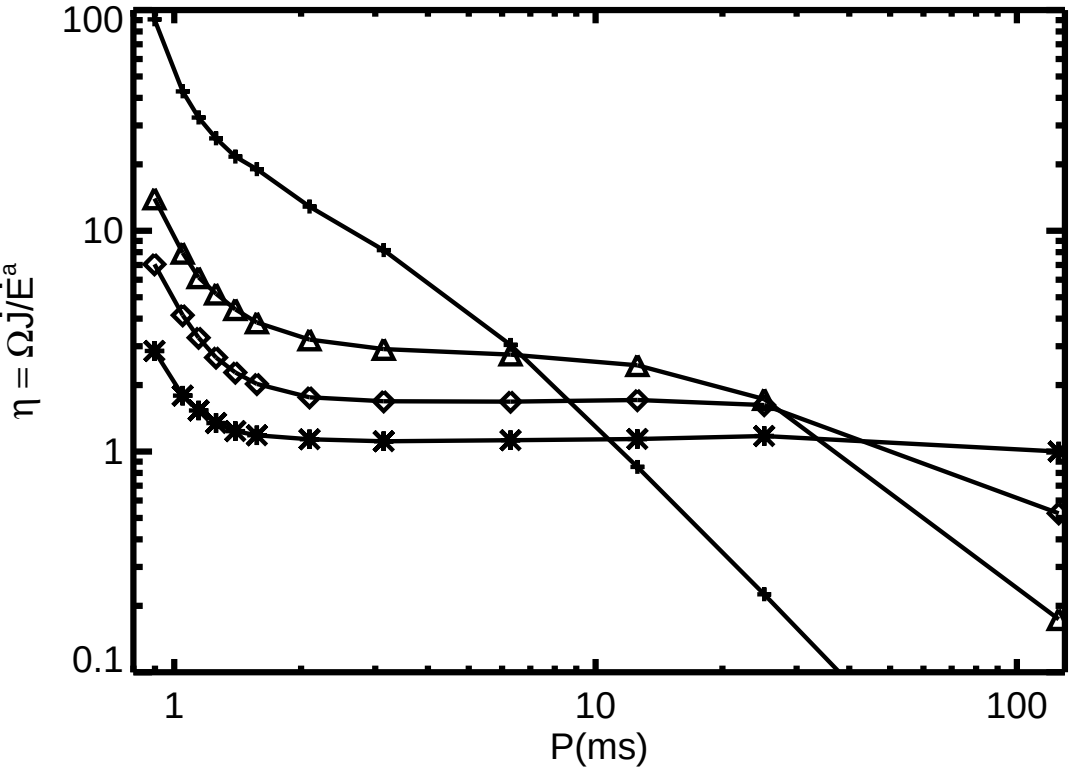

Figure 2.4: $\eta = \Omega\dot{J}/\dot{E}^a$ is the ratio of spin-down power lost by the PNS to the asymptotic wind power (eq. [2.12]). This figure shows η as a function of rotation period P for $L_{\bar{\nu}_e} = 8 \times 10^{51}$ ergs s^{-1} and monopole magnetic field strengths $B_\nu = 10^{13}$ G (cross), 10^{14} G (triangle), 2.5×10^{14} G (diamond), and 10^{15} G (asterisk). For the highly magnetized solutions (with R_A well off the surface) nearly all of the extracted rotational energy escapes to large radii ($\eta \simeq 1$), but for low B_ν and high Ω most of the rotational energy is used to unbind the wind and hence $\eta \gtrsim 1$. For slowly rotating, thermally-driven winds (low B_ν and Ω) $\eta \ll 1$ because the rotational power lost by the PNS is insignificant in comparison to the thermal energy supplied by neutrino heating.

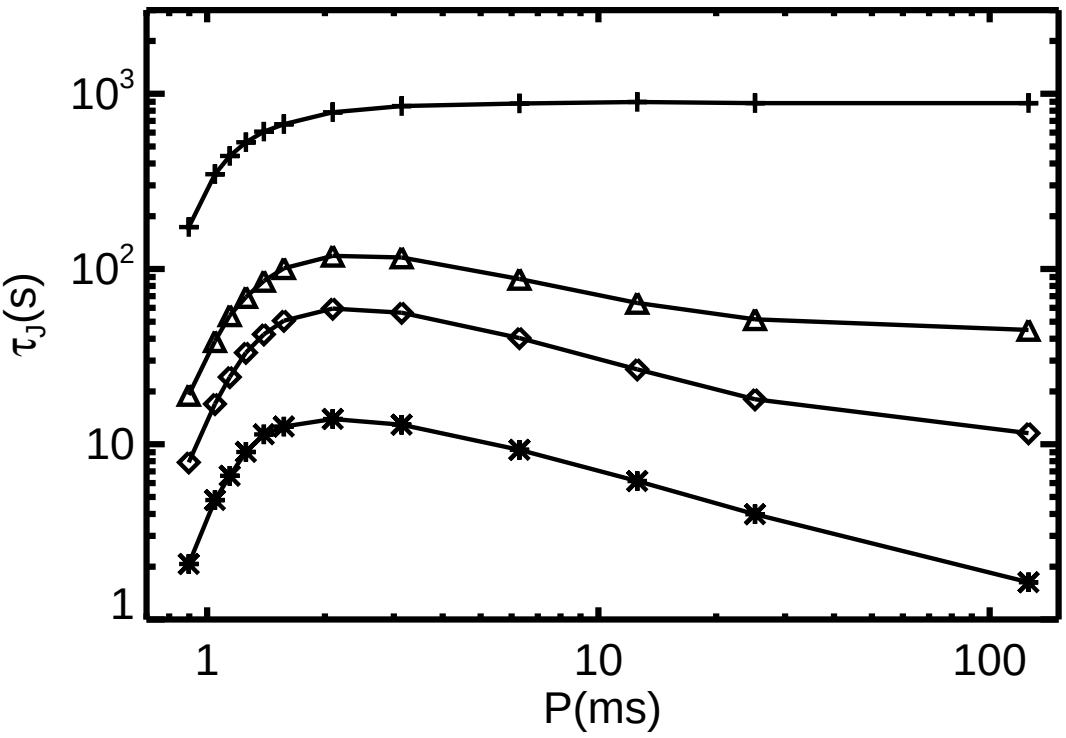

Figure 2.5: Spin-down timescale $\tau_{\rm J} \equiv \Omega/\dot{\Omega}$ as a function of rotation period P for $L_{\bar{\nu}_e} = 8{\times}10^{51}$ ergs s^{-1} and 4 monopole surface magnetic field strengths: $B_\nu = 10^{13}$ G (cross), 10^{14} G (triangle), 2.5×10^{14} G (diamond), and 10^{15} G (asterisk). The decrease in $\tau_{\rm J}$ for rapid rotation is due to the exponential enhancement in $\dot{M}$ for P $\lesssim$ 2-3 ms (eq. [2.24]). The surface dipole field $B_\nu^{\rm dip}$ associated with the effective monopole field B_ν scales as $B_\nu^{\rm dip} \propto B_\nu P$ (see eq. [2.30]), which implies that the true dipole field appropriate to this figure can be much greater than B_ν for large P. Note that an approximate analytic expression for $\tau_{\rm J}$ in the magnetically-driven limit ($P \lesssim P_{\rm FMR}$; eq. [2.18]) is given in equation (2.23).

driven limit is found to be

$$\tau_{\rm J}|_{\rm FMR} \simeq 440\,\eta^{-1}\,B_{14}^{-4/3}\dot{M}_{-3}^{-1/3}P_{\rm ms}^{-2/3}\,{\rm s}. \tag{2.23}$$

This result shows explicitly that while increasing the mass-loading places a greater strain on the field lines ($R_A \propto \dot{M}^{-1/3}$) and hence reduces the net loss of angular momentum per gram ($\mathcal{L} = \Omega R_A^2 \propto \dot{M}^{-2/3}$), the additional mass-loss carries enough total angular momentum to increase the overall spin-down rate. The high mass-loss accompanying the Kelvin-Helmholtz epoch can therefore efficiently extract the rotational energy of the PNS.

Figure 2.5 shows $\tau_{\rm J}$ calculated directly from our wind solutions as a function of P at $L_{\bar{\nu}_e,51} = 8$ for several magnetic field strengths (see also Table 2.1). Our numerical results agree well with the analytic estimates in equation (2.23) for winds that are in the FMR limit (i.e., $P \lesssim P_{\rm FMR}$; eq. [2.18]). The sharp decline in $\tau_{\rm J}$ at short P is due to the fact that $\tau_{\rm J} \propto \dot{M}^{-1/3}$ and that $\dot{M}$ is enhanced by centrifugal flinging for rapid rotation. Note, however, that only for $B_\nu \gtrsim 10^{15}$ G is $\tau_{\rm J} \sim \tau_{\rm KH} \sim 10$ s for a millisecond rotator. For $B_\nu = 10^{13}$ G and large P the solutions are primarily thermally-driven and $\tau_{\rm J}$ is independent of P; this occurs because both the Alfvén radius R_A and mass-loss rate $\dot{M}$ (and hence $\tau_{\rm J}$) are independent of rotation rate for thermally-driven winds.

The Alfvén radius and spin-down times calculated in equations (2.22) and (2.23) depend on the mass-loss rate $\dot{M}$ from the PNS, which itself depends on the PNS's rotation rate and magnetic field strength. Figure 2.6 shows our determination of $\dot{M}$ as a function of Ω for field strengths $B_\nu = 10^{13}$, 10^{14}, 2.5×10^{14}, and 10^{15} G at $L_{\bar{\nu}_e,51} = 8$, and $B_\nu = 2.5 \times 10^{14}$ G at $L_{\bar{\nu}_e,51} = 3.5$. The mass-loss rate increases rapidly with rotation for $P \lesssim$ 2-3 ms and also increases with B_ν, though it saturates for the largest magnetic field strengths, as can be seen by comparing the $B_\nu = 2.5 \times 10^{14}$ G and 10^{15} G solutions. For sufficiently large B_ν, such that $R_A \gtrsim R_{\rm s}$, we find empirically that $\dot{M}$ is given by

$$\dot{M} \simeq \dot{M}_{\rm NRNM} \exp\left[(\Omega/\Omega_{\rm cf})^2\right] \equiv \dot{M}_{\rm cf}, \tag{2.24}$$

where $\dot{M}_{\rm NRNM}$ is the mass-loss rate for NRNM winds (eq. [2.15]) and $\Omega_{\rm cf} \approx$

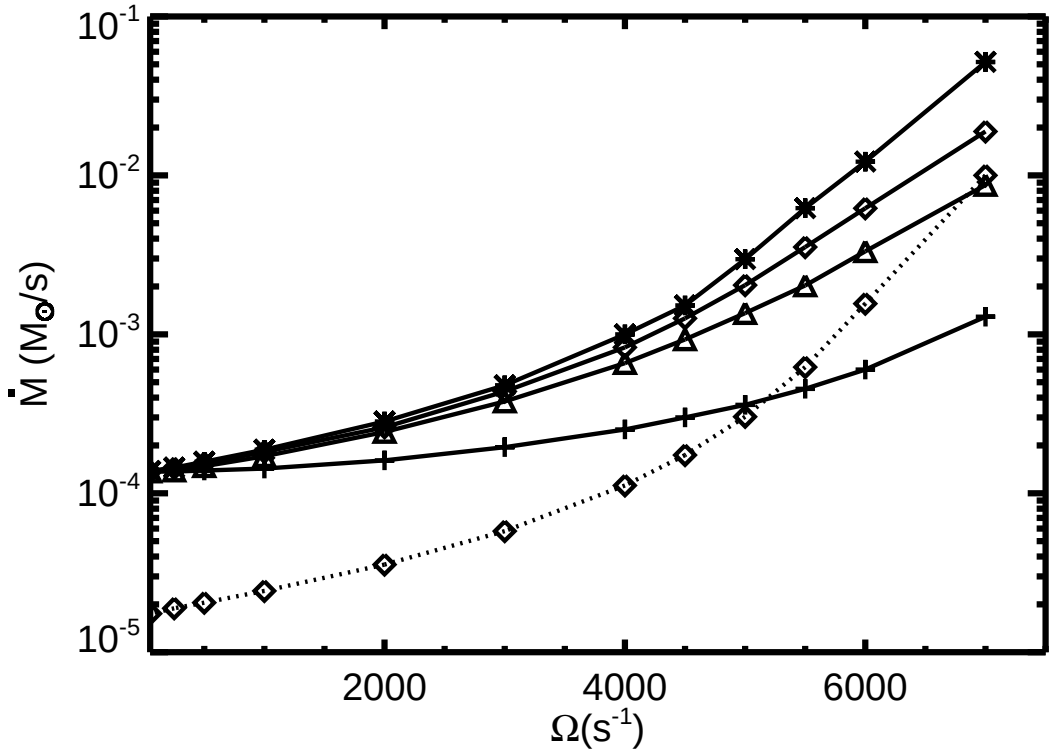

Figure 2.6: mass-loss rate $\dot{M}$ as a function of the rotation rate Ω at $L_{\bar{\nu}_e} = 8 \times 10^{51}$ ergs s^{-1} for $B_\nu = 10^{13}$ G (cross), $B_\nu = 10^{14}$ G (triangle), 2.5×10^{14} G (diamond), and 10^{15} G (asterisk); also shown is $\dot{M}(\Omega)$ for $L_{\bar{\nu}_e} = 3.5 \times 10^{51}$ ergs s^{-1} and $B_\nu = 2.5 \times 10^{14}$ G (dotted, diamond). $\dot{M}$ increases with increasing Ω and B_ν because centrifugal support expands the hydrostatic atmosphere (see Fig. 2.7). For sufficiently large B_ν ($\gtrsim B_{\rm cf}$; eq. [2.26]), however, $\dot{M}(\Omega)$ no longer increases with increasing B_ν because the wind corotates past the sonic point. An approximate fit to the numerical results in this limit is given by equation (2.24).

$2700(L_{\bar{\nu}_e,51}/8)^{0.08}$ s^{-1}.

The enhanced mass-loss shown in Figure 2.6 is due to the effect of strong magnetic fields and rapid rotation on the subsonic, hydrostatic structure of PNS winds. Figures 2.7 and 2.8 show the density and temperature profiles, respectively, for winds with $B_\nu = 10^{15}$ G and $L_{\bar{\nu}_e,51} = 8$ at several rotation rates. For the most rapidly rotating solution (solid line), Figure 2.7 shows that centrifugal support is sufficient to expand the scale height of the hydrostatic atmosphere at small radii, resulting in the much higher mass-loss rates seen in Figure 2.6. Analytically, we expect the centrifugal support to be important when $R_\nu \Omega \gtrsim c_{\mathrm{s},\nu}$, where $c_{\mathrm{s},\nu}$ is the sound speed at the PNS neutrinosphere. We find that the inner sound speed depends only weakly on the neutrino luminosity: $c_{\mathrm{s},\nu} \approx 0.12(L_{\bar{\nu}_e,51}/8)^{0.08}$ c, and thus that mass-loss is enhanced for

$$\Omega \gtrsim 3600(L_{\bar{\nu}_e,51}/8)^{0.08}\,\mathrm{s}^{-1}. \tag{2.25}$$

This region is denoted "$\dot{M}$ Enhanced" in Figure 2.1. Equation (2.25) is in good agreement with our numerically determined value of Ω_{cf} defined in equation (2.24).

The enhancement of $\dot{M}$ implied by equations (2.24) and (2.25) does not explicitly depend on the magnetic field strength. However, centrifugal support of the PNS atmosphere only occurs if the field can sustain corotation out to the sonic radius R_{s}; otherwise rotation has much less of an effect on the mass-loss rate (see the solutions with low B_ν in Fig. 2.6). The requirement of corotation out to R_{s} can be written as $R_A > R_{\mathrm{s,cf}}$ (eq. [2.19]), which in turn implies $B_\nu > B_{\mathrm{cf}}$, where

$$B_{\mathrm{cf}} \simeq 2 \times 10^{14}\,\eta^{-3/4}\dot{M}_{-3}^{1/2}P_{\mathrm{ms}}^{1/2}\,\mathrm{G}. \tag{2.26}$$

For $B_\nu \gtrsim B_{\mathrm{cf}}$, the mass-loss from the PNS no longer increases with increasing B_ν (see Fig. 2.6) because the wind already co-rotates out to the sonic radius where $\dot{M}$ is set. In deriving B_{cf} in equation (2.26), we have used equation (2.22) for R_A because, under most conditions, a wind that is centrifugally-supported will automatically be in the FMR limit, although the converse is not necessarily true. We note that even relatively weakly-magnetized PNS's that are rapidly rotating will experience some degree of enhanced mass-loss. For instance, for $\Omega = 7000$ s^{-1},

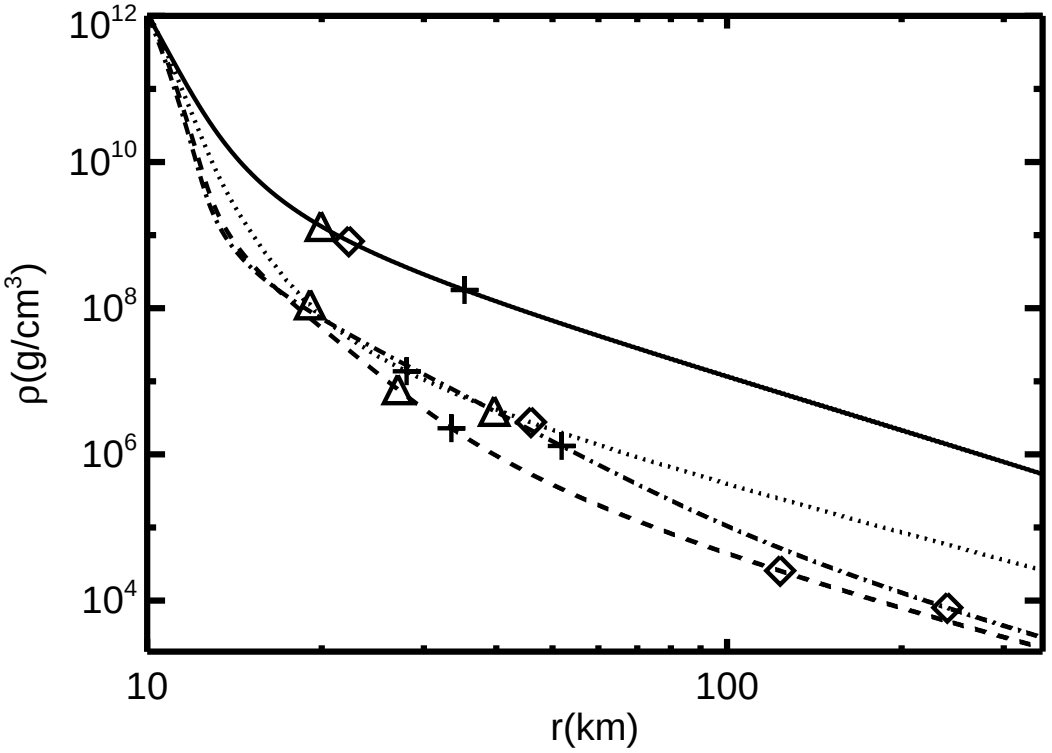

Figure 2.7: The density profiles in the inner ~ 100 km for magnetically-driven wind solutions at $L_{\bar{\nu}_e,51} = 8$, $B_\nu = 10^{15}$ G, $\Omega = 7000$ s^{-1} (solid), 5000 s^{-1} (dotted), 2000 s^{-1} (dashed), and 500 s^{-1} (dot-dashed). Triangles, crosses, and diamonds mark the slow point, the radius where $T = 0.5$ MeV, and the Alfén radius, respectively. For all of the solutions, the supersonic portion of the density profile is altered from that of a thermally-driven solution due to magnetic acceleration. For solutions with $\Omega \gtrsim 3000$ s^{-1} the density scale height in the subsonic portion of the wind (interior to the triangle) is significantly larger due to centrifugal support. This enhances the mass-loss rate as shown in Figure 2.6.

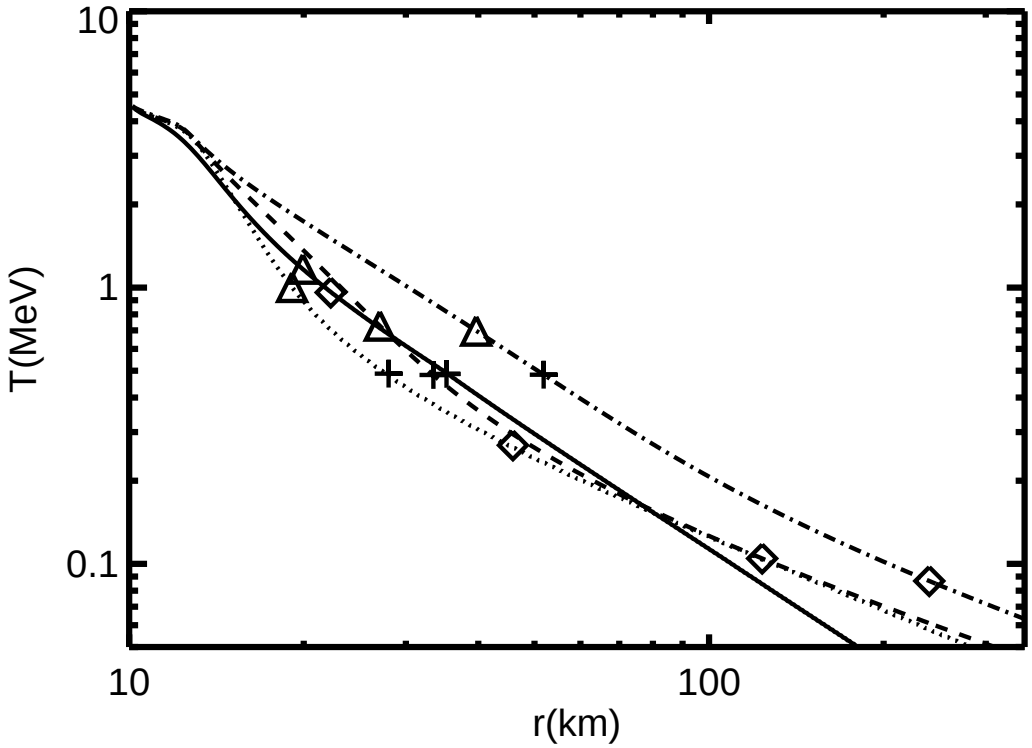

Figure 2.8: The temperature profiles in the inner $\sim$ 100 km for magnetically-driven wind solutions at $L_{\bar{\nu}_e,51} = 8$, $B_\nu = 10^{15}$ G, $\Omega = 7000$ s^{-1} (solid), 5000 s^{-1} (dotted), 2000 s^{-1} (dashed), and 500 s^{-1} (dot-dashed). Triangles, crosses, and diamonds mark the slow point, the radius where $T = 0.5$ MeV, and the Alfén radius, respectively. Notice that in all but the most rapidly-rotating case the $T = 0.5$ MeV radius is located between the slow point and the Alfvén radius, which implies that there is significant magnetic acceleration of the wind at the $T = 0.5$ MeV radius. As shown in Figure 2.12, this significantly reduces the dynamical time at $T = 0.5$ MeV, making magnetically-driven PNS winds more favorable for r-process nucleosynthesis than thermally-driven winds (see §2.4.3).

even the lowest field strength solution in Figure 2.6 ($B_\nu = 10^{13}$ G) has a mass-loss rate almost an order of magnitude larger than its NRNM value.

The non-relativistic calculations we have presented here are only applicable for magnetizations $\sigma < 1$; this is equivalent to requiring $R_A < R_{\rm L} \equiv c/\Omega$, the radius of the light cylinder. For $\sigma > 1$ the PNS wind becomes relativistic and its spin-down properties will change (see §2.4.1 for a discussion). Using equation (2.24) for $\dot{M}$ (i.e., assuming $B_\nu > B_{\rm cf}$), the magnetization is given by

$$\sigma \simeq 0.05 B_{14}^2 P_{\rm ms}^{-2} (L_{\bar{\nu}_e,51}/8)^{-2.5} \exp[-5.4 P_{\rm ms}^{-2} (L_{\bar{\nu}_e,51}/8)^{-0.16}]. \quad (2.27)$$

The $\sigma = 1$ boundary is denoted by a dotted line in Figure 2.1. PNSs with $\sigma > 1$ and $L_{\bar{\nu}_e,51} \gtrsim 0.1$ will experience a relativistic phase accompanied by significant mass-loss; this mass-loss keeps the wind mildly relativistic, in contrast to the much higher σ spin-down that will commence following $\tau_{\rm KH}$ ($L_{\bar{\nu}_e,51} \ll 0.1$).

2.4 Applications and Discussion

2.4.1 Magnetized PNS Evolution

With our numerical results in hand that sample a wide range of PNS wind conditions, we can begin to address the time evolution of a cooling, magnetized PNS. In the early stages following the launch of SN shock the PNS is likely hot and inflated, with a radius exceeding the value of $R_\nu = 10$ km that we have assumed in all of the calculations presented in this paper. This early phase is likely to be thermally-driven for all but the most highly-magnetized proto-magnetars, and, if a dynamo is at work, the large-scale field itself may still be amplifying during this phase (Thompson & Duncan 1993). Using the collapse calculations of Bruenn, De Nisco, & Mezzacappa (2001) (from a 15 $M_\odot$ progenitor of Woosley & Weaver 1995) T01 fit an approximate functional form to the PNS radial contraction: $R_\nu \propto t^{-1/3}$ such that $R_\nu(1\ {\rm s}) \simeq 15$ km and $R_\nu(2\ {\rm s}) \simeq 12$ km. The recent SN simulations of Buras et al. (2003, 2006) with Boltzmann neutrino transport find a similar neutrinosphere radius at $t \sim 1\,{\rm s}$ after bounce.

We do not attempt to address the uncertainties in early-time PNS cooling calculations, especially in the presence of large fields and rapid rotation. Rather, we assume that the PNS has cooled to its final radius and completely established its global field by a time $t_0 \sim 1$ s following core-collapse; we can then use the calculations presented in this paper to investigate the subsequent evolution of the PNS. Following t_0 we assume a simplified PNS cooling evolution (similar to that used in TCQ, motivated by Figure 14 of Pons et al. 1999):

$$L_{\bar{\nu}_e,51}(t) = L_0 \left(\frac{t}{\tau_{\rm KH}}\right)^{-\delta} : t_0 < t < \tau_{\rm KH}$$
$$L_{\bar{\nu}_e,51}(t) = L_0 \, \exp[-(t-\tau_{\rm KH})/\tau_{\rm KH}] : t > \tau_{\rm KH}, \quad (2.28)$$

where, for definitiveness in what follows, we take $L_0 = 0.2$, $t_0 = 1$ s, $\tau_{\rm KH} = 40$ s, and $\delta = 1$. This cooling evolution is approximate because magnetar-strength fields and rapid rotation could alter $\tau_{\rm KH}$ or the form of the cooling profile (e.g., δ) by affecting the neutrino opacity or the dynamics of the contraction itself (e.g., Villain et al. 2004; Dessart et al. 2006). For instance, in 1D collapse calculations with rotation, Thompson, Quataert, & Burrows (2005) found that for $P \sim 1$ ms, the total neutrino luminosity at $t \simeq 0.6$ s after bounce is $\sim 50\%$ smaller than in a non-rotating PNS.

The dominant uncertainty in applying our results to magnetized PNS evolution is that we have assumed a monopole field geometry. To relate our results to more realistic dipole simulations, we use the recent axisymmetric, relativistic MHD simulations of B06, who simulate neutron star spin-down for $\sigma \approx 0.3 - 20$. B06 show that the energy and angular momentum-loss rates from aligned dipole spin-down can be described accurately by monopole formulae provided they are normalized to just the open magnetic flux; for instance, we can accurately apply our results for $\tau_{\rm J}$ (eq. [2.23]) with a suitable renormalization of B_ν.

To apply the results of B06 we need to estimate the open magnetic flux in PNS winds. In force-free spin-down calculations motivated by pulsars it is generally assumed that the radius of the last closed magnetic field line (the "Y point" R_Y) is coincident with the light cylinder (Contopoulos et al. 1999; Gruzinov 2005) so that the ratio between the fraction of open magnetic flux in the dipole and

monopole cases is $R_\nu/R_Y = R_\nu/R_{\rm L}$. This assumption is supported by force-free simulations (Spitkovsky 2006; McKinney 2006), which show that when mass-loading is completely negligible ($\sigma \to \infty$), $R_Y \simeq R_{\rm L}$. However, B06 show that rapidly rotating, mildly mass-loaded MHD winds have a larger percentage of open magnetic flux than vacuum or force-free spin-down would imply (i.e., $R_Y < R_{\rm L}$). From Table 4 of B06 we fit the approximate power law

$$R_Y/R_{\rm L} \simeq 0.31\sigma^{0.15} \tag{2.29}$$

for the range $\sigma \in [0.298, 17.5]$ and for a fixed rotation period of order one millisecond. Although there are uncertainties in quantitatively extrapolating B06's results, reaching the pure force-free limit with $R_Y \simeq R_{\rm L}$ appears to require $\sigma \gg 1$. We therefore conclude that magnetized, rapidly rotating PNS winds (with $\sigma \in \{10^{-3}, 10^3\}$ for $t < \tau_{\rm KH}$ under most circumstances) will typically possess excess open magnetic flux.

Because the results of B06 for $R_Y/R_{\rm L}$ cover only a relatively narrow portion of PNS parameter-space we must proceed with caution in generalizing their results to our calculations; on the other hand, their basic conclusion shows a weak dependence on σ and Ω, and has a solid theoretical explanation (Mestel & Spruit 1987). Hence, we have attempted to apply the results of B06 to gain insight into the multi-dimensional generalization of our calculations, but we check at every step that our calculations are not overly sensitive to extrapolations of B06's results. Combining equation (2.29) with the empirical formula B06 provide (their eq. [25]) relating the effective monopole surface field $B_\nu^{\rm mon}$ to the true equatorial dipole field $B_\nu^{\rm dip}$ we find

$$B_\nu^{\rm mon} \simeq 0.6 B_\nu^{\rm dip} \frac{R_\nu}{R_{\rm L}} \left(\frac{R_Y}{R_{\rm L}}\right)^{-1} \simeq 0.4 B_\nu^{\rm dip} P_{\rm ms}^{-1} \sigma^{-0.15}, \tag{2.30}$$

which remains approximately valid for a substantial range in σ, provided we enforce $R_{\rm Y} = R_{\rm L}$ for $\sigma \gtrsim 10^3$ and keep $R_Y > R_\nu$.

Using equation (2.30) we substitute $B_\nu^{\rm mon}$ for B_ν in the results of §2.3 and integrate from t_0 to $\tau_{\rm KH}$ using our fiducial cooling evolution (eq. [2.28]) to obtain the total energy and mass-loss during the Kelvin-Helmholtz epoch ($E_{\rm tot}^a$ and $\Delta M_{\rm tot}$,

respectively) as a function of the fixed dipole surface field $B_\nu^{\rm dip}$ and for initial rotation periods $P_0 \in \{1, 10\}$ ms. Although a neutron star will eventually impart any remaining rotational energy after $\tau_{\rm KH}$ to its surroundings through an ultra-relativistic, pulsar-like outflow, we concentrate on the wind evolution prior to the end of the Kelvin-Helmholtz phase because our calculations are primarily suited to studying mass-loaded spin-down and because we are interested in energy that can be extracted sufficiently early to affect the rapidly outward-propagating SN shock. In performing our calculations when the wind is relativistic ($\sigma > 1$), we continue using equation (2.24) for $\dot{M}$ and employ the relativistic spin-down formula given by B06 (their eq. [26]):

$$\dot{E}^a_{\rm REL} \simeq 1.5 \times 10^{47} (B^{\rm dip}_{14})^2 P^{-4}_{\rm ms} \left(\frac{R_Y}{R_{\rm L}}\right)^{-2} \text{ ergs s}^{-1}, \tag{2.31}$$

evaluated for $R_Y/R_{\rm L}$ given by equation (2.29).

Although it is possible that equation (2.29) may not be accurate far outside the parameter regime B06 considered, we found that re-running the calculations at fixed $R_{\rm Y}/R_{\rm L} = 1/3$ changed $E^a_{\rm tot}$ by, at most, a factor of a few. A similar uncertainty in our calculations is that we have used our equatorial $\dot{M}$ over all 4π steradian; thus, we have probably overestimated $\Delta M_{\rm tot}$ by a factor of ~ 2 due to the effects of closed magnetic flux and because centrifugal flinging concentrates $\dot{M}$ at low latitudes. Although a direct comparison of the mass-loss rate between our solutions and the dipole simulations of B06 is difficult, we find that the dependence of $\dot{M}$ on Ω is similar between our solutions when the surface temperature in B06's simulations is scaled to an appropriate neutrino luminosity.

Our estimates for $E^a_{\rm tot}$ and $\Delta M_{\rm tot}$ during the Kelvin-Helmholtz phase are presented in Figures 2.9 and 2.10 for values of $B_\nu^{\rm dip}$ ranging from $10^{12} - 10^{16}$ G. The single dominant phase contributing the majority of the energy extracted for a given initial rotation rate P_0 is denoted by the line style (thermally-driven [NRNM] = dotted; non-relativistic, magnetically-driven [FMR] = solid; relativistic, magnetically-driven [REL] = 3 dot-dash). While all PNSs pass through each wind phase sometime during $\tau_{\rm KH}$ (see Fig. 2.1), PNSs can still be usefully classified into 3 types based on which wind phase dominates the total energy-loss during

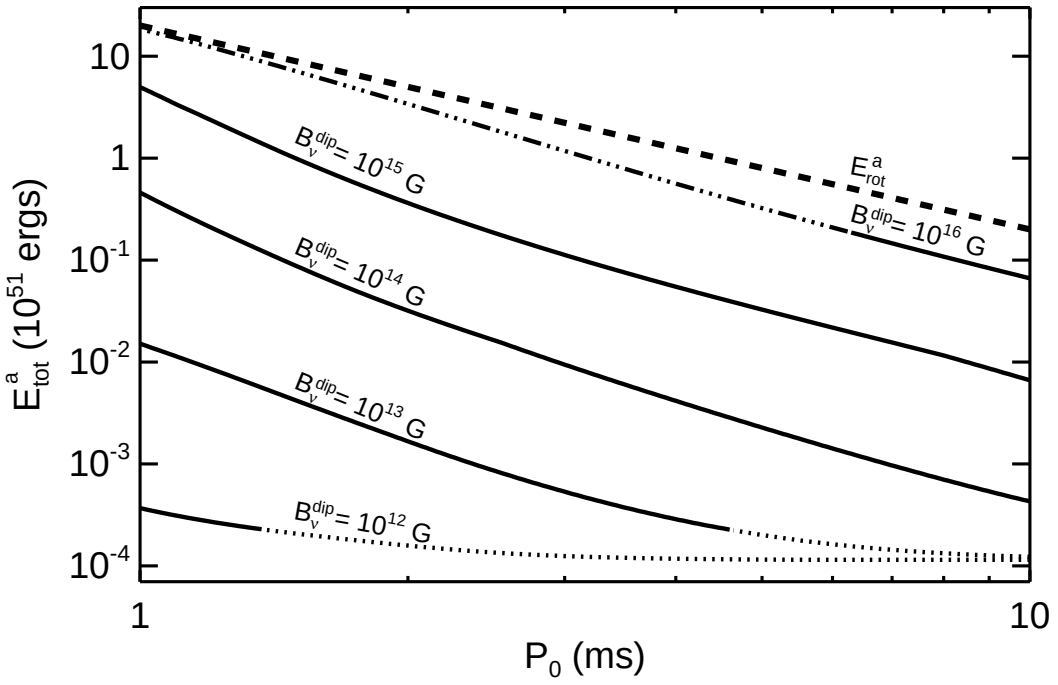

Figure 2.9: $E^a_{\rm tot}$ as a function of the PNS initial period P_0 for fixed dipole surface fields that range from those typical of rotation-powered pulsars to those capable of producing hyper-energetic SNe. $E^a_{\rm tot}$ is the total energy carried by the PNS wind at infinity, calculated by evolving the PNS from time $t_0 = 1$ s to $\tau_{\rm KH} = 40$ s, assuming the PNS cooling evolution of equation (2.28) and using results from the aligned dipole simulations of B06 to relate $B_\nu^{\rm dip}$ to our monopole calculations (see eq. [2.30]). The line style denotes the wind phase that dominates the total energy-loss (dotted = thermally-driven; solid = non-relativistic, magnetically-driven; 3 dot-dash = relativistic, magnetically-driven). The dashed line at the top shows the total initial rotational energy of the PNS. For $B_\nu^{\rm dip} = 10^{12}$ G neutrino-heated, thermally-driven outflow dominates for $P_0 \gtrsim 1$ ms, while for $B_\nu^{\rm dip} = 10^{16}$ G almost the entire rotational energy of the PNS is extracted by a relativistic, magnetized wind during the Kelvin-Helmholtz phase.

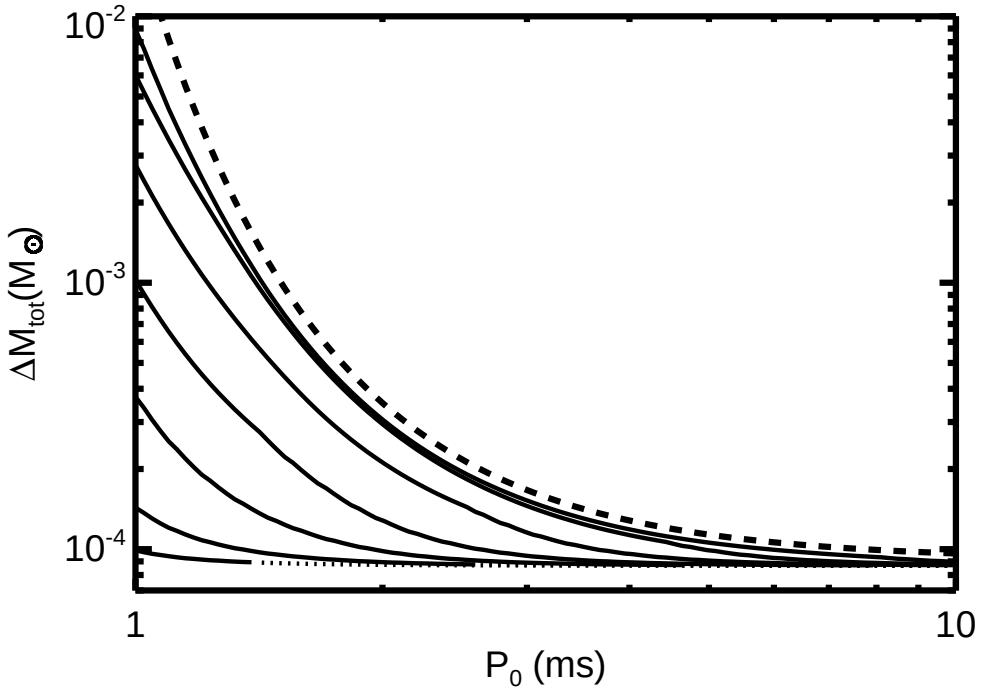

Figure 2.10: The total mass extracted via a PNS wind ($\Delta M_{\rm tot}$) from time $t_0 = 1$ s to $\tau_{\rm KH} = 40$ s as a function of the PNS initial period P_0 for dipole surface fields $B_\nu^{\rm dip} = 10^{12}, 3\times10^{12}, 10^{13}, 3\times10^{13}, 10^{14}, 3\times10^{14}$, and 10^{15} G (from bottom to top). These calculations assume the PNS cooling evolution of equation (2.28) and use the aligned dipole simulations of B06 to relate $B_\nu^{\rm dip}$ to our monopole calculations (see eq. [2.30]). The line style denotes the wind phase that dominates the total energy-loss (dotted = thermally-driven; solid = non-relativistic, magnetically-driven; 3 dot-dash = relativistic, magnetically-driven). The results of this figure demonstrate that for $P_0 \lesssim 2{-}3$ ms and $B_\nu^{\rm dip} \gtrsim 10^{13}$ G, centrifugal flinging enhances the total mass extracted from a PNS wind during $\tau_{\rm KH}$. An analytic approximation to $\Delta M_{\rm tot}$ for high B_ν is given in equation (2.34) and is shown with a thick dashed line. For $P \lesssim 3$ ms, $\Delta M_{\rm tot}$ is essentially the same for the $B_\nu^{\rm dip} = 3\times10^{14}$ G and 10^{15} G models because of the saturation of $\dot{M}$ at fixed Ω for $B \gtrsim B_{\rm cf}$.

$\tau_{\rm KH}$:

(1) $\mathbf{Thermally-Driven\,Winds}$ ($\mathbf{B_{14}^{dip} \lesssim 10^{-2} P_{ms}^{2}}$) :

For low magnetic field strengths, Figures 2.9 and 2.10 show that the total mass and energy-loss are effectively at the NRNM values for a large range of initial periods: $\Delta M_{\rm tot}^{\rm NRNM} \simeq 10^{-4}(t_0/1{\rm s})^{-1.5}{\rm M}_\odot$, $E_{\rm tot}^{\rm NRNM} \simeq 2\times10^{47}(t_0/1{\rm s})^{-2.2}$ ergs. Energy and mass-loss from this class of PNSs is generally modest and is dominated by early times. Analysis of the Parkes multibeam survey suggests that half of all pulsars are born with $B_\nu^{\rm dip} < 3\times10^{12}$ G (Vranesevic et al. 2004), implying that NRNM winds dominate the majority of neutron star births, independent of the birth-period distribution. Spin-down during $\tau_{\rm KH}$ is negligible for PNSs of this type and the supernova remnants associated with the production of NRNM PNSs will not be significantly modified by the small energy injected during the cooling phase.

(2) $\mathbf{Non-Relativistic}$, $\mathbf{Magnetically-Driven\,Winds}$

($\mathbf{10^{-2} P_{ms}^{2} \lesssim B_{14}^{dip} \lesssim 2 P_{ms}^{2} \exp[2 P_{ms}^{-2}]}$) : For $\sim 10^{13}-10^{15}$ G surface field strengths, Figure 2.9 shows that $E_{\rm tot}^{a}$ is dominated by a non-relativistic, magnetically-driven outflow during $\tau_{\rm KH}$ for most periods between 1 and 10 ms. Note that most observed Galactic magnetars have field strengths in this range (Kouveliotou et al. 1998). Figure 2.9 shows that for $B\sim10^{15}$ G and $P\lesssim2$ ms, more than 10^{51} ergs can be lost to a non-relativistic, magnetically-driven outflow during τ_{KH}, and that, over a broad range of initial spin period, the energy extracted is many times larger than from a slowly rotating PNS. Because non-relativistic outflows are efficiently collimated along the rotational axis by magnetic stresses (B06), the energy per unit solid angle at the pole may exceed that of the SNe, potentially altering the SNe shock's morphology and nucleosynthetic yield.

If, for the purposes of an analytic estimate, we assume that $R_Y = R_{\rm L}/3$ then

the total energy extracted for this class of PNS can be approximated as[4]

$$E_{\rm tot}^{\rm FMR} \simeq 10^{50} (B_{14}^{\rm dip})^{4/3} P_{\rm ms}^{-8/3} \times [\tau_{\rm f}^{1/6} - t_0^{1/6}] \exp[1.3 P_{\rm ms}^{-2}] \, {\rm ergs}, \quad (2.32)$$

where $\tau_{\rm f} \equiv \min\{\tau_{\rm KH}, \tau_{\rm REL}\}$, t_0 and $\tau_{\rm f}$ are in seconds, and

$$\tau_{\rm REL} \simeq 7 \, {\rm s} (B_{14}^{\rm dip})^{-0.8} P_{\rm ms}^{1.6} \exp[2.2 P_{\rm ms}^{-2}] \quad (2.33)$$

is the time after which the wind becomes relativistic. The weak dependence of equation (2.32) on $\tau_{\rm KH}$ and t_0 shows that the total energy extracted in the magnetically-dominated phase is relatively insensitive to our choice for the PNS thermal evolution because the energy-loss is distributed almost equally per decade in time. For the same reason, $E_{\rm tot}^{\rm FMR}$ is relatively insensitive to the precise time during the Kelvin-Helmholtz epoch at which the PNS cools to its final radius.

Figure 2.10 shows that the total mass-loss from PNSs is enhanced for $P \lesssim 3$ ms and $B_\nu^{\rm dip} \gtrsim 10^{13}$ G; the total mass-loss increases with $B_\nu^{\rm dip}$, saturating for $B_\nu^{\rm dip} \gtrsim 3 \times 10^{14}$ G (i.e., $B_\nu \gtrsim B_{\rm cf}$; see eq. [2.26]). Assuming no evolution of Ω, the integrated mass-loss is approximately

$$\Delta M_{\rm tot} \simeq 10^{-4} \, t_0^{-1.5} \exp[5.4 P_{\rm ms}^{-2}] \, {\rm M}_\odot \quad (2.34)$$

for large B_ν. For $P_0 \approx 1$ ms and $P_0 \approx 3$ ms, the total mass extracted is thus $\sim 10^2$ and ~ 2 times greater, respectively, than from a non-rotating, non-magnetic PNS. Equation (2.34) is shown with a dashed line in Figure 2.10.

(3) **Relativistic, Magnetically − Driven Winds**
($\mathbf{B_{14}^{dip} \gtrsim 2 P_{ms}^2 \exp[2 P_{ms}^{-2}]}$) : For $B_\nu^{\rm dip} = 10^{16}$ G and $P_0 \lesssim 6$ ms, the energy-loss from PNSs is dominated by a relativistic, magnetically-driven outflow during the Kelvin-Helmholtz phase. As Figure 2.9 illustrates, PNSs of this type lose $\approx 10 - 100\%$ of their total rotational energy during $\tau_{\rm KH}$. For sufficiently rapid rotation such PNSs

[4]Equation (2.32) also assumes that $\delta = 1$, that strict corotation can be maintained by the magnetic field (this criteria is well-satisfied because late times dominate the energy release, and winds at late times have lower $\dot{M}$ and are easier to support magneto-centrifugally), and that Ω does not evolve significantly (i.e., $\tau_J \gtrsim \tau_{\rm KH}$); this is well-satisfied for field-strengths at which the outflow energy is indeed extracted via a non-relativistic outflow.

are therefore candidates for the central engine of hyper-energetic SNe and LGRBs (see §2.4.2). PNS winds of this type differ from the ultra-relativistic ($\sigma \gg 10^3$), pulsar-like phase that begins once neutrino heating completely subsides in two important ways: (1) neutrino heating causes significant mass-loss that maintains modest σ ($\lesssim 10^2 - 10^3$); and (2) mass-loss leads to more open magnetic flux (eq. [2.29]) than in the pure force-free case and thus the PNS spins down more rapidly (see eq. [2.31]).

2.4.2 Hyper-Energetic SNe and Long Duration Gamma-Ray Bursts

One observational manifestation of early energy-loss from rapidly rotating proto-magnetars may be "hyper-energetic" SNe, which we define as having energy greater than a SN's usual $\sim 10^{51}$ ergs. SNe significantly energized by proto-magnetar winds are naturally asymmetric given the preferred direction associated with the rotation axis of the PNS, and if energized sufficiently early, their nucleosynthetic yield may be appreciably modified; additionally, in some cases proto-magnetar winds may provide conditions favorable for long-duration GRBs within just seconds of the progenitor core collapse (Thompson 1994; Wheeler et al. 2000; TCQ). In order to possess $\gtrsim 10^{51}$ ergs of rotational energy a PNS must be born with a period $P_0 \lesssim 4$ ms, and, as Figure 2.9 illustrates, such a large energy is extracted during the Kelvin-Helmholtz epoch only, for $B_\nu^{\rm dip} \gtrsim 10^{15}$ G, if the energetically-dominant form of outflow is at least mildly relativistic. Using equation (2.31), the spin-down timescale for relativistic outflow from a proto-magnetar is

$$\tau_{\rm J}^{\rm REL} \simeq 350 (B_{15}^{\rm dip})^{-2} P_{\rm ms}^2 \left(\frac{R_Y/R_{\rm L}}{1/3} \right)^2 {\rm s}. \tag{2.35}$$

When $R_{\rm Y} \approx R_{\rm L}$ ($\sigma \gg 1$), equation (2.35) reduces to the canonical force-free ("vacuum dipole") spin-down timescale, but as was discussed in §2.4.1, neutrino-heated mass flux (which is significantly enhanced for $P \sim 1$ ms) maintains modest σ at early times, and therefore the PNS may spin down up to an order of magnitude faster during the Kelvin-Helmholtz epoch (B06).

For a surface dipole field typical of observed Galactic magnetars ($\sim 10^{14} - 10^{15}$ G) the SN shock is only energized with $\gtrsim 10^{51}$ ergs during $\tau_{\rm KH}$ for initial periods $\lesssim 1 - 2$ ms; however, such a large total rotational energy ($\gtrsim 10^{52}$ ergs) probably cannot be typical of magnetar birth because even if it is not extracted during $\tau_{\rm KH}$ this rotational energy will eventually be transferred to the surrounding environment, and observations of Galactic magnetar SN remnants are inconsistent with such a large energy (e.g., Vink & Kuiper 2006)[5]. In addition, the rate of hyper-energetic SNe is probably much smaller than the rate of magnetar births: Podsiadlowski et al. (2004) estimate that the hyper-energetic SNe rate is only $\sim 0.01 - 0.1\%$ of the radio pulsar birthrate, while Woods & Thompson (2004) estimate that the Galactic magnetar birthrate is at least $\sim 10\%$ of the radio pulsar birthrate.

Consider, however, a rarer class of proto-magnetar with rapid initial rotation ($P_0 \sim 1$ ms) and a somewhat stronger global magnetic field ($B_\nu^{\rm dip} \approx 3 \times 10^{15} - 10^{16}$ G; if a rapid birth period is indeed the cause of such a strong field, these assumptions are not independent). Figure 2.9 shows that winds from PNSs with these characteristics are dominated energetically by at least mildly relativistic outflow. Evolving a proto-magnetar of this type with $P_0 = 1$ ms using the calculations described in §2.4.1 we find that the total energy extracted during the Kelvin-Helmholtz phase is $1.1 \times 10^{52} (1.8 \times 10^{52})$ ergs for a surface dipole field strength of $3 \times 10^{15} (10^{16})$ G; this represents 50%(80%) of the total rotational energy of the PNS. We find that almost all of this energy is extracted with $\sigma < 10^3$. More specifically, for $B_\nu^{\rm dip} = 3 \times 10^{15} (10^{16})$ G, we find that $\approx 7 \times 10^{51} (1.1 \times 10^{52})$ ergs of rotational energy is extracted with $\sigma < 10$ in the first 5(2) s following the launch of the SN shock; the assumption of excess open magnetic flux over the pure force-free case (eq. [2.29]) is therefore especially well-justified because wind solutions with precisely these parameters ($B^{\rm dip} \sim 10^{15} - 10^{16}$ G, $P \sim 1$ ms, and $\sigma \sim 0.1 - 10$) have been calculated by B06. The rapid spin-down (eq. [2.35]) and efficient energy extraction that occurs immediately following the birth of a magnetar of this type

[5] One caveat to this argument is that a significant portion of the rotational energy could escape as gravitational waves in a time $\ll \tau_{\rm J}$ (see Stella et al. 2005).

may energize the SN shock sufficiently rapidly to enhance its ^{56}Ni nucleosynthetic yield (e.g., Nakamura et al. 2001), one of the observational signatures of hyper-energetic SNe (however, see Soderberg 2006). We note, however, that the ability of proto-magnetar winds to affect the SN nucleosynthesis is sensitive to the evolution of the magnetic field and radius of the PNS, since the time for the PNS to contract to its final radius is similar to the time over which energy must be extracted to affect the ^{56}Ni yield.

Although a significant portion of the PNS rotational energy emerges with $\sigma < 10$, which causes enhanced spin-down at early times, we find that the total energy extracted is distributed almost uniformly in $\log(\sigma)$ in the range $\sigma \in \{0.1, 1000\}$. Indeed, for $B_\nu^{\rm dip} = 3\times10^{15}(10^{16})$ G we find that $2\times10^{51}(4\times10^{51})$ ergs is extracted with $10 < \sigma < 100$ in the first 18(7) s, and that an additional $10^{51}(3\times10^{51})$ ergs is extracted with $100 < \sigma < 1000$ by 39(32) s following the launch of the SN shock. If the Poynting-Flux of this outflow can be efficiently converted to kinetic energy (e.g., Drenkhahn & Spruit 2002), then the high energy to mass density implied by the wind's large σ will result in acceleration to a comparably large asymptotic Lorentz factor. The fact that a significant portion of the PNS rotational energy emerges with $\sigma \sim 10 - 1000$ on a timescale $\tau_{\rm J}^{\rm REL} \sim \tau_{\rm KH} \sim 10 - 100$ s thus makes the birth of proto-magnetars with $P_0 \sim 1$ ms and $B_\nu^{\rm dip} \sim 3\times10^{15} - 10^{16}$ G a viable candidate for the central engine of LGRBs. Indeed, it is important to note that for initial PNS periods that give the right energetics for LGRBs ($P \approx 1-3$ ms) and surface magnetic fields that give the right timescale for LGRBs ($B_\nu^{\rm dip} \approx 3\times10^{15} - 10^{16}$ G) the magnetization of the resulting proto-magnetar wind - which is not a free parameter of the problem - is consistent with the Lorentz factors inferred from LGRBs ($\Gamma \sim 100$; Lithwick & Sari 2001; Granot & Kumar 2005). One shortcoming of our calculations, however, is that we cannot address whether proto-magnetar winds will have large-scale collimation, as suggested by observations of some LGRB afterglows (e.g., "jet breaks"; Rhoads 1997, 1999; Frail et al. 2001). As noted in the introduction, the collimation of the relativistic wind may depend on its interaction with less relativistic material (which is ejected earlier and is more likely to be collimated about the pole; B06) or the stellar mantle

(e.g., Wheeler et al. 2000; Uzdensky & MacFadyen 2006).

2.4.3 r-process Nucleosynthesis

PNS winds are a plausible candidate for the astrophysical source of heavy r-process nuclides (Woosley & Hoffman 1992; Meyer et al. 1992). The chief requirement for the r-process in PNS winds successfully reaching the critical third abundance peak at $A \approx 195$ is that the ratio of neutrons to seed nuclei (the "neutron-to-seed" ratio) remain high until the outflow cools to the point at which r-process can commence ($T \approx 0.1$ MeV). As many previous investigations have emphasized (e.g., Hoffman, Woosley, & Qian 1997; hereafter HWQ), the primary wind properties necessary to achieve and maintain a large neutron-to-seed ratio are: (a) a high asymptotic wind entropy[6] S^a, (b) a small asymptotic electron fraction Y_e^a (large neutron fraction), and (c) a short dynamical timescale $\tau_{\rm dyn}$, where we follow HWQ in defining $\tau_{\rm dyn}$ as[7]

$$\tau_{\rm dyn} \equiv \left[\frac{T}{v_r|dT/dr|}\right]_{T=0.5{\rm MeV}} \sim \left[\frac{r}{v_r}\right]_{T=0.5{\rm MeV}}, \tag{2.36}$$

where the second equality only holds as an order-of-magnitude estimate. The dynamical time is defined at $T = 0.5$ MeV because this is the radius at which α-particles, the building blocks of seed nuclei, first form.

HWQ present numerical calculations delineating the regions of $(S^a, \tau_{\rm dyn}, Y_e^a)$ parameter space necessary for nucleosynthesis to reach the third abundance peak, assuming an adiabatic cooling model. In general, they find that the condition for successful r-process takes the approximate functional form

$$S^a \gtrsim (\tau_{\rm dyn})^{1/3}\mathcal{F}, \tag{2.37}$$

[6]More precisely the r-process requires a high wind entropy at $T = 0.5$ MeV ($S_{0.5\,{\rm MeV}}$); however, entropy from neutrino heating saturates inside the radius where $T = 0.5$ MeV so that $S_{0.5\,{\rm MeV}} \simeq S^a$(indeed, as discussed in §2.2.2, we artificially set $\dot{q}_\nu = 0$ for $T < 0.5$ MeV). In §2.4.3 we will distinguish between $S_{0.5\,{\rm MeV}}$ and S^a when we consider the more radially-extended effects that wave heating can have on the wind entropy.

[7]We caution that $\tau_{\rm dyn}$ is sometimes defined in terms of the density scale height and this dynamical timescale, under the radiation-dominated and approximately constant entropy conditions at $T \approx 0.5$ MeV, is a factor of 3 shorter than that defined in equation (2.36).

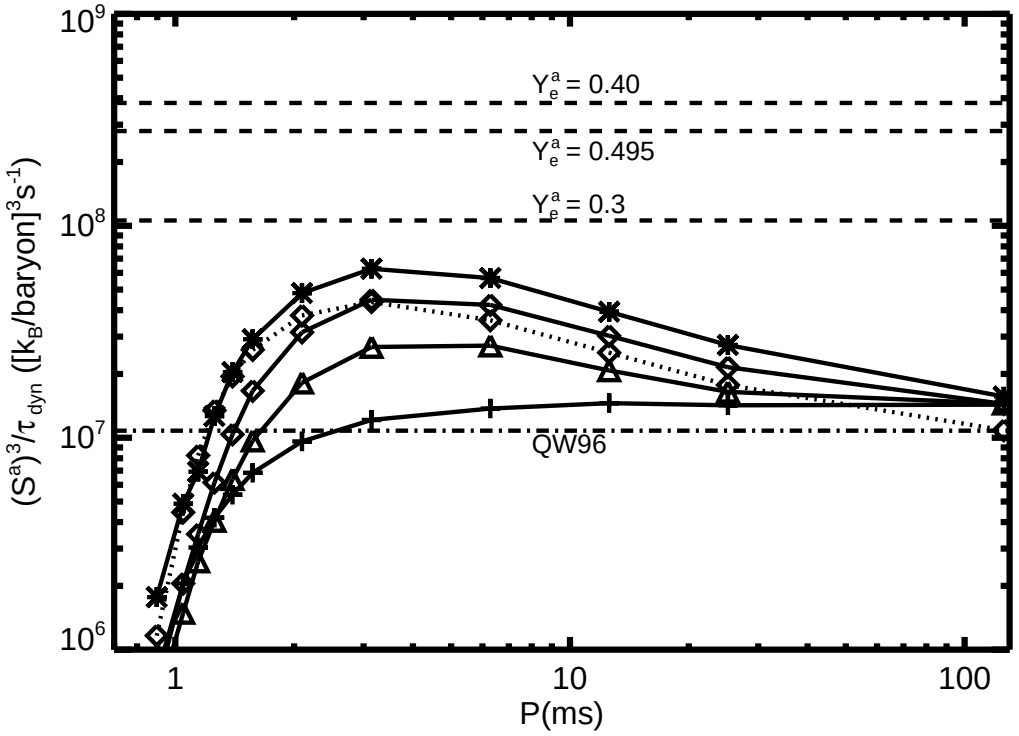

Figure 2.11: $(S^a)^3/\tau_{\rm dyn}$ as a function of the rotation period P for monopole magnetic field strengths $B_\nu = 10^{13}$ G (cross), 10^{14} G (triangle), 2.5×10^{14} G (diamond), and 10^{15} G (asterisk) at $L_{\bar\nu_e} = 8\times10^{51}$ ergs s^{-1}, where S^a is asymptotic wind entropy and $\tau_{\rm dyn}$ is the dynamical time evaluated at $T = 0.5$ MeV (eq. [2.36]). The ratio $(S^a)^3/\tau_{\rm dyn}$ is also shown for $B_\nu = 2.5\times10^{14}$ G at $L_{\bar\nu_e} = 3.5\times10^{51}$ ergs s^{-1} (diamond, dotted). Shown with dashed lines are the approximate thresholds above which r-process can proceed to the third abundance peak ($A\approx195$), taken from the numerical study of Hoffman, Woosley, & Qian 1997 (their Table 5), for several Y_e^a; notice that the threshold actually decreases with Y_e^a for $Y_e^a \gtrsim 0.46$. The dot-dashed line is $(S^a)^3/\tau_{\rm dyn}$ calculated from the analytic expressions given by Qian & Woosley (1996) for NRNM winds at $L_{\bar\nu_e} = 8\times10^{51}$ ergs s^{-1} (their eqs. [48a] and [61]). This figure highlights that strongly magnetized, rapidly rotating PNS winds produce conditions significantly more favorable for successful third peak r-process; the optimal conditions obtain for $B_\nu \gtrsim 10^{14}$ G and $P\sim2-10$ ms because $\tau_{\rm dyn}$ is reduced to a fraction of the rotation period by magneto-centrifugal acceleration (see Fig. 2.12). The decrease in $(S^a)^3/\tau_{\rm dyn}$ for $P\lesssim3$ ms arises because, for sufficiently rapid rotation, magneto-centrifugal acceleration reduces the advection time of wind material through the heating region, thus decreasing the asymptotic entropy S^a(eq. [2.38]).

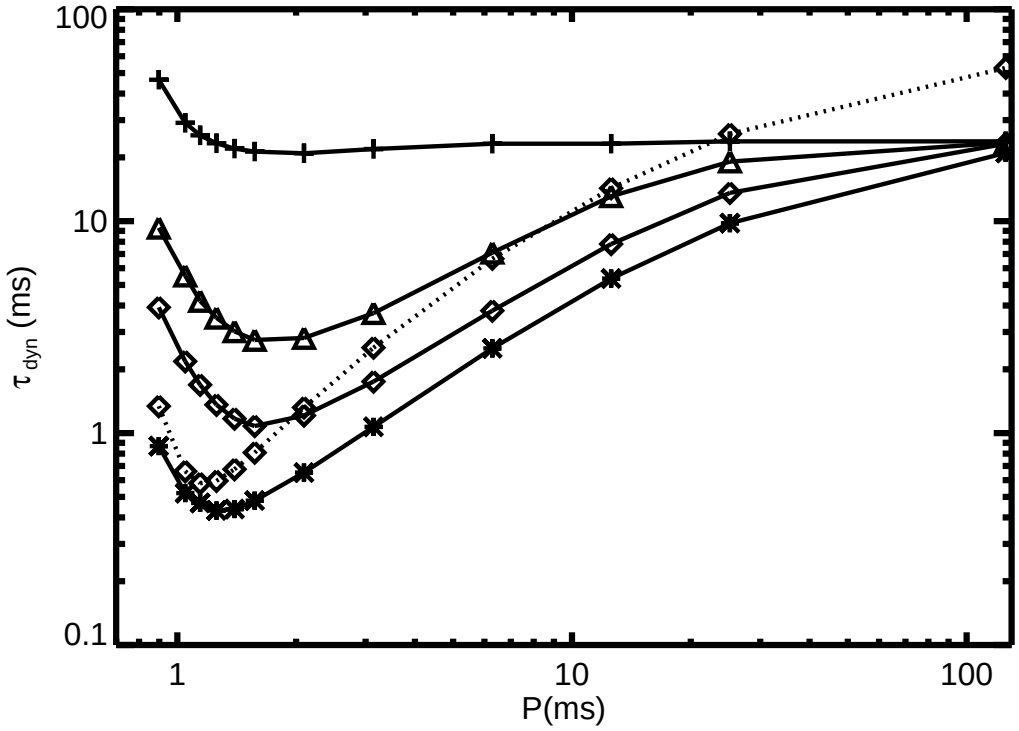

Figure 2.12: The dynamical time $\tau_{\rm dyn}$ at the radius where $T = 0.5$ MeV (eq. [2.36]) as a function of the PNS rotation period (P) at $L_{\bar{\nu}_e} = 8 \times 10^{51}$ ergs s^{-1} for monopole field strengths $B_\nu = 10^{13}$ G (cross), 10^{14} G (triangle), 2.5×10^{14} G (diamond), and 10^{15} G (asterisk). The dynamical time is also shown for $B_\nu = 2.5 \times 10^{14}$ G at $L_{\bar{\nu}_e} = 3.5 \times 10^{51}$ ergs s^{-1} (diamond, dotted). For slow rotation and weak magnetic fields, $\tau_{\rm dyn}$ approaches a constant value (≈ 20 ms at $L_{\bar{\nu}_e} = 8 \times 10^{51}$ ergs s^{-1}). For larger B_ν, $\tau_{\rm dyn}$ decreases to a fraction of the PNS rotation period due to magneto-centrifugal acceleration around the $T = 0.5$ MeV radius; the field required to minimize $\tau_{\rm dyn}$ is approximately $B_{\rm cf}$ (eq. [2.26]). For very rapid rotation ($P \lesssim$ 2-3 ms), centrifugally-enhanced mass-loss reduces the Alfvén radius, which in turn decreases the effectiveness of magneto-centrifugal acceleration and increases $\tau_{\rm dyn}$. The large reduction in $\tau_{\rm dyn}$ in strongly magnetized, rapidly rotating PNS winds provides conditions more favorable for successful r-process nucleosynthesis (see Fig. 2.11).

where $\mathcal{F}$ is a function of only Y_e^a (see HWQ eqs. [20a,b] for analytic approximations to these results). Hence, at fixed neutron abundance (i.e., fixed Y_e^a) a successful r-process is favored for large values of the ratio $(S^a)^3/\tau_{\rm dyn}$. However, for a wide range of reasonable PNS properties, detailed NRNM wind calculations show that this ratio falls short of that required to reach the third peak (QW; Otsuki et al. 2000; Wanajo et al. 2001; T01). Given that magnetar birth is relatively common and that rapid rotation may be its key ingredient, we have quantified the effects that magnetar-strength fields and rapid rotation have on the PNS wind properties that determine whether third peak r-process is successful.

Figure 2.11 shows $(S^a)^3/\tau_{\rm dyn}$ from our magnetized wind solutions at $L_{\bar{\nu}_e,51} = 8$ and $B_\nu = 10^{13}$, 10^{14}, 2.5×10^{14}, and 10^{15} G as a function of the PNS rotation period; also shown is $(S^a)^3/\tau_{\rm dyn}$ for $B_\nu = 2.5 \times 10^{14}$ G and $L_{\bar{\nu}_e,51} = 3.5$ (dashed line). To put our results in context, we plot the entropy threshold given by HWQ (their Table 5) at the lowest $\tau_{\rm dyn}$ they consider (≈ 5 ms; choosing such a low $\tau_{\rm dyn}$ will be justified below) with a dashed line for several Y_e^a. We plot several Y_e^a because the entropy required for successful r-process depends sensitively on Y_e^a, but a modest change to Y_e^a in our wind calculations would not significantly alter S^a or $\tau_{\rm dyn}$ from those obtained with $Y_e^a = 0.4$. Figure 2.11 shows that the presence of a magnetar-strength field and mildly rapid rotation moves the critical wind parameters almost an order-of-magnitude closer to successful third peak r-process in the space of $(S^a)^3/\tau_{\rm dyn}$.[8] We examine the reasons for this result below.

In rapidly rotating, strongly-magnetized PNS winds, centrifugal-flinging pushes matter quickly through the heating region, which reduces S^a. Our calculations find that, for $B_\nu \gtrsim B_{\rm cf}$ (eq. [2.26]), S^a is approximately given by

$$S^a \simeq S^a_{\rm NRNM} \exp[-\Omega/\Omega_S], \tag{2.38}$$

where $\Omega_S \simeq 3500(L_{\bar{\nu}_e,51}/8)^{0.15}$ s^{-1} and $S^a_{\rm NRNM} \simeq 70(L_{\bar{\nu}_e,51}/8)^{-0.2}$ is the asymptotic entropy for NRNM winds in units of k_B/baryon.

[8]This conclusion disagrees with those of Nagataki & Kohri (2001), who also considered the effects of rotation and magnetic fields on PNS winds; however, these authors were unable to consider fields larger than $\sim 10^{11}$ G because of the complicated critical point topology they encountered in computing more highly-magnetized wind solutions.

At face value, the exponential decrease in entropy implied by equation (2.38) appears to stifle the chances for successful third peak r-process in rapidly rotating, strongly-magnetized PNS winds. However, because such PNS winds are magnetically-driven, $\tau_{\rm dyn}$ will also decrease with increasing Ω; hence, success for the r-process depends on the competition between changes in $\tau_{\rm dyn}$ and S^a. As Figure 2.8 illustrates, in magnetically-driven PNS winds the $T = 0.5$ MeV radius ($R_{0.5{\rm MeV}}$) is generally outside the sonic point and the heating region (interior to which S^a is set); therefore, while periods $\lesssim$ 2–3 ms are required to significantly affect the dynamics in the subsonic heating region and alter $\dot{M}$ or S^a (the "$\dot{M}$ Enhanced" region of Fig. 2.1), $\tau_{\rm dyn}$ is significantly reduced for more modest rotation rates (the much larger "Magnetically-Driven" region in Fig. 2.1).

Figure 2.12 shows $\tau_{\rm dyn}$ from our magnetized wind solutions at $L_{\bar{\nu}_e,51} = 8$ and $B_\nu = 10^{13}$, 10^{14}, 2.5×10^{14}, and 10^{15} G as a function of the PNS rotation period; also shown is $\tau_{\rm dyn}$ for $B_\nu = 2.5 \times 10^{14}$ G and $L_{\bar{\nu}_e,51} = 3.5$ (dashed line). For rotation periods $\sim 1 - 10$ ms and $B_\nu \gtrsim 10^{15}$ G our solutions obtain $\tau_{\rm dyn} \approx 0.3 - 3$ ms, just a fraction of the rotation period, while for slow rotation $\tau_{\rm dyn}$ approaches a value ≈ 20 ms for $L_{\bar{\nu}_e,51} = 8$, similar to that derived by QW (their eq. [61]). As a comparison of the $B_\nu = 2.5 \times 10^{14}$ and 10^{15} G solutions in Figure 2.12 shows, the effects of magnetic fields on $\tau_{\rm dyn}$ saturate for sufficiently large fields. Indeed, the monopole surface field required to minimize $\tau_{\rm dyn}$ is approximately $B_{\rm cf}$ (eq. [2.26]). Ignoring centrifugal enhancement of $\dot{M}$ and using equations (2.15) and (2.30), this corresponds to a surface dipole field $\sim 10^{15}(P/4\,{\rm ms})^{3/2}(L_{\bar{\nu}_e,51}/8)^{1.25}$ G; hence, surface fields typical of observed Galactic magnetars are probably sufficient to minimize $\tau_{\rm dyn}$ at early times in a PNS's thermal evolution. Thus, if observed Galactic magnetars were born with periods in the range 2 ms $\lesssim P \lesssim$ 10 ms we conclude that there is an enhanced likelihood that r-process was successful in their PNS winds.

We should caution that the comparison between our calculations and the thresholds of HWQ in Figure 2.12 was made for $\tau_{\rm dyn} = 5$ ms, which was the most rapid outflow HWQ considered; this is, however, almost an order of magnitude longer than the dynamical time associated with some of our solutions. Constraints

similar to HWQ at $\tau_{\rm dyn} \sim 3\,$ms are obtained by Meyer & Brown (1997). A somewhat different threshold is obtained by Sasaqui et al. (2006), who emphasize a previously neglected light-element r-process seed production channel. In fact, recent work by Meyer (2002) shows that the threshold for r-process nucleosynthesis may be modified at very short $\tau_{\rm dyn}$ compared to standard expectations (i.e., Y_e^a must be less than 0.5). In order to accurately assess whether r-process nucleosynthesis in proto-magnetar winds will proceed to the third abundance peak and beyond, or whether the nucleosynthesis that results from these outflows may be used to constrain the birth rate of proto-magnetars, a survey of nucleosynthesis calculations should be carried out at short $\tau_{\rm dyn}$. In fact, the critical question of whether this modest S^a, very-low $\tau_{\rm dyn}$ mode of r-process can reproduce the seemingly universal solar abundance curve above Ba (e.g., Cowan et al. 2005) must ultimately be answered through detailed nucleosynthesis calculations on our wind solutions (such calculations are currently in progress) and by including a better treatment of Y_e in the wind. The effects of GR not included in our calculations will tend to increase S^a and Y_e^a, on balance probably increasing the likelihood of successful r-process (Fuller & Qian 1996; Cardall & Fuller 1997).

T01 found that in NRNM winds $S^a \propto (\tau_{\rm dyn})^{0.2}$; thus, even though $S^a \propto L_{\bar{\nu}_e}^{-0.2}$ increases with time as the PNS cools, it is difficult for a NRNM wind that does not produce conditions favorable for third peak r-process (eq. [2.37]) at early times to enter the regime for a successful r-process at later times. We might expect a modification to the PNS $(S^a, \tau_{\rm dyn})$ evolutionary track in the case of a proto-magnetar because the dynamical time in a magnetically-driven PNS wind is no longer set solely by the neutrino heating. In order to address this question, we explored how $(S^a)^3/\tau_{\rm dyn}$ changes as the PNS cools. As shown in Figure 2.11, from our calculations at $L_{\bar{\nu}_e,51} = 3.5$ and $B_\nu = 2.5 \times 10^{14}$ G we find that $(S^a)^3/\tau_{\rm dyn}$ changes by less than a factor of 2 from those at $L_{\bar{\nu}_e,51} = 8$ and $B_\nu = 2.5 \times 10^{14}$ G; in particular, the peak value of $(S^a)^3/\tau_{\rm dyn}$ at $P \sim 3$ ms remains essentially unchanged. Thus the conditions for r-process in magnetically-driven PNS winds do not vary strongly with luminosity over the range we have explored.

To conclude this section, we briefly consider what constraints can be placed on

r-process in proto-magnetar winds if they are to be capable of having a significant effect on the heavy element abundance evolution of the Galaxy. If most SNe produce r-process elements, the total r-process-rich wind mass ejected per SN must be $\sim 10^{-6} - 10^{-5}$ $M_\odot$ to account for the total Galactic yield (e.g., Qian 2000); hence, because the magnetar birthrate is $\sim 10\%$ of the total neutron star birthrate, at least $\sim 10^{-5} - 10^{-4}$ $M_\odot$ of r-process-rich material must be ejected per magnetar birth (this number is quite uncertain because the magnetar birthrate is uncertain; see Woods & Thompson 2004). Because r-process in proto-magnetar winds is only likely to be successful for $P \gtrsim 2-3$ ms, rotation does not significantly enhance mass-loss from the PNS (Fig. 2.10). As a result, the required yield of r-process rich material per magnetar birth is similar to our estimates for the total mass extracted in NRNM PNS winds ($\sim 10^{-4}$ $M_\odot$). Thus we conclude that if proto-magnetar winds are the dominant source for Galactic r-process, the r-process probably must occur early in the PNS cooling evolution (in the first few seconds, even earlier than for normal PNSs)[9]. The former in part justifies our concentration on high $L_{\bar{\nu}_e}$ in Figure 2.11 and means that the question of whether magnetar birth is a significant source for Galactic r-process is especially sensitive to the early evolution of the magnetic field and radius of the PNS.

It is also worth noting that on the basis of a comparison between the solar r-process abundance pattern with meteoritic abundances of ^{129}I and ^{182}Hf, Qian, Vogel, & Wasserburg (1998) (see also Wasserburg et al. 1996) suggest a diversity of r-process sites. In particular, they argue for a site with high frequency (roughly the Galactic SN rate) that generates the $A \approx 195$ nuclei and a site 10 times less frequent that produces nuclei near $A \approx 135$. In order to satisfy the observational constraints, the latter site must eject 10 times the mass of the high-frequency site, per event. Although we have not proven that magnetars produce an r-process in any mass range the $\sim 10\%$ birth fraction of magnetars, the characteristically larger total ejected mass (Fig. [2.10]), and the very different thermodynamics of their winds relative to NRNM PNS winds make it tempting to associate proto-

[9]Of course, if the magnetar birthrate has been underestimated and is comparable to the total NS birthrate then r-process could occur somewhat later in the PNS evolution.

magnetar winds with the low-frequency enrichment events advocated by Qian, Vogel & Wasserburg (1998).

Wave Heating

QW show that by including a heating source in addition to neutrinos outside a few PNS radii, the wind entropy is increased, the dynamical time is reduced, and the chances for a successful r-process can be substantially improved. Such an extended heating mechanism operates above the sun, where convectively excited waves are believed to heat the extended solar corona (for recent work see Cranmer & van Ballegooijen 2005). The neutrino cooling luminosity of a PNS also drives vigorous convection during the Kelvin-Helmholtz epoch (e.g., Burrows & Lattimer 1986; Burrows, Hayes, & Fryxell 1995). It is likely that a fraction of the convective energy flux will be deposited into outgoing waves, which will then propagate into the PNS atmosphere and deposit their energy and momentum on a length scale of order a few PNS radii. The relative importance of hydrodynamic and MHD wave excitation likely depends on the magnetic field strength of the PNS. Here we focus on heating by MHD waves in the magnetospheres of strongly magnetized PNSs (Suzuki & Nagataki 2005), though hydrodynamic wave excitation may be important as well (e.g., Burrows et al. 2006a,b). If the energy flux in MHD waves at the PNS surface is $F_{\rm w}(R_\nu) = (1/2)\rho v_A^3(\delta B/B_r)^2|_{R_\nu}$, we estimate that the total wave heating $\dot{Q}_{\rm w} \approx 4\pi R_\nu^2 F_{\rm w}(R_\nu)$ is given by

$$\dot{Q}_{\rm w} \simeq 10^{48}(B_{15})^3 \left(\frac{\delta B_\nu/B_\nu}{0.1}\right)^2 \text{ergs s}^{-1}, \tag{2.39}$$

where $\delta B_\nu \equiv \delta B(R_\nu)$ is the amplitude of the waves excited at the PNS surface (with a density $\rho(R_\nu) \approx 10^{12}$ g cm^{-3}). The ratio of the wave heating in equation (2.39) to the total neutrino heating $\dot{Q}_\nu = 4\pi \int_{R_\nu}^{\infty} r^2 \rho \dot{q}_\nu dr$ in the absence of rotation can be approximated as

$$\frac{\dot{Q}_{\rm w}}{\dot{Q}_\nu} \approx 0.03(B_{15})^3 \left(\frac{\delta B_\nu/B_\nu}{0.1}\right)^2 \left(\frac{L_{\bar{\nu}_e,51}}{8}\right)^{-2.8}, \tag{2.40}$$

where $\dot{Q}_\nu \approx 4.4 \times 10^{49}(L_{\bar{\nu}_e,51}/8)^{2.8}$ ergs s^{-1} is taken from our NRNM calculations and agrees reasonably well with the results of T01 (their Table 1). Equation

(2.40) illustrates that, for efficient wave excitation, wave heating at early times may become important for field strengths $\gtrsim 10^{14} - 10^{15}$ G. Equation (2.40) also appears to suggest that wave heating will become substantially more important as the PNS cools and $L_{\bar{\nu}_e}$ drops; however, whether this in fact occurs is unclear because the energy flux in waves and the surface amplitude δB_ν will likely decrease with $L_{\bar{\nu}_e}$ as the convective flux decreases.

In order to quantify the effects that wave heating have on the entropy and dynamical time in rotating PNS winds, we consider a concrete model in which we add Alfvén wave pressure and heating to our solutions. In the entropy equation (eq. [2.9]), this leads to an additional source term of the form

$$\dot{q}_{\rm w}(r) = \frac{v_A}{v_r + v_A} \frac{F_{\rm w}(R_\nu)}{\chi R_\nu \rho} \left(\frac{R_\nu}{r}\right)^2 \exp\left[\frac{-(r - R_\nu)}{\chi R_\nu}\right], \tag{2.41}$$

where the factor $v_A/(v_r + v_A) < 1$ accounts for the work done by the Alfvén waves. Equation (2.41) concentrates the total wave heating ($\dot{Q}_{\rm w} = 4\pi \int_{R_\nu}^{\infty} r^2 \rho \dot{q}_{\rm w} dr$) on a radial length scale $\approx \chi R_\nu$. Radially propagating Alfvén waves also exert a pressure on the fluid ($\rm P_w$), which contributes a term to the right hand side of the radial momentum equation (eq. [2.3]) of the form (Lamers & Cassinelli 1999; Suzuki & Nagataki 2005)

$$-\frac{1}{\rho}\frac{d\rm P_w}{dr} = \frac{\dot{q}_{\rm w}}{2(v_r + v_A)} - \frac{(\delta B)^2}{32\pi\rho}\frac{3v_r + v_A}{v_r + v_A}\frac{1}{\rho}\frac{d\rho}{dr}, \tag{2.42}$$

where

$$(\delta B)^2 = \frac{8\pi\chi R_\nu \rho \dot{q}_{\rm w}}{v_r + v_A}. \tag{2.43}$$

We consider a variety of dissipation lengths ($R_\nu \chi$) and surface wave amplitudes (δB_ν) and assess the effects of Alfvén wave heating on our wind solutions. For reasons discussed at the end of §2.4.3, we are primarily interested in the effect that wave heating has on r-process at early times; thus, we concentrate on wave heating applied to high luminosity solutions.

Our wave heating calculations are summarized in Table 2.3. Motivated by the r-process threshold of HWQ (eq. [2.37]), we quantify the improvement towards a

successful r-process through an "improvement factor":

$$I_{\rm w}(\dot{Q}_{\rm w},\chi) \equiv \frac{[S^3_{0.5{\rm MeV}}/\tau_{\rm dyn}]_{\dot{Q}_{\rm w}}}{[S^3_{0.5{\rm MeV}}/\tau_{\rm dyn}]_{\dot{Q}_{\rm w}=0}}, \tag{2.44}$$

where $S_{0.5{\rm MeV}}$ is the entropy at the radius where $T = 0.5$ MeV. Figure 2.11 shows that for $L_{\bar{\nu}_e,51} = 8, B_\nu = 10^{15}$ G, and $P = 3$ ms (corresponding to the peak in Fig. 2.11) an improvement factor $I_{\rm w} \gtrsim 6$ is required to exceed the HWQ threshold for third-peak r-process for $Y_e^a \approx 0.4$, while for a NRNM solution at $L_{\bar{\nu_e},51} = 8$ successful r-process requires $I_{\rm w} \gtrsim 25$. We should note, however, that HWQ assumed adiabatic expansion through the α-process temperature range ($T \approx 0.5 - 0.2$ MeV), while for large χ wave heating is important at these radii and the expansion is not adiabatic. This may modify the $I_{\rm w}$ required for successful r-process.

For $P \simeq 3(130)$ ms, $B = 10^{15}$ G, and $L_{\bar{\nu}_e,51} = 8$, we find that $I_{\rm w} \gtrsim 6(25)$ requires an amplitude $\delta B_\nu/B_\nu \gtrsim 0.5 - 0.7$ and a dissipation length $\chi \sim 3$.[10] This wave amplitude corresponds to a total wave heating $\gtrsim 4 \times 10^{49}$ ergs s^{-1}, which is comparable to the total neutrino heating for this solution and is $\sim 10^{-3}$ of the neutrino luminosity at early times. The fact that a comparable wave energy is required in the slow and rapidly rotating limits appears somewhat coincidental. For the non-rotating solutions, the wave heating only reduces the dynamical time to ~ 2 ms, never reaching the regime of $\tau_{\rm dyn} \lesssim 1$ ms obtained in rotating PNS winds. The entropy increase at $T = 0.5$ MeV is, however, larger in the non-rotating case because the $T = 0.5$ MeV radius is at larger radii (and thus $S_{0.5{\rm MeV}}$ is closer to S^a). Although the actual wave dissipation mechanism in the PNS atmosphere is uncertain, we note that for initial amplitudes of $\delta B_\nu/B_\nu \sim 0.5$, conservation of action implies that the waves are nonlinear with $\delta B/B_r \sim 1$ at $\sim 3 - 4R_\nu$, similar to the dissipation lengths (χ) that are optimal for r-process. Also note that for more rapidly rotating solutions ($P \approx 1$ ms), significantly more wave heating is

[10] For very small χ, the wave heating effectively acts as an increase to the neutrino luminosity, which decreases the asymptotic entropy S^a (recall that – absent wave heating – the entropy decreases with increasing luminosity). For large χ, on the other hand, the heating is concentrated outside the $T = 0.5$ MeV radius and, while S^a increases substantially, the entropy at $T = 0.5$ MeV remains relatively unaffected.

required for successful r-process: even $\delta B_\nu \approx B_\nu$ is insufficient at $B \approx 10^{15}$ G. This is because the total neutrino heating itself increases at $P \sim 1$ ms (ρ is larger in the neutrino heating region due to magneto-centrifugal support), so a given amount of wave heating has less of an effect on the solution.

For lower neutrino luminosities, smaller $\dot{Q}_{\rm w}$ can lead to successful r-process. For example, at $L_{\bar{\nu}_e,51} = 3.5$ and $B = 2.5 \times 10^{14}$ G, we find that, for $P = 3(130)$ ms, $\dot{Q}_{\rm w} \gtrsim 10^{49}(5 \times 10^{48})$ ergs s^{-1} and $\chi \sim 3$ is required to eclipse the HWQ r-process threshold for $Y_e^a = 0.4$.[11] The required wave heating in this case is again comparable to the total neutrino heating, but is only $\sim 6 \times 10^{-4}(3 \times 10^{-4})$ of the neutrino luminosity of the PNS. At even lower L_ν, a yet smaller fraction of the neutrino luminosity in wave heating would be capable of yielding successful r-process. However, as discussed in the previous section, constraints on the r-process rich material required per magnetar-birth imply that the r-process must be successful at relatively high neutrino luminosities. We thus conclude that wave heating leads to successful r-process if $\gtrsim 10^{-4} - 10^{-3}$ of the PNS's neutrino luminosity emerges in wave power at early times in the Kelvin Helmholtz epoch, and that this required level of wave heating is essentially independent of magnetic field strength and rotation rate (for $P \gtrsim 2$ ms).

Although the mechanism and formula we describe here are appropriate to proto-magnetars with large magnetic fields, it is possible that hydrodynamic (as opposed to MHD) wave heating is important and generic to normal PNS birth. In this case, waves may be generated by convective motions as the PNS cools, or via global modes of the PNS similar to those observed by Burrows et al. (2006a,b), that persist into the cooling epoch. As in the MHD case, a fraction of the total neutrino luminosity ($10^{-4}-10^{-3}$) must emerge in wave power over $\tau_{\rm KH}$ to produce conditions suitable for the r-process. Because such a mechanism may operate generically (and

[11] Suzuki & Nagataki (2005) found that for non-rotating solutions with Alfvén wave heating, r-process was successful for $\dot{Q}_{\rm w} \simeq 2 \times 10^{48}$ ergs s^{-1} and $\chi \sim 5-10$ at $L_{\bar{\nu}_e,51} \sim 1$. Our results are similar to theirs although their required wave heating is somewhat larger than an extrapolation of our results would suggest. However, they used different mean neutrino energies than we have assumed and obtain $\dot{M} \sim 2 \times 10^{-6}$ M$_\odot$ s^{-1}, roughly 3 times greater than we predict from equation (2.15) at $L_{\bar{\nu}_e,51} = 1$. This larger mass-loading may explain why their calculations required somewhat more wave heating to enter the regime of successful r-process.

not just in proto-magnetars) the requirement of an early-time r-process highlighted above for the proto-magnetars and in §4.3 is somewhat alleviated.

2.4.4 Additional Applications

While most magnetar formation probably results from the core collapse of a massive star, magnetars may also form through the accretion-induced collapse (AIC) of a white dwarf (Nomoto et al. 1979; Usov 1992; Woosley & Baron 1992). Rapid rotation will automatically accompany AIC due to the accretion of mass and angular momentum prior to collapse, and a strong field may accompany the final stages of the contraction of the PNS, amplified through either magnetic flux-freezing of the progenitor white dwarf's field or via dynamo action (Duncan & Thompson 1992). The properties of PNSs formed following AIC would thus be very similar to those of the proto-magnetars that we have considered in this paper and the resulting proto-magnetar wind would be accurately modeled using our calculations. AIC may thus give rise to a LGRB with properties similar to those considered in §2.4.2. However, LGRBs from AIC will not produce significant amounts of Ni (Woosley & Baron 1992; Dessart et al. 2006) and hence will not be associated with a simultaneous hyper-energetic Type-Ic SN, as in, e.g. GRB 980425/SN1998bw or GRB 030329/2003dh (Galama et al. 1998; Hjorth et al. 2003; Stanek et al. 2003; Woosley & Bloom 2006). Instead, AIC should be associated with a class of SN-less LGRBs like GRB 060505 and 060614 (Fynbo et al. 2006; Gal-Yam et al. 2006; Della Valle et al. 2006). A prediction of this model is that these LGRBs should be associated with both relatively old (few Gyr) and relatively young ($\sim$100 Myr) stellar populations. If some SN-less LGRBs are found to be associated with old stellar populations, it would strongly support the AIC interpretation.

Although we have focused on magnetized PNS evolution in this paper, the physical conditions we have considered are quite similar to those expected in a neutrino-cooled accretion disk surrounding a newly-formed black hole in the "collapsar" model for LGRBs (Woosley 1993; Paczynski 1998; MacFadyen & Woosley

1999). For concreteness, consider the properties of a thin accretion disk with an accretion rate $\dot{M}_{\rm acc} = 0.2 M_\odot$ s^{-1} and viscosity parameter $\alpha = 0.01$ at a fiducial radius of ≈ 100 km, or approximately 10 Schwarzschild radii above a non-rotating black hole of mass $3M_\odot$. According to the calculations of Chen & Beloborodov (2006), at these radii (where $P \approx 10$ ms) the disk is optically thick to neutrinos, the surface temperature of the disk is very similar to that of a PNS neutrinosphere ($\approx 2-3$ MeV), and the total neutrino luminosity of the disk is $L_\nu \simeq 0.04 \dot{M}_{\rm acc} c^2 \approx 1.4 \times 10^{52}$ ergs s^{-1} (their Fig. 18), comparable to that of a PNS at early times (note that at lower accretion rates the disk will be optically thin to neutrinos). If this disk were threaded with a large-scale poloidal field with a strength corresponding to that expected for MRI turbulence, $B \approx 10^{14} - 10^{15}$ G (plasma $\beta \approx 10 - 100$), the physical conditions would indeed resemble those in proto-magnetar winds. Thus neutrino-magneto-centrifugal driving may be important in setting the mass-loading and energy-loss rate in outflows from collapsar disks. Indeed, Levinson (2006) has calculated the mass loading of neutrino-driven outflows in general relativistic MHD for conditions anticipated in collapsar disks, finding qualitatively similar results to those discussed in this paper for PNS winds.

As a final context in which our calculations may be relevant, we note that a magnetized accretion flow like that considered above for collapsars or a short-lived, rapidly rotating proto-magnetar may be formed following the merger of a NS-NS binary (Paczynski 1986; Eichler et al. 1989; Rosswog & Liebendörfer 2003). Our calculations would also describe magnetized outflow from these objects, but additional work is needed to explore this application in more detail.

2.5 Conclusions

We have solved the one-dimensional non-relativistic neutrino-heated MHD wind problem in order to study the effects that magnetic fields and rotation have on PNS wind evolution following the launch of the SN shock but prior to the end of the Kelvin-Helmholtz cooling epoch. Figure 2.1 summarizes the physical regimes of PNS winds in the presence of rotation and magnetic fields. We map

our monopole solutions onto the axisymmetric, relativistic dipole calculations of B06, thus taking into account the effects that neutrino-driven mass-loss have on the fraction of open magnetic flux and the PNS spin-down rate. Our primary conclusions are as follows:

- We identify three types of PNSs based on the dominant character of their energy-loss during the Kelvin-Helmholtz epoch (see Figure 2.9):

  (1) For slow rotation and low magnetic field strengths ($B_{14}^{\rm dip} \lesssim 10^{-2} P_{\rm ms}^2$, where $B^{\rm dip} = 10^{14} B_{14}^{\rm dip}$ G is the surface dipole field strength of the PNS and $P = 1 P_{\rm ms}$ ms is its birth period), a neutrino-heated, thermally-driven wind dominates energy and mass-loss from the PNS; most radio pulsars were probably this type at birth.

  (2) For larger rotation rates and field strengths ($10^{-2} P_{\rm ms}^2 \lesssim B_{14}^{\rm dip} \lesssim 2 P_{\rm ms}^2 \exp[2 P_{\rm ms}^{-2}]$), a non-relativistic, magnetically-driven wind dominates during the Kelvin-Helmholtz epoch. Most observed Galactic magnetars ($\sim 10\%$ the birthrate of radio pulsars) were probably of this type at birth. For $B \sim 10^{15}$ G and $P \lesssim 2$ ms, greater than 10^{51} ergs can be lost to a non-relativistic, magnetically-driven outflow during τ_{KH}, and, over a broad range of initial spin period, the energy extracted is many times larger than from a slowly rotating PNS (see Fig. 2.9). The outflow from this type of PNS is likely to be collimated by magnetic stresses and the asymmetric injection of energy may be sufficient to generate an anisotropy in the morphology of the SNe remnant.

  (3) For rapid rotation and field strengths somewhat larger than those observed from Galactic magnetars ($B_{14}^{\rm dip} \gtrsim 2 P_{\rm ms}^2 \exp[2 P_{\rm ms}^{-2}]$), a relativistic, magnetically-driven wind dominates energy-loss during the Kelvin-Helmholtz epoch. Although the birthrate of PNSs of this type is probably small (if they are produced at all), they may be capable of producing hyper-energetic SNe and long-duration gamma-ray bursts.

- For $P \approx 3(1)$ ms and $B_\nu^{\rm dip} \gtrsim 10^{15}$ G the total mass-loss during the Kelvin-Helmholtz epoch is enhanced by a factor of $\approx 2(10^2)$ relative to a non-rotating PNS (Fig. 2.10).

- For initial PNS spin periods of $P \approx 1$ ms and magnetic field strengths of $B_\nu^{\rm dip} \approx 3 \times 10^{15} - 10^{16}$ G, we find that $\gtrsim 10^{52}$ ergs of rotational energy is extracted on a timescale of $10 - 40$ seconds and that the magnetization σ of the outflow is $\sim 0.1 - 1000$. The energy, luminosity, timescale, and mass-loading of the late-time outflow are all consistent with those required to explain long duration gamma-ray bursts (assuming efficient dissipation of magnetic energy into kinetic energy at large radii; e.g., Drenkhahn & Spruit 2002). In addition, outflows from such PNSs have the property that the PNS rotational energy is extracted with a roughly uniform distribution in $\log(\sigma)$ over the timescale $\tau_{\rm KH}$. For these modest σ winds, especially at early times, energy-loss from the PNS is enhanced relative to pure force-free spindown because of additional open magnetic flux (see the discussion in §2.4.1). Thus, a significant portion of the PNS rotational energy can be extracted in just a few seconds following the launch of the SN shock, perhaps sufficiently rapidly to increase the nucleosynthetic yield of the SN (e.g., ^{56}Ni).

- Winds from PNSs with $B_\nu^{\rm dip} \gtrsim 10^{15}$ G and $P \approx 2 - 10$ ms produce conditions almost an order-of-magnitude more favorable for third-peak r-process nucleosynthesis in the space of $(S^a)^3/\tau_{\rm dyn}$ than do winds from more slowly-rotating, less-magnetized PNSs (see Fig. 2.11). For these rotation rates, the asymptotic entropy is similar to that of a non-rotating, non-magnetized wind, while the dynamical time is significantly reduced by magnetic acceleration (see Fig. 2.12). The very different thermodynamic properties of rapidly rotating proto-magnetar winds (relative to non-rotating PNS winds) may contribute to the inferred diversity of r-process sites (e.g., Qian et al. 1998).

- Heating by outgoing hydrodynamic or MHD waves may be important in PNS winds. We find that if $\gtrsim 10^{-4} - 10^{-3}$ of the PNS's neutrino luminosity

emerges in wave power at early times in the Kelvin-Helmholtz epoch, then r-process is successful in PNS winds. This conclusion is relatively independent of magnetic field strength and rotation period for $P \gtrsim 2$ ms.

Acknowledgements

We thank Niccolo Bucciantini and Jon Arons for helpful discussions. We also thank Martin White and Marc Davis for computational time on their Beowulf cluster. T.A.T. thanks the Aspen Center for Physics, where this work germinated, for its hospitality. EQ and BDM were supported in part by NSF grant AST 0206006, NASA grants NAG5-12043 and NNG05GO22H, an Alfred P. Sloan Fellowship, the David and Lucile Packard Foundation, and a NASA GSRP Fellowship to BDM.

Table 2.1 PNS Wind Properties for $L_{\bar{\nu}_e} = 8 \times 10^{51}$ ergs s^{-1}, $R_\nu = 10$ km, & $M = 1.4$ M$_\odot$

B_ν (G)	Ω (s^{-1})	P (ms)	$\dot{M}$ (M$_\odot$ s^{-1})	σ	τ_J (s)	S [a] (k$_B$/baryon)	$\tau_{\rm dyn}$ [b] (ms)	R_s [c] (km)	R_A (km)	$\dot{E}$ [d] (10^{51} ergs s^{-1})	η [e]
10^{15}	6000	1.0	1.2×10^{-2}	0.055	4.8	13.7	0.52	19	31	4.7	1.80
10^{15}	4000	1.6	1.0×10^{-3}	0.30	12.6	24.1	0.48	23	67	1.2	1.18
10^{15}	2000	3.1	2.8×10^{-4}	0.26	12.9	40.6	1.1	35	120	0.31	1.14
10^{15}	1000	6.3	1.9×10^{-4}	0.099	9.3	52.2	2.5	55	180	0.11	1.11
10^{15}	500	13	1.6×10^{-4}	0.029	6.2	59.5	5.4	87	240	4.0×10^{-2}	1.14
10^{15}	250	25	1.5×10^{-4}	8.0×10^{-3}	4.0	64.5	9.8	140	310	1.5×10^{-2}	1.18
10^{15}	50	130	1.4×10^{-4}	3.4×10^{-4}	1.6	69.0	21	420	500	1.7×10^{-3}	1.00
10^{14}	6000	1.0	3.3×10^{-3}	2.0×10^{-3}	39	20.2	5.5	68	21	0.13	7.9
10^{14}	4000	1.6	6.6×10^{-4}	4.5×10^{-3}	101	29.9	2.8	48	29	0.046	3.8
10^{14}	2000	3.1	3.8×10^{-4}	3.0×10^{-3}	116	46.2	3.7	76	44	0.013	2.9
10^{14}	1000	6.3	2.4×10^{-4}	1.1×10^{-3}	88	57.8	7.1	150	61	4.6×10^{-3}	2.7
10^{14}	500	13	1.7×10^{-4}	3.1×10^{-4}	64	64.8	13	310	77	1.8×10^{-3}	2.5
10^{14}	250	25	1.5×10^{-4}	8.2×10^{-5}	52	68.0	19	520	88	7.9×10^{-4}	1.7
10^{14}	50	130	1.4×10^{-4}	3.4×10^{-6}	45	69.8	24	730	95	3.6×10^{-4}	0.17
10^{13}	6000	1.0	6.0×10^{-4}	1.1×10^{-4}	350	39.1	29	530	16	2.7×10^{-3}	43
10^{13}	4000	1.6	2.5×10^{-4}	1.2×10^{-4}	670	52.6	21	510	18	1.4×10^{-3}	19
10^{13}	2000	3.1	1.6×10^{-4}	4.6×10^{-5}	850	64.3	22	640	20	6.5×10^{-4}	13
10^{13}	1000	6.3	1.4×10^{-4}	1.3×10^{-5}	880	68.3	23	710	21	4.2×10^{-4}	3.0
10^{13}	500	13	1.4×10^{-4}	3.3×10^{-6}	880	69.7	23	740	21	3.7×10^{-4}	0.85
10^{13}	250	25	1.4×10^{-4}	8.5×10^{-7}	880	69.7	24	740	22	3.5×10^{-4}	0.23
10^{13}	50	130	1.4×10^{-4}	3.4×10^{-8}	880	69.9	24	750	22	3.4×10^{-4}	0.0093

[a] The asymptotic wind entropy.

[b] The dynamical time evaluated at $T = 0.5$ MeV (see eq. [2.36]).

[c] The radius of the adiabatic sonic point. For large B_ν and Ω the slow point and adiabatic sonic point are very close to each other, while for low B_ν and Ω they approach the Alfvén and fast magnetosonic radii, respectively.

[d] The asymptotic wind power.

[e] The ratio of the rotational power lost by the PNS to the asymptotic wind power (see eq. [2.12]).

Table 2.2 PNS Wind Properties at $B_\nu = 2.5 \times 10^{14}$ G, $R_\nu = 10$ km, and $M = 1.4$ $M_\odot$

$L_{\bar{\nu}_e,51}$ [a]	Ω (s^{-1})	P (ms)	$\dot{M}$ ($M_\odot\ s^{-1}$)	σ	τ_J (s)	S [b] (k_B/baryon)	τ_{dyn} [c] (ms)	R_s [d] (km)	R_A (km)	$\dot{E}$ [e] (10^{51} ergs s^{-1})	η [f]
8	6000	1.0	6.2×10^{-3}	0.0067	17.0	16.5	2.2	31	23	0.57	4.1
8	4000	1.6	8.3×10^{-4}	0.022	50.7	26.2	1.1	28	37	0.17	2.0
8	2000	3.1	2.6×10^{-4}	0.017	56.3	42.8	1.8	43	61	0.047	1.7
8	1000	6.3	1.8×10^{-4}	6.4×10^{-3}	40.4	54.3	3.8	75	87	0.016	1.7
8	500	13	1.5×10^{-4}	1.9×10^{-4}	26.7	61.8	7.8	140	117	6.1×10^{-3}	1.7
8	250	25	1.4×10^{-4}	5.0×10^{-4}	18.1	66.4	14	270	150	2.4×10^{-3}	1.6
8	50	130	1.4×10^{-4}	2.1×10^{-5}	11.6	69.5	23	680	190	4.6×10^{-4}	0.52
3.5	6000	1.0	1.6×10^{-3}	0.027	47	14.3	0.66	20	28	0.37	2.3
3.5	4000	1.6	1.1×10^{-4}	0.17	150	27.6	0.81	23	57	0.091	1.3
3.5	2000	3.1	3.6×10^{-5}	0.13	152	48.0	2.5	36	100	0.025	1.2
3.5	1000	6.3	2.4×10^{-5}	0.048	108	62.0	6.7	58	150	8.5×10^{-3}	1.2
3.5	500	13	2.1×10^{-5}	0.014	69	71.2	14.3	94	200	3.2×10^{-3}	1.3
3.5	250	25	1.9×10^{-5}	3.8×10^{-3}	43	77.1	26	160	260	1.2×10^{-3}	1.4
3.5	50	130	1.8×10^{-5}	1.6×10^{-4}	15.8	83.1	53	550	450	1.1×10^{-4}	1.5

[a] The anti-electron neutrino luminosity in units of 10^{51} ergs s^{-1}.

[b] The asymptotic wind entropy.

[c] The dynamical time evaluated at $T = 0.5$ MeV (see eq. [2.36]).

[d] The radius of the adiabatic sonic point. For large B_ν and Ω the slow point and adiabatic sonic point are very close to each other, while for low B_ν and Ω they approach the Alfvén and fast magnetosonic radii, respectively.

[e] The asymptotic wind power.

[f] The ratio of the rotational power lost by the PNS to the asymptotic wind power (see eq. [2.12]).

Table 2.3 PNS Wind Properties with Wave Heating at $L_{\bar{\nu}_e} = 8 \times 10^{51}$ ergs s^{-1} and $B_\nu = 10^{15}$G

Ω (s^{-1})	P (ms)	$(\delta B/B)\|_{R_\nu}$ [a]	χ	$\dot{Q}_\nu$ [b] (10^{50} ergs s^{-1})	$\dot{Q}_w$ [c] (10^{50} ergs s^{-1})	$\dot{M}$ ($M_\odot$ s^{-1})	τ_{dyn} [d] (ms)	$S_{0.5MeV}$ [e] (k_B/baryon)	$R_{0.5\,MeV}$ [f] (km)	I_w [g]
50	130	-	-	0.44	0	1.4×10^{-4}	21.0	69.0	73.2	1
50	130	0.2	3	0.39	0.054	1.6×10^{-4}	11.4	75.0	65.0	2.37
50	130	0.7	1	0.38	0.65	3.4×10^{-4}	4.2	92.5	62.5	12.0
50	130	0.7	3	0.44	0.37	2.9×10^{-4}	1.9	119	51.2	55
50	130	0.7	10	0.44	0.48	2.4×10^{-4}	2.0	88.5	44.9	22.2
2000	3.1	-	-	0.53	0	2.8×10^{-4}	1.07	40.6	33.4	1
2000	3.1	0.7	0.3	0.30	0.65	4.8×10^{-4}	0.96	44.1	37.4	1.4
2000	3.1	0.7	1	0.54	0.64	5.0×10^{-4}	0.92	68.9	41.4	5.7
2000	3.1	0.7	3	0.56	0.57	4.3×10^{-4}	1.02	78.6	40.3	7.6
2000	3.1	0.7	10	0.60	0.42	3.7×10^{-4}	1.00	55.3	35.2	2.7
2000	3.1	1.0	3	0.63	1.76	5.6×10^{-4}	0.99	109	46.8	21.2
6000	1.0	-	-	5.57	0	1.2×10^{-2}	0.52	13.7	30.8	1
6000	1.0	0.7	3	6.53	0.36	1.3×10^{-2}	0.74	14.5	35.9	0.83
6000	1.0	1.0	1	6.04	0.74	1.4×10^{-2}	0.79	15.6	41.8	0.96
6000	1.0	1.0	3	5.91	0.74	1.3×10^{-3}	0.94	15.4	41.1	0.80

[a] The fractional wave amplitude at the PNS surface.

[b] Total neutrino heating rate.

[c] Total wave heating rate.

[d] The dynamical time evaluated at $T = 0.5$ MeV (see eq. [2.36]).

[e] The wind entropy at $T = 0.5$ MeV. Note that $S_{0.5\mathrm{MeV}} \neq S^a$ because, in general, wave heating extends outside the $T = 0.5$ MeV radius.

[f] The radius where $T = 0.5$ MeV.

[g] The ratio of $(S_{0.5\mathrm{MeV}})^3/\tau_{\mathrm{dyn}}$ with wave heating to without wave heating (eq. [2.44]).

Chapter 3

Short GRBs with Extended Emission from Proto-Magnetar Spin-Down

B. D. Metzger, E. Quataert, T. A. Thompson (2008), MNRAS, 385, 1455-1460.[1]

Abstract

Evidence is growing for a class of gamma-ray bursts (GRBs) characterized by an initial $\sim 0.1 - 1$ s spike of hard radiation followed, after a $\sim 3 - 10$ s lull in emission, by a softer period of extended emission lasting $\sim 10 - 100$ s. In a few well-studied cases, these "short GRBs with extended emission" show no evidence for a bright associated supernova (SN). We propose that these events are produced by the formation and early evolution of a highly-magnetized, rapidly-rotating neutron star (a "proto-magnetar") which is formed from the accretion-induced collapse (AIC) of a white dwarf (WD), the merger and collapse of a WD-WD binary, or, perhaps, the merger of a double neutron star binary. The initial emission spike is powered by accretion onto the proto-magnetar from a small disk that is formed during the AIC or merger event. The extended emission is produced by a relativis-

tic wind that extracts the rotational energy of the proto-magnetar on a timescale $\sim 10 - 100$ s. The ~ 10 s delay between the prompt and extended emission is the time required for the newly-formed proto-magnetar to cool sufficiently that the neutrino-heated wind from its surface becomes ultra-relativistic. Because a proto-magnetar ejects little or no ^{56}Ni ($< 10^{-3} M_{\odot}$), these events should not produce a bright SN-like transient. We model the extended emission from GRB 060614 using spin-down calculations of a cooling proto-magnetar, finding reasonable agreement with observations for a magnetar with an initial rotation period of ~ 1 ms and a surface dipole field of $\sim 3 \times 10^{15}$ G. If GRBs are indeed produced by AIC or WD-WD mergers, they should occur within a mixture of both early and late-type galaxies and should not produce strong gravitational wave emission. An additional consequence of our model is the existence of X-ray flashes unaccompanied by a bright SN and not associated with massive star formation.

3.1 Introduction

Swift and HETE-2 have demonstrated that long- and short-duration gamma-ray bursts (GRBs) originate from distinct stellar progenitors. Long GRBs track ongoing star formation and result from the death of massive stars (Stanek et al. 2003). On the other hand, short GRBs have now been localized to both early and late-type host galaxies of moderate redshift (Barthelmy et al. 2005; Berger et al. 2005; Bloom et al. 2006), indicating a more evolved progenitor population.

Even among the classes of "long" and "short" GRBs, however, diversity is emerging. One example is GRB 060505 detected by the Burst Alert Telescope (BAT) on-board *Swift*. This long-duration burst showed no evidence for a bright supernova (SN) despite residing inside a star-forming region (Ofek et al. 2007; Fynbo et al. 2007), suggesting that it may result from a "failed-SN" collapsar (Woosley 1993). Another particularly striking example is GRB 060614, which, although officially classified as a long-duration burst based solely on its 102 s T_{90} duration, more closely resembles a standard short GRB in other ways. This *Swift* burst showed no energy-dependent time lag (Gehrels et al. 2006) and, like GRB

060615, no SN was detected down to an optical brightness ~ 100 times fainter than SN1998bw (Gal-Yam et al. 2007). Additional clues to the nature of GRB 060614 are revealed through the evolution of its prompt emission. The BAT lightcurve begins with an initial spike of hard emission (lasting ~ 5 s) which is followed, after a lull in emission (lasting ~ 5 s), by a softer 'hump' of extended emission (lasting ~ 100 s). This is followed by a remarkably standard X-ray, optical, and ultra-violet afterglow (Mangano et al. 2007).

The hybrid long/short properties of GRB 060614 led Gal-Yam et al. (2006) and Gehrels et al. (2006) to propose that it forms the prototype for a new class of GRBs, which we call "short GRBs with extended emission" (or SGRBEEs) (see, however, Fynbo et al. 2006). Roughly a quarter of the short bursts detected by *Swift* (including GRBs 050709 and 050724) show evidence for high energy extended emission (EE) distinct from the standard afterglow and late-time flares; this suggests that SGRBEEs may actually be fairly common. Indeed, Norris & Bonnell (2006; NB06) found a handful of short GRBs in the BATSE catalog qualitatively similar to GRB 060614. Although NB06's sample represents only $\sim 1\%$ of the BATSE short bursts, a soft tail of EE would generally not have been detectable. NB06 also find that the dynamic range in the ratio of prompt to extended flux (and fluence) of SGRBEEs appears to be very large, $\sim 10^4$. This large burst-to-burst variation in the relative energy released during the prompt and extended phases suggests that these components are physically decoupled.

One explanation for EE from an otherwise short GRB is the interaction of the relativistic outflow with the circumburst environment. However, when the EE is sufficiently bright to be accurately sampled, its time evolution is highly variable and cannot be smoothly extrapolated back from the onset of the X-ray afterglow (Nakar 2007). A multi-peaked lightcurve is also difficult to produce from the shock heating of a binary companion (MacFadyen et al. 2005). Based on its similarity to prompt emission, the EE in SGRBEEs most likely results from late-time central engine activity.

A popular model for the central engine of short GRBs is accretion onto a black hole (BH) formed from a compact object merger (COM) (Paczynski 1986).

SGRBEEs pose a challenge to COM scenarios because their long durations and two-component nature are difficult to produce in models powered purely by accretion. The accretion timescale of the compact disk produced from a merger event, although comparable to the duration of the initial spike, cannot explain the long duration of the EE, especially in cases when the latter produces the bulk of the observed fluence. For BH-NS mergers, the fall-back of matter ejected into highly eccentric orbits during the tidal disruption of the NS may be sufficient to power the EE (Rosswog 2007), but whether the regular delay between the prompt and EE phases, and the large variation in the flux of each, can be reproduced remains to be determined (see, however, Faber et al. 2006).

The NS kicks required to produce a compact binary and the potentially long delay until merger imply that a significant fraction of COMs should have large offsets from their host galaxies (Bloom, Sigurdsson, & Pols 1999; Fryer et al. 1999). Although the offset distribution of short GRBs as a whole appears marginally consistent with current COM population synthesis models (Belczynski et al. 2006), well-localized SGRBEEs thus far appear exclusively inside or near the starlight of their host galaxies; indeed, their average offset from host center is only ~ 2.5 kpc (Troja et al. 2007). The high incidence of SGRBEEs with detected optical afterglows ($\sim 90\%$) also suggests that these events reside inside the disk of their host galaxies (Troja et al. 2007).

In this Letter, we propose that SGRBEEs are produced by the formation and early evolution of a strongly-magnetized, rapidly-rotating neutron star (a "proto-magnetar") which is formed from the accretion-induced collapse (AIC) of a white dwarf (WD) (Nomoto & Kondo 1991), the merger and collapse of a WD-WD binary (King et al. 2001), or, perhaps, the merger of a double neutron (NS) star binary (Gao & Fan 2006). The initial spike of emission is powered by accretion onto the proto-magnetar from a small disk formed during the AIC or merger (§3.2). The EE is produced by a relativistic wind that extracts the rotational energy of the magnetar on a timescale $\sim 10 - 100$ s (§3.3), a picture similar to that originally proposed by Usov (1992). The $\sim 3 - 10$ s delay between the prompt and EE is the time required for the proto-magnetar to cool sufficiently that the neutrino-heated

wind from its surface becomes ultra-relativistic. In §3.4 we summarize our results and the predictions of our model. For concreteness we focus our discussion on AIC and WD-WD merger channels of isolated magnetar birth.

3.2 Accretion Phase

In either AIC (Nomoto & Kondo 1991) or a WD-WD merger (e.g., Yoon et al. 2007), the WD (or merged WD binary) will be rapidly-rotating prior to collapse and must eject a sizable fraction of its mass into a disk during the collapse in order to conserve angular momentum. Indeed, the 2D MHD AIC calculations performed by Dessart et al. (2007; D07) show that a quasi-Keplerian $\sim 0.1-0.5 M_\odot$ accretion disk forms around the newly-formed proto-neutron star (PNS), extending from the PNS surface at $R_{\rm NS} \sim 30$ km to large radii (with a half-mass radius of a few $R_{\rm NS}$).

We propose that the prompt emission in SGRBEEs is powered by the accretion of this disk onto the PNS. This scenario is not unlike most other COM models with the important exception that the accreting object is a NS rather than a BH. The characteristic timescale for accretion is the viscous timescale $t_{\rm visc} = R^2/\alpha\Omega_K H^2$, given by

$$t_{\rm visc} \approx 1\,{\rm s}\left(\frac{M}{M_\odot}\right)^{-1/2}\left(\frac{0.1}{\alpha}\right)\left(\frac{R_0}{4R_{\rm NS}}\right)^{3/2}\left(\frac{H/R_0}{0.2}\right)^{-2}, \tag{3.1}$$

where α is the viscosity parameter and M is the PNS mass; R_0, H, and $\Omega_{\rm K} \equiv (GM/R_0^3)^{1/2}$ are the disk's radius, scale height, and Keplerian rotation rate, respectively. For $H \approx 0.2R_0$, as expected for a neutrino-cooled disk accreting at $\dot{M} \sim 0.1-1\,M_\odot$ s^{-1} (Chen & Beloborodov 2007), $t_{\rm visc} \sim 0.1-1$ s, comparable to the duration of the prompt spike.

At early times, the accretion ram pressure $P_{\rm R} \simeq \rho v_{\rm ff}^2/2 \approx \dot{M} v_{\rm ff}/8\pi R^2$ (where $v_{\rm ff} = (GM/R)^{1/2}$) exceeds the magnetic pressure $P_{\rm M} = B^2/8\pi$ at the PNS surface:

$$\frac{P_{\rm R}}{P_{\rm M}} \approx 10\left(\frac{\dot{M}}{0.1 M_\odot\,{\rm s}^{-1}}\right)\left(\frac{M}{M_\odot}\right)^{1/2}\left(\frac{\phi_B}{10^{27}{\rm G\,cm^2}}\right)^{-2}\left(\frac{R_{\rm NS}}{30\,{\rm km}}\right)^{3/2}. \tag{3.2}$$

Here $\phi_B = 10^{27}(B[R_{\rm NS}]/10^{15}{\rm G})(R_{\rm NS}/10\,{\rm km})^2$ G cm^2 is the NS's conserved magnetic flux. Thus, although we postulate that the NS possesses a surface field

strength $\sim 10^{15}$ G once contracting to its final radius $R_{\rm NS} \sim 10$ km, the field should not significantly alter the early-time dynamics of the accretion-powered phase (Ghosh & Lamb 1978).

The total energy released when a $\sim 0.1 - 0.5 M_\odot$ disk accretes onto a NS ($\sim 10^{52} - 10^{53}$ ergs) is more than sufficient to explain the isotropic γ-ray energy of the prompt spike of GRB 060614 ($\simeq 1.8 \times 10^{50}$ ergs). However, as we discuss further in §3.3, a major obstacle to driving a relativistic wind from the vicinity of a newly-formed PNS is the baryon-rich wind from the hot surface of the PNS. Since the mass-loss from a rapidly-rotating, highly-magnetized PNS is augmented by centrifugal effects (Thompson et al. 2004; hereafter TCQ04), D07 argue that an early-time relativistic outflow from the PNS is unlikely. Although we agree with D07's conclusion for moderately low latitudes, the centrifugal enhancement of mass-loss along the rotation axis is negligible; hence, the total mass-loss per solid angle near the rotation axis is approximately given by its non-rotating value of $M_\Omega \sim 10^{-5} M_\odot$ str^{-1} (Thompson et al. 2001; hereafter T01). Thus, if the energy deposited per solid angle above the pole exceeds $E_\Omega \sim 10^{51}$ ergs str^{-1} the Lorentz factor of the outflow may reach $\Gamma \sim E_\Omega / M_\Omega c^2 \sim 100$, sufficient to overcome compactness constraints which can be placed on short GRBs (Nakar 2007).

One possibility for effectively baryon-free energy deposition is $\nu - \bar{\nu}$ annihilation along the rotation axis. For instance, Setiawan et al. (2006) find that $\sim 2 \times 10^{50}$ ergs is released by annihilations from a $\sim 0.1 M_\odot$ disk accreting at $\dot{M} \sim 0.3 M_\odot$ s^{-1}, as would be expected following AIC. An MHD jet is perhaps a more promising source of the relativistic material that produces the prompt emission. Although jets from NS X-ray binaries are in general less powerful than their BH counterparts (Migliari & Fender 2006), the NS X-ray binary Circinus X-1 produces one of the most relativistic microquasar jets known (Fender et al. 2004).

3.3 Spin-Down Phase

Whether produced by the core collapse of a massive star or the AIC of a WD, a PNS must radiate its gravitational binding energy via optically-thick neutrino

emission during the first $t_{\rm KH} \sim 40$ s of its life (Burrows & Lattimer 1987). A small fraction of this neutrino flux is reabsorbed by baryons in the atmosphere of the PNS, driving a wind from its surface. In the presence of a sufficiently strong magnetic field and rapid rotation, magnetic stresses tap into the PNS's rotational energy, enhancing the energy-loss in the wind (TCQ04). The proto-magnetar is unlikely to have a significant effect on the accretion-powered phase for $t \lesssim t_{\rm visc} \sim 1$ s (see eq. [3.2]). On somewhat longer timescales, however, the disk mass and accretion rate will decrease, and the PNS will be spun up through accretion and by its Kelvin-Helmholtz contraction. Thus, as $\dot{M}$ decreases from its peak value, the disk will be cleared away and the proto-magnetar wind will expand relatively freely into space.

In Chapter 2, we calculated the properties of PNS winds with magnetic fields and rotation during the first $t_{\rm KH} \sim 40$ s after core bounce. The importance of the magnetic field in accelerating a wind is quantified by the magnetization $\sigma \equiv B^2/4\pi\rho c^2$ evaluated at the light cylinder radius $R_{\rm L} \equiv c/\Omega$, where Ω is the PNS's rotation rate. If the magnetic energy is fully converted into the kinetic energy of bulk motion, either directly or through thermalization and subsequent thermal or magnetic pressure-driven expansion (e.g., Drenkhahn & Spruit 2002), then at sufficiently large radii $\Gamma \sim \sigma(R_{\rm L}) \equiv \sigma_{\rm LC}$ (for $\sigma_{\rm LC} > 1$). Hence, for a PNS to produce an ultra-relativistic outflow, $\sigma_{\rm LC}$ must be $\gg 1$.

Figure 3.1 shows our calculation of $\sigma_{\rm LC}$ and the wind energy-loss rate $\dot{E}$ as a function of time t after core bounce for a PNS with initial rotation period $P_0 = 1$ ms for three surface dipole field strengths: $B_0 = 10^{15}$ G, 3×10^{15} G, and 10^{16} G. In all models, the wind is nonrelativistic ($\sigma_{\rm LC} < 1$) for $t \lesssim 1 - 10$ s because at early times the PNS is hot and its already substantial neutrino-driven mass-loss rate is enhanced by centrifugal slinging. However, as the PNS cools and spins down, Figure 3.1 shows that $\sigma_{\rm LC}$ rises rapidly, exceeding ~ 10 by $t \sim 3 - 10$ s. Because an ultra-relativistic outflow is necessary to produce nonthermal GRB emission, the $\sim 3 - 10$ s timescale required for the wind to reach large $\sigma_{\rm LC}$ corresponds to the delay between the accretion-powered prompt spike and the spin-down-powered EE in our model.

3.3.1 Extended Emission Light Curve Model

In an attempt to directly connect central engine physics to observed GRB properties, we have modeled the emission produced by a spinning-down proto-magnetar using the wind evolution calculations (Fig. 3.1) and an internal shock emission model. By invoking strong shocks, we assume that the Poynting-flux of the wind is efficiently converted into kinetic energy somewhere between the light cylinder radius ($\sim 10^7$ cm) and the internal shock radii ($\sim 10^{13} - 10^{15}$ cm). This assumption is motivated by observations of the Crab Nebula and other pulsar wind nebulae, where detailed modeling requires efficient conversion of magnetic to kinetic energy (Kennel & Coroniti 1984). Although we do not exclude the possibility that the wind remains Poynting-flux dominated at large radii, we leave the analogous light curve calculation in a magnetic dissipation model to future work.

In the internal shock model, the emission of a GRB is powered by "dissipation" (i.e., electron acceleration and radiation) of the relative kinetic energy between distinct components of a relativistic wind. Since we do not have a quantitative model for the (potentially stochastic) processes that set the short timescale variability in a proto-magnetar wind, we discretize the relativistic outflow into N shells released at constant intervals dt in time. A shell released at time t is given Lorentz factor $\Gamma = \sigma_{\rm LC}(t)$, energy $E = \dot{E}(t)dt$, and mass $M = E/\Gamma c^2$, where $\sigma_{\rm LC}(t)$ and $\dot{E}(t)$ are taken from Figure 3.1. The "shell averaged" light curve that we present in Figure 3.2 is taken in the limit that $N \rightarrow \infty$ and $dt \rightarrow 0$ and is insensitive to the shell discretization prescription adopted. We begin releasing shells when $\sigma_{\rm LC} > 10$ because the 2D MHD simulations of Bucciantini et al. (2006) show that above $\sigma_{\rm LC} \sim 10$ the outflow transitions from being hoop-stress collimated along the rotation axis to expanding more isotropically; hence, we do not expect the material ejected at $\sigma_{\rm LC} \gtrsim 10$ to interact with much of the material ejected when $\sigma_{\rm LC} \lesssim 10$. We stop releasing shells when neutrino heating effectively ceases at $t = t_{\rm KH}$ because we do not have a reliable model for $\sigma_{\rm LC}(t)$ after this point. This is a reasonable approximation if $\dot{E}$ or the dissipation efficiency drops significantly

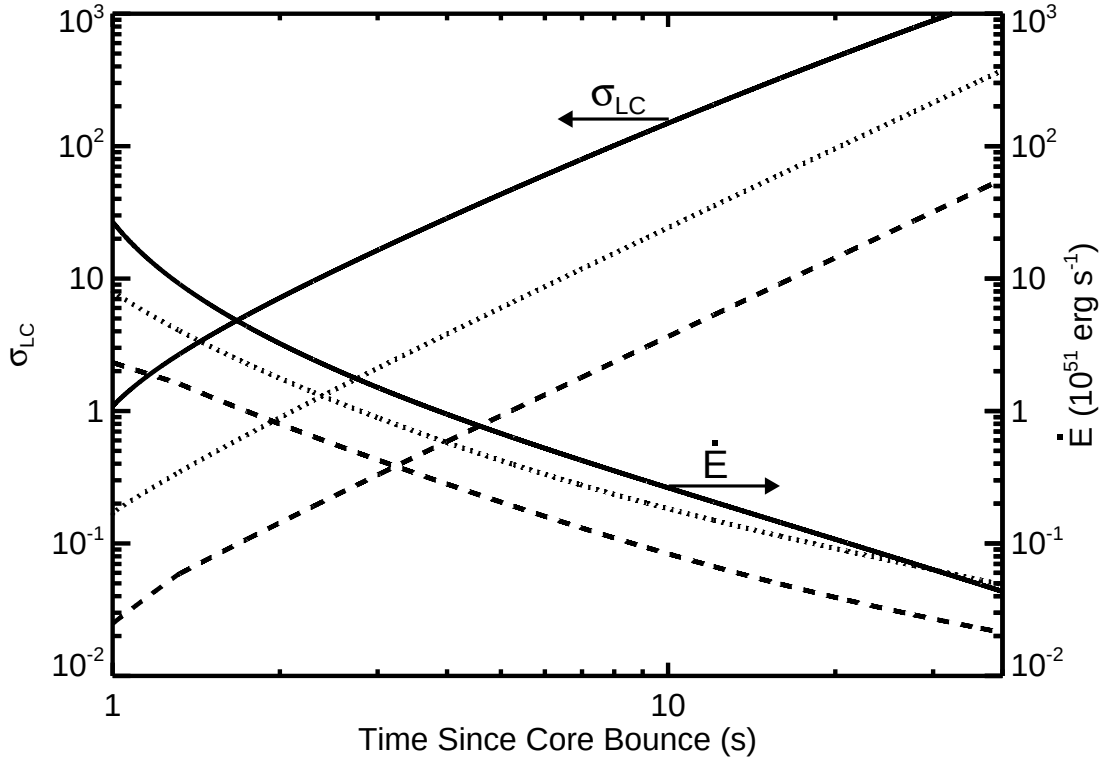

Figure 3.1: Magnetization at the light cylinder $\sigma_{\rm LC}$ (*Left Axis*) and energy-loss rate $\dot{E}$ (*Right Axis*) as a function of time since core bounce for a proto-magnetar with initial rotation period $P_0 = 1$ ms and three surface dipole magnetic field strengths: $B_0 = 10^{15}$ G (*dashed line*), 3×10^{15} G (*dotted line*), and 10^{16} G (*solid line*).

once the outflow transitions from a modest-σ wind to a very high-σ, pulsar-like wind at $t = t_{\rm KH}$ (as suggested by, e.g., Thompson 1994 and TCQ04).

Upon release, each shell propagates forward in radius with constant velocity until it collides with another shell. From the properties of the collision, we calculate (1) the "thermal" energy released by dissipation of the shells' relative kinetic energy, (2) the observed spike of radiation (using the technique summarized in §2 of Genet et al. 2007), and (3) the final mass and energy of the composite shell, which then continues to propagate forward. We assume that a fraction ϵ_e of the energy released by each collision goes into relativistic electrons, which radiate their energy through synchrotron emission. Efficient synchrotron cooling is justified if

even a modest fraction of the magnetic flux at the light cylinder is preserved to large radii. Thomson scattering of the nonthermal radiation is taken into account, but photospheric emission is not calculated.

Figure 3.2 shows our calculation of the EE light curve for the wind solutions given in Figure 3.1. We find that the efficiency for converting the relative kinetic energy of the outflow to thermalized energy is $\sim 10-20\%$. Provided that $\epsilon_e \gtrsim 0.1$, these efficiencies are consistent with those typically inferred for short GRBs (e.g., Nakar 2007). Proto-magnetar winds possess a significant reservoir of "free energy" and achieve high efficiency because $\Gamma(t)$ increases monotonically, allowing faster material ejected at later times to catch up with the slower material ejected earlier.

To first order, our simplified model produces light curves similar to the EE observed from SGRBEEs. The peak flux is larger for more rapidly-rotating, strongly-magnetized PNSs and the time to peak flux is smaller. In Figure 3.2 we also show the late-time BAT light curve from GRB 060614 (from Butler & Kocevski 2007) for comparison with our models. We find reasonable agreement between the data and the model with $B_0 = 3 \times 10^{15}$ G, suggesting that the progenitor of GRB 060614 possesses a surface field strength somewhat larger than those of Galactic magnetars. If synchrotron internal shock emission is indeed the correct model for the radiation from a proto-magnetar wind, the softening of the EE can also be qualitatively understood. Due to the monotonic rise of $\Gamma(t)$, the Lorentz factor of the aggregate shell increases with time; however, the field strength in the wind $B \sim B(R_{\rm L})(r/R_{\rm L})^{-1}$ declines as the internal shock radius increases. In our model, these effects combine to decrease the synchrotron peak energy $E_{\rm peak} \propto \Gamma B$ by a factor of ~ 10 during the period of observable emission. This predicted degree of spectral softening is stronger than the factor of ~ 2 decrease in $E_{\rm peak}$ inferred for GRB 060614 by Zhang et al. (2007); indeed, the observed constancy of $E_{\rm peak}$ is a problem generic to most internal shock models.

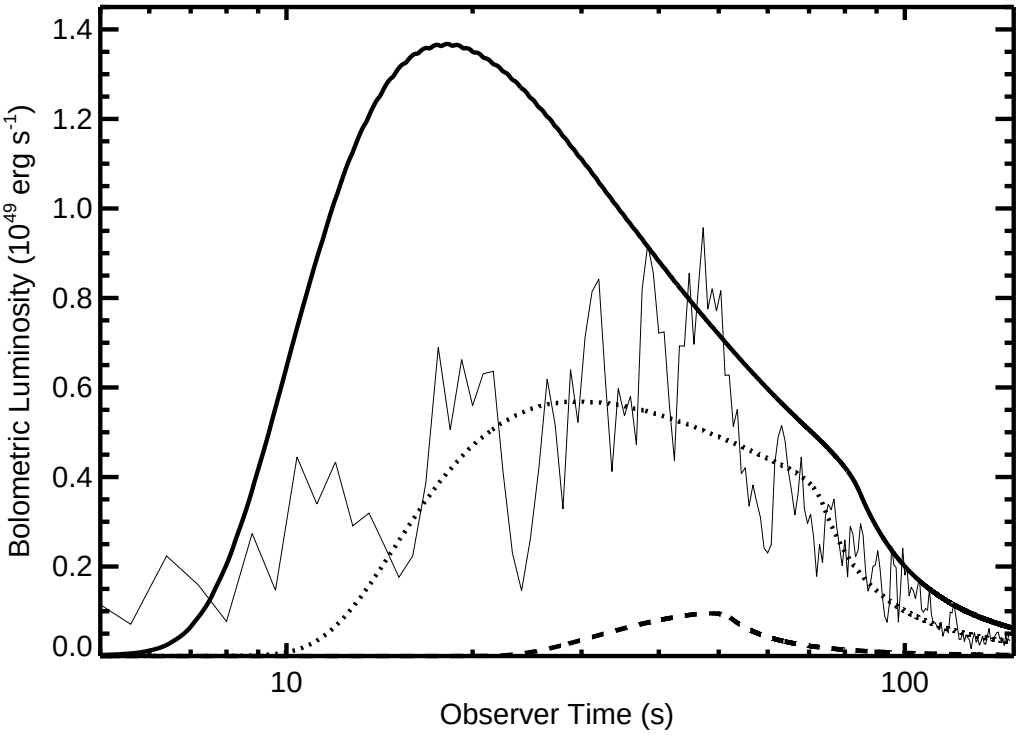

Figure 3.2: Luminosity of internal shock emission from the proto-magnetar winds in Figure 3.1; electron acceleration efficiency $\epsilon_e = 0.5$ is assumed. Note the lack of emission at early times because the outflow is non-relativistic. The gradual onset of the emission once $\sigma_{\rm LC} > 10$ is due to the large Thomson optical depth, which decreases as the outflow expands. The late-time decline in emission is the onset of curvature emission from the last shock, produced by the shell released at $t_{\rm KH} = 40$ s. The late-time BAT light curve from GRB 060614, shown with a light solid line and scaled to the physical isotropic luminosity, is reproduced in a time-averaged sense by the $B_0 = 3 \times 10^{15}$ G model.

3.4 Discussion

Short GRBs with extended emission challenge the paradigm that short GRBs result exclusively from COMs. The central engine in these systems may instead be a newly-formed magnetar. The timeline of our model is summarized as follows:

- AIC or WD-WD merger produces a proto-magnetar and a disk of mass $\sim 0.1 M_\odot$ ($t \sim t_{\rm dyn} \sim 100$ ms)
- Disk accretes onto the proto-magnetar, generating the prompt emission spike ($t \sim t_{\rm visc} \sim 0.1 - 1$ s; see eq. [3.1])
- Free proto-magnetar wind transitions from non-relativistic to ultra-relativistic ($t \sim 3 - 10$ s; see Fig. 3.1)
- Proto-magnetar spins down, generating X-ray emission on observed longer timescale ($t \sim 10 - 100$ s; see Fig. 3.2)

A model similar to the one described here was proposed by Gao & Fan (2006); in their model, late-time flares from short GRBs are powered by dipole spin-down of a super-massive, transiently-stable magnetar formed by a NS-NS merger. However, current evidence suggests that SGRBEEs form a distinct population with only modest offsets from their host galaxies (Troja et al. 2007). If transiently-stable magnetars from NS-NS mergers indeed produce most SGRBEEs, an equal number would be expected with large offsets.

A more promising channel of isolated magnetar birth may be the AIC of a WD or the merger and collapse of a WD-WD binary. The rate of these events is difficult to constrain directly because the Ni mass synthesized in a PNS wind is less than $\sim 10^{-3} M_\odot$ (Chapter 4) and is therefore unlikely to produce a bright optical transient. There is, however, indirect evidence that isolated magnetar birth occurs in nature. The rapidly-rotating, highly magnetic WD RE J0317-853 has a mass $M = 1.35 M_\odot$ and was likely produced from a WD-WD merger; if RE J0317-853's progenitor binary had been slightly more massive, it would probably have collapsed to a rapidly-rotating magnetar (King et al. 2001). Isolated

NS birth via AIC is also one of the only Galactic r-process sites consistent with current observations of elemental abundances in metal-poor halo stars (Qian & Wasserburg 2007). Although unmagnetized PNS winds fail to produce successful r-process (T01), proto-magnetar winds may be sufficiently neutron-rich to produce $\sim 0.1 M_{\odot}$ in r-process elements (D07; Chapter 4). For AIC or WD-WD mergers to produce the entire Galactic r-process yield requires a rate $\sim 10^{-5} - 10^{-6}$ yr^{-1}, comparable to the observed local short GRB rate (Nakar 2007). Finally, Levan et al. (2006) argue that the correlation found by Tanvir et al. (2005) between a subset of short GRBs and local large-scale structure is evidence for a channel of isolated magnetar birth, if these bursts are produced by SGR-like flares.

A theory for SGRBEEs must explain the large burst-to-burst variation in the ratio of the flux/fluence of the prompt and EE components (NB06). The angular momentum of AIC and WD-WD mergers may vary between events, resulting in a wide distribution in both the properties of the accretion disk formed (which influences the prompt emission) and the rotation rate of the proto-magnetar (which determines the EE). Event-to-event variability may also result from the viewing angle $\theta_{\rm obs}$ of the observer with respect to the rotation axis. The spin-down power of the magnetar varies as $\dot{E} \propto \sin^2(\theta_{\rm obs})$ for $\sigma_{\rm LC} \gg 1$; hence, the light curves in Figure 3.2 remain reasonably accurate for moderately large $\theta_{\rm obs}$, but a viewer looking down the rotation axis ($\theta_{\rm obs} \sim 0^{\circ}$) may observe little or no EE. Conversely, equatorial viewers would observe EE but no prompt spike; therefore, this model predicts a class of long-duration X-ray flashes (XRFs) not associated with very massive star formation or accompanied by a SN. Such an event may have already been observed. GRB 060428b is an XRF with a light curve similar to the EE from GRB 060614 which was localized inside a red galaxy at redshift $z = 0.347$. Assuming this galaxy is the host, GRB 060428b released an isotropic energy $\sim 2 \times 10^{50}$ ergs, comparable to EE of GRB 060614, and showed no SN component at one month down to an optical brightness ~ 20 times fainter than SN1998bw (Perley et al., in prep).

Because the EE flow is symmetric in azimuth, equatorial viewers should not observe a classic jet-break (although a more shallow break is possible; Thompson 2005). Furthermore, although only $\Gamma \gtrsim 10$ material contributes to the EE in

Figure 3.2, the magnetar releases $\sim 10^{52}$ ergs in earlier, mildly relativistic material ($\Gamma \sim 1 - 10$; see Fig. 3.1) that is hoop-stress collimated along the PNS rotation axis. This material may become visible as a radio transient as it slows down and becomes non-relativistic on a timescale of months to years. If AIC or WD-WD mergers indeed produce SGRBEEs, these events should be bound to both early and late type galaxies; indeed, the well-known SGRBEEs 050709 and 050724 were localized to a star forming galaxy and an elliptical galaxy, respectively (Villasenor et al. 2005; Berger et al. 2005). Unlike COMs, magnetar birth from AIC or WD-WD mergers should not produce strong gravitational wave emission, and because the magnetar will not collapse to a BH, its magnetic energy could power late-time X-ray flares.

Although we have concentrated on spin-down-powered EE, isolated NS birth may produce the EE of SGRBEEs in other ways. Specifically, the accretion disk produced by a WD-WD merger *prior to collapse* (e.g., Yoon et al. 2007) may accrete onto the NS at later times, powering a bipolar outflow similar to that produced during the prompt accretion episode; in this case, the delay until EE reflects the accretion timescale at the WD radius ($\sim 10^9$ cm), which D07 estimate is $t_{\rm visc} \sim 100$ s for $\alpha \sim 0.1$. Late-time accretion and spin-down powered EE can be distinguished based on the presence or absence, respectively, of a jet break and the observed ratio of SGRBEEs to off-axis, purely-EE XRFs. Assuming that jets from the prompt and delayed accretion episodes are similarly collimated, SGRBEEs with accretion-powered EE should not be visible off-axis; by contrast, if the EE is powered by magnetar spin-down at least as many off-axis XRFs are expected as standard SGRBEEs.

Finally, it is important to distinguish the observable signature of a magnetar produced by an AIC, WD-WD merger, or NS-NS merger from that produced by the core collapse of a massive star, which may instead produce a traditional long-duration GRB (e.g., Chapter 2). The magnetic fields and rotation rates of the magnetars produced via these channels may differ, which would modify $\dot{E}$ and σ of the wind (Fig. 3.1) and hence its observable properties. Although isolated magnetar spin-down may be comparatively simple because the proto-magnetar

wind expands relatively freely into space, a free magnetar wind is nearly isotropic and so its emission is relatively weak and difficult to detect. By contrast, the wind from a magnetar produced via core collapse is collimated into a bipolar jet by the overlying stellar mantle (Uzdensky & MacFadyen 2006; Komissarov & Barkov 2007; Bucciantini et al. 2007) and the observed emission can be much brighter due to the jet's modest opening solid angle.

Acknowledgements

We thank J. Bloom, N. Bucciantini, N. Butler, D. Perley, A. Spitkovsky, and E. Troja for helpful discussions and information. EQ and BDM were supported by the David and Lucile Packard Foundation and a NASA GSRP Fellowship.

Chapter 4

On the Conditions for Neutron-Rich Gamma-Ray Burst Outflows

B. D. Metzger, T. A. Thompson, E. Quataert, ApJ, 676:1130-1150, 2008 April 1.[1]

Abstract

We calculate the structure and neutron content of neutrino-heated magneto-hydrodynamic winds driven from the surface of newly-formed magnetars ("proto-magnetars") and from the midplane of hyper-accreting disks, two of the possible central engines for gamma-ray bursts (GRBs) and hyper-energetic supernovae (SNe). Both the surface of proto-magnetars and the midplane of neutrino-cooled accretion flows (NDAFs) are electron degenerate and neutron-rich (neutron-to-proton ratio $n/p \gg 1$). If this substantial free neutron excess is preserved to large radii in ultra-relativistic outflows, several important observational consequences may result. Weak interaction processes, however, can drive n/p to ~ 1 in the nondegenerate regions that obtain just above the surfaces of NDAFs and proto-magnetars. Our calculations show that mildly relativistic (Lorentz factor

$\Gamma \lesssim 10$) neutron-rich outflows from NDAFs are possible in the presence of a strong poloidal magnetic field. However, neutron-rich winds possess a minimum mass-loss rate that likely precludes simultaneously neutron-rich and ultra-relativistic ($\Gamma \gtrsim 100$) NDAF winds accompanying a substantial accretion power. In contrast, proto-magnetars are capable of producing neutron-rich long-duration GRB outflows $\sim 10-30$ seconds following core bounce for sub-millisecond rotation periods; such outflows would, however, accompany only extremely energetic events, in which the GRB + SN energy budget exceeds $\sim 4 \times 10^{52}$ ergs. Neutron-rich highly relativistic outflows may also be produced during some *short*-duration GRBs by geometrically thick accretion disks formed from compact object mergers. The implications for r-process nucleosynthesis, optical transients due to non-relativistic neutron-rich winds, and Nickel production in proto-magnetar and NDAF winds are also briefly discussed.

4.1 Introduction

The rapid variability and large energies that characterize cosmological gamma-ray bursts (GRBs) strongly implicate stellar-mass compact objects as their central engines. Indeed, the association of several long-duration GRBs (LGRBs) with Type Ibc supernovae (SNe) suggests that LGRBs result from relativistic outflow accompanying rapid accretion onto a newly-formed black hole (a "collapsar"; Woosley 1993; MacFadyen & Woosley 1999; Woosley & Bloom 2006) or the spin-down of a newly-formed magnetar (e.g., Usov 1992; Thompson 1994; Blackman & Yi 1998; Wheeler et al. 2000; Thompson, Chang, & Quataert 2004, hereafter TCQ04). Short-duration GRBs may result from black hole accretion-powered outflows following the tidal disruption and coalescence of compact binaries (Paczyński 1986, 1991; Eichler et al. 1989; Narayan et al. 1992; Ruffert et al. 1997; Janka et al. 1999).

A unique property of both the surface of a newly-formed neutron star (a "proto-neutron star" or PNS; Burrows & Lattimer 1986) and in some cases the midplane of hyper-accreting disks is a significant excess of free neutrons (elec-

tron fraction $Y_e \ll 0.5$), resulting from β-equilibrium under electron degeneracy (Pruet et al. 2003; Beloborodov 2003a, hereafter B03a).[2] While degeneracy at the neutrinosphere of PNS is assured, hyper-accreting disks are viscously heated and only possess a neutron excess in places where they are sufficiently dense and efficiently neutrino-cooled. If present at all, these neutrino-dominated accretion flows (or NDAFs) are thus geometrically-thin and confined to small radii in the disk (Popham et al. 1999). Recent neutrino-cooled α-disk calculations show that an NDAF only forms outside the last stable orbit for steady-state mass accretion above a critical "ignition" rate, given by

$$\dot{M}_{\rm ign} \approx 0.07(0.02) M_3^{4/3} \alpha_{0.1}^{5/3} M_\odot \, {\rm s}^{-1} \tag{4.1}$$

for black hole mass $M = 3M_3 M_\odot$ and spin $a = 0(0.95)$, where $\alpha = 0.1\alpha_{0.1}$ is the disk viscosity parameter (Chen & Beloborodov 2007, hereafter CB07). Disk mass accretion rates ($\dot{M}_D$) greater than $\dot{M}_{\rm ign}$, and thus neutron-rich NDAFs, are plausible in both collapsar and binary merger scenarios (e.g., Popham et al. 1999).

For lower accretion rates or larger radii than characterize NDAFs, cooling is inefficient and the accretion is geometrically-thick and quasi-virial, forming an advection dominated accretion flow (Narayan & Yi 1994; Narayan et al. 2001). Although NDAFs must come into β-equilibrium before accreting (B03a), this is not necessarily the case for thick disks; the neutron content of a thick disk may therefore depend on the matter that feeds it. We discuss the likely neutron content of thick disk winds more in §4.5.5 and §4.6.3.

If the neutron excess that characterizes proto-magnetars and NDAFs can be preserved to large radii in the outflows that they power (where Y_e obtains its asymptotic value Y_e^a; see Table 4.2 for definitions of commonly used variables), observable consequences may result. The dynamics of the GRB jet may be altered by the presence of a dominant neutron component (Derishev, Kocharovsky, and Kocharovsky 1999), which at proton-neutron decoupling could result in the emission of multi-GeV photons and neutrinos (Bahcall & Mészáros 2000; Mészáros

[2] In this paper we define a neutron excess as a neutron-to-proton ratio $n/p = (1 - Y_e)/Y_e > 1$, where we assume free nucleons and Y_e is the proton-to-baryon ratio or "electron fraction."

& Rees 2000; Razzaque & Mészáros 2006a) and cause a significant reheating of the outflow (Rossi et al. 2006). Furthermore, a large neutron-to-proton ratio n/p may reduce the fireball's asymptotic baryon contamination (Fuller et al. 2000; Vlahakis et al. 2003), contribute an additional component to the GRB light curve (Pruet & Dalal 2002; Bulik, Sikera, & Moderski 2002; Fan & Wei 2004; Fan et al. 2005; Dermer & Atoyan 2006) and a unique beta-decay signature (Razzaque & Mészáros 2006b), alter the subsequent afterglow emission (Beloborodov 2003b), and affect the fireball's nucleosynthetic yield (Lemoine 2002; Pruet et al. 2002; B03a). Although not all of these consequences strictly require a neutron excess, most are far more conspicuous when $n/p \gg 1$, partly because only excess neutrons will ultimately remain free if α-particle formation is efficient (e.g., Lemoine 2002). Identification or strong upper limits on any of these effects would teach us much about the composition of GRB outflows.

In this paper we examine the processes that shape the neutron content of outflows from GRB progenitors, motivated by the promise that the distinctive neutron-rich GRB signature holds as a tool for constraining the elusive central engine, whose properties are masked by the otherwise rather generic dynamical evolution of the outflow (e.g., the "fireball" model; Rees & Mészáros 1992). In particular, we focus on NDAFs and proto-magnetars rather than thick accretion disks, not because these models are necessarily favored to produce GRBs, but rather because for neutron-rich central engines an asymptotically neutron-rich outflow is plausible *a priori*. The goal of our analysis is to determine the conditions under which and degree to which these neutron-rich central engines can produce equally neutron-rich outflows.

Determining the asymptotic neutron content of winds driven from the neutron-rich base of PNSs and NDAFs is nontrivial because the neutron fraction will evolve due to weak interactions under the comparatively nondegenerate conditions that characterize scales immediately larger than that of the central engine. In §4.1.1 we discuss the relevant processes that may "deneutronize" the outflow, driving n/p back to ~ 1. Indeed, in §4.2 we show that thermally-driven outflows from PNSs and NDAFs are generally deneutronized by, if nothing else, electron neutrino ab-

sorption. Although thermally-driven winds of this kind possess little or no neutron excess, they also cannot produce GRBs because they do not reach ultra-relativistic speeds (Lorentz factor $\Gamma \gg 1$). Winds driven directly from the surface of PNSs or the midplane of NDAFs require an energetically-dominant Poynting flux to reach large Γ because of the significant mass-loss driven by viscous and neutrino heating (e.g., Levinson & Eichler 1993); this requires rapid rotation and a strong magnetic field. If, through such enhanced magnetic acceleration matter is advected from the PNS surface or the NDAF midplane sufficiently rapidly to avoid deneutronization, the outflow will retain the large neutron-to-proton ratio that characterizes its degenerate base. The magnetocentrifugal acceleration required to maintain low Y_e (high n/p), however, also enhances the wind's mass-loss rate over its purely thermally-driven value (TCQ04). This raises the question of whether simultaneously neutron-rich and ultra-relativistic outflows are possible under physically realizable conditions.

To address these issues quantitatively we have calculated the neutron content of magnetically-driven winds from proto-magnetars and hyper-accreting NDAF disks by solving the equations of one-dimensional neutrino-heated magnetohydrodynamics (MHD). We have studied in detail the effects of magnetic fields and rotation on PNS winds in a previous work, assuming a constant Y_e (Chapter 2). In §4.4 we include the evolution of Y_e in these calculations in order to determine the asymptotic electron fraction Y_e^a from proto-magnetar outflows. In §4.5 we adapt our calculations to the NDAF context by following outflow from the accretion disk midplane for several flux tube angles, employing the α-disk NDAF models of CB07 as boundary conditions. We present a summary of our results in §4.6, including a discussion of the prospect for neutron-rich outflows from central engines of both long and short-duration GRBs. Our analysis and conclusions can be summarized in the broadest terms as follows: the conditions for $n/p \gg 1$ are simultaneously the conditions for short advection timescale, large mass-loss rate, and low asymptotic Lorentz factor. Thus only under very restrictive conditions do both $n/p \gg 1$ and high Γ obtain. The most promising possibilities appear to be outflows from sub-millisecond proto-magnetars and from geometrically thick disks

with $\dot{M}_D \lesssim \dot{M}_{\rm ign}$ (see Table 4.1).

4.1.1 Deneutronizing Processes

Despite the presence of neutron-rich material at the base of NDAF and PNS outflows, this neutron excess may not be preserved. Because conditions above the PNS surface and the accretion disk midplane are typically nondegenerate, equilibrium between the pair-capture reactions

$$e^- + p \rightarrow n + \nu_e, \tag{4.2}$$

$$e^+ + n \rightarrow p + \bar{\nu}_e \tag{4.3}$$

favor $Y_e > 0.5$ in the potentially pair-rich atmosphere through which the wind must accelerate. Furthermore, in the presence of an electron neutrino(antineutrino) energy density $u_{\nu_e}(u_{\bar{\nu}_e})$ the inverse, neutrino absorption reactions

$$\nu_e + n \rightarrow e^- + p, \tag{4.4}$$

$$\bar{\nu}_e + p \rightarrow e^+ + n, \tag{4.5}$$

which dominate pair-captures abruptly above the launching surface of the outflow, drive the system toward an asymptotic electron fraction given by

$$Y_e^\nu \equiv \left(1 + \frac{u_{\bar{\nu}_e}}{u_{\nu_e}} \frac{\langle \epsilon_{\bar{\nu}_e} \rangle - 2\Delta + 1.2\Delta^2/\langle \epsilon_{\bar{\nu}_e} \rangle}{\langle \epsilon_{\nu_e} \rangle + 2\Delta + 1.2\Delta^2/\langle \epsilon_{\nu_e} \rangle}\right)^{-1}, \tag{4.6}$$

where $\Delta = 1.293$ MeV is the neutron-proton mass difference, $\langle \epsilon_{\nu_e} \rangle (\langle \epsilon_{\bar{\nu}_e} \rangle)$ is the mean electron neutrino(antineutrino) energy (Qian et al. 1993; Qian & Woosley 1996, hereafter QW96), and the superscript ν denotes that the electron fraction given by equation (4.6) is set solely by the properties of the local neutrino radiation field.

Equation (4.6) shows that when the electron neutrino and antineutrino fluxes are comparable and have a similar spectrum, as is generically the case for NDAFs and PNSs during the latter's Kelvin-Helmholtz cooling phase (Burrows & Lattimer 1986), equilibrium between neutrino absorptions also favors a comparatively

neutron-poor state ($Y_e \sim 0.5$).[3] Such a deneutronizing luminosity of neutrinos must be present, self-consistently, for matter to cool to the dense, degenerate conditions required for low Y_e in the first place. The total neutrino luminosity from a neutron-rich NDAF, for instance, must exceed

$$L_{\nu,\rm ign} \equiv \eta \dot{M}_{\rm ign} c^2 \approx 5 \times 10^{51} M_3^{4/3} \alpha_{0.1}^{5/3} \,{\rm ergs\ s^{-1}}, \tag{4.7}$$

where $\eta \approx 0.04(0.15)$ for $a = 0(0.95)$ (CB07) and we have used equation (4.1) for $\dot{M}_{\rm ign}$. Similarly, detailed numerical calculations show that a cooling PNS's electron neutrino/antineutrino luminosity is approximately given by

$$L_\nu \approx 10^{52} (t/\,1\,{\rm s})^{-1} \,{\rm ergs\ s^{-1}} \tag{4.8}$$

from a time $t \approx 1$ s after core bounce until the end of the Kelvin-Helmholtz epoch at $t = \tau_{\rm KH} \sim 10 - 100$ s (see, e.g., Pons et al. 1999, Fig. 14).

To contrast the large neutron fraction in an NDAF's midplane with the much lower value favored in equilibrium with the NDAF's neutrino flux, Figure 4.1 shows the midplane electron fraction Y_e^D (*dashed line*) and the equilibrium electron fraction set by neutrino absorption Y_e^ν (*solid line*) as a function of disk cylindrical radius R_0 (in units of gravitational radii $R_g \equiv GM/c^2$) for a steady-state NDAF solution taken from CB07 with $\alpha = 0.03$, $M = 3M_\odot$, $a = 0$, and $\dot{M}_D = 0.2 M_\odot$ s^{-1}. The local neutrino energy densities (u_{ν_e},$u_{\bar{\nu}_e}$) and mean energies ($\langle\epsilon_{\nu_e}\rangle$,$\langle\epsilon_{\bar{\nu}_e}\rangle$) used to calculate Y_e^ν from equation (4.6) were obtained by integrating the total flux incident on a given position just above the disk midplane at radius R_0, where Y_e^a for an outflow launched near R_0 is set. The disk neutrino emission is assumed to originate from axisymmetric annuli of negligible vertical height with a radial structure taken from CB07's one-dimensional, height-integrated calculations. We assume that all relevant lines of site are optically thin in calculating Y_e^ν; this is a good approximation because the vertical neutrino optical depth through the disk

[3] During deleptonization, efficiently neutrino-cooled central engines release slightly more ν_e's than $\bar{\nu}_e$'s; in addition, the ν_e and $\bar{\nu}_e$ spectra (and thus mean energies) also differ slightly due to the difference between the mean e^- and e^+ energies, the e^- and e^+ capture cross sections, and, in the neutrino optically thick case, the ν_e and $\bar{\nu}_e$ neutrinosphere temperatures and geometries. Although $Y_e^\nu \lesssim 0.5$ is possible in some cases, these relatively modest effects are unlikely to yield $Y_e^\nu \ll 0.5$.

is $\lesssim 1$ at all radii and because the disc scale height increases more rapidly than $\propto R_0$ so that the outer disk's atmosphere has an unobstructed view of the interior flow. Differential gravitational redshifts between emission and absorption radii are taken into account, although geodesic bending is ignored.

Figure 4.1 shows that the disk midplane is very neutron-rich for $R_0 \lesssim 30 - 100R_g$ (the NDAF portion of the disk), reaching a neutron-to-proton ratio as large as ~ 30 at small radii. However, Figure 4.1 also shows that $Y_e^\nu \sim 0.5$ at all radii, so that if the outflow comes into equilibrium with the disk's neutrino luminosity it will be driven back to a relatively neutron-poor state ($n/p \sim 1$). Also note that $Y_e^\nu > 0.485$ at all radii, allowing possible ^{56}Ni synthesis in a disk wind, again should the nucleons come into equilibrium with the neutrino flux (Pruet et al. 2004).[4] Since the outer disk is radiatively-inefficient and therefore particularly prone to large mass outflows (Blandford & Begelman 1999), disk wind-aided stellar explosions provide one way to produce optically luminous SNe in collapsar models for LGRBs (MacFadyen & Woosley 1999), where Ni masses up to $\sim 0.5 M_\odot$ have been inferred (e.g., GRB980425/SN1998bw; Iwamoto et al. 1998; Woosley, Eastman, & Schmidt 1999).

4.2 Thermally-Driven Winds

In spite of nondegenerate pair captures and neutrino absorptions (eqs. [4.2]–[4.5]), the high neutron fraction in NDAFs and proto-magnetar outflows will be preserved if deneutronization proceeds slower than a fluid element's advection from the surface. In evaluating this possibility in the case of NDAFs, previous investigations have assumed that the disk is turbulent and that the relevant outflow rate is of the order of the turnover frequency of a typical turbulent eddy ($\sim \Omega_{\rm K}$, the

[4] Although we find that $Y_e^\nu > 0.485$ at all disk radii using mean neutrino energies from CB07's height-integrated disk calculations, precisely whether $Y_e^\nu > 0.485$ or $Y_e^\nu < 0.485$ is difficult to determine with confidence because the neutrino spectra are sensitive to the disk's vertical temperature profile, which is theoretically uncertain, and to neutrino transport if the disk midplane is neutrino optically thick (Sawyer 2003). If viscous heating is important in the wind, additional entropy deposition may drive $Y_e^a \gtrsim 0.485$, allowing ^{56}Ni production even if $Y_e^\nu < 0.485$.

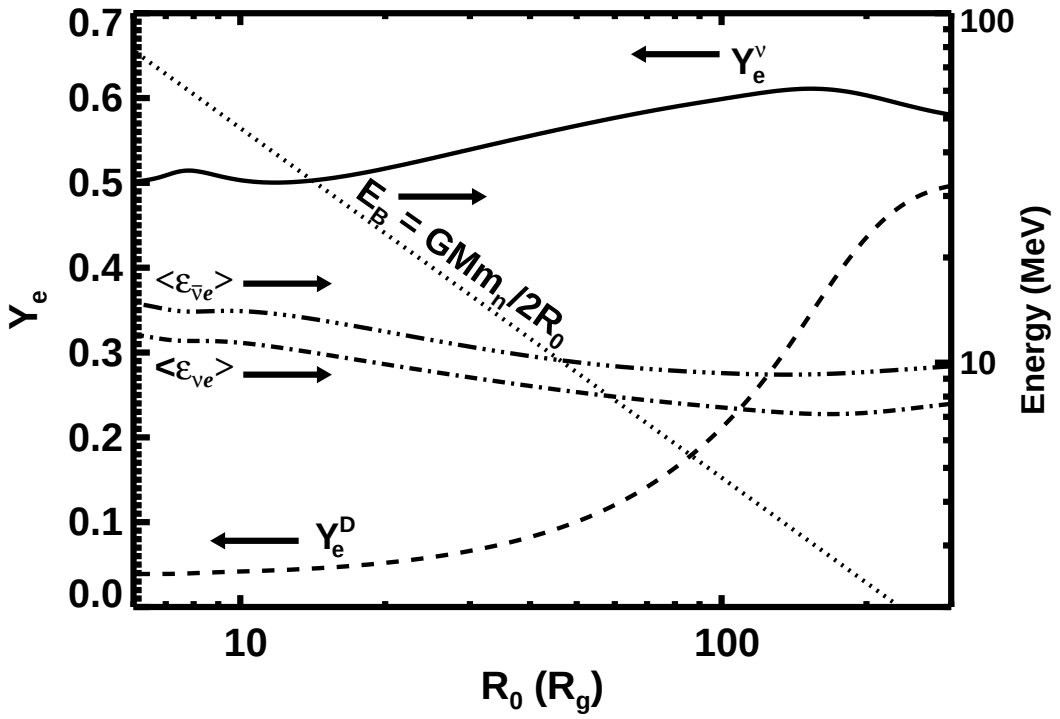

Figure 4.1: [LEFT AXIS] Electron fraction in neutrino absorption equilibrium Y_e^ν (eq. [4.6]; *solid line*) as a function of the wind launching radius R_0 (in units of gravitational radii $R_g = GM/c^2$) calculated from the thin, height-integrated $\alpha-$disk accretion model of Chen & Beloborodov (2007) with $\alpha = 0.03$, black hole mass $M = 3M_\odot$, black hole spin $a = 0$, and accretion rate $\dot{M}_D = 0.2\ M_\odot\ \mathrm{s}^{-1}$. Also shown is the midplane electron fraction Y_e^D (*dashed line*) taken directly from CB07's calculation. Note that the disk midplane is very neutron-rich inside $R_0 \sim 30R_g$, with a neutron-to-proton ratio $n/p = (1 - Y_e)/Y_e$ exceeding 10. However, if outflow driven from the disk comes into equilibrium with the disk's neutrino radiation then the asymptotic neutron-to-proton ratio is driven back to ~ 1 because $Y_e^\nu \sim 0.5$ at all radii. Also note that neutrino equilibrium favors $Y_e^a > 0.485$ at large radii, a requisite condition for producing ^{56}Ni in neutrino-driven outflows. [RIGHT AXIS] The dot-dash(triple-dot-dash) line shows the mean electron neutrino(antineutrino) energy incident on the base of outflows driven from radius R_0. Also shown (*dotted line*) is the binding energy E_B of a nucleon in a Keplerian thin disk, where the black hole's gravitational potential is assumed to be Newtonian for simplicity. The disk is the most neutron-rich at radii where $E_B \gtrsim \langle\epsilon_{\nu_e}\rangle, \langle\epsilon_{\bar{\nu}_e}\rangle$ and thus where more than one neutrino absorption is required to unbind a nucleon. This shows that purely neutrino-driven winds from small radii in the disk must come into equilibrium with neutrino absorptions and will thus obtain $Y_e^a \simeq Y_e^\nu \sim 0.5$ ($n/p \sim 1$). At larger radii ($R_0 \sim 50 - 200R_g$), $E_B \lesssim \langle\epsilon_{\nu_e}\rangle, \langle\epsilon_{\bar{\nu}_e}\rangle$, and so deneutronization of a wind by neutrino absorption is less likely.

Keplerian rotation rate), concluding that low Y_e is preserved under most conditions appropriate to hyper-accreting disks (Pruet et al. 2003; B03a). Specifically, Pruet et al. (2003) argue that because NDAFs are generally dense, degenerate, and gas pressure-dominated, if a fluid element is carried out of the midplane adiabatically in an eddy turnover time, pair creation is somewhat suppressed and low Y_e is preserved (i.e., $Y_e^a \approx Y_e^D$ obtains). B03a also compares $\Omega_{\rm K}$ to the neutrino absorption rates (eqs. [4.4]−[4.5]), reaching a similar conclusion to Pruet et al. (2003) except for very high disk neutrino luminosities ($L_\nu \gtrsim 10^{53}$ erg s^{-1}), corresponding to $\dot{M}_D \gtrsim 1 M_\odot$ s^{-1}. This leaves a wide range of astrophysically plausible accretion rates ($\dot{M}_{\rm ign} \lesssim \dot{M}_D \lesssim 1 M_\odot$ s^{-1}) for which outflow, if it escapes the disk in an eddy turnover time, would be asymptotically neutron-rich.

Several arguments can, however, be raised against the conclusion that low Y_e is preserved in NDAF outflows. Although some degree of turbulence and turbulent mixing must accompany the accretion torque (e.g., via the MRI; Balbus & Hawley 1998), its scale and efficiency are unclear.[5] Even if present, large-scale turbulence is not likely to drive outflow from a thin disk; thus, an eddy turnover time is not the relevant timescale to compare to the weak interaction rates. Outflow from the surface of a thin accretion disk must be heated, passing through a sonic point as it accelerates out of the black hole's potential. Thus, the advection time of a self-consistent, viscous or neutrino-heated wind sets the residence time for a fluid element in regions of potential deneutronization. This timescale is generally much longer than $\Omega_{\rm K}^{-1}$.

Indeed, the neutrino-driven PNS winds that accompany the Kelvin-Helmholtz cooling of slowly rotating, non-magnetized PNSs generically come into equilibrium with the neutrino absorption rates, obtaining $Y_e^a = Y_e^\nu$ (QW96; Thompson et al. 2001, hereafter T01). To see that the neutron fraction of a purely neutrino-driven NDAF wind must also come into equilibrium with the neutrino rates we adapt an argument first presented by QW96 in the PNS context. First, note that a

[5]NDAFs cool efficiently and are not unstable to radial convection, except perhaps at small radii in the case of neutrino optically thick accretion (Lee et al. 2005); it is also not clear that NDAFs are vertically-convective (Hirose, Krolik, & Stone 2006), as this depends on the unknown vertical viscous dissipation profile (see the discussion in Blaes 2007).

typical nucleon with mass $m_{\rm n}$ launched in a wind from radius R_0 of a thin Keplerian disk requires an energy $E_B \simeq GMm_{\rm n}/2R_0 \approx 80(R_0/6R_g)^{-1}$ MeV to escape the black hole's gravitational potential, where we have assumed Newtonian gravity for simplicity. In addition to Y_e^D and Y_e^ν, in Figure 4.1 we show for comparison E_B and the mean electron neutrino and antineutrino energies used to calculate Y_e^ν. The mean neutrino energies vary only weakly with radius because the neutrino flux released from an NDAF's inner disk is relatively hot (Popham et al. 1999; CB07) and dominates the neutrino heating at all outflow radii (relative to the neutrino emission from larger radii in the disk). By balancing viscous heating and optically thin neutrino cooling at the radius $R_{\rm p} \sim 1 - 10R_g$ where most of the disk's emission originates, we find that an NDAF's mean neutrino energy incident on any disk radius is approximately given by

$$\langle \epsilon_\nu \rangle \approx 5.1 T_D \approx 18 \alpha_{0.1}^{1/5} M_3^{-1/5} (R_{\rm p}/6R_g)^{-3/10}\,{\rm MeV}, \tag{4.9}$$

where T_D is the disk's midplane temperature at $R_{\rm p}$. Equation (4.9), which agrees well with our calculation of $\langle \epsilon_\nu \rangle$ in Figure 4.1, is valid so long as the inner disk is optically thin to neutrinos ($\tau_\nu \lesssim 1$), which remains true for accretion rates below $\approx 0.7(0.05)\alpha_{0.1} M_\odot\,{\rm s}^{-1}$ for electron neutrinos and $\approx 2.0(0.14)\alpha_{0.1} M_\odot\,{\rm s}^{-1}$ for electron antineutrinos for $a = 0(0.95)$ and $M = 3M_\odot$ (CB07). For larger $\dot{M}_D$ the disk is opaque to neutrinos ($\tau_{\nu_e}, \tau_{\bar{\nu}_e} \gtrsim 1$) and the mean neutrino energy is approximately given by its Fermi-Dirac blackbody value

$$\langle \epsilon_\nu \rangle \approx 3.2 T_\nu \approx 16 M_3^{-1/2} \dot{M}_{D,0.1}^{1/4} (R_{\rm p}/6R_g)^{-1/2}\,{\rm MeV}, \tag{4.10}$$

where $\dot{M}_D = 0.1 \dot{M}_{\rm D,0.1} M_\odot\,{\rm s}^{-1}$ and T_ν is the temperature at the disk's neutrinosphere.

Despite the relatively high mean neutrino energies shown in Figure 4.1 and implied by equations (4.9) – (4.10), $\langle \epsilon_\nu \rangle$ is still much less than $E_B (\sim R_{\rm p})$ because NDAFs are efficiently neutrino-cooled. Thus, each nucleon in a thermally-driven outflow originating from an inner NDAF must absorb several neutrinos in the process of being unbound from the black hole's potential. Through these multiple absorptions the wind's electron fraction is unavoidably brought into equilibrium

with the neutrino flux at Y_e^ν (QW96), a consequence of the fact that neutrino absorptions (eqs. [4.4]−[4.5]) both dominate the wind heating and determine $Y_e^a \simeq Y_e^\nu$.

This conclusion may hold even for winds driven from near the NDAF's relatively loosely-bound outer edge. NDAFs only exist interior to an "ignition" radius $R_{\rm ign}$, which we estimate as the location at which optically thin cooling by nondegenerate pair capture on free nuclei (eqs. [4.2]−[4.3]) balances viscous heating for a thick disk:[6]

$$R_{\rm ign} \approx 10 \dot{M}_{D,0.1}^{6/5} M_3^{-8/5} \alpha_{0.1}^{-2} R_{\rm g}. \tag{4.11}$$

For the disk parameters associated with the solution in Figure 4.1 ($\alpha = 0.03, M = 3M_\odot, \dot{M}_D = 0.2 M_\odot \ {\rm s}^{-1} \gg \dot{M}_{\rm ign}$), equation (4.11) gives $R_{\rm ign} \approx 100 R_{\rm g}$, corresponding to the radius interior to which the disk possesses a significant neutron excess ($Y_e^D \ll 0.5$). By requiring that $R_{\rm ign}$ exceed the radius of the innermost stable circular orbit, $R_{\rm isco} \simeq 6(1) R_g$ for black hole spin $a = 0(0.95)$, one recovers the numerically-determined value for $\dot{M}_{\rm ign}$ given in equation (4.1) to reasonable accuracy.

Using equations (4.9) and (4.10), the ratio of the binding energy at $R_{\rm ign}$ to the mean neutrino energy from the inner disk is approximately given by

$$\begin{aligned} \frac{E_B(R_{\rm ign})}{\langle \epsilon_\nu \rangle} \quad &\sim 3 \dot{M}_{\rm D,0.1}^{-6/5} M_3^{9/5} \alpha_{0.1}^{9/5} \left(\frac{R_{\rm p}}{6 R_g} \right)^{3/10} : \tau_\nu \lesssim 1 \\ &\sim 3 \dot{M}_{\rm D,0.1}^{-29/20} M_3^{21/10} \alpha_{0.1}^{2} \left(\frac{R_{\rm p}}{6 R_g} \right)^{1/2} : \tau_\nu \gtrsim 1 \end{aligned} \tag{4.12}$$

Equation (4.12) shows that $E_B(R_{\rm ign}) \gtrsim \langle \epsilon_\nu \rangle$ for $\alpha \gtrsim 0.1$ and for most physical values of $\dot{M}_D$; thus, winds thermally-driven from even $R_0 \sim R_{\rm ign}$ would have $Y_e^a \approx Y_e^\nu \sim 0.5$. Although equation (4.12) implies that winds driven from the outer portions of high-$\dot{M}_D$, low-α NDAFs may remain neutron-rich, the astrophysical

[6] Equation (4.11) overestimates $R_{\rm ign}$ for large $R_{\rm ign}$ (i.e., large $\dot{M}_D$ and low α) because cooling via electron capture requires a threshold energy $\Delta - m_e c^2 \sim 1$ MeV that exceeds the disk temperature at large radii. Furthermore, NSE favors composite nuclei for $R_0 > R_\alpha \sim 100 R_g$; nuclear disintegration is a significant heat source around $R_0 \sim R_\alpha$ and we have overestimated cooling for $R_0 > R_\alpha$ because pair capture rates are lower on composite nuclei.

situations most likely to result in extended disks, collapsars and He core-black hole mergers (Fryer & Woosley 1998), are also likely to have lower values of $\dot{M}_D$. Furthermore, NDAFs become unstable to self-gravity (Toomre Q < 1) at $R_{\rm ign}$ for $\dot{M}_D \gtrsim 2\alpha_{0.1}^{10/7} M_3^{3/11} M_\odot \ {\rm s}^{-1}$, comparable to the accretion rates for which $E_B(R_{\rm ign}) < \langle \epsilon_\nu \rangle$. The dynamics at these radii is not well understood so it is difficult to draw definitive conclusions concerning the neutron content of outflows launched from large radii in high-$\dot{M}_D$, low-α disks.

In addition to neutrino heating, viscous heating may thermally drive outflows from the surface of NDAFs. Pruet et al. (2004) have shown, in the context of a wind driven by viscous heating supplied through a simple α prescription, that entropy added to the outflow lifts electron degeneracy before the outflow falls out of β-equilibrium. This drives n/p to a value near unity via nondegenerate pair captures, even without the aid of neutrino absorption. However, the ability of viscous heating to generically drive outflows from thin disks is unknown, as this depends in detail on where energy is deposited, a major uncertainty in current thin disk theory (Blaes 2007). Recent radiation MHD thin disk simulations suggest that very little energy dissipation occurs in the disk corona (Turner 2004; Hirose, Krolik, & Stone 2006; Blaes et al. 2006b; Krolik et al. 2007), where a wind would most likely be launched. Regardless of potential viscous entropy contributions, the existence of the neutrino flux discussed in the preceding paragraphs is assured. We thus conclude that purely thermally-driven winds from the vicinity of compact objects, even those with a significant surface neutron excess, are unlikely to be neutron-rich asymptotically.

4.3 Magnetically-Driven Winds

Winds driven directly from the surfaces of NDAFs and PNSs solely by viscous or neutrino heating are inherently mass-loaded and thus make poor candidates for producing GRBs. The high energy-to-baryon ratio required of ultra-relativistic GRB outflows (asymptotic wind Lorentz factor $\Gamma \gtrsim 10 - 100$; e.g., Lithwick & Sari 2001) can, however, be achieved if rapid rotation and a strong poloidal magnetic

field supply an energetically dominant Poynting flux. The ratio of Poynting flux to kinetic energy flux at the light cylinder $R_{\rm L} \equiv c/\Omega$ is given by (for $\sigma > 1$)

$$\sigma \equiv \left. \frac{B^2}{4\pi\rho c^2} \right|_{R_{\rm L}}, \tag{4.13}$$

where B is the magnetic field strength, ρ is the rest mass density, Ω is the rotation rate of the central star or disk, and we have assumed that the outflow is moving only mildly relativistically at $R_{\rm L}$. If the magnetic energy is fully converted into the kinetic energy of bulk motion, either directly or through thermalization and subsequent thermal or magnetic pressure-driven expansion (e.g., Drenkhahn & Spruit 2002), then $\Gamma \sim \sigma$; Poynting-flux dominated GRB outflows therefore require $\sigma \gtrsim 10 - 100$.

In the case of magnetically-driven, high-σ NDAF or PNS winds, matter may be advected from the wind's base sufficiently quickly to remain effectively adiabatic, with its initial degeneracy never lifted due to insufficient heating. The pair-capture reactions (eqs. [4.2]−[4.3]) then continue to favor low Y_e above the PNS surface or disk midplane. In the PNS case this ineffective heating becomes manifest as an exponential drop in the asymptotic wind entropy with increasing Ω, which occurs for rotation periods $P = 2\pi/\Omega \lesssim 2-3$ ms (see eq. [2.38]) in the presence of a sufficiently strong surface dipole magnetic field ($B_\nu^{\rm dip} \sim 10^{14} - 10^{15}$ G); note that the large fields and rapid rotation required are similar to those required for proto-magnetars to produce LGRBs in the first place. It is therefore likely that GRB jets from proto-magnetars or NDAFs are not completely deneutronized by pair captures.

Even with degeneracy intact and pair production suppressed, to remain neutron-rich a GRB-producing wind must advect material from its base sufficiently rapidly to overcome neutrino absorptions. This requires significant magnetocentrifugal support in the outflow's inner, hydrostatic atmosphere, where Y_e^a is set. For the reasons discussed in §4.2, magnetocentrifugal forces acting on a wind launched from a radius R must contribute a factor $\sim GMm_{\rm n}/R\langle\epsilon_\nu\rangle \gg 1$ more energy than neutrino heating in unbinding the outflow to avoid deneutronization. Inevitably, such acceleration in the wind's subsonic region leads to significantly enhanced mass-loss

(TCQ04; Chapter 2). *Thus, the very conditions required to preserve low Y_e in a proto−magnetar or NDAF wind threaten to simultaneously over−pollute the outflow with baryons, reducing σ and stiflying the outflow's GRB potential.*

In the following sections we address some of these issues by calculating the neutron content of magnetized proto-magnetar and NDAF winds. In particular, we consider the conditions under which outflows from proto-magnetars (§4.4) and NDAFs (§4.5) can remain neutron-rich while simultaneously maintaining sufficiently low mass-loading to remain plausible GRB central engines.

4.4 Proto-Magnetar Winds

4.4.1 Evolution Equations and Numerical Procedure

As in Chapter 2, we calculate the structure of rapidly rotating PNS winds by solving the equations of one-dimensional neutrino-heated, ideal MHD in the equatorial plane of the PNS. Using the time-dependent "inhomogeneous" 2N-RK3 scheme described in Brandenburg (2003), we solve for the wind density ρ, temperature T, radial velocity v_r, azimuthal magnetic field B_ϕ, and azimuthal velocity v_ϕ as a function of radius r according to equations (2.2)-(2.5) and equation (2.9) in Chapter 2. In this work we extend our previous calculations by simultaneously solving for the electron fraction Y_e, thus determining the wind's asymptotic neutron abundance.

The electron fraction Y_e evolves as the wind emerges off the PNS surface due to weak interactions according to:

$$\frac{d}{dt}Y_e = (1-Y_e)(\lambda_{\nu_e n\rightarrow pe^-} + \lambda_{e^+ n\rightarrow p\bar{\nu}_e}) - Y_e(\lambda_{\bar{\nu}_e p\rightarrow ne^+} + \lambda_{e^- p\rightarrow n\nu_e}), \tag{4.14}$$

where $d/dt \equiv \partial/\partial t + v_r(\partial/\partial r)$ and the λ's are the weak interaction rates; we take the pair capture rates (eqs. [4.2]–[4.3]) and the neutrino capture rates (eqs. [4.4]–[4.5]) from B03a (neglecting proton/neutron recoil to good approximation; Strumia & Vissani 2003). We have included the full effects of electron degeneracy, including

the outgoing electron and positron blocking factors in calculating the neutrino capture rates. In calculating all of the weak interaction rates we assume that the electrons and positrons are relativistic. This is a good approximation for neutrino capture because the average neutrino(antineutrino) energy (and hence the resultant electron(positron) kinetic energy) always far exceeds the electron rest mass. We set the pair capture rates equal to zero for $T < 0.5$ MeV in order to artificially account for the disappearance of pairs; the evolution of Y_e is not sensitive to this cutoff because for $T \sim 0.5$ MeV pair capture is always dominated by neutrino absorption. We neglect the effects that α-particle formation has on the evolution of Y_e; this is a reasonable approximation because for cases in which the formed $\alpha-$particle fraction is the most significant (i.e., $Y_e^a \sim 0.5$) and is thus likely to have its greatest effect on the evolution of Y_e, Y_e^a almost obtains by the radius where most α-particles form. We also neglect the effects that magnetic fields have on the electron and positron distribution functions and, hence, on the interaction rates and equation of state, although these effects become important for the largest field strengths that we consider ($B = 10^{16}$ G) and should be included in more detailed work (e.g., Lai & Qian 1998; Duan & Qian 2004). Lastly, we neglect the small effect that general relativity (GR) has on the evolution of Y_e; in non-rotating PNS winds GR slightly increases Y_e^a (Fuller & Qian 1996), primarily due to neutrino gravitational redshifts and the deeper gravitational potential.

Because we are interested in the wind structure along open magnetic flux, we assume a monopole radial field structure, $B_r = B_\nu(R_\nu/r)^2$, where B_ν is the surface magnetic field, and R_ν is the neutrinosphere radius. Since Y_e^a is set near the PNS surface, Y_e is more sensitive to the surface field strength than to the field's precise radial scaling, and so our results are likely relatively insensitive to our monopole assumption.

For asymptotically relativistic PNS outflows, using the conserved magnetic flux $\Phi_{\rm B} = B_\nu R_\nu^2 = B(R_{\rm L})R_{\rm L}^2$ and a spherically symmetric mass flux $\dot{M} = 4\pi\rho v_r r^2 = 4\pi c R_{\rm L}^2 \rho(R_{\rm L})$ we have that the magnetization from equation (4.13) is given by

$$\sigma = B_\nu^2 R_\nu^4 \Omega^2 / \dot{M} c^3 \tag{4.15}$$

Although for asymptotically non-relativistic outflows ($\sigma < 1$), σ as defined by equation (4.15) is no longer the ratio of Poynting-to-kinetic energy flux at $R_{\rm L}$, σ remains a useful dimensionless quantity for characterizing the importance of the magnetic field in accelerating the outflow.

With the exception of the evolution of Y_e and its effects on the other thermodynamic wind variables, our boundary conditions and microphysics are similar to those used in Chapter 2; thus, we review only the most essential aspects of these here. Our neutrino heating(cooling) rates include charged-current neutrino absorption(pair capture) (eqs. [4.2]−[4.5]), neutrino(pair) annihilation, and inelastic neutrino-lepton scattering (QW96; T01), corrected for solid angle and redshift effects (Salmonson & Wilson 1999; T01). We index stages of the PNS thermal evolution in terms of the electron antineutrino luminosity $L_{\bar{\nu}_e}$. We scale all other neutrino luminosities ($L_{\nu_e}, L_{\nu_\mu}, L_{\bar{\nu}_\mu}, L_{\nu_\tau}$, and $L_{\bar{\nu}_\tau}$) as in TCQ04: $L_{\nu_e} = L_{\bar{\nu}_e}/1.3 = 1.08 L_{\nu_\mu}$, where μ denotes each of the other four neutrino/antineutrino species. Note that the total neutrino luminosity is then $L_\nu \simeq 4.6 L_{\bar{\nu}_e}$. Following T01, all first energy moments at the neutrinosphere ($\langle\epsilon_\nu\rangle \equiv \langle E_\nu^2\rangle/\langle E_\nu\rangle$, where E_ν is the neutrino energy) were scaled with luminosity as $\langle\epsilon_\nu\rangle \propto L_\nu^{1/4}$, anchoring $\{\langle\epsilon_{\nu_e}\rangle, \langle\epsilon_{\bar{\nu}_e}\rangle, \langle\epsilon_{\nu_\mu}\rangle\}$ at $\{11, 14, 23\}$MeV for $L_{\bar{\nu}_e,51} = 8$, where $L_{\bar{\nu}_e,51}$ is the electron antineutrino luminosity in units of 10^{51} ergs s^{-1}. Higher energy moments necessary for the heating calculations ($\langle\epsilon_{\nu_e}^n\rangle, \langle\epsilon_{\bar{\nu}_e}^n\rangle$, etc.) are related to the first through appropriate integrals over the assumed Fermi-Dirac surface distribution. With these scalings we note that electron antineutrino luminosities $L_{\bar{\nu}_e,51} = \{8, 3.5, 1\}$ result in a neutrino-driven asymptotic electron fraction $Y_e^\nu = \{0.48, 0.50, 0.53\}$ according to equation (4.6); neutrino absorptions therefore favor $n/p \sim 1$ throughout the PNS's Kelvin-Helmholtz cooling epoch (T01). Although we have assumed neutrino spectra based on current calculations of non-rotating PNSs, for rotating PNSs the mean neutrino energies along the equator may be lower due to gravity-darkening, which would increase Y_e^ν from the non-rotating value (e.g., Fryer & Heger 2000; Thompson, Quataert, & Burrows 2005; Dessart et al. 2006).

We assume Newtonian gravity for a fixed central PNS mass $M = 1.4 M_\odot$ and a neutrinosphere radius $R_\nu = 10$ km which is characteristic of the PNS's final,

cooled state. Although R_ν is probably larger than 10 km for the first few seconds following the launch of the SN shock (e.g., Buras et al. 2003), neutron-rich GRB-producing outflows, which are the focus of this paper, are only possible at relatively late times, once the PNS has fully contracted to its most rapidly rotating state (see §4.4.4). Our code is non-relativistic but we still calculate flows with $\sigma > 1$, which accelerate to relativistic speeds outside the light cylinder, because $\dot{M}$ and Y_e are set very close to the PNS surface, where the wind still moves non-relativistically. We set the neutrinosphere density of the wind ρ_ν so that the neutrino optical depth to infinity is $\tau_\nu \simeq \frac{2}{3}$; ρ_ν ranges from $\sim 10^{12}$ g cm^{-3} for high luminosity, rapidly rotating solutions to $\gtrsim 10^{13}$ g cm^{-3} for our lowest luminosity solutions (see Table 4.3). In general, we find that Y_e^a is relatively insensitive to ρ_ν. The electron fraction at the neutrinosphere Y_e^0 is chosen to ensure that equilibrium between the weak interaction rates in equation (4.14) is established at R_ν.

The value of the magnetic flux $\Phi_{\rm B} = B_\nu R_\nu^2$, stellar rotation rate Ω, and neutrino luminosity L_ν uniquely identify a wind solution. By letting the wind come into steady-state we obtain eigenvalues for the mass-loss rate $\dot{M}$ (normalized to 4π sr), specific angular momentum-loss rate $\mathcal{L}$, and Bernoulli integral $\mathcal{B}$ (see eqs. [2.6], [2.7], and [2.10]). Because our code is non-conservative, the radial conservation of these quantities is used to verify the code's accuracy. Steady state conditions are generally established on a fast magnetosonic crossing-time, which is typically $\lesssim 10$ ms. The total asymptotic energy lost in the wind is given by $\dot{E}^a = \mathcal{B}^a \dot{M}$, where $\mathcal{B}^a$ is the Bernoulli integral evaluated at large radii. The rate of angular momentum-loss in the wind is given by $\dot{J}_W = \mathcal{L}\dot{M} = \Omega R_A^2 \dot{M}$, where R_A is the Alfvén radius defined by $B_r(R_A)/\sqrt{4\pi\rho(R_A)} = v_r(R_A)$.

4.4.2 Numerical Results

We have calculated the MHD structure of PNS winds for several combinations of surface monopole magnetic field strength B_ν, rotation rate Ω, and electron antineutrino luminosity $L_{\bar{\nu}_e} = L_{\bar{\nu}_e,51} \times 10^{51}$ ergs s^{-1} in order to study the neutron fraction in proto-magnetar outflows. Some of these results are summarized in

Table 4.3.

Figure 4.2 shows our calculation of the asymptotic electron fraction Y_e^a of proto-magnetar winds as a function of Ω at neutrino luminosity $L_{\nu_e,51} = 8$ and 3.5 for $B_\nu = 10^{14}, 10^{15}$, and 10^{16} G. Figure 4.2 and Table 4.3 show that for slow rotation and low magnetic field strengths Y_e^a obtains the neutrino absorption equilibrium value $Y_e^\nu \sim 0.5$ (eq. [4.6]), as is expected from studies of slowly-rotating, non-magnetized PNSs (QW96; T01) and from the arguments given in §4.2. As the rotation rate and magnetic field strength increase, Y_e^a decreases because the material is advected sufficiently rapidly from the surface due to magnetocentrifugal slinging that Y_e "freezes out" before coming into equilibrium with neutrino absorptions.

Figure 4.2 also shows that for a sufficiently strong magnetic field, $B_\nu \gtrsim 10^{14} - 10^{15}$ G, $Y_e^a(\Omega)$ no longer increases with increasing B_ν, saturating to a profile $Y_e^{a,\rm sat}(\Omega)$ that we find is reasonably well-fit by a single empirical formula for all of the rotation rates and neutrino luminosities that we have considered ($\Omega \leq 9000$ s^{-1}; $1 \lesssim L_{\bar{\nu}_e,51} \lesssim 10$, corresponding to times $\sim 1 - 10$ s following bounce):

$$Y_e^{a,\rm sat} = \frac{Y_e^0 + Y_e^\nu}{2} + \frac{Y_e^0 - Y_e^\nu}{2} \tanh\left[\frac{\Omega - \Omega_{\rm n}}{\Delta\Omega_{\rm n}}\right], \tag{4.16}$$

where $\Omega_{\rm n} \approx 7800$ s^{-1}, $\Delta\Omega_{\rm n} \approx 2000$ s^{-1}, and Y_e^0 is the electron fraction at the neutrinosphere (typically, $Y_e^0 \approx 0.01 - 0.05$; see Table 4.3). Equation (4.16) and Figure 4.2 show that proto-magnetars must have submillisecond ($P \lesssim P_{\rm n} \equiv 2\pi/\Omega_{\rm n} \approx 0.8$ ms), near break-up, rotation in order to produce asymptotically neutron-rich outflows; furthermore, because $\Delta\Omega_{\rm n}/\Omega_{\rm n} \ll 1$ the transition from $n/p \gg 1$ to $n/p \sim 1$ occurs over a very limited range in Ω. Therefore, because a PNS possesses a rotational energy

$$E_{\rm rot} = \frac{1}{2} I \Omega^2 \approx 4 \times 10^{52} \left(\frac{\Omega}{\Omega_{\rm n}}\right)^2 \text{ ergs}, \tag{4.17}$$

where $I \approx (2/5) M R_\nu^2$ is the PNS moment of inertia, we conclude that neutron-rich outflows from magnetar birth would require a GRB plus SN energy totaling $\gtrsim 4 \times 10^{52}$ ergs.

As an example of a neutron-rich wind solution, the left panel of Figure 4.3

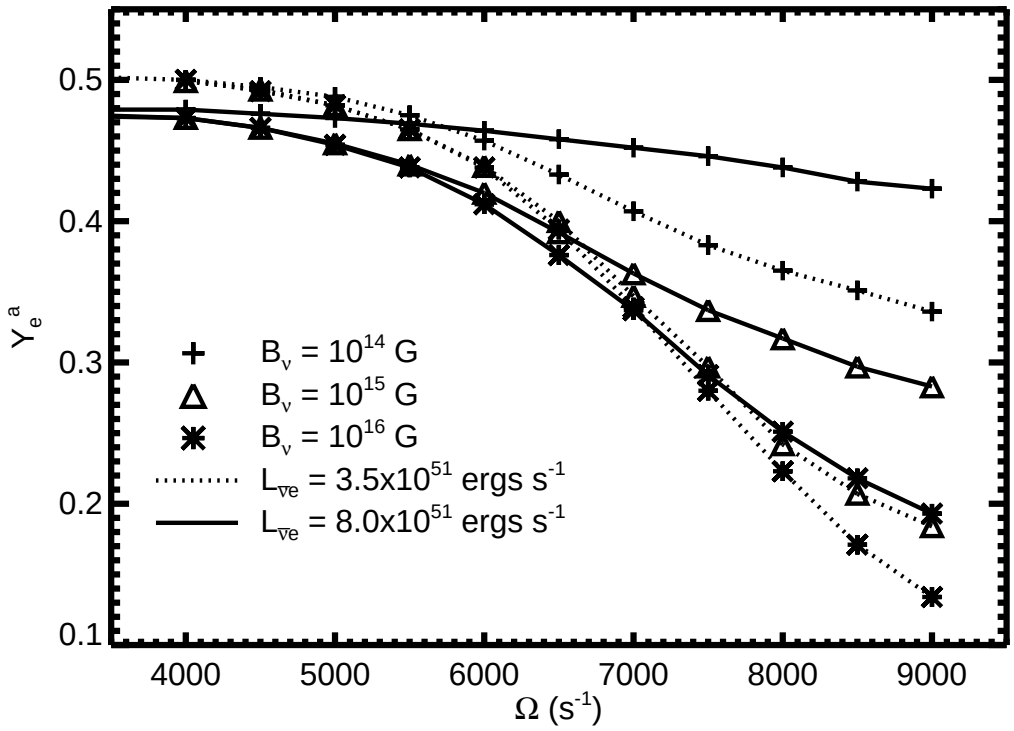

Figure 4.2: Asymptotic electron fraction Y_e^a for magnetocentrifugally-driven PNS winds as a function of rotation rate Ω at $L_{\bar{\nu}_e} = 8 \times 10^{51}$ ergs s^{-1} and $L_{\bar{\nu}_e} = 3.5 \times 10^{51}$ ergs s^{-1} for $B_\nu = 10^{14}$ G, $B_\nu = 10^{15}$ G, and $B_\nu = 10^{16}$ G. For slow rotation and weak magnetic fields, Y_e^a approaches its neutrino absorption equilibrium value $Y_e^\nu \sim 0.5$ (eq. [4.6]). For more rapid rotation and stronger magnetic fields, Y_e^a is reduced because matter is advected from the PNS surface sufficiently rapidly that it falls out of β-equilibrium before neutrino absorptions dominate degenerate pair captures (see Fig. 4.3). For sufficiently large B_ν, Y_e^a no longer decreases with increasing B_ν because the wind corotates past a few scale heights above the PNS surface, where Y_e^a is set. An approximate fit to our numerical results in this limit is given by equation (4.16).

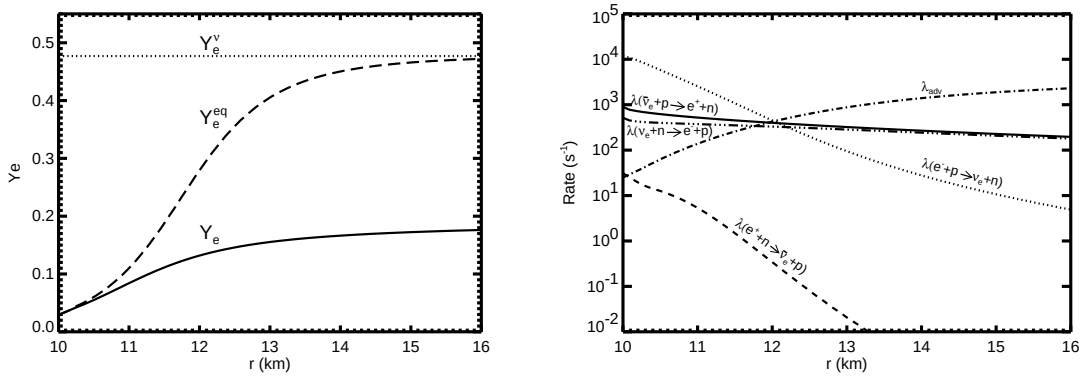

Figure 4.3: *Left*: Electron fraction Y_e (*solid line*) in the inner 6 km of a magnetically-driven PNS wind with $M = 1.4M_\odot$, $R_\nu = 10$ km, $B_\nu = 10^{16}$ G, and $\Omega = 9000$ s^{-1}; also shown is the local equilibrium electron fraction $Y_e^{\rm eq}$ (*long dashed line*), obtained by setting the left hand side of equation (4.14) equal to zero. The electron fraction is very small at the PNS surface ($Y_e \approx 0.05$). As matter accelerates away from the surface, $Y_e \approx Y_e^{\rm eq}$ as long as matter moves sufficiently slowly to maintain local equilibrium with the weak interaction rates. Because Y_e is out of equilibrium by the time neutrino absorptions dominate pair captures, the asymptotic electron fraction Y_e^a is $\ll 0.5$, despite the fact that $Y_e^{\rm eq}$ asymptotes to $Y_e^\nu \approx 0.48$ at large radii. *Right*: Rates in the wind that determine the radial evolution of Y_e. The dotted(short dashed) lines show the electron(positron) absorption rates (eqs. [4.2]−[4.3]). The electron neutrino and antineutrino absorption rates (eqs. [4.4]−[4.5]) are shown with a triple-dot-dash and solid line, respectively; the wind advection rate $\lambda_{\rm adv} \equiv v_r/r$ is shown with a dot-dashed line. The asymptotic electron fraction obtained by the wind $Y_e^a \approx 0.19$ is appreciably lower than the neutrino absorption equilibrium value ($Y_e^\nu \approx 0.48$) that obtains for slower rotating or non-magnetized winds. Lower Y_e^a obtains because magnetocentrifugal acceleration is sufficiently strong that matter "freezes out" of β-equilibrium at small radii (corresponding to $\lambda_{\rm adv}$ rising above the weak interaction rates at $r \approx 12$ km), before the neutrino absorption rates begin to dominate the electron capture rate. Equilibrium still favors neutron-rich matter at freeze-out because matter is advected from the PNS surface sufficiently quickly that neutrino heating is suppressed and degeneracy is never completely lifted.

shows the electron fraction Y_e as a function of radius just above the PNS surface for a solution with $L_{\bar{\nu}_e,51} = 8, B_\nu = 10^{16}$ G, and $\Omega = 9000$ s^{-1} (rotation period $P \approx 0.7$ ms). This relatively high luminosity solution corresponds to a time ≈ 1 s after core bounce (see eq. [4.8]). Figure 4.3 also shows Y_e^ν and the equilibrium electron fraction $Y_e^{\rm eq}$ obtained by setting the time derivative on the left hand side of equation (4.14) equal to zero. The right panel of Figure 4.3 shows the individual rates in the wind that determine the evolution of Y_e: electron absorption (eq. [4.2], *dotted line*), positron absorption (eq. [4.3], *dashed line*), electron neutrino absorption (eq. [4.4], *triple − dot − dashed line*), electron antineutrino absorption (eq. [4.5]; *solid line*), and the wind's advection rate $\lambda_{\rm adv} \equiv v_r/r$ (*dot − dashed line*). The slight difference between the neutrino and antineutrino absorption rates at large radii, although difficult to discern on the scale of this plot, implies that $Y_e^\nu \simeq 0.48$ for this solution.

Figure 4.3 shows that the electron fraction at the base of the outflow is very neutron-rich ($Y_e^0 \approx 0.05$). This results from the equilibrium established between the electron and electron neutrino capture rates (*dotted* and *triple − dot − dashed lines*, respectively) under the degenerate surface conditions ($\rho_\nu \approx 10^{12}$ g cm^{-3}, $\mathrm{T}_\nu \approx 4.2$ MeV $\ll 14$ MeV $\approx \mu_e$, where μ_e is the electron chemical potential at the neutrinosphere), which strongly suppresses the thermal positron population relative to electrons. Thus our value of Y_e^0 is significantly larger than the pure pair-capture equilibrium value given in Figure 1 of B03a because we have included neutrino absorptions; for vanishing neutrino luminosity, however, the results of B03a Figure 1 would obtain. Indeed, for solutions with lower $L_{\bar{\nu}_e} = 1.3 L_{\nu_e}$ electron neutrino absorption becomes less important and Y_e^0 decreases (see Table 4.3).

As matter accelerates off of the PNS surface, Figure 4.3 shows that Y_e rises above Y_e^0. Because the wind initially moves slowly relative to the relevant weak interaction rates, at small radii Y_e remains in approximate equilibrium at the value $Y_e \approx Y_e^{\rm eq} < Y_e^\nu$. However, as magnetocentrifugal slinging accelerates matter away from the PNS surface, $\lambda_{\rm adv} = v_r/r$ also rises rapidly, eclipsing the weak interaction rates by $r \approx 12$ km. At this point Y_e "freezes out" at a value $Y_e^a \simeq 0.19$; this occurs before neutrino absorptions dominate the electron capture rates (which is

why $Y_e \approx Y_e^{\rm eq}$ is still relatively low).

4.4.3 Conditions for Neutron-Rich Outflows from Proto-Magnetars

The mass-loss rate for purely thermal, neutrino-driven PNS winds $\dot{M}_{\rm th}$ can be derived analytically by requiring that the energy used to unbind a typical nucleon $E_B = GMm_{\rm n}/R_\nu$ be supplied entirely by the neutrino heating $Q_\nu \equiv \int_{R_\nu}^{\infty} \dot{q}_\nu dr/v_r$ that a nucleon experiences in accelerating from the PNS surface to large radii (QW96), where $\dot{q}_\nu$ is the net neutrino heating rate per baryon, which is dominated by neutrino absorption (eqs. [4.4]−[4.5]). By repeating this derivation but instead requiring that $Q_\nu \lesssim \langle\epsilon_\nu\rangle$ (see §4.2) we obtain the minimum mass-loss rate that must accompany a neutron excess over the neutrino-driven value

$$\frac{\dot{M}}{\dot{M}_{\rm th}} \gtrsim \phi_{\rm n} \equiv \frac{GMm_{\rm n}}{R_\nu \langle\epsilon_\nu\rangle} \approx 20 M_{1.4} \langle\epsilon_{\bar{\nu}_e,10}\rangle^{-1} R_{10}^{-1}, \tag{4.18}$$

where (QW96)

$$\dot{M}_{\rm th} \approx 10^{-6} L_{\bar{\nu}_e,51}^{5/3} \langle\epsilon_{\bar{\nu}_e,10}\rangle^{10/3} M_{1.4}^{-2} R_{10}^{5/3}\, {\rm M}_\odot\, {\rm s}^{-1}, \tag{4.19}$$

$R_\nu = 10R_{10}\,{\rm km}$, $M = 1.4M_{1.4}M_\odot$, and $\langle\epsilon_\nu\rangle \approx \langle\epsilon_{\bar{\nu}_e}\rangle = 10\langle\epsilon_{\bar{\nu}_e,10}\rangle$ MeV. In our numerical calculations we have assumed that $L_\nu \propto \langle\epsilon_\nu\rangle^4$ so that $\dot{M}_{\rm th} \propto L_\nu^{5/2}$.

In Figure 4.4 we show $\dot{M}$ for the same wind solutions for which Y_e^a is shown in Figure 4.2. Figure 4.4 shows that $\dot{M}$ is substantially enhanced over its thermally-driven value $\dot{M}_{\rm th}$ in the presence of a strong magnetic field and rapid rotation. This enhanced mass-loss occurs because a strong magnetic field forces the outflow to corotate above the PNS surface and rapid corotation brings the wind's sonic radius $R_{\rm s}$ much closer to the surface, into the corotating region; this increases the hydrostatic scale height and the wind density at $R_{\rm s}$, thereby increasing $\dot{M}$. Because the magnetic field, as opposed to neutrinos, is primary responsible for unbinding matter from a rapidly rotating proto-magnetar, the outflow can have $\dot{M} > \dot{M}_{\rm th}\phi_{\rm n}$ and can thus remain neutron-rich. Indeed, Figure 4.4 shows that $\dot{M}$

increases exponentially with Ω and a comparison with Figure 4.2 shows that Y_e^a first noticeably decreases below Y_e^ν once equation (4.18) is satisfied.

Figure 4.4 also shows that for modest magnetic field strengths $\dot{M}$ increases with increasing B_ν, but that for sufficiently large B_ν, $\dot{M}$ saturates to a value $\dot{M}_{\rm cf}$ in the "centrifugal limit" (e.g., Lamers & Cassinelli 1999). For $\Omega \approx \Omega_{\rm n}$ (or, equivalently, $Y_e^a \approx 0.25$) we find that

$$\dot{M}_{\rm cf}(\Omega_{\rm n}) \approx 6 \times 10^{-2} (L_{\bar{\nu}_e,51}/8)^{2.2} M_\odot \, {\rm s}^{-1}, \tag{4.20}$$

which is over an order of magnitude greater than the mass-loss required, $\dot{M}_{\rm th}\phi_{\rm n} \approx 3 \times 10^{-3} (L_{\bar{\nu}_e,51}/8)^{2.25} M_\odot \ s^{-1}$ (eq. [4.18]), for just a mild neutron excess relative to the neutrino-driven value (i.e., $Y_e^a \lesssim Y_e^\nu$).

Figures 4.2 and 4.4 show that at fixed Ω, $\dot{M} \rightarrow \dot{M}_{\rm cf}$ and $Y_e^a \rightarrow Y_e^{a,{\rm sat}}$ (eq. [4.16]) for similar magnetic field strengths. To understand why this occurs note that the requirement for fully centrifugally-enhanced mass-loss is that the magnetic field must be sufficiently strong to enforce corotation beyond the radius where $\dot{M}$ is set; because a wind approximately corotates to its Alfvén radius R_A and its mass-loss rate is set at its sonic radius $R_{\rm s}$ the condition for $\dot{M} \rightarrow \dot{M}_{\rm cf}$ is that $R_A \gtrsim R_{\rm s}$. In analogy, because Y_e^a obtains near the PNS surface (see Fig. 4.3), the condition for $Y_e^a \rightarrow Y_e^{a,{\rm sat}}$ is that $R_A \gtrsim R_\nu$. In the centrifugal limit the sonic radius for an equatorial wind is given by $R_{\rm s} = (GM/\Omega^2)^{1/3}$ (e.g., Lamers & Cassinelli 1999), so that $R_{\rm s}(\Omega_{\rm n}) \approx 13$ km $\sim R_\nu$. Thus the conditions for fully enhanced mass-loss and fully enhanced neutron-richness are approximately the same because the sonic radius is close to the PNS surface for the near break-up rotation rates required to produce neutron-rich outflow.

Finally, although we have focused on equatorial proto-magnetar winds, the properties of the outflow will vary with latitude. In particular, $\dot{M}$ and Y_e^a will decrease and increase with increasing angle θ from the equator, respectively, approaching $\dot{M}_{\rm th}$ and Y_e^ν for nearly polar outflow ($\theta \rightarrow 90^\circ$) because of the reduced centrifugal acceleration along nearly vertical field lines ($\dot{M}$ and $\dot{M}_{\rm th}$ here are per solid angle). Thus, it may seem plausible that outflows driven from intermediate latitudes could maintain moderately low Y_e yet become significantly more rela-

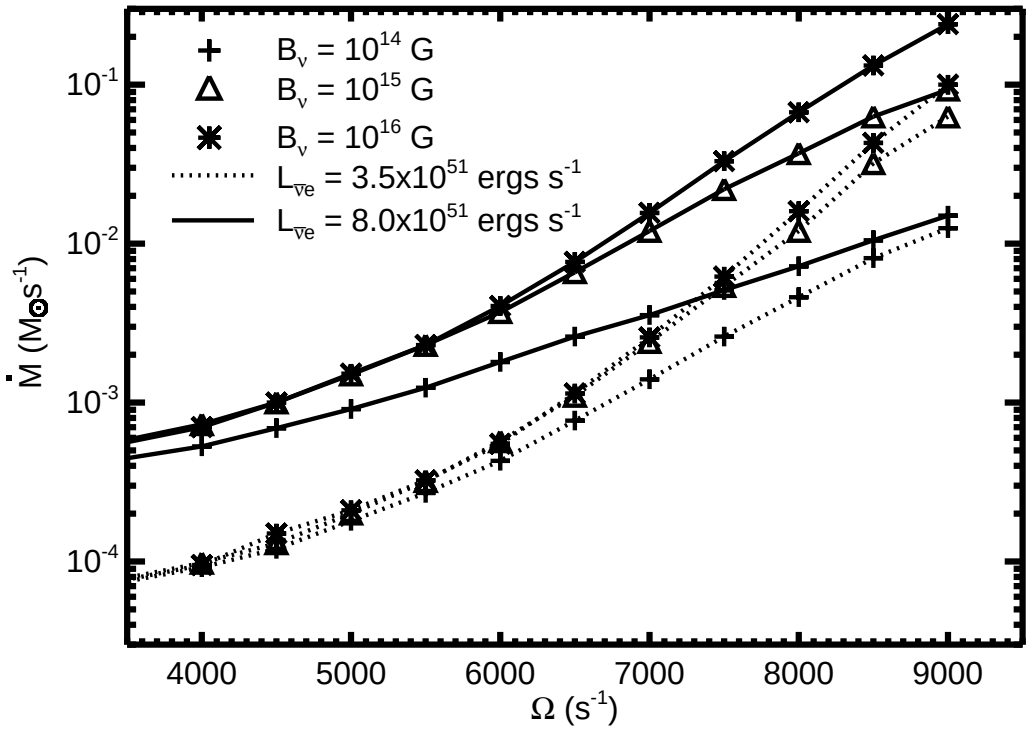

Figure 4.4: Mass-loss rate $\dot{M}$ for the same solutions for which Y_e^a is shown in Figure 4.2. Due to centrifugal slinging, $\dot{M}$ increases with B_ν and Ω and is substantially larger than its thermally-driven, non-rotating value, which is $\dot{M}_{\rm th} \approx 2 \times 10^{-4}(2 \times 10^{-5}) M_\odot$ s^{-1} for $L_{\bar{\nu}_e,51} = 8(3.5)$. By comparing $\dot{M}$ with Y_e^a in Figure 4.2 note that winds with large $\dot{M}$ have low Y_e^a; in particular, $\dot{M} \gtrsim \phi_{\rm n}\dot{M}_{\rm th} \approx 15 - 20\dot{M}_{\rm th}$ (eq. [4.18]) is required for Y_e^a to noticeably decrease below its neutrino-driven value Y_e^ν.

tivistic than matter driven from near the equator. Even high-latitude outflows, however, require $\dot{M} \gg \dot{M}_{\rm th}$ (eq. [4.18]) to attain $Y_e^a < Y_e^\nu$, making such a scenario unlikely, as we will show explicitly through NDAF disk wind calculations in §4.5. Furthermore, the limited solid angle occupied by such a hypothetical mid-latitude wind would preclude it from carrying a significant portion of the PNS's spin-down luminosity, which is primarily extracted by outflow originating near the equator (e.g., Bucciantini et al. 2006).

4.4.4 Implications for GRBs

We have shown that proto-magnetars born with $P < P_{\rm n} \approx 0.8$ ms produce energetic, neutron-rich winds; it therefore appears that the birth of very rapidly rotating proto-magnetars should produce neutron-rich GRBs. This is, however, not necessarily the case. Even strongly magnetized proto-magnetar winds are baryon-loaded at very early times following the launch of the SN shock because the PNS is very hot and its already substantial thermally-driven mass-loss is enhanced due to centrifugal slinging. In fact, a proto-magnetar requires several seconds to contract and cool to the point that a wind launched from its surface achieves the high magnetization $\sigma \gtrsim 10$–100 required to explain the Lorentz factors inferred from GRBs. By the time a proto-magnetar cools to the point that its wind becomes ultra-relativistic, it may no longer rotate sufficiently rapidly to remain neutron-rich.

In Figure 4.5 we explore this possibility quantitatively by showing the magnetization σ of a PNS's outflow (eq. [4.15]) as a function of the PNS rotation period P from evolutionary calculations of a cooling, spinning down proto-magnetar with an initial period $P_0 = 0.6$ ms $< P_{\rm n}$ and for three different fixed surface dipole magnetic field strengths:[7] $B_\nu^{\rm dip} = 10^{15}$ G, 3×10^{15} G, and 10^{16} G. These evolutionary

[7]The minimum stable neutron star rotation period $P_{\rm min}$ is uncertain theoretically because it depends on the uncertain supranuclear density equation of state (EOS); depending on the EOS, detailed studies find that $P_{\rm min} = 0.53 - 1.7$ ms for $M \simeq 1.4 M_\odot$ (Cook, Shapiro, & Teukolsky 1994, Table 8). Thus, although we take the specific value $P_0 = 0.6$ ms in our calculations

calculations, which are described in more detail in §2.4.1, assume a PNS cooling evolution similar to that given in equation (4.8) and map the one-dimensional neutrino-heated monopole wind calculations of Chapter 2 onto a more physical dipole geometry using the axisymmetric two-dimensional relativistic MHD calculations of Bucciantini et al. 2006 (hereafter B06). Although Figure 4.5 only shows calculations for one initial rotation period $P_0 = 0.6$ ms, the PNS's spin-down timescale is dominated by times at which it is slowly rotating; hence, the evolutionary tracks for PNSs born with $P_0 \lesssim 0.6$ ms are similar to those shown in Figure 4.5 for $P > 0.6$ ms, following a brief initial spin-down phase.

Figure 4.5 shows that PNSs born with $P < P_{\rm n}$ and $B_\nu^{\rm dip} \gtrsim 3 \times 10^{15}$ G spin down to a relatively neutron-poor state ($P > P_{\rm n}$) in just a few seconds, before cooling sufficiently to produce an ultra-relativistic ($\sigma \gg 1$) outflow; these proto-magnetars could therefore not produce neutron-rich GRBs. On the other hand, a PNS born with $B_\nu^{\rm dip} = 10^{15}$ G spins down more slowly and is thus capable of producing an ultra-relativistic, neutron-rich outflow $\sim 10 - 30$ seconds following core bounce. Of the proto-magnetar's initial rotational energy of $E_{\rm rot} \sim 6 \times 10^{52}$ ergs, a substantial portion ($\sim 2 \times 10^{52}$ ergs) is extracted when $\sigma < 10 - 100$; although this early wind is potentially too mass-loaded to produce a GRB, it may enhance the energy and alter the morphology of the accompanying SN shock (TCQ04; Chapter 2; Bucciantini et al. 2007a). The remaining $\sim 4 \times 10^{52}$ ergs, part of which could produce a neutron-rich GRB, emerges when $\sigma > 10 - 100$ on a somewhat longer spin-down timescale $\tau_{\rm J}$, which is $\sim 10^2 - 10^3$ s, depending on the fraction of the proto-magnetar's surface threaded by open magnetic flux (B06).

In §4.3 we emphasized the need for magnetic acceleration to produce neutron-rich outflows from compact objects. Despite the absence of magnetic fields, however, Dessart et al. (2006) find neutron-rich ($Y_e^a \sim 0.25$), purely neutrino-driven outflows in 2D radiation-hydrodynamical simulations of the very early evolution ($t \lesssim 800$ ms after core bounce) of a rapidly rotating neutron star newly-formed

to illustrate the conditions under which proto-magnetars can produce neutron-rich GRBs, if $P_{\rm min} > P_{\rm n} \approx 0.8$ ms the conclusions of this section are much simpler: proto-magnetars cannot produce neutron-rich outflow. Conversely, the detection of a neutron-rich GRB outflow from a confirmed magnetar birth would provide a constraint on the EOS.

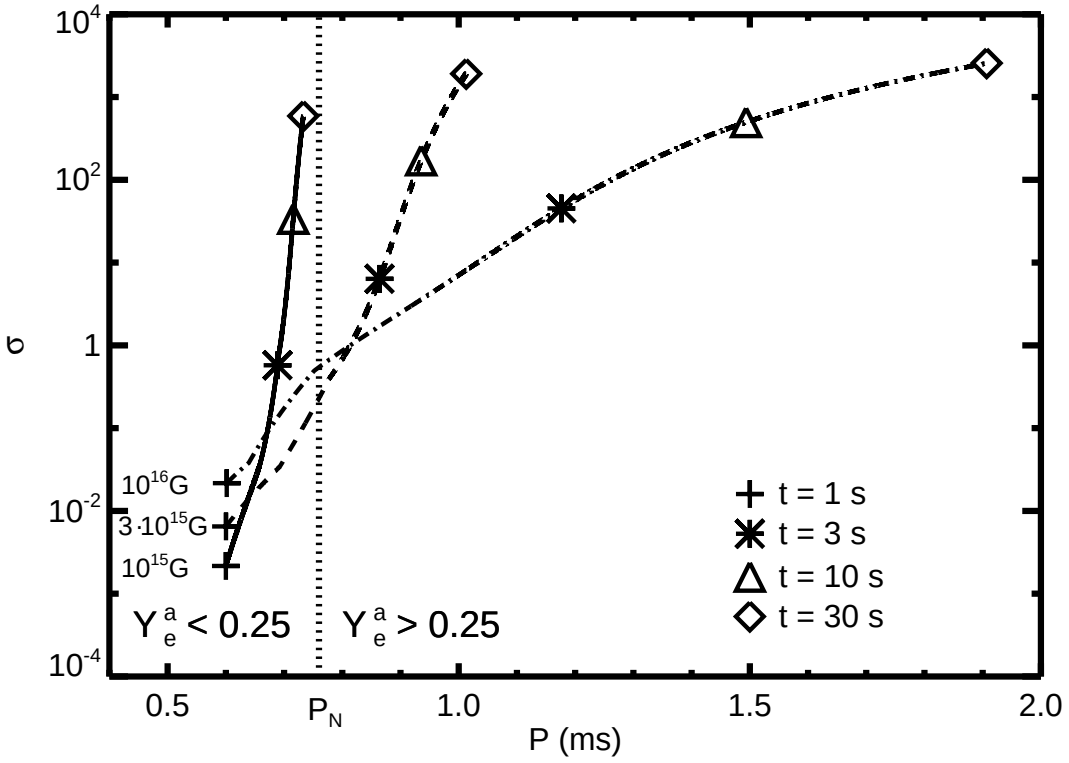

Figure 4.5: Magnetization σ of a PNS's outflow (eq. [4.15]) as a function of the PNS rotation period P from evolutionary spin-down calculations performed during the Kelvin-Helmholtz cooling of a proto-magnetar with initial rotation period $P_0 = 0.6$ ms at a time $t = 1$ s after core bounce and for different fixed surface dipole magnetic field strengths: $B_\nu^{\rm dip} = 10^{15}$ G, 3×10^{15} G, and 10^{16} G; for reference, times $t = 1$, 3, 10, and 30 seconds after core bounce are shown along the evolutionary tracks. So long as the rotation period of the proto-magnetar remains less than $P \sim P_{\rm n} \approx 0.8$ ms its outflow remains neutron-rich (see eq. [4.16]). The proto-magnetars with $B_\nu^{\rm dip} = 3 \times 10^{15}$ G and 10^{16} G spin-down to a relatively neutron-poor state in just a few seconds, before cooling sufficiently to produce $\sigma \gg 1$ outflows. In contrast, the proto-magnetar with $B_\nu^{\rm dip} = 10^{15}$ G spins down less rapidly, allowing the PNS to produce simultaneously neutron-rich and ultra-relativistic outflow $\sim 10 - 30$ s following core bounce.

following the accretion-induced collapse (AIC) of a white dwarf. Because these calculations show that very rapidly rotating PNSs can produce neutron-rich outflows without the aid of magnetic acceleration, it may appear that neutron-rich GRB outflows could be possible under less restrictive conditions than described in this section. The purely neutrino-driven neutron-rich outflows found by Dessart et al. (2006) are only possible, however, because at very early times following core bounce the PNS is inflated with respect to its final, cooled radius and because a PNS rotating near break-up is strongly oblately deformed. Because the equatorial neutrinosphere radius R_ν can therefore exceed ~ 100 km at early times (see Dessart et al. 2006, Fig. 7), the gravitational binding energy of a nucleon on the PNS surface at a moderately low latitude is $E_B \sim 10(R_\nu/100\,\mathrm{km})^{-1}$ MeV, comparable to the mean energy of the neutrinos driving the outflow (typically $\approx 10-15$ MeV during the PNS's early cooling phase). Thus, despite the fact that neutrino absorptions favor a $proton-rich$ composition ($Y_e^\nu > 0.5$) because the electron neutrino flux dominates the electron antineutrino flux during early deleptonization (especially in the presence of rapid rotation; Thompson, Quataert, & Burrows 2005), less than a single neutrino is required to unbind a typical nucleon (i.e., $\phi_\mathrm{n} \lesssim 1$; eq. [4.18]); matter driven from low latitudes can therefore partially retain the neutron-rich composition of the PNS surface. Although purely neutrino-driven neutron-rich outflows are thus possible from PNSs at *very early times* ($\lesssim 1$ s) after core bounce, as the PNS cools and its radius shrinks ϕ_n will increase; purely neutrino-driven neutron-rich outflows will therefore not be possible after a few seconds following core bounce, even if the PNS remains distorted by continuing to rotate near break-up. In particular, once the PNS has cooled and contracted sufficiently to produce a GRB outflow, neutron-rich winds will only be possible if they are magnetically-driven and satisfy the constraints described in this section.

4.5 Accretion Disk Winds

In this section we describe calculations of the structure and neutron content of axisymmetric, one-dimensional MHD winds launched from NDAFs. As

shown schematically in Figure 4.6, we perform our calculations along a spherical, monopole flux tube centered about the position "C" a distance $R_0 \tan\theta$ directly below the black hole along the disk rotation axis, where R_0 is the distance from the black hole to the wind's launching point just above the accretion disk midplane and $\theta \in [0°, 90°)$ is the angle that the flux tube makes with respect to the midplane. The distance from a given position "P" along the outflow to the black hole and monopole center are denoted r and s, respectively. The physical solid angle of the wind $\Delta\Omega$ is chosen such that the conserved mass outflow rate is given by $\dot{M} = \Delta\Omega \rho v_{\rm p} s^2 = 4\pi \rho_0 v_{\rm p,0} R_0^2$ so that $\Delta\Omega = 4\pi \cos^2\theta$, where $v_{\rm p}$ is the poloidal wind velocity, ρ is the wind's density, and '0' denotes quantities evaluated at the base of the outflow;[8] note that for equatorial outflow ($\theta = 0$) $\dot{M}$ reduces to the definition used in §4.4 for proto-magnetar winds. Although this choice for $\Delta\Omega$ is somewhat arbitrary, the quantities of most interest, σ and Y_e^a, do not depend on our normalization for $\dot{M}$.

As in the proto-magnetar case, we assume an open poloidal magnetic field $B_{\rm p} = B_0 (s_0/s)^2$, where $s_0 = R_0/\cos\theta$ and B_0 is the strength of the poloidal field at the outflow's base. As discussed by Levinson (2006), whose formulation and geometry are similar to ours, a more consistent approach would be to seek a self-similar solution to the trans-field equation (e.g., Li et al. 1992; Contopoulos 1994). However, simultaneously including the wind's slow point topology and consequent neutrino-heated mass-loss in such a formalism is difficult without multi-dimensional neutrino-heated MHD calculations, a formidable numerical challenge. In addition, the large-scale poloidal field threading NDAF disks is uncertain and so a more detailed calculation does not seem warranted.

As discussed in the proto-magnetar case, Y_e^a is generally determined fairly close to where the wind is launched near the disk midplane and so the precise radial scaling of $B_{\rm p}$ ($\propto s^{-2}$) is likely less important than its magnitude near the base of the wind $\approx B_0$. The properties of the wind, however, can depend strongly

[8] We use '0' to denote quantities at the base of the outflow instead of 'ν' (as was used in §4.4) because, unlike in the PNS case, the disk midplane can be neutrino transparent and therefore may not posses a neutrinosphere.

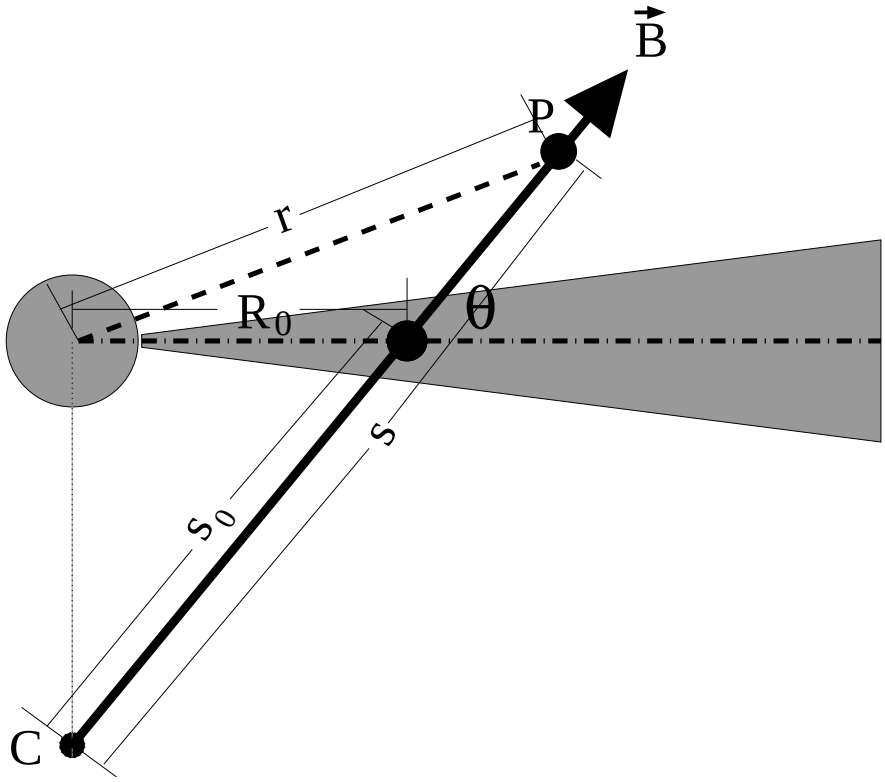

Figure 4.6: Geometry of NDAF disk winds. The wind is calculated along a flux tube that is inclined at an angle θ with respect to the accretion disk midplane. The calculation is started from a location just above the disk midplane a distance R_0 from the central black hole and at a distance s_0 from the monopole center (position "C"). A generic point "P" along the outflow is located at a distance r from the central black hole and a distance s from the monopole center.

on θ. In particular for $\theta < 60^\circ$ matter that co-rotates at the Keplerian orbital velocity which is perturbed from the disk along the field line is unstable and can escape to infinity, even without additional energy deposition (Blandford & Payne 1982). This results in significant mass-loading for field lines with $\theta < 60^\circ$; in addition, the field develops a substantial base toroidal component $B_{\phi,0}$. For $\theta < 60^\circ$, NDAF winds are therefore slow, heavily mass-loaded, have $B_{\phi,0} \gg B_0$, and possess properties that are relatively independent of θ. On the other hand, more vertical flux tubes ($60^\circ < \theta < 90^\circ$), which resemble equatorial proto-magnetar winds more than equatorial disk winds, have lower $\dot{M}$, accelerate to faster asymptotic speeds, and possess properties that depend sensitively on θ; in particular, the wind becomes increasing relativistic as $\theta \rightarrow 90^\circ$ (Daigne & Mochkovitch 2002), and ultra-relativistic outflows from nearly vertical field lines may be capable of producing GRBs.

In terms of B_0 and $\dot{M}$ the magnetization (eq. [4.13]) of an NDAF wind launched from radius R_0 is given by

$$\sigma = B_0^2 R_0^4 \Omega_{\rm K}^2 / \dot{M} c^3, \tag{4.21}$$

where we have assumed that the base of the outflow rotates at approximately the Keplerian rate $\Omega_{\rm K} = (GM/R_0^3)^{1/2}$. The rate of angular momentum lost through a non-relativistic ($\sigma < 1$) wind is given by $\dot{J}_W = \dot{M} R_A^2 \Omega_{\rm K}$, while for relativistic ($\sigma > 1$) winds $R_A \simeq R_{\rm L}$ and $\dot{J}_W \simeq \dot{E}_{\rm mag}/\Omega_{\rm K} \simeq \sigma \dot{M} c^2/\Omega_{\rm K}$, where $\dot{E}_{\rm mag}$ is the wind's energy-loss rate. The ratio of $\dot{J}_W$ to the disk's angular momentum-loss rate $\dot{J}_D = \dot{M}_D R_0^2 \Omega_{\rm K}$ is therefore given by

$$\begin{aligned} \frac{\dot{J}_W}{\dot{J}_D} &\simeq (\dot{M} R_A^2 / \dot{M}_D R_0^2) = (\dot{M} s_A^2 / \dot{M}_D s_0^2) : \sigma < 1 \\ &\simeq (B_0^2 R_0^2 / \dot{M}_D c) : \sigma > 1 \end{aligned} \tag{4.22}$$

Although a wind with $\dot{J}_W < \dot{J}_D$ is physical because stresses internal to the disk can transfer angular momentum outwards, allowing accretion at $\dot{M}_D$ to proceed, a wind for which $\dot{J}_W > \dot{J}_D$ is unphysical because it violates conservation of angular momentum.

4.5.1 Numerical Procedure

We calculate NDAF wind solutions starting from a location just above the accretion disk midplane at a fixed cylindrical radius $R_0 = 14R_g \approx 6 \times 10^6$ cm, which is roughly the location of the disk's peak neutrino flux. The wind's local neutrino luminosities and energies are determined from CB07's marginally neutrino optically thin $\dot{M}_D = 0.2M_\odot$ s^{-1}, $\alpha = 0.03$ NDAF solution. We focus on winds driven from low $\dot{M}_D$, neutrino transparent disks because low $\dot{M}_D$ accretion, due to its lower neutrino-driven mass-loss, is probably more likely to produce neutron-rich, ultra-relativistic outflow. When considering NDAFs with $\dot{M}_D < 0.2M_\odot$ s^{-1} (down to $\dot{M}_D \approx \dot{M}_{\rm ign}$; eq. [4.1]), we scale the boundary conditions and neutrino emission properties analytically from the $\dot{M}_D = 0.2M_\odot$ s^{-1} solution, as discussed below.

We use Newtonian gravity, including just the point mass of a $M = 3M_\odot$ black hole. This is a reasonable approximation because our calculation begins at a radius greater than twice the radius of the innermost stable circular orbit. The evolution equations for $v_{\rm p}$, v_ϕ, B_ϕ, ρ, and T are the same as those used in the PNS case with r replaced by s, except that the gravitational acceleration in the radial momentum equation (eq. [2.3]) is now the component projected along the field line:

$$g_s = \frac{GM(s - s_0 \sin^2\theta)}{(s^2 + \sin^2\theta[s_0^2 - 2ss_0])^{3/2}}. \tag{4.23}$$

Our microphysics is essentially identical to that in the PNS case. In particular, the electron fraction is evolved according to equation (4.14), again with r replaced by s; note that because of the disk's significantly lower density, degeneracy effects are less important near the base of the wind than in the PNS case. The electron and anti-electron neutrino energy fluxes ($F_{\nu_e}, F_{\bar{\nu}_e}$) used to calculate the neutrino absorption and heating rates near R_0 are computed from CB07's $\alpha-$disk solution in the same manner as the local neutrino energy densities that were used to calculate Y_e^ν for Figure 4.1; to within a factor of ~ 2 the total spherically-equivalent neutrino luminosity obeys $L_\nu = L_{\nu_e} + L_{\bar{\nu}_e} \equiv 4\pi R_0^2(F_{\nu_e} + F_{\bar{\nu}_e}) \approx \eta \dot{M}_D c^2$, where $\eta \approx 0.04$ is the total radiative efficiency for a non-rotating black hole from CB07. In a similar

manner as for PNSs, we take the neutrino flux intercepted by the outflow to be approximately constant with radius for $r \lesssim R_0$ and to decrease $\propto r^{-2}$ for $r \gtrsim R_0$ (T01 eq. [24]; see Surman & McLaughlin 2004, 2005 for a more detailed treatment). Although the geometry that we assume is simplistic, Y_e^a is set relatively close to the base of the wind and thus depends primarily on the neutrino energy density in the vicinity of R_0. Indeed, as Figure 4.3 illustrates, the advection and pair capture rates rise and fall above the base of the outflow, respectively, much more rapidly than the neutrino absorption rates decrease; this would likely remain true for any realistic geometry.

Unlike PNSs, NDAFs do not produce significant tau or muon neutrino emission and so annihilations and neutral-current interactions from these neutrino species are ignored. The mean electron and anti-electron neutrino energies near R_0, which are not expected to vary strongly with $\dot{M}_D$ for neutrino optically thin accretion (see eq. [4.9]), are taken from Figure 4.1 as $\langle \epsilon_{\nu_e} \rangle = 10.5$ MeV and $\langle \epsilon_{\bar{\nu}_e} \rangle = 13.1$ MeV; from CB07's solution we also determine that $F_{\bar{\nu}_e} \simeq 1.2 F_{\nu_e}$ near R_0 so that $Y_e^\nu \approx 0.51$ (see eq. [4.6] and Fig. 4.1). We set the wind's inner density ρ_0 equal to the disk midplane density ρ_D if the electron neutrino optical depth along s to the midplane is $\tau_\nu \lesssim \frac{2}{3}$; otherwise, we instead choose ρ_ν to enforce $\tau_\nu \simeq \frac{2}{3}$ at s_0.

Although viscous heating generally dominates neutrino heating in the midplane of NDAFs, recent radiation MHD simulations suggest that little energy is dissipated in the disk corona (Turner 2004; Hirose, Krolik, & Stone 2006; Blaes et al. 2006b; Krolik et al. 2006). For this reason, we neglect viscous heating in the wind entirely and set the base temperature T_0 of the wind by balancing neutrino cooling with just neutrino heating, as in the PNS case; note, however, that significant viscous heating in the wind would likely result in both additional mass-loss and deneutronization. The disk's midplane temperature T_D, which is set by the balance between viscous heating and neutrino cooling (see eqs. [4.9]−[4.10]), is therefore generally higher than T_0.

Although NDAFs are efficiently cooled and geometrically-thin, radial pressure support is not completely negligible and so the disk's angular rotation frequency Ω, which we use to set the wind's inner angular velocity, is slightly sub-Keplerian:

$\Omega^2 = \Omega_{\rm K}^2(1 - H^2/R_0^2)$, where $H \approx 0.2R_0$ is the disk scale height near R_0, which, like T_D, is approximately independent of $\dot{M}_D$ for neutrino optically thin accretion.

Our disk wind calculations can be compared with similar one-dimensional flux tube calculations by Daigne & Mochkovitch 2002 (DM02), Pruet et al. 2004 (P04), and Levinson 2006 (L06). DM02 calculated the requisite conditions for ultra-relativistic outflow from hyper-accreting disks, including neutrino heating and cooling and, in the neutrino optically thin case, a simplified viscous heating prescription. Because DM02 was primarily concerned with obtaining $\dot{M}$ as a function of disk conditions, they only considered wind conditions near the sonic point; in addition, DM02 assumed co-rotation rather than accounting for the magnetic field explicitly. L06 improved upon the calculations of DM02 by including the full equations of general relativistic MHD. Although L06 explored the effects of finite B_0, L06 concentrated, like DM02, on the sub-slow magnetosonic regime and his calculations did not capture the Alfvén or fast magnetosonic radii. Although this approach allowed L06 to calculate $\dot{M}$ as a function of the open magnetic flux and L_ν, the base toroidal field $B_{\phi,0}$ remained a free parameter in L06's formulation. Because $B_{\phi,0}$ is associated with the conserved magnetic induction it is fixed in our calculations by the fact that our steady-state winds pass smoothly through all three MHD critical points. L06 speculated on the potential deneutronization of magnetized NDAF winds by noting the similarity between the advection and relevant weak interaction rates; he did not, however, calculate the evolution of Y_e explicitly.

Finally, P04 investigated nucleosynthesis in collapsar disk winds by solving the equations of hydrodynamics and by evolving Y_e from the disk midplane. P04 included neutrino heating and viscous heating through an $\alpha-$prescription; although they neglected neutrino absorptions in evolving Y_e, they also argued for the generic deneutronization of thermally-driven winds. Although P04 did not include the effects of magnetic fields on the wind explicitly, their outflows were calculated along well-defined, vertically-directed flux tubes and were artificially forced to co-rotate outside the base of the wind, presumably to mimic the effect of a strong poloidal magnetic field. Our calculations are, to the best of our knowledge, the first to fully

calculate the effects of MHD on the evolution of Y_e in NDAF outflows and the first to capture all three MHD critical points.

4.5.2 Numerical Results

The solid lines in Figure 4.7 show calculations of the mass-loss rate $\dot{M}$, asymptotic electron fraction Y_e^a, magnetization σ (eq. [4.21]), and angular momentum-loss rate $\dot{J}_W$ compared to that required for accretion $\dot{J}_D$ (eq. [4.22]) for NDAF winds with base poloidal field $B_0 = 10^{13}$ G, 10^{14} G, and 10^{15} G as a function of flux tube angle θ for the $\dot{M}_D = 0.2\ M_\odot\ \mathrm{s}^{-1}$, $\alpha = 0.03$, $M = 3M_\odot$, $a = 0$ NDAF solution of CB07 (the solution on which Figure 4.1 was based). Because magnetic pressure at the base of the outflow exceeds the total thermal pressure in the midplane of the disk for $B_0 \gtrsim 2 \times 10^{15}$ G, fields much stronger than those we have considered in Figure 4.7 are probably unphysical because they could not be self-consistently anchored to the disk. Our disk wind calculations are summarized in Table 4.4.

Figure 4.7 shows that $\dot{M}$ is very large and relatively independent of θ for $\theta \lesssim 60^\circ$ but that for $\theta \gtrsim 60^\circ$ $\dot{M}$ decreases rapidly with increasing θ. The mass-loss rate also increases with increasing B_0, except for the largest angles, for which $\dot{M}$ saturates for sufficiently large B_0, no longer increasing with increasing B_0 (as in the PNS case; see Fig. 4.4). There is no similar saturation for smaller θ because the large values of $\dot{M}$ preclude the outflow from co-rotating out to the sonic point for physical B_0.[9]

Figure 4.7 also shows that although Y_e^a is relatively low (~ 0.3) for the high-B_0, low-θ wind solutions, all of the solutions in Figure 4.7 with $Y_e^a \ll Y_e^\nu \simeq 0.51$ are unphysical because they have $\dot{J}_W > \dot{J}_D$ and thus extract angular momentum at a rate exceeding that required for accretion through the disk from which the wind's boundary conditions were derived; in fact, invoking the criterion $\dot{J}_W < \dot{J}_D$

[9]Because the base of the wind rotates at a slightly sub-Keplerian rate due to radial pressure support in the disk, even for $\theta < 60^\circ$ mass-loss would saturate at $\dot{M} \approx 4\pi R_0^2 \rho_0 c_{s,0} \sim 10 - 100 M_\odot$ s^{-1} for sufficiently large B_0 ($\sim 10^{16}$ G; the co-rotating limit), where $c_{s,0} \sim 0.1$ c is the sound speed near the base of the outflow.

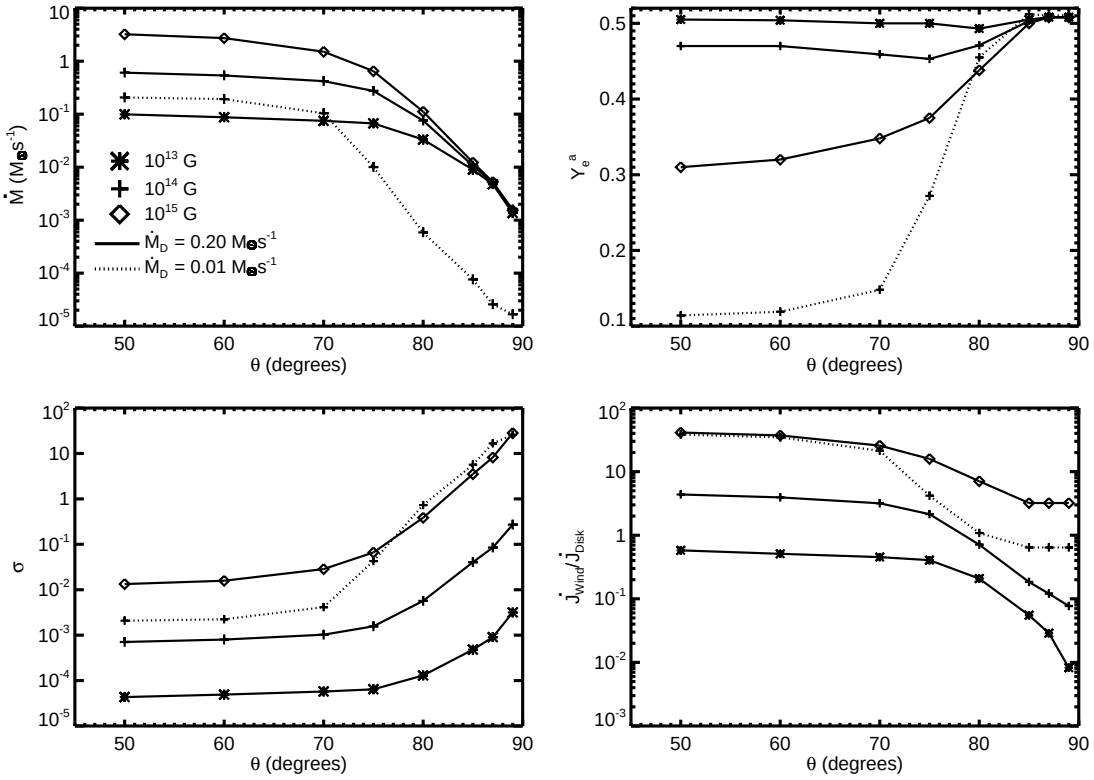

Figure 4.7: mass-loss-rate $\dot{M}$, asymptotic electron fraction Y_e^a, magnetization σ (eq. [4.21]), and the ratio of the wind to accretion angular momentum-loss rates $\dot{J}_W/\dot{J}_D$ (eq. [4.22]) for NDAF winds as a function of the angle θ between the wind's flux tube and the disk midplane (see Fig. 4.6); base poloidal magnetic field strengths $B_0 = 10^{13}$ G (*asterisk*), 10^{14} G (*cross*), and 10^{15} G (*diamond*) are considered. The solutions were calculated starting from a location just above the disk midplane at a radius $R_0 = 14R_g \approx 6 \times 10^6$ cm from the central $M = 3M_\odot$, non-rotating ($a = 0$) black hole and employed boundary conditions derived from the $\alpha-$disk NDAF solution of Chen & Beloborodov (2007) with $\alpha = 0.03$ and accretion rate $\dot{M}_D = 0.2M_\odot$ s^{-1} (*solid lines*). Also shown are wind solutions for $\dot{M}_D \approx 10^{-2}M_\odot$ s^{-1} and $B_0 = 10^{14}$ G. For $\theta \lesssim 60°$ the wind properties are relatively independent of θ while for $\theta \gtrsim 60°$, $\dot{M}$ decreases and σ increases rapidly with θ. For the most vertical field lines ($\theta \to 90°$), along which the outflow experiences minimal centrifugal support, $\dot{M}$ approaches its purely thermal, neutrino-driven value $\dot{M}_{\rm th}$ (eq. [4.24]). Of the solutions shown, only those with $\dot{J}_W/\dot{J}_D < 1$ are physical. All of the physical solutions for $\dot{M}_D = 0.2M_\odot$ s^{-1} are non-relativistic ($\sigma < 1$) and do not possess an asymptotic neutron excess ($Y_e^a \approx Y_e^\nu \simeq 0.51$). Winds from the $\dot{M}_D = 10^{-2}M_\odot$ s^{-1} NDAF have lower $\dot{M}$ and larger σ than the winds driven from the higher $\dot{M}_D$ disk; however, the solutions for $\dot{M}_D = 10^{-2}M_\odot$ s^{-1} with $\dot{J}_W < \dot{J}_D$ still have $Y_e^a \sim 0.5$.

(see eq. [4.22]), the only physical solutions in Figure 4.7 are those with $B_0 = 10^{13}$ G for all θ and $B_0 = 10^{14}$ G for $\theta \gtrsim 80°$. Also note from Figure 4.7 that, in addition to having $Y_e^a \sim 0.5$, all of the physical solutions for $\dot{M}_D = 0.2 M_\odot$ s^{-1} are non-relativistic ($\sigma < 1$). Because our calculations have thoroughly spanned the physical parameter space of B_0 and θ, this conclusion is robust, at least for $\dot{M}_D = 0.2 M_\odot$ s^{-1}.

For lower $\dot{M}_D$ the deneutronizing neutrino luminosity and neutrino-driven mass-loss rate are lower and thus relativistic, neutron-rich outflow may be more likely. To explore this possibility we have also calculated wind solutions for outflows driven from an NDAF with $\dot{M}_D = 10^{-2} M_\odot$ s^{-1} $\simeq \dot{M}_{\rm ign}(\alpha = 0.03)$, keeping the other parameters identical to those of the higher $\dot{M}_D$ case ($\alpha = 0.03$, $M = 3M_\odot$, $R_0 = 14 R_g$). To compute these low $\dot{M}_D$ solutions we decreased the neutrino fluxes by a factor of 20 from our $\dot{M}_D = 0.2 M_\odot$ s^{-1} calculation, left the mean neutrino energies unchanged (they are not expected to vary strongly with $\dot{M}_D$; see eq. [4.9]), and decreased the disk midplane density $\rho_0 \sim \rho_D \propto \dot{M}_D$. We only calculated solutions with $B_0 \lesssim 3 \times 10^{14}$ G because for larger field strengths the magnetic pressure would exceed the thermal pressure in the disk.

In Figure 4.7 we show the $\dot{M}_D = 10^{-2} M_\odot$ s^{-1} calculations for $B_0 = 10^{14}$ G with a dotted line for comparison with the higher $\dot{M}_D$ solutions. Although the properties of these low $\dot{M}_D$ winds and their dependence on θ qualitatively resemble the higher $\dot{M}_D$ solutions, Y_e^a and $\dot{M}$ are generally lower and σ is higher than for the winds driven from the more neutrino-luminous disk. Most notably, the high-θ solutions are now both physical ($\dot{J}_W < \dot{J}_D$) and relativistic ($\sigma > 1$), illustrating that nearly vertically-directed outflows from low-$\dot{M}_D$ NDAFs represent plausible GRB central engines. However, these high-θ, relativistic winds still possess no significant neutron excess ($Y_e^a \sim 0.5$); this means that, even for $\dot{M}_D \approx \dot{M}_{\rm ign}$, simultaneously neutron-rich and ultra-relativistic outflow appears unlikely. One might think that $\dot{M}_D$ (and hence L_ν) could be lowered further until neutron-rich, ultra-relativistic outflow was possible at some intermediate latitude; a key difference, however, between the NDAF problem considered here and the PNS problem considered in §4.4 is that, unlike in the PNS case, the disk's neutrino

luminosity cannot be decreased below $L_{\nu,\rm ign} = \eta \dot{M}_{\rm ign}(\alpha = 0.03)c^2 \sim 10^{51}$ ergs s^{-1} (eq. [4.7]). For $\dot{M}_D < \dot{M}_{\rm ign}$ the disk is geometrically thick, and the midplane is not necessarily degenerate and neutron-rich (see §4.5.5).

4.5.3 Analytic Constraints

As in the PNS case, the purely thermal, neutrino-driven mass-loss rate from NDAFs can be estimated analytically by requiring that the energy used to unbind a typical nucleon E_B be supplied entirely by neutrino heating; equation (4.19) can therefore also be used to estimate $\dot{M}_{\rm th}$ for NDAF disk winds, provided that $R_\nu \rightarrow R_0$, $\langle \epsilon_\nu \rangle$ is taken from equations (4.9) and (4.10), and that, as discussed below, we include the effects of the lower effective gravity $g_{\rm eff}$ near the base of the outflow than in the PNS case. For neutrino optically thin accretion we find that $\dot{M}_{\rm th}$ for NDAFs is given by

$$\dot{M}_{\rm th} \approx 10^{-3} \left(\frac{\dot{M}_D}{\dot{M}_{\rm ign}}\right)^{5/3} \left(\frac{g_{\rm eff}/(GM/R_0^2)}{H/R_0}\right)^{-1} M_3^{119/90} \alpha_{0.1}^{301/90} \left(\frac{R_{\rm p}}{6R_g}\right)^{-1} \left(\frac{R_0}{6R_g}\right)^{79/60} M_\odot \text{ s}^{-1} \quad (4.24)$$

where we have used equation (4.7) to scale the neutrino luminosity to the value $L_{\nu,\rm ign}$ associated with the ignition accretion rate $\dot{M}_{\rm ign}$ (eq. [4.1]) because NDAFs only exist for $\dot{M}_D > \dot{M}_{\rm ign}$.

The purely neutrino-driven mass-loss rate for PNSs (eq. [4.19]) was derived for outflows emerging antiparallel to the PNS's gravitational field and by assuming substantially sub-break-up rotation. NDAF winds, however, are driven from the disk midplane at an angle inclined with respect to the black hole's gravitational field (i.e., $\theta \neq 0$) and even non-magnetized centrifugal support can be important near the base of the outflow because the disk rotates at nearly the Keplerian rate. This means that the effective surface gravity $g_{\rm eff}(\theta)$, which is the difference between the gravitational acceleration inward along s ($g_s(\theta)$; eq. [4.23]) and the centrifugal acceleration outward along s (v_ϕ^2/s), is always less than the gravitational acceleration for purely equatorial outflow ($g_s(\theta = 0) = GM/R_0^2$) that was used to

derive $\dot{M}_{\rm th}$ for PNSs. Assuming that the wind conserves angular momentum away from s_0 (i.e., $v_\phi = \Omega R_0 (s/s_0)^{-1}$) and concentrating on the wind's inner, quasi-hydrostatic atmosphere, we find that $g_{\rm eff}/(GM/R_0^2)$ is roughly constant with θ and is approximately equal to $(H/R_0) \approx 0.3 \alpha_{0.1}^{1/10} M_3^{-1/10} (R_0/6R_g)^{7/20}$, where H is the NDAF's vertical scale height near R_0; this calculation justifies our characteristic scaling for $g_{\rm eff}$ in equation (4.24).

Although equation (4.24) represents the thermal, neutrino-driven mass-loss rate from an NDAF, only the nearly-vertical, $\theta = 89^\circ$ wind solutions shown in Figure 4.7 (which experience minimal centrifugal support) in fact reach $\dot{M} \sim \dot{M}_{\rm th}$. Thus, equation (4.24) should be taken as the absolute *minimum* NDAF mass-loss rate; in the presence of even a modest magnetic field with a non-vertical inclination, $\dot{M}$ is significantly larger that $\dot{M}_{\rm th}$. Because NDAFs possess an absolute minimum mass-loss rate, their outflows also posses an absolute maximum magnetization $\sigma_{\rm max}$, which is given by

$$\sigma_{\rm max} = \frac{B_0^2 \Omega_{\rm K}^2 R_0^4}{\dot{M}_{\rm th} c^3} \approx 10 (\alpha\beta_\phi)^{-1} \left(\frac{\beta_\phi}{\beta_{\rm p}}\right) \left(\frac{\dot{M}_D}{\dot{M}_{\rm ign}}\right)^{-2/3} \left(\frac{g_{\rm eff}/(GM/R_0^2)}{H/R_0}\right) \times M_3^{1/9} \alpha_{0.1}^{-16/9} \left(\frac{R_{\rm p}}{6R_g}\right)^{23/20} \left(\frac{R_0}{6R_g}\right)^{-199/60}, \quad (4.25)$$

where $\beta_{\rm p}$ is the ratio of the disk's midplane thermal pressure P_D to the magnetic pressure associated with the wind's base poloidal field $B_0^2/8\pi$ and β_ϕ is similarly defined for the disk's midplane toroidal magnetic field $B_{\phi,D}$. In equation (4.25) we have written $\sigma_{\rm max}$ in terms of $(\alpha\beta_\phi)^{-1}$ because for angular momentum transport via the MRI, local shearing box simulations find that $\alpha\beta_\phi \sim 1$ (Hawley, Gammie, & Balbus 1995); we also write equation (4.25) in terms of $\beta_\phi/\beta_{\rm p} = B_0^2/B_{\phi,D}^2$ because if the open poloidal field is generated through a dynamo from the toroidal field this ratio is unlikely to exceed unity (and is probably much less).

Equation (4.25) shows that $\sigma_{\rm max} \propto \dot{M}_D^{-2/3}$, which explains why the low $\dot{M}_D$ solutions in Figure 4.7 produced more relativistic outflows than the high $\dot{M}_D$ solutions under the physical constraint $\beta_{\rm p} > 1$ that we imposed on our calculations. Equation (4.25) also shows that NDAFs can, in principle, produce ultra-relativistic ($\sigma \gg 10^2 - 10^3$) outflows from small radii ($R_0 \sim R_{\rm isco}$), provided that a significant

fraction of the magnetic energy present in the disk is associated with a large-scale, open poloidal field (i.e., $\beta_{\rm p} \sim \beta_{\rm t}$). For $\alpha = 0.1$, $M = 3M_\odot$, $\beta_{\rm p} = \beta_\phi$, $\alpha\beta_\phi = 1$, and for accretion onto a rapidly rotating black hole (so that $R_0 \approx R_{\rm p} \approx 2R_g$) equation (4.25) gives $\sigma_{\rm max} \approx 10^2(\dot{M}_D/\dot{M}_{\rm ign})^{-2/3}$. In this case ultra-relativistic outflow could occur for $\dot{M}_D \sim \dot{M}_{\rm ign}$ and could thus accompany a substantial accretion power $\dot{E}_{\rm acc} \equiv \eta\dot{M}_D c^2 \sim \eta\dot{M}_{\rm ign}(\alpha = 0.1)c^2 \sim 10^{51}$ ergs s^{-1}. Because $\dot{E}_{\rm acc}$ represents the maximum MHD luminosity of a GRB-producing jet, this shows that, under ideal conditions, disk winds from NDAFs form plausible GRB central engines.

Equation (4.25) shows that under some circumstances ultra-relativistic outflow from NDAF disks is plausible. However, the maximum magnetization for material with a *neutron excess* $\sigma^{\rm n}_{\rm max}$ is lower than $\sigma_{\rm max}$ because the minimum mass-loss rate that must accompany a neutron excess is substantially larger than $\dot{M}_{\rm th}$ according to the same arguments that were used in §4.4.3 for the PNS case; indeed, using equation (4.25) and the NDAF analog of equation (4.18) we find that

$$\sigma^{\rm n}_{\rm max} \equiv \frac{\sigma_{\rm max}\langle\epsilon_\nu\rangle 2R_0}{GMm_{\rm n}} \approx 2(\alpha\beta_\phi)^{-1}\left(\frac{\beta_\phi}{\beta_{\rm p}}\right)\left(\frac{\dot{M}_D}{\dot{M}_{\rm ign}}\right)^{-2/3}\left(\frac{g_{\rm eff}/(GM/R_0^2)}{H/R_0}\right) \times M_3^{-4/45}\alpha_{0.1}^{-71/45}\left(\frac{R_{\rm p}}{6R_g}\right)^{17/20}\left(\frac{R_0}{6R_g}\right)^{-139/60}. \quad (4.26)$$

Equation (4.26) shows that neutron-rich, relativistic outflow is very unlikely from NDAF disks. For $\dot{M}_D = \dot{M}_{\rm ign}$, $\alpha = 0.1$, $M = 3M_\odot$, $\beta_{\rm p} = \beta_\phi$, $\alpha\beta_\phi = 1$, and for outflow launched from near $R_{\rm isco}$ of a rapidly spinning black hole ($R_0 = R_{\rm p} = 2R_g$), equation (4.26) gives $\sigma^{\rm n}_{\rm max} \sim 10$, insufficient to explain the ultra-relativistic outflows inferred from GRBs.

If the fiducial scalings of equation (4.26) are not adopted, ultra-relativistic outflow with a neutron excess may be possible in some circumstances. For instance, if $\alpha = 0.01$ instead of $\alpha = 0.1$ (again for $\dot{M}_D = \dot{M}_{\rm ign}$, $M = 3M_\odot$, $\beta_{\rm p} = \beta_\phi$, $\alpha\beta_\phi = 1$, $R_0 = R_{\rm p} = 2R_g$) then $\sigma^{\rm n}_{\rm max} \sim 10^2 - 10^3$. In this case, however, $\dot{E}_{\rm acc}(\alpha = 0.01) \sim 10^{50}(\dot{M}_D/\dot{M}_{\rm ign})$ ergs s^{-1} and so a very large fraction of the accretion energy would need to be deposited in the ultra-relativistic outflow to explain the observed luminosities of GRBs. Likewise, although $\alpha\beta_{\rm p} \ll 1$ is

possible if the poloidal field threading the disk is not the result of a local dynamo (instead resulting from, e.g., magnetic flux advected from large radii in the disk; e.g., Spruit & Uzdensky 2005), the constraint $\dot{J}_W < \dot{J}_D$ (eq. [4.22]) independently requires that $\alpha\beta_{\rm p} \gtrsim 2/3(R_0/R_g)^{-1/2}(R_0/H) \approx 4\alpha_{0.1}^{-1/10}M_3^{1/10}(R_0/R_g)^{-17/20}$; thus, outflow launched from near $R_{\rm isco}$ must have $\beta_{\rm p}\alpha \gtrsim 1$ because otherwise it would carry away angular momentum at a rate exceeding that required for matter to accrete at the rate $\dot{M}_D$. Lastly, we reiterate that the true thermally-driven mass-loss rate can, in principle, far exceed the purely neutrino-driven value $\dot{M}_{\rm th}$ (eq. [4.24]) if viscous heating is important near the base of the wind; if this were the case, $\sigma^{\rm n}_{\rm max}$ would be substantially reduced below the value given by equation (4.26). We thus conclude that neutron-rich GRB outflows are unlikely from NDAF disk winds.

4.5.4 Cross-Field Neutron Diffusion

In the previous section we have argued that highly relativistic ($\sigma \gtrsim 100-1000$) winds driven from the innermost radii of NDAFs are unlikely to be intrinsically neutron-rich. However, free neutrons are uncharged and may collisionally diffuse across magnetic field lines to the polar region (hereafter, the "jet") from an adjacent, more baryon-rich wind (Eichler & Levinson 1999; Levinson & Eichler 2003, hereafter LE03; McKinney 2005b). If the total neutron mass diffusion rate $\dot{M}^{\rm diff}_{\rm n}$ dominates the mass-loading of the polar jet then the highly relativistic polar outflow will be significantly "polluted" by neutrons and may end up neutron-rich after all.

Neutron diffusion into the polar jet from the adjacent mass-loaded wind is limited to a surface area $\sim 4\pi s_\alpha^2\varphi$, where s_α is the distance from the base of the wind to where free nucleons recombine into $\alpha-$particles (which are charged and therefore cannot efficiently diffuse across field lines) and we have assumed that $s_\alpha \gg R_0/\varphi$, where $\varphi = \pi/2 - \theta \ll 1$ is the opening angle of the jet. Neutron diffusion is limited by elastic proton collisions, with a rate $\langle\sigma_{\rm n-p}v_{\rm rel}\rangle \simeq 10^{-15}$ cm^3 s^{-1} and a corresponding mean free path $\lambda_{\rm n-p} \simeq v_{\rm th}/(n_{\rm p}\langle\sigma_{\rm n-p}v_{\rm rel}\rangle)$, where $n_{\rm p}$ and $v_{\rm th} \approx (kT/m_{\rm n})^{1/2}$ are the proton number density and the ion thermal speed,

respectively. Following LE03, we assume that the density gradient length scale separating the mass-loaded wind and the axial jet is given by $l \sim (v_{\rm th}\tau_{\rm dyn}\lambda_{\rm n-p})^{1/2}$, where $\tau_{\rm dyn} \equiv s/v_{\rm p}$ is the wind's dynamical timescale.[10] Using the number flux of neutrons diffusing into the jet of $F_{\rm n} \approx n_{\rm n} v_{\rm th}(\lambda_{\rm n-p}/l)$, we estimate that

$$\dot{M}_{\rm n}^{\rm diff} \sim 4\pi\varphi s_\alpha^2 m_{\rm n} F_{\rm n}|_{s_\alpha} = \left(\frac{4\pi s_\alpha k T_\alpha \dot{M}}{\langle\sigma_{\rm n-p} v_{\rm rel}\rangle}\right)^{1/2}$$
$$\sim 10^{-8}\left(\frac{kT_\alpha}{\rm MeV}\right)^{1/2}\left(\frac{s_\alpha}{10^8\ {\rm cm}}\right)^{1/2}\left(\frac{\dot{M}}{0.1 M_\odot\ {\rm s}^{-1}}\right)^{1/2} M_\odot {\rm s}^{-1} \tag{4.27}$$

where $\dot{M} \approx 4\pi\varphi^2 m_{\rm n} v_{\rm p}(n_{\rm p} + n_{\rm n})s^2$, $n_{\rm n}$, and $T_\alpha \equiv T(s_\alpha)$ are the wind's mass-loss rate, neutron number density, and temperature at $\alpha-$particle recombination, respectively, and we have assumed that $Y_e \simeq 0.5$ in the wind. We evaluate equation (4.27) at s_α because $\dot{M}_{\rm n}^{\rm diff}$ is dominated by the largest radii at which the wind is still primarily free nucleons.

For the relatively moderate entropies ($S^a \lesssim 10^2$ k$_B$ baryon^{-1}) that characterize neutrino-heated, magnetocentrifugally-driven winds (see Tables 4.3 and 4.4), $\alpha-$particles form at a high temperature ($T_\alpha \sim 1$ MeV), which obtains relatively close to the base of the wind ($s_\alpha \lesssim 10^7$ cm). In this case, even for $\dot{M} \sim M_\odot$ s^{-1}, equation (4.27) gives $\dot{M}_{\rm n}^{\rm diff} \lesssim 10^{-8} M_\odot$ s^{-1}. If the axial jet is itself driven from the disk, $\dot{M}_{\rm n}^{\rm diff}$ is thus significantly lower than the minimum mass-loss already supplied by neutrino heating (eq. [4.24]); hence, cross-field neutron diffusion is ineffective at segregating neutrons in low entropy NDAF winds.

If, on the other hand, the axial jet is powered by $\nu - \bar{\nu}$ annihilation or the Blandford-Znajek process and has little or no intrinsic baryon-loading (such as if it threads the black hole's event horizon), then $\dot{M}_{\rm n}^{\rm diff}$, although small, may dominate the mass loading of the jet. For instance, for a polar jet power of $\dot{E} \sim 10^{50} - 10^{51}$

[10] This choice for l is appropriate for a very abrupt transition in the wind's density with cylindrical radius, such as between field lines threading the disk and those threading the black hole's event horizon. A perhaps more natural (but less conservative) choice for l is the cylindrical radius in the wind at $\alpha-$particle recombination ($\approx \varphi s_\alpha$), which would produce an even smaller $\dot{M}_{\rm n}^{\rm diff}$ than is given in equation (4.27).

erg s^{-1} equation (4.27) shows that diffusive neutron mass-loading from an encasing wind with a mass-loss rate $\dot{M} \sim 10^{-2} M_{\odot}$ s^{-1} would, by itself, limit the jet's asymptotic Lorentz factor to $\Gamma \sim 10^4 - 10^5$. Asymptotically neutron-rich outflow may result in this case if the jet remains "clean" to large radii; elucidating the observable consequences of such very high-Γ neutron-rich outflows will, however, require additional work. Lastly, we note that although our calculations show that NDAF winds probably possess moderate entropy, previous works that have considered diffusion into the jet have focused on very high entropy outflows characteristic of hydrodynamic "fireballs" in the GRB literature (LE03; McKinney 2005b). These calculations find larger $\dot{M}_{\rm n}^{\rm diff}$ than we have estimated in equation (4.27) in large part because $\alpha-$particles do not form until much larger radii in high entropy winds. Furthermore, if $Y_e^a \lesssim 0.5$ in the encasing baryon-rich wind and some neutrons remain free to radii larger than s_α, $\dot{M}_{\rm n}^{\rm diff}$ may be larger than predicted by equation (4.27). Evaluating the free neutron fraction that remains in magnetically-driven disk winds following the freeze-out of any α-process or r-process capture that may occur following $\alpha-$particle recombination is, however, beyond the scope of this paper.

4.5.5 Thick Accretion Disk Winds

For both proto-magnetars, where $L_\nu \propto t^{-1}$ starting $\sim$ 1 s following core bounce (eq. [4.8]), and NDAFs, where $L_\nu \propto \dot{M}_D \propto t^{-5/3}$ is expected at late times from "fall-back" accretion (Chevalier 1989; Woosley & Weaver 1995) or $\dot{M}_D \propto t^{-\alpha}$ with $\alpha \sim 1$ due to the viscous evolution of a disk of finite mass, the low neutrino luminosities attained at late times are the most favorable for ultra-relativistic, neutron-rich outflows. However, while proto-magnetars must maintain sub-millisecond rotation for most of the Kelvin-Helmholtz cooling epoch to produce late-time neutron-rich GRB outflows, for NDAFs, which always rotate at nearly the Keplerian rate, the difficulty is more fundamental; for $L_\nu \lesssim L_{\nu,\rm ign}$ (eq. [4.7]) the disk is no longer efficiently cooled and the disk midplane may no longer remain dense, degenerate, and neutron-rich. For both collapsars and the

accretion accompanying compact object mergers there will thus come a time $t_{\rm ign}$ after which $\dot{M}_D < \dot{M}_{\rm ign}$ and the disk will transition from an NDAF to an advection-dominated thick disk (Narayan & Yi 1994; Narayan et al. 2001).

Although NDAFs enter β-equilibrium on an accretion timescale (B03a), thick disks generally do not. Using equation (48) from B03a we find that weak equilibrium is only established in a thick disk at radii smaller than a critical β-equilibrium radius R_β, which is given by

$$R_\beta = 34(14)(\dot{M}_D/\dot{M}_{\rm ign})^{10/13}\alpha_{0.1}^{-4/39}M_3^{4/39}R_g \tag{4.28}$$

for accretion onto a black hole with spin $a = 0(0.95)$. Since $R_\beta < R_{\rm isco}$ for $\dot{M}_D \lesssim 0.1(0.03)\dot{M}_{\rm ign}$, equation (4.28) shows that matter accreting through a thick disk at a rate $\dot{M}_D \ll \dot{M}_{\rm ign}$ is not in weak equilibrium at any radius. The neutron content of the disk at small radii for $t \gg t_{\rm ign}$ (and thus of any potential late-time GRB-producing outflow) will therefore depend on the composition of the matter feeding it. In particular, late-time GRB outflows from collapsar disks, which are continually fed from large radii by their progenitor's stellar He envelope (which has $Y_e \sim 0.5$), will not be neutron-rich.

On the other hand, accretion disks formed from compact object mergers, which are usually fed from the tidal disruption of at least one neutron star[11] (e.g., Rosswog & Ramirez-Ruiz 2002), are initially neutron-rich. However, the disks formed from compact object mergers are expected to be more compact than collapsar disks (with circularization radii $\lesssim 10-30R_g$) and are probably not continually supplied with substantial mass from large radii; the late-time neutron content of thick disks from compact object mergers therefore depends on the evolution of Y_e^D immediately following the NDAF to thick disk transition at $t_{\rm ign}$. Since equation (4.28) shows that a thick disk with $\dot{M}_D \lesssim \dot{M}_{\rm ign}$ does have sufficient time to enter weak equilibrium, the late-time electron fraction in a thick disk from a compact object merger depends on whether weak equilibrium near $R_{\rm isco}$ in a thick disk for $\dot{M} \sim \dot{M}_{\rm ign}$ favors a neutron-rich or a proton-rich composition. Although NDAFs

[11] An exception are the mergers of black hole-white dwarf binaries, which may produce long-duration GRBs (Fryer et al. 1999b).

are always sufficiently dense and degenerate to favor a neutron-rich composition, weak equilibrium in a thick disk only favors $n/p > 1$ for radii *smaller* than a critical neutron-rich radius $R_{\rm n}$; using B03a equation (50) we find that

$$R_{\rm n} = 24(2)(\dot{M}_D/\dot{M}_{\rm ign})^2 \alpha_{0.1}^{4/3} M_3^{-4/3} R_g \tag{4.29}$$

for accretion onto a black hole with spin $a = 0(0.95)$. Equation (4.29) shows that when a disk transitions from an NDAF to a thick disk, the matter near $R_{\rm isco}$ may be driven to either a neutron-rich or a proton-rich state, depending on α, M, and the extent of the disk. Thus, although disk winds from NDAFs are unlikely to produce neutron-rich GRB outflows, neutron-rich outflows may be possible from the thick disks associated with compact object mergers at late times ($t \gtrsim t_{\rm ign}$) or from collapsar disks at $t \sim t_{\rm ign}$ (i.e., after the thick disk transition but before the disk is fed by additional, neutron-poor material from large radii).

4.6 Discussion

By calculating the structure and neutron content of neutrino-heated MHD winds driven from the neutron-rich surfaces of proto-magnetars and NDAFs, we have delineated the conditions under which a large neutron excess can be preserved in these outflows. We have focused on the conditions for simultaneously neutron-rich and ultra-relativistic outflows because magnetized winds from hyper-accreting disks and newly-formed magnetars are plausible GRB central engines; despite being difficult to distinguish on other grounds, each of these central engines may possess a distinctive nucleonic signature. If the consequences of neutron-rich GRB outflows enumerated in §4.1 can be identified or constrained, magnetar and black hole models for GRBs may thus be observationally distinguishable.

Although GRB central engines are often neutron-rich (Pruet et al. 2003; B03a), we find that ultra-relativistic neutron-rich outflows are possible only under surprisingly limited circumstances. Central engines that are sufficiently dense and degenerate to be neutron-rich must be efficiently neutrino-cooled. For the resulting sub-virial temperatures, several of the thermal neutrinos released by the

central engine must be absorbed by a typical nucleon for it to escape the deep gravitational potential due to neutrino-driving alone. Since neutrino absorptions from efficiently neutrino-cooled central engines usually favor an asymptotic electron fraction $Y_e^a \gtrsim 0.5$, purely neutrino-driven outflows are generally driven back to a relatively neutron-poor state, with the precise value of Y_e^a determined by the neutrino spectrum of the central source (see eq. [4.6] and surrounding discussion).

Additional forces (e.g., magnetocentrifugal) can prevent deneutronization by supplying most of the binding energy needed to escape the central engine's gravitational potential well. However, Y_e^a is set so close to the base of the outflow that the very inner, hydrostatic atmosphere of the wind must be altered for $Y_e^a \ll 0.5$ to obtain; this unavoidably increases the wind's mass-loss rate $\dot{M}$ (see eq. [4.18]). Indeed, a generic anti-correlation between $\dot{M}$ and Y_e^a is evident in our numerical calculations shown in Figures 4.2, 4.4, and 4.7. Neutron-rich GRB outflows are thus difficult to produce because the minimum neutron-rich mass-loss rate often precludes ultra-relativistic speeds. Other heating (e.g., viscous) that may be present in the outflow in addition to neutrinos (which *must* be present) will only further increase $\dot{M}$ and, through additional entropy deposition and pair creation, further deneutronize the outflow.

Our conclusion that simultaneously ultra-relativistic and neutron-rich outflow is difficult to produce depends on the assumption that Y_e^ν is not significantly less than 0.5. Therefore, to be more precise, the conclusion of this paper is that the nucleonic content of ultra-relativistic outflows driven from efficiently neutrino-cooled central engines is typically set by an equilibrium with neutrino absorptions. Thus, if the neutrino spectra and luminosities of PNSs and NDAFs are significantly different from what current calculations find, and $Y_e^\nu \ll 0.5$, neutron-rich outflows from GRB central engines may be more common. The next step in improving our understanding of magnetocentrifugal winds from GRB central engines is to include the effects of a strong magnetic field on the neutrino interactions and the equation of state for the leptons. For the parameters considered in this work, the latter should be more important, modifying the pressure and entropy profiles.

With these general constraints in mind, we now discuss the prospects for

neutron-rich outflows from individual central engines. Our conclusions are summarized in Table 4.1.

4.6.1 Proto-Magnetars

Proto-magnetars with surface magnetic field strengths $B_\nu \gtrsim 10^{14} - 10^{15}$ G can produce neutron-rich outflows, but only for rotation periods $P \lesssim P_{\rm n} \approx 0.8$ ms (see Fig. 4.2). If the minimum stable neutron star rotation period $P_{\rm min}$ exceeds $P_{\rm n}$, then neutron star birth should not be accompanied by substantially neutron-rich outflow.[12] On the other hand, if $P_{\rm n} \lesssim P_{\rm min}$ and steady-state neutron-rich winds from magnetar birth are indeed possible, they should be restricted to events with a total GRB plus SN energy exceeding $E_{\rm rot}(P_{\rm n}) \approx 4 \times 10^{52}$ ergs (absent significant gravitational wave losses). Such extremely energetic events are likely rare, even among GRBs. Furthermore, not all magnetar births that release $\gtrsim 4 \times 10^{52}$ ergs will necessarily produce *simultaneously* ultra-relativistic and neutron-rich outflows because proto-magnetar winds are heavily mass-loaded at early times following core bounce. If the proto-magnetar's dipole field strength exceeds $B_\nu^{\rm dip} \sim 10^{15}$ G, spin-down is so rapid that neutron-rich outflow is unlikely by the time the PNS has cooled sufficiently that $\sigma \gtrsim 100 - 1000$ (see Fig. 4.5). Since the PNS spin-down power for $P \approx P_{\rm n}$ and $B_\nu^{\rm dip} \approx 10^{15}$ G is $\sim 3 \times 10^{49}$ ergs s^{-1} (Spitkovsky 2006; B06), neutron-rich GRBs from proto-magnetars possess a maximum beaming-corrected luminosity $L_\gamma \sim 10^{49}(\epsilon/0.3)$ ergs s^{-1}, where ϵ is the efficiency for converting outflow to gamma-ray energy.

4.6.2 NDAFs

Although neutron-rich GRB outflows are possible from a subset of proto-magnetars, we find that they are unlikely to originate from NDAFs under any

[12] As discussed in §4.4.4, an exception may arise for neutrino-driven winds produced at very early times after core bounce following the accretion-induced collapse (AIC) of a white dwarf (Dessart et al. 2006); similarly, in the absence of an overlying, accreting stellar mantle, an early-time ejection of $\sim 10^{-3} - 10^{-1} M_\odot$ of low-Y_e material may result from the core bounce shock's "break-out" or the subsequent neutrino-heated shock revival (e.g., Hillebrandt, Wolff, & Nomoto 1984; Fryer et al. 1999a)

Table 4.1 Neutron Content of Outflows from GRB Central Engines

Central Engine	Neutron-Rich GRB Outflow?	Conditions/Comments
Magnetar, CC[(a)]	Sometimes	Subset with SN + long-duration GRB energy $\gtrsim 4 \times 10^{52}$ ergs; restricted to GRB luminosities $\lesssim 3 \times 10^{49}$ ergs s^{-1}; see §4.4.2 and §4.6.1 $\sim 0.1 M_\odot$ of non-relativistic ($v \gtrsim 0.3$ c) free neutrons ejected prior to neutron-rich GRB outflow
Magnetar, AIC[(b)]	Sometimes	Same as CC; additional $\sim 10^{-3} - 10^{-1} M_\odot$ non-relativistic low-Y_e matter ejected at early times;[(c)] SN-like component optically-dim due to $\lesssim 10^{-3} M_\odot$ total ^{56}Ni production; see §4.6.4
NDAF, CC	Unlikely	Disk midplane enters weak equilibrium;[(d)] outflow enters neutrino absorption equilibrium ($Y_e^a \simeq Y_e^\nu$); see §4.5.3
NDAF, COM[(e)]	Unlikely	Same as CC; additional $\sim 10^{-3} - 10^{-1} M_\odot$ non-relativistic low-Y_e matter may be ejected at early times[(f)]
Low-$\dot{M}_D$ RIAF,[(g)] CC	Unlikely	Disk midplane may not enter weak equilibrium, and stellar mantle feeding the disk has $Y_e \sim 0.5$; outflow likely viscously-driven with $Y_e^a \sim Y_e^D$; see §4.5.5 and §4.6.3
Low-$\dot{M}_D$ RIAF, COM	Possible	Neutron star tidal debris feeding the disk has $Y_e \ll 0.5$, but composition altered by β-equilibrium at high $\dot{M}_D$; low $\dot{M}_D$-RIAF may remain neutron-rich during NDAF to RIAF transition (see §4.5.5); due to low-$\dot{M}_D$, probably accompanies only relatively long short-duration GRBs
High-$\dot{M}_D$ RIAF, CC	Unlikely	Disk midplane enters weak equilibrium; large neutrino-driven mass-loss likely precludes relativistic disk winds
High-$\dot{M}_D$ RIAF, COM	Unlikely	Same as CC

[(a)] Core Collapse (CC)

[(b)] Accretion-Induced Collapse (AIC)

[(c)] e.g., Hillebrandt, Wolff, & Nomoto (1984); Fryer et al. (1999a); Dessart et al. (2006, 2007)

[(d)] Pruet et al. (2003); B03a

[(e)] Compact Object Merger (COM)

[(f)] e.g., Rosswog et al. (1999b)

[(g)] Radiatively-Inefficient Accretion Flow (RIAF)

circumstances. In agreement with previous works (e.g., Daigne & Mochkovitch 2002; Levinson 2006), we find that outflows with $\sigma \gtrsim 100$ are possible from the innermost radii of NDAFs around rapidly rotating black holes ($a \approx 1$), despite the minimum neutrino-driven mass-loss rate (eq. [4.24]). The significantly larger $\dot{M}$ required for a large neutron excess, however, precludes neutron-rich NDAF outflows from attaining $\sigma \gtrsim 1-10$ for significant accretion powers (eq. [4.26]). Furthermore, because modest entropy, magnetocentrifugally-driven winds only possess free nuclei over a relatively limited range of radii, cross-field diffusion is ineffective at polluting otherwise neutron-poor axial jets with free neutrons from adjacent, more heavily baryon-loaded winds (see §4.5.4).

Although we find that neutron-rich winds from NDAFs are unlikely, several caveats should be discussed. Pruet et al. (2004) suggest that "bubbles" of neutron-rich material may escape the disk via chaotically-heated buoyant magnetic filaments, a picture similar to some models for GRBs (Narayan et al. 1992; Katz 1997; Kluźniak & Ruderman 1998). Although this possibility cannot be ruled out, current thin disk simulations do not find significant energy deposition in low density, coronal regions (e.g., Hirose, Krolik, & Stone 2006), and whether such low-Y_e bubbles can remain neutron-rich despite the pair-capture deneutronization that accompanies such chaotic heating is unclear. If the Blandford-Znajek mechanism or $\nu-\bar{\nu}$ annihilation above the disk's rotation axis powers the GRB outflow instead of a disk wind, the base of the GRB-producing jet may be effectively baryon-free because the field lines would then thread the black hole's event horizon instead the disk midplane; what ultimately sets the wind's baryon-loading in this case is unclear. Our calculations show that neutrino-heated disk winds will form a modest entropy "sheath" around such a baryon-free jet. If, however, the wind encasing the jet possesses a much higher entropy (e.g., Pruet et al. 2001), cross-field neutron diffusion is more effective (Levinson & Eichler 2003; McKinney 2005b) and may result in asymptotically neutron-rich polar outflow. Furthermore, even if the outflow's field lines don't thread the disk, it is in principle possible that some form of chaotic mass-loading may pollute the baryon-poor base of the jet with matter from the neutron-rich disk midplane. We note, however, that current simulations find

very little matter entraining the jet from the disk, thus requiring implementation of a numerical density floor along the polar axis (e.g., Proga & Begelman 2003; Proga et al. 2003).

4.6.3 Thick Disks

Although NDAFs exist over a range of accretion rates that are relevant to both long and short-duration GRBs, GRB-producing outflows can also be powered by the accretion of matter that is not efficiently neutrino-cooled. Such geometrically-thick, radiatively-inefficient accretion flows (RIAFs) exist for both $\dot{M}_D < \dot{M}_{\rm ign}$ ("low-$\dot{M}_D$ RIAFs"), for which the density is too low for efficient neutrino cooling near $R_{\rm isco}$, and for $\dot{M}_D \gg \dot{M}_{\rm ign}$ ("high-$\dot{M}_D$ RIAFs"), for which matter advects into the black hole faster than it cools (e.g., Di Matteo, Perna, & Narayan 2002). High $\dot{M}_D$ RIAFs, while possibly relevant to "prompt" collapsars (MacFadyen & Woosley 1999), are probably most relevant to compact object mergers given their smaller expected disk radii and shorter accretion timescales. Low-$\dot{M}_D$ RIAFs are relevant to both the late stages of collapsars and compact binary mergers.

Like NDAFs, high-$\dot{M}_D$ RIAFs enter β-equilibrium before accreting and, although they are not as neutron-rich as NDAFs, they also typically have $Y_e^D \ll 0.5$ (e.g., Surman & McLaughlin 2004; Lee et al. 2005, hereafter L05). High-$\dot{M}_D$ RIAFs are confined to radii in the disk smaller than the "trapping" radius $R_{\rm t}$, the point interior to which matter has insufficient time to cool before accreting; $R_{\rm t}$ exists outside $R_{\rm isco}$ for mass accretion rates greater than $\dot{M}_{\rm t} \approx 9(2)\alpha_{0.1}^{1/3} M_\odot$ s^{-1} for $a = 0(0.95)$ and $M = 3M_\odot$ (CB07). Although radiatively-inefficient on the whole, disks with $\dot{M}_D > \dot{M}_{\rm t}$ still release a substantial neutrino luminosity because $\dot{M}_{\rm t}$ is large and accretion is still efficiently cooled for radii larger than $R_{\rm t}$; indeed, for steady-state accretion, Di Matteo, Perna, & Narayan (2002) find that as $\dot{M}_D$ increases beyond $\dot{M}_{\rm t}$, L_ν saturates to a value $\sim 10^{53}$ ergs s^{-1}. This substantial neutrino luminosity will drive significant neutrino-heated mass-loss, thereby severely limiting the asymptotic Lorentz factor Γ of any outflow driven from the RIAF's surface. Using the simulations of L05 (their Fig. 6), we estimate that the

neutrinosphere temperature of a high-$\dot{M}_D$ RIAF near $R_{\rm t}$ is roughly $T_\nu \sim 3$ MeV (corresponding to a mean neutrino energy $\langle \epsilon_\nu \rangle \sim 10$ MeV); thus, from equation (4.19) we estimate that the minimum, neutrino-driven mass-loss rate from the innermost radii of high-$\dot{M}_D$ RIAFs is $\dot{M}_{\rm th} \approx 10^{-3} - 10^{-2} M_\odot$ s^{-1}. For a wind driven from the surface of a high-$\dot{M}_D$ RIAF to reach $\Gamma \gtrsim 100$ would thus require an MHD luminosity $\dot{E} \gtrsim 10^{53} - 10^{54}$ ergs s^{-1}, which is comparable to the entire accretion power for $\dot{M}_D \sim \dot{M}_{\rm t} \sim 1 - 10 M_\odot$ s^{-1} and is substantially larger than the outflow powers typically inferred from short-duration GRBs (e.g., Bloom et al. 2005). GRB-producing outflows, whether neutron-rich or not, are thus unlikely to originate from disk winds produced by high-$\dot{M}_D$ RIAFs.

Unlike NDAFs and high-$\dot{M}_D$ RIAFs, low-$\dot{M}_{\rm D}$ RIAFs may not enter weak equilibrium on an accretion timescale (eq. [4.28]); thus, the electron fraction in a low-$\dot{M}_D$ thick disk's midplane can remain approximately equal to that of the material used to form the disk initially. Because of the low neutrino luminosity and positive Bernoulli parameters of low-$\dot{M}_D$ RIAFs, viscous heating likely dominates neutrino heating in outflows driven from low-$\dot{M}_D$ thick disks, thereby making deneutronization by neutrinos unlikely. Although nondegenerate pair-captures may drive $Y_e \rightarrow 0.5$ depending on the precise viscous energy deposition profile in the wind, this possibility is less likely than for NDAF outflows because weak equilibrium is already slow in the disk midplane and because the accretion and outflow advection rates for thick disks are comparable. Furthermore, if acceleration from the midplane is enhanced due to magnetocentrifugal slinging, pair-capture deneutronization would be further suppressed. Thus, outflows driven from low-$\dot{M}_D$ RIAFs probably retain the electron fraction of the disk's original composition. As a result, outflows driven at late times from collapsars, which are fed from the progenitor star's relatively neutron-poor envelope (e.g., $Y_e \simeq 0.5$ for a purely He composition), probably do not possess a significant neutron excess. In this case, significant ^{56}Ni could be produced in the disk's outflow, powering a bright SN (MacFadyen & Woosley 1999).

Although disks formed from compact object mergers are usually initially neutron-rich, they are compact and nearly all of the matter goes through an NDAF

phase in which weak equilibrium modifies the initial composition of the disk; their composition at late times therefore depends on how they transition from an NDAF to a low-$\dot{M}_D$ thick disk. Depending on α, the size of the disk, and the mass of the black hole, the composition of the thick disk immediately following the NDAF to low-$\dot{M}_D$ RIAF transition at $t_{\rm ign}$ can be either neutron-rich or proton-rich (see eq. [4.29]). Although by no means assured, neutron-rich GRBs outflows may thus be possible from thick disks in both collapsars immediately following $t_{\rm ign}$ (especially if the variability imposed by the NDAF-thick disk transition actually causes the GRB; Giannios 2007) and in short-duration GRBs from compact object mergers. In either case, neutron-rich GRB outflows should be restricted to events with accretion power (and thus maximum GRB luminosity) less than $L_{\nu,\rm ign}$ (eq. [4.7]).

4.6.4 Non-Relativistic Neutron-Rich Winds

Optical Transients

Relativistic, GRB-producing outflows from proto-magnetars and hyper-accreting disks are possible under specialized circumstances, but non-relativistic winds are also likely to be present, probably occur in a wider variety of progenitors, and probably carry more total energy. The composition of such non-relativistic winds may also lead to an observable signature, most directly via radiation from ejecta that is reheated by the decay of radioactive elements in the wind. One possibility in the case of magnetar birth is that the heavily mass-loaded wind that emerges at early times (carrying a total mass up to $\sim 0.01-0.1 M_\odot$ for a millisecond rotator; Dessart et al. 2007; see Fig. 2.10) could produce a bright SN-like event. However, by combining the mass-loss rate that accompanies a significant neutron excess (eq. [4.18]) with the fiducial PNS cooling evolution $L_\nu(t)$ given in equation (4.8), we find that the total PNS mass-loss capable of being processed into ^{56}Ni under NSE (which requires no significant neutron excess; Hartmann, Woosley, & El Eid 1985) cannot exceed $M_{\rm Ni}^{\rm max} \sim \int_{1\,\rm s}^{\tau_{\rm KH}} \dot{M}_{\rm th}\phi_{\rm n} dt \sim 10^{-3} M_\odot$, much too small to contribute appreciably to an optical light curve powered by ^{56}Ni, and subsequent

^{56}Co, decay (e.g., see Kulkarni 2005, Fig. 7).[13]

The modest optical luminosity associated with the decay of a mass $\sim M_{\rm Ni}^{\rm max}$ of Ni is consistent with the rather stringent upper limits on the SN component accompanying some short-duration GRBs (e.g., GRB050509B; Hjorth et al. 2005); this supports the viability of a model in which short-duration GRBs are powered by the rapid spin-down of a magnetized, rapidly rotating magnetar, formed following the accretion-induced collapse (AIC) of a white dwarf (Usov 1992) or resulting from the merger of a double neutron star binary (a "super-pulsar"; Rosswog et al. 2003). It is less clear how much of the substantial mass-loss driven from the accretion disk formed during the merger of two compact objects will be processed into ^{56}Ni. Quantifying this will require additional work.

Even if little mass is ejected with $Y_e^a \gtrsim 0.5$ (capable of producing ^{56}Ni), both proto-magnetars and hyper-accreting disks could in principle produce detectable transients due to the presence of neutron-rich non-relativistic outflows. For example, a proto-magnetar that is born rotating sufficiently rapidly to produce late-time, relativistic neutron-rich matter must also eject a total mass $M_{\rm n} \gtrsim 0.1 M_\odot$ in slower ($v \gtrsim 0.3$ c) free neutrons at earlier times. The detectability of such neutron-rich non-relativistic outflows is, however, uncertain. Any neutrons that ultimately remain free in the wind will β-decay into protons on a timescale $\tau_\beta \approx 900$ s at a radius $\gtrsim 10^{13}$ cm; thus, one observable manifestation of neutron-rich outflow may be Li-Paczynski mini-SN ("Macronovae") powered by the thermal energy released by this decay ($\approx 6 \times 10^{49} (M_{\rm n}/0.1 M_\odot)$ ergs), which may be detectable on hour-day timescales following the birth of the central object (Li & Paczyński 1998; Kulkarni 2005).

[13]Enhanced Ni production is still possible in the core collapse context via early energization of a successful SN shock due to rapid spin-down (TCQ04). A proto-magnetar's spin-down luminosity is substantially enhanced over the vacuum-dipole rate at early times following the launch of the SN shock by the excess magnetic flux opened by neutrino-heated, centrifugally-driven mass-loss (B06). In this case, the enhanced Ni yield is produced by additional shock heating of the stellar progenitor, not directly in the wind itself.

r-process Nucleosynthesis

Rather than leaving free neutrons, the decompression of slowly moving, modest entropy, and moderately neutron-rich ($0.1 \lesssim Y_e^a \lesssim 0.4$) matter is more likely to produce anomalous neutron-rich isotopes (e.g., ^{62}Ni, ^{66}Zn, ^{68}Zn, ^{87}Rb, ^{88}Sr; Hartmann, Woosley, & El Eid 1985), and in some cases may be capable of producing r-process elements (e.g., Freiburghaus et al. 1999). Thus, as a final application of our calculations, we briefly consider the possibility of r-process element synthesis in proto-magnetar and NDAF winds. Given their intrinsic neutron-rich nature, outflows from neutron star formation have long been considered one of the most promising r-process sites (Woosley & Hoffman 1992; Meyer et al. 1992); however, the conditions necessary for a successful third-peak r-process have not been realized in detailed studies of non-rotating, non-magnetized PNS winds (QW96; Otsuki et al. 2000; Sumiyoshi et al. 2000; Wanajo et al. 2001; T01). In Chapter 2 we studied the effects of magnetic fields and rotation on the r-process in PNS winds for $P \gtrsim P_{\rm n}$ and constant Y_e; although we did not find solutions with a successful third-peak r-process (based on the criteria of Hoffman, Woosley, & Qian 1997, hereafter HWQ97), we did not consider the additional benefits of low Y_e^a caused by very rapid rotation ($P < P_{\rm n}$).

Even accounting for the possibility of low Y_e discussed in this paper, we find that all of the NDAF and most of the proto-magnetar wind solutions we have considered still fail to meet the criteria for third-peak r-process of HWQ97, mainly because the beneficial effects of low Y_e are counteracted by the detrimental effects that the accompanying rapid advection has on the wind's asymptotic entropy S^a.[14] One possibility is that energy deposition by acoustic or MHD waves could raise the asymptotic entropy of low-Y_e winds (Suzuki & Nagataki 2005; Chapter 2). In

[14]By the arguments given in §4.2, for a PNS wind to remain neutron-rich the thermal energy deposited in the wind per baryon cannot exceed the neutrinosphere's mean neutrino energy $\langle \epsilon_\nu \rangle$. Thus, because most heating occurs near the PNS surface (at a temperature $\approx 0.7 T_\nu$; QW96, eq. [47]), the entropy added to a neutron-rich wind cannot exceed $\Delta S \sim \langle \epsilon_\nu \rangle / 0.7 T_\nu \approx 5\ k_B$ baryon^{-1} (compare S^a and Y_e^a in Tables 4.3 and 4.4), which is substantially less than that deposited in non-magnetized, non-rotating PNS winds $\Delta S \approx G M m_{\rm n} / 0.7 T_\nu R_\nu \approx 70 (L_{\bar{\nu}_e,51}/8)^{-1/4}$ k_B baryon^{-1} (QW96; T01).

addition, despite their extremely low entropy, some of the most rapidly rotating and highly magnetized proto-magnetar solutions that we have calculated (e.g., the $B_\nu = 10^{16}$ G and $\Omega = 9000$ Hz solution shown in Figure 4.3) do eclipse the third-peak r-process threshold of HWQ97. This occurs because r-process synthesis of nuclei with mean mass A (typically ~ 195 for the third peak) by neutron captures on seed nuclei with mean proton number $\bar{Z}$ (typically $\sim 30 - 40$) is possible for $Y_e^a \lesssim \bar{Z}/A \approx 0.15 - 0.20$, even in outflows with vanishingly small S^a (see the discussion in Wheeler et al. 1998). The dynamical timescales for our very low Y_e^a solutions are, however, much shorter than those considered by HWQ97 and several commonly made assumptions become suspect for such rapidly expanding outflows (Meyer 2002); thus, detailed nucleosynthesis calculations, which include all of the relevant rate equations, need to be completed in the regime of low S^a, low Y_e^a, and very rapid outflow before r-process success is assured.

The very rapid rotation and strong magnetic fields associated with the successful r-process winds that we find are extreme and will not accompany most core-collapse SNe; the substantial amount of neutron-rich material ($\gtrsim 0.1 M_\odot$) ejected by such a proto-magnetar, however, means that just a few very rapidly rotating proto-magnetar births of this kind per Myr would noticeably affect the Galactic r-process abundance (Qian 2000). Conversely, if the r-process yield from events like this do not resemble the observed abundances, the number of sub-millisecond magnetar births in our Galaxy can be strongly constrained; similar constraints can be placed on the incidence of the accretion-induced collapse (AIC) of a white dwarf, which produces a similar yield of low Y_e material (e.g., Woosley & Baron 1992; Fryer et al. 1999a; Dessart et al. 2006, 2007).

Acknowledgements

We thank Niccolo Bucciantini and Jon Arons for helpful discussions. We thank Wen-xin Chen and Andrei Beloborodov for making their accretion disk solutions available to us. EQ and BDM were supported in part by NASA grant NNG05GO22H, the David and Lucile Packard Foundation, and a NASA GSRP

Fellowship to BDM. Wind profiles are available upon request from BDM.

Table 4.2 Definitions for Commonly Used Variables

Variable	Definition
Y_e	Electron fraction (ratio of free protons to nucleons)
$Y_e^{\rm D}$	Disk midplane electron fraction
Y_e^0	Electron fraction at the base of the wind
Y_e^a	Asymptotic electron fraction in the wind
$Y_e^{\rm eq}(r)$	Electron fraction in local weak equilibrium, defined via $dY_e/dt\vert_{Y_e^{\rm eq}} = 0$ (eq. [4.14])
Y_e^ν	Asymptotic electron fraction in neutrino absorption equilibrium ($Y_e^{\rm eq}(r \to \infty) = Y_e^\nu$; eq. [4.6])
$Y_e^{a,{\rm sat}}$	Asymptotic electron fraction that obtains in the co-rotating, strong B limit in our simulations (eq. [4.16])
$\dot{M}$	Wind mass-loss rate
$\dot{M}_{\rm th}$	Purely thermal, neutrino-driven mass-loss rate (eqs. [4.19], [4.24])
$\dot{M}_{\rm cf}$	Magnetocentrifugally-enhanced wind mass-loss rate that obtains in the co-rotating, strong B limit
$\dot{M}_D$	Disk mass accretion rate
$\dot{M}_{\rm ign}$	Minimum "ignition" NDAF accretion rate (eq. [4.1])
$\dot{M}_{\rm n}^{\rm diff}$	Total neutron mass diffusion rate into the accretion disk's polar region from an encasing baryon-rich wind (eq. [4.27]).
r	Distance along the outflow to the center of the PNS or black hole
R_ν	Radius of the PNS neutrinosphere and the base of the PNS wind
R_0	Distance from the black hole to the base of the NDAF wind (see Fig. 4.6)
s	Distance along the outflow to the monopole center in our NDAF wind calculations (see Fig. 4.6)
s_0	Distance from the monopole center to the base of the NDAF wind (see Fig. 4.6)
R_g	Black hole's gravitational radius (GM/c^2, where M is the black hole mass)
$R_{\rm L}$	Light cylinder radius of the PNS or accretion disk wind
$R_{\rm A}$	Alfvén radius of the PNS wind
$R_{\rm s}$	Sonic radius of the PNS wind
$R_{\rm isco}$	Radius of the black hole's innermost stable circular orbit
$R_{\rm ign}$	"Ignition" radius interior to which accretion proceeds through a thin NDAF instead of a thick disk (eq. [4.11])
$R_{\rm p}$	Radius of the NDAF's peak integrated neutrino emission
$R_{\rm t}$	"Trapping" radius interior to which neutrinos cannot escape and efficiently cool the disk before accreting
R_β	Radius interior to which a thick disk enters weak equilibrium on an accretion timescale (eq. [4.28])
$R_{\rm n}$	Radius interior to which a thick disk favors a neutron-rich composition in weak equilibrium (eq. [4.29])
$\dot{J}_{\rm W}$	Rate that angular momentum is extracted by the NDAF wind
$\dot{J}_{\rm D}$	Rate that angular momentum must be extracted from the disk for accretion to proceed at the rate $\dot{M}_D$
Ω	Rotation rate of the PNS and the base of the PNS wind
$\Omega_{\rm n}$	Rotation rate above which the PNS wind is significantly neutron-rich ($Y_e^a \lesssim 0.25$; see eq. [4.16])
Ω_K	Keplerian rotation rate of the accretion disk
P	Rotation period of the PNS and the base of the PNS wind
$P_{\rm n}$	Rotation period below which the PNS wind is significantly neutron-rich
σ	Magnetization (potential asymptotic Lorentz factor) of PNS/NDAF winds (eqs. [4.13], [4.15], [4.21])
$\sigma_{\rm max}$	Maximum magnetization of neutrino-heated NDAF winds (eq. [4.25])
$\sigma_{\rm max}^{\rm n}$	Maximum magnetization of neutrino-heated NDAF winds with a neutron excess (eq. [4.26])
$\langle\epsilon_\nu\rangle$	Mean neutrino energy emitted by the PNS or NDAF
L_ν	Electron neutrino/antineutrino luminosity from a PNS or NDAF
$L_{\nu,{\rm ign}}$	Minimum electron neutrino/antineutrino luminosity which must accompany an NDAF
E_B	Binding energy of a nucleon in the gravitational potential of the PNS or black hole
$\phi_{\rm n}$	Factor by which $\dot{M}$ must exceed $\dot{M}_{\rm th}$ for a PNS or NDAF wind to maintain a significant neutron excess (eq. [4.18])

Table 4.3 PNS Wind Properties

$L_{\bar{\nu}_e}$ 10^{51} ergs s^{-1}	B_ν G	Ω s^{-1}	P ms	ρ_ν [a] g cm^{-3}	Y_e^0 [b]	Y_e^a [c]	$\dot{M}$ $M_\odot$ s^{-1}	σ	S^a [d] k_B baryon^{-1}
8	10^{16}	1000	6.3	4×10^{12}	0.03	0.48	1.9×10^{-4}	10	55
.....	10^{16}	4000	1.6	4×10^{12}	0.03	0.47	7×10^{-4}	40	28
.....	10^{16}	6000	1.0	3×10^{12}	0.03	0.41	4×10^{-3}	17	16
.....	10^{16}	8000	0.8	1.7×10^{12}	0.04	0.26	6×10^{-2}	1.9	10
.....	10^{16}	9000	0.7	1.3×10^{12}	0.05	0.19	2.4×10^{-1}	0.6	8
.....	10^{15}	4000	1.6	4×10^{12}	0.03	0.47	7×10^{-4}	0.4	28
.....	10^{15}	6000	1.0	3×10^{12}	0.03	0.42	4×10^{-3}	0.18	17
.....	10^{15}	8000	0.8	1.7×10^{12}	0.04	0.32	4×10^{-2}	0.03	11
.....	10^{15}	9000	0.7	1.3×10^{12}	0.05	0.28	9×10^{-2}	0.016	10
.....	10^{14}	4000	1.6	4×10^{12}	0.03	0.48	7×10^{-4}	4×10^{-3}	35
.....	10^{14}	6000	1.0	3×10^{12}	0.03	0.46	1.8×10^{-3}	4×10^{-3}	23
.....	10^{14}	8000	0.8	1.7×10^{12}	0.04	0.44	7×10^{-3}	1.6×10^{-3}	18
.....	10^{14}	9000	0.7	1.3×10^{12}	0.05	0.42	1.5×10^{-2}	1.0×10^{-3}	16
3.5	10^{16}	1000	6.3	7×10^{12}	0.011	0.50	2.8×10^{-5}	70	64
.....	10^{16}	4000	1.6	7×10^{12}	0.011	0.50	1.0×10^{-4}	300	31
.....	10^{16}	6000	1.0	6×10^{12}	0.011	0.44	6×10^{-4}	120	17
.....	10^{16}	8000	0.8	4×10^{12}	0.014	0.22	0.016	7	9
.....	10^{16}	9000	0.7	3×10^{12}	0.015	0.13	0.10	1.5	7
.....	10^{15}	4000	1.6	7×10^{12}	0.011	0.50	1.0×10^{-4}	3	31
.....	10^{15}	6000	1.0	6×10^{12}	0.011	0.44	6×10^{-4}	1.2	17
.....	10^{15}	8000	0.8	4×10^{12}	0.014	0.24	0.014	0.08	10
.....	10^{15}	9000	0.7	3×10^{12}	0.016	0.18	0.06	0.024	8
.....	10^{14}	4000	1.6	7×10^{12}	0.011	0.50	9×10^{-5}	3×10^{-2}	32
.....	10^{14}	6000	1.0	6×10^{12}	0.011	0.46	4×10^{-4}	1.5×10^{-2}	19
.....	10^{14}	8000	0.8	4×10^{12}	0.014	0.37	5×10^{-3}	2.6×10^{-3}	13
.....	10^{14}	9000	0.7	3×10^{12}	0.016	0.34	0.013	1.2×10^{-3}	12
1	10^{15}	7000	0.9	2.0×10^{13}	0.003	0.42	9×10^{-5}	10	14
.....	10^{15}	8000	0.8	1.7×10^{13}	0.003	0.23	1.0×10^{-3}	1.1	9
.....	10^{15}	9000	0.7	1.2×10^{13}	0.004	0.11	0.011	0.14	6

[a] Density at the base of the wind, set to enforce neutrino optical depth $\tau_\nu \approx 2/3$.

[b] Electron fraction at the base of the wind.

[c] The asymptotic electron fraction of the wind.

[d] The asymptotic entropy of the wind.

Table 4.4 NDAF Wind Properties

$\dot{M}_D$ $M_\odot\,s^{-1}$	B_0 G	θ degrees	$B_{\phi,0}$ [a] G	ρ_0 [b] g cm^{-3}	$Y_e^{0(c)}$	$Y_e^{a(d)}$	$\dot{M}$ $M_\odot\,s^{-1}$	σ	$\dot{J}_W/\dot{J}_D$ [e]	$S^{a(f)}$ k_B baryon^{-1}
0.2	10^{15}	50	2.4×10^{15}	1.9×10^{10}	0.07	0.31	3.2	0.013	40	9
.....	10^{14}	50	1.6×10^{15}	2.6×10^{10}	0.06	0.47	0.61	7×10^{-4}	4	13
.....	10^{13}	50	1.1×10^{15}	4×10^{10}	0.05	0.51	0.10	4×10^{-5}	0.6	18
.....	10^{15}	60	2.2×10^{15}	1.6×10^{10}	0.09	0.32	2.7	0.016	40	10
.....	10^{14}	60	1.4×10^{15}	2.2×10^{10}	0.06	0.47	0.54	8×10^{-4}	4	13
.....	10^{13}	60	9×10^{14}	3×10^{10}	0.04	0.50	0.09	5×10^{-5}	0.5	18
.....	10^{15}	70	1.6×10^{15}	1.4×10^{10}	0.11	0.35	1.5	0.028	40	11
.....	10^{14}	70	1.1×10^{15}	2.0×10^{10}	0.08	0.46	0.42	1.0×10^{-3}	3	13
.....	10^{13}	70	8×10^{14}	3×10^{10}	0.06	0.50	0.08	6×10^{-5}	0.5	18
.....	10^{15}	80	5×10^{14}	3×10^{10}	0.05	0.44	0.11	0.39	7	10
.....	10^{14}	80	2.8×10^{14}	3×10^{10}	0.05	0.47	0.08	6×10^{-3}	0.7	18
.....	10^{13}	80	2.8×10^{14}	4×10^{10}	0.04	0.49	0.07	1.3×10^{-4}	0.21	24
.....	10^{15}	85	1.9×10^{14}	4×10^{10}	0.04	0.50	0.012	4	3	10
.....	10^{14}	85	1.1×10^{14}	4×10^{10}	0.03	0.50	0.011	0.04	0.18	18
.....	10^{13}	85	6×10^{13}	4×10^{10}	0.03	0.50	0.009	5×10^{-4}	0.06	24
.....	10^{15}	87	1.2×10^{14}	5×10^{10}	0.03	0.51	5×10^{-3}	8	3	16
.....	10^{14}	87	8×10^{13}	5×10^{10}	0.03	0.51	5×10^{-3}	0.08	0.12	23
.....	10^{13}	87	2.4×10^{13}	6×10^{10}	0.03	0.51	5×10^{-3}	9×10^{-4}	0.029	29
.....	10^{15}	89	1.3×10^{14}	1.0×10^{11}	0.02	0.51	1.5×10^{-3}	28	3	40
.....	10^{14}	89	5×10^{13}	1.0×10^{11}	0.02	0.51	1.6×10^{-3}	0.27	0.07	48
.....	10^{13}	89	9×10^{12}	1.0×10^{11}	0.02	0.51	1.4×10^{-3}	3×10^{-3}	0.008	53
0.01	10^{14}	50	8×10^{14}	5×10^{9}	0.06	0.11	0.21	2.1×10^{-3}	40	9
....	10^{14}	60	8×10^{14}	5×10^{9}	0.06	0.12	0.19	2.2×10^{-3}	30	9
....	10^{14}	70	5×10^{14}	5×10^{9}	0.06	0.15	0.10	4×10^{-3}	21	9
....	10^{14}	75	1.3×10^{14}	5×10^{9}	0.06	0.27	0.010	0.04	4	12
....	10^{14}	80	4×10^{13}	5×10^{9}	0.06	0.46	6×10^{-4}	0.7	1.1	17
....	10^{14}	85	2.2×10^{13}	5×10^{9}	0.06	0.51	8×10^{-5}	6	0.6	36
....	10^{14}	87	1.5×10^{13}	5×10^{9}	0.06	0.51	2.6×10^{-5}	17	0.6	55
....	10^{14}	89	1.3×10^{13}	5×10^{9}	0.06	0.51	1.7×10^{-5}	26	0.6	60

[a] Azimuthal magnetic field at the base of the wind.

[b] Density at the base of the wind.

[c] Electron fraction at the base of the wind.

[d] The asymptotic electron fraction of the wind.

[e] The ratio of angular momentum lost in the wind to that lost through the disk (eq. [4.22]); solutions with $\dot{J}_W > \dot{J}_D$ are unphysical.

[f] The asymptotic entropy of the wind.

Chapter 5

Time-Dependent Models of Accretion Disks Formed from Compact Object Mergers

B. D. Metzger, A. L. Piro, E. Quataert (2008), MNRAS, 390, 781-797.[1]

Abstract

We present time-dependent models of the remnant accretion disks created during compact object mergers, focusing on the energy available from accretion at late times and the composition of the disk and its outflows. We calculate the dynamics near the outer edge of the disk, which contains the majority of the disk's mass and determines the accretion rate onto the central black hole. This treatment allows us to follow the evolution over much longer timescales (100 s or longer) than current hydrodynamic simulations. At late times the disk becomes advective and its properties asymptote to self-similar solutions with an accretion rate $\dot{M}_d \propto t^{-4/3}$ (neglecting outflows). This late-time accretion can in principle provide sufficient energy to power the late-time activity observed by *Swift* from some short-duration gamma-ray bursts. However, because outflows during the advective phase unbind

the majority of the remaining mass, it is difficult for the remnant disk alone to produce significant accretion power well beyond the onset of the advective phase. Unless the viscosity is quite low ($\alpha \lesssim 10^{-3}$), this occurs before the start of observed flaring at ~ 30 s; continued mass inflow at late times thus appears required to explain the late-time activity from short-duration gamma-ray bursts. We show that the composition of the disk freezes-out when the disk is relatively neutron rich (electron fraction $Y_e \simeq 0.3$). Roughly $10^{-2} M_\odot$ of this neutron-rich material is ejected by winds at late times. During earlier, neutrino-cooled phases of accretion, neutrino irradiation of the disk produces a wind with $Y_e \simeq 0.5$, which synthesizes at most $\sim 10^{-3} M_\odot$ of ^{56}Ni. We highlight what conditions are favorable for ^{56}Ni production and predict, in the best cases, optical and infrared transients peaking $\sim 0.5 - 2$ days after the burst, with fluxes a factor of ~ 10 below the current observational limits.

5.1 Introduction

The most popular model for the creation of short-duration gamma-ray bursts (GRBs) is either binary neutron star (NS/NS) or black hole-neutron star (BH/NS) coalescence (Paczynski 1986, 1991; Eichler et al. 1989; Narayan et al. 1992). Support for the merger hypothesis comes from their durations of $\lesssim 2$ s, observations of well-localized short GRBs in galaxies without strong star formation (Berger et al. 2005; Gehrels et al. 2005; Hjorth et al. 2005), and the lack of a detectable coincident supernovae (Hjorth et al. 2005; Bloom et al. 2006; Soderberg et al. 2006; Ferrero et al. 2007), as is found in the case of long ($\gtrsim 2$ s) GRBs (Galama et al. 1998; Hjorth et al. 2003; Stanek et al. 2003).

Previous theoretical studies of the merger process have focused on one of two stages. The first is the *dynamical* portion in which the less massive companion is tidally disrupted by the more massive BH (Lee & Kluzniak 1995, 1998, 1999; Kluzniak & Lee 1998; Janka et al. 1999; Rosswog et al. 2004) or NS (Ruffert et al. 1996; Ruffert & Janka 1999; Oechslin & Janka 2006). The details of whether a dynamical instability (Rasio & Shapiro 1994; Lai et al. 1994) or Roche lobe overflow

occurs depends on the mass ratio and the nuclear equation of state (Bildsten & Cutler 1992; Uryu & Eriguchi 1999).

Nevertheless, generally $\sim 0.01 - 0.1 M_{\odot}$ of material remains in a remnant disk following the dynamical stage. The accretion of this material onto the central object gives rise to the second, *disk* portion of the merger. The energetics and timescale of the accretion phase are reasonably consistent with observations of short GRBs, as was shown by models of steady-state, azimuthally symmetric, vertically averaged disks (Popham et al. 1999; Narayan et al. 2001; Kohri & Mineshige 2002; Di Matteo et al. 2002; Chen & Beloborodov 2007). More recently, these disks have been modeled with time-dependent calculations in 1D (Janiuk et al. 2004), 2D (Lee et al. 2004, 2005b), and 3D (Setiawan et al. 2004, 2006). The typical time interval that present multi-dimensional calculations can simulate is on the order of the burst duration or less ($\sim 1 - 2$ s for 2D and ~ 50 ms for 3D).

Recent observations of short GRBs by *Swift*, however, indicate continued activity from the central engine on much longer timescales. X-ray flares with durations of ~ 100 s after a delay of ~ 30 s have been seen from several bursts (Barthelmy et al. 2005; Villasenor et al. 2005; Campana et al. 2006; La Parola et al. 2006). Stacked lightcurves of many bursts indicate continued activity on a similar timescale (Lazzati et al. 2001; Montanari et al. 2005). In one extreme case, GRB 050724 displayed an X-ray flare 12 hours post-burst. This flaring activity has been attributed to a number of different sources, including fragmentation of a rapidly rotating core (King et al. 2005), magnetic regulation of the accretion flow (Proga & Zhang 2006), fragmentation of the accretion disk (Perna et al. 2005; although this explanation may have difficulty reproducing the observed timescales, Piro & Pfahl 2007), differential rotation in a post-merger millisecond pulsar (Dai et al. 2007), and an infalling tidal tail of material stripped from the disrupted NS (Lee & Ramirez-Ruiz 2007; Rosswog 2007).

In order to determine whether the late-time activity from short GRBs is consistent with a compact merger origin, the disk evolution should be followed for timescales much longer than the initial viscous time. With this aim, we perform time-dependent calculations modeling the disk as an annulus that contains the

majority of the mass. This simplification allows us to study the disk evolution for arbitrarily long timescales, and to readily determine important properties such as the disk's composition and when it becomes advective. We are also able to survey much of the parameter space of initial disk mass and angular momentum. In §5.2 we discuss the initial conditions for disks formed from compact object mergers. This is followed by §5.3, in which we summarize the main assumptions of our ring model. In §5.4 we present the results of our calculations and summarize the main properties of the models. We then calculate outflows from our disk solutions in §5.5. We investigate the composition of the outflows and argue that they generally consist of neutron-rich isotopes, but can produce ^{56}Ni in some circumstances. The presence or lack of an optical transient from short GRBs therefore provides an important constraint on progenitor models. We conclude in §5.6 with a discussion of our results. In Appendix A we summarize the Green's function solution to the viscous spreading of a ring, which is important for connecting our ring model to the true extended disk geometry. In Appendix B we present analytic self-similar solutions that reproduce many of the features of our numerical solutions.

5.2 Initial Conditions

The dynamical phase of NS/NS or BH/NS mergers has been studied extensively using a number of different numerical techniques and methods for including general relativity (GR). Here we summarize some of the most relevant features for our study (for a more detailed review, see Lee & Ramirez-Ruiz 2007).

When the lighter companion NS is first tidally disrupted, a debris disk is formed within only a few dynamical timescales. The initial disk mass, $M_{d,0}$, is generally larger for more asymmetric mass ratios (i.e., small q, where q is the ratio of the lighter to the heavier binary component). For example, Shibata & Taniguichi (2006) find that for a NS/NS merger with $q = 0.7$ that $M_{d,0} = 0.03\ M_\odot$, but for $q = 0.9$ the disk is much less massive with $M_{d,0} = 10^{-3}\ M_\odot$. Another trend is that including strong gravity gives less massive remnant disks. The BH spin is also important, with larger spin favoring disk formation (Rasio et al. 2005) and the

production of a tidal tail. These have masses of $\simeq 0.01-0.05\ M_\odot$ and may provide prolonged mass inflow (Lee & Ramirez-Ruiz 2007), but for simplicity this will be ignored here. Taken together, these simulations generally find $M_{d,0} \simeq 0.01-0.3 M_\odot$, with the disk containing a substantial fraction of the angular momentum of the disrupted companion.

In the standard picture of NS-NS mergers, the resulting hypermassive NS collapses to a BH shortly following the merger. However, simulations show that when (and if) collapse actually occurs depends on the mass of the central NS and its ability to transport angular momentum to the surrounding disk (Shibata et al. 2005; Shibata & Taniguchi 2006; Shibata et al. 2006). In fact, if the NS remains supported by differential rotaton for several seconds (Baumgarte et al. 2000; Morrison et al. 2004; Duez et al. 2004, 2006) or loses sufficient mass via a centrifugally-driven outflow (e.g., Thompson et al. 2004; Dessart et al. 2008a), the NS itself may power the GRB (e.g., Price & Rosswog 2006). In this paper we assume that the central object promptly collapses to a BH; our model, however, would be reasonably applicable for the case of a central NS as well, the primary difference being that the significant neutrino flux from the newly-formed NS and from the boundary layer between the disk and the NS could modify the composition and thermal properties of the disk.

We present some characteristic numbers to motivate our choice of initial conditions. Consider a binary with masses M and m ($M > m$), where the latter is the NS (with radius R) that is tidally disrupted. The disruption radius, a_t, is estimated to be (Kopal 1959, adding Fishbone's 1973 10% strong-gravity correction)

$$a_t \simeq 2.4R \left(\frac{M+m}{m}\right)^{1/3}. \tag{5.1}$$

The characteristic orbital period at this radius is

$$P_t \simeq 23.4 \left(\frac{R^3}{Gm}\right)^{1/2} \simeq 2 \times 10^{-3} m_{1.4}^{-1/2} R_6^{3/2} \text{ s}, \tag{5.2}$$

where $m_{1.4} = m/1.4\ M_\odot$ and $R_6 = R/10^6$ cm, with an orbital angular momentum of

$$J_t \simeq (G(M+m)a_t)^{1/2}\, m \simeq 6 \times 10^{49} (1/q+1)^{2/3} m_{1.4}^{3/2} R_6^{1/2} \text{ ergs s}, \tag{5.3}$$

where $q = m/M$. The disrupted NS also contains spin angular momentum. This is negligible since the NS is not strongly affected by tidal coupling (Bildsten & Cutler 1992). Even a rapidly rotating NS ($\simeq 5$ ms) has an associated angular momentum of merely $\sim 10^{48}$ ergs s.

Once disrupted, a considerable fraction of the NS is either lost from the system or immediately swallowed by the BH. The remaining material forms a thick torus surrounding the central BH. Its associated viscous timescale can be estimated by assuming that the majority of the mass of the torus lies at a single radius, $r_{d,0}$. Taking the angular momentum of the disk to be $J_d \simeq (GMr_{d,0})^{1/2} M_{d,0}$, we estimate

$$r_{d,0} \simeq 3 \times 10^7 M_3^{-1} M_{0.1}^{-2} \left(\frac{J_{49}}{2}\right)^2 \text{ cm}, \tag{5.4}$$

where $M_3 = M/3\ M_\odot$, $M_{0.1} = M_{d,0}/0.1\ M_\odot$, and $J_{49} = J_d/10^{49}$ ergs s. For a disk with half-thickness H, the viscous timescale is

$$t_{\rm visc,0} = \alpha^{-1} \left(\frac{r_d}{H}\right)^2 \left(\frac{r_d^3}{GM}\right)^{1/2} \simeq 6 \times 10^{-2} \alpha_{0.1}^{-1} M_3^{-1/2} r_7^{3/2} \left(\frac{H}{0.5 r_d}\right)^{-2} \text{ s}, \tag{5.5}$$

where $\alpha = 0.1\alpha_{0.1}$ is the standard dimensionless viscosity (Shakura & Sunyaev 1973), $r_7 = r_{d,0}/10^7$ cm, and we have scaled to an initial ratio of $H/r_d = 0.5$, consistent with our numerical solutions. The initial viscous time $t_{\rm visc,0}$ is roughly the time at which the central BH begins accreting in earnest. The strong dependence of $t_{\rm visc,0}$ on disk mass and radius demonstrates that the initial evolution of the disk is sensitive to the outcome of the dynamical phase of the merger. But as we will show, the late time evolution is much less sensitive to initial conditions and is well described by self-similar solutions.

5.3 Physics of the Expanding Ring Model

Given these initial conditions, one would like to know how the disk then evolves. Modeling the entire disk requires resolving timescales over $\sim 4 - 6$ orders of magnitude. This makes it expensive to carry out simulations for long periods of time. We consider instead a simplified model that captures most of the features of

interest. At any given time, t, the disk can be broken into three regions depending on the local viscous time, $t_{\rm visc}$, which increases with radius, roughly as $t_{\rm visc} \sim r^{3/2}$. At small radii, $t_{\rm visc} < t$, and the disk comes into steady-state. This is the region most often modeled in previous studies (Popham et al. 1999; Narayan et al. 2001; Kohri & Mineshige 2002; Di Matteo et al. 2002; Chen & Beloborodov 2007). The radii where $t_{\rm visc} \sim t$ contain the majority of the disk's mass and angular momentum. Therefore, this region determines the viscous evolution of the rest of the disk, including the mass accretion rate that is fed to the interior steady-state region. Motivated by this fact, we focus on this radius and model the disk as a ring. Exterior to this point is a third region where $t_{\rm visc} > t$, but this contains a small amount of mass and is negligible for the viscous evolution.

5.3.1 Dynamical Equations

Our ring model treats the disk as a single annulus that is evolved forward in time. In this picture, the properties of the ring, such as its surface density Σ and temperature T, are representative of the location where Σr^2 peaks. The main drawback of this method is that the material in the disk is in fact distributed spatially in radius. Thus, although the mass of the disk in the vicinity of r_d is $\simeq \pi\Sigma r_d^2$, the total mass of the disk (integrated over all radii) is $M_d = A\pi\Sigma r_d^2$, where A is a factor of order unity that accounts for the distinction between the total mass of the disk and the mass of the material near r_d. Similarly, we write the total angular momentum of the disk as $J_d = B(GMr_d)^{1/2}\pi r_d^2\Sigma$. At early times the constants A and B depend on the initial conditions of how matter is spatially distributed; however, at times much greater than the initial viscous time (given by eq. [5.5]), material initially concentrated at a given radius becomes spread out in a manner determined by the viscosity. As described in detail in Appendix A, we choose the constants A and B by setting the solution of our simplified ring model at late times equal to the Green's function solution for a spreading ring with a viscosity $\nu \propto r^{1/2}$ (as is appropriate for the radiatively inefficient disk at

late-times). This fixes $A = 3.62$ and $B = 3.24$.[2] Conveniently $A/B \simeq 1$, so that it is a good approximation to take $J_d \simeq (GMr_d)^{1/2} M_d$.

The time evolution of the disk is determined by the conservation equations. Conservation of mass is

$$\frac{d}{dt}\left(A\pi\Sigma r_d^2\right) = -\dot{M}_d, \tag{5.6}$$

where $\dot{M}_d$ is in general the total mass-loss rate, which could include both accretion and a wind (for now we ignore the effects of a wind). Conservation of angular momentum is

$$\frac{d}{dt}\left[B(GMr_d)^{1/2}\pi\Sigma r_d^2\right] = -\dot{J}, \tag{5.7}$$

where $\dot{J}$ is the angular momentum-loss rate. Equations (5.6) and (5.7) provide two coupled equations that can be solved for the dependent variables r_d and Σ.

The accretion rate must depend on the characteristic mass and viscous timescale of the ring, so we use

$$\dot{M}_d = f M_d / t_{\rm visc}, \tag{5.8}$$

where $t_{\rm visc} = r_d^2/\nu$ and ν is the viscosity. The factor f is set like A and B to match the exact solution of a spreading ring with $\nu \propto r^{1/2}$ (Appendix A), which gives $f = 1.6$.[3] Requiring a no-torque boundary condition at a radius r_*, we take

$$f = 1.6/[1 - (r_*/r_d)^{1/2}]. \tag{5.9}$$

In contrast, a steady-state disk obeys $\dot{M}_d = 3\pi\nu\Sigma$ (ignoring the no-torque condition), which instead gives $f = 3/A \simeq 0.83$.

For the viscosity, we use an α-prescription,

$$\nu = \alpha c_s H, \tag{5.10}$$

where $c_s = (P/\rho)^{1/2}$ is the isothermal sound speed. The equation of state includes contributions from radiation pressure, gas pressure, relativistic degeneracy pressure, and neutrino pressure as in Di Matteo et al. (2002).

[2] In fact, when the total angular momentum is conserved, the viscous evolution is independent of A/B as long as A/B is nearly constant with time.

[3] Although we set $t_{\rm visc} = r^2/\nu$, any prefactors that could go into this prescription would just be absorbed into a re-definition of f.

5.3.2 Energetics

For the energy equation, we take

$$q_{\rm visc} = q_\nu^- + q_{\rm adv}, \tag{5.11}$$

where $q_{\rm visc}$ is the viscous heating, q_ν^- is the neutrino cooling (using the prescriptions given by Di Matteo et al. 2002, which includes neutrino optical-depth effects), $q_{\rm adv}$ is the advective heat flux, and all q values correspond to half the disk thickness.

For a disk rotating at the Keplerian frequency $\Omega = (GM/r_d^3)^{1/2}$,

$$q_{\rm visc} = \frac{9}{8}\nu\Omega^2\Sigma = \frac{9}{8fA}\frac{GM\dot{M}_d}{\pi r_d^3}\left[1 - \left(\frac{r_*}{r_d}\right)^{1/2}\right], \tag{5.12}$$

where the prefactor $9/(8fA) \simeq 0.2$ is different from the steady-state value of 3/8. The advective term, $q_{\rm adv}$, is set as in Di Matteo et al. (2002), with the only difference being that the radial velocity is the expansion rate of the ring's radius

$$V_r = \frac{dr_d}{dt} = \frac{2\dot{M}}{A\pi r_d\Sigma}, \tag{5.13}$$

where we have taken $\dot{J} = 0$.

Fusion to α-particles produces heating in addition to $q_{\rm visc}$, with

$$q_{\rm nucl} = 6.8 \times 10^{28}\rho_{10}\frac{dX_\alpha}{dt}H, \tag{5.14}$$

where all quantities are expressed in cgs units, $\rho_{10} = \rho/10^{10}$ g cm^{-3} and X_α is the mass fraction of α-particles. Note that in our case $q_{\rm nucl} > 0$ since α-particles are synthesized as the disk expands (in contrast to studies that follow cooling from photodisintegration as material moves inward). In our calculations we do not include $q_{\rm nucl}$ in solving equation (5.11) because we were not able to find reasonable solutions when doing so (for reasons explained in §5.4.1).

5.3.3 Composition

An advantage of the ring model is that other properties of the disk, such as its composition, can be cast into differential equations and integrated along with

equations (5.6) and (5.7). Since the neutron content of the disk is particularly important for determining the properties of the disk's outflows, we evolve the electron fraction Y_e using

$$\frac{dY_e}{dt} = -Y_e r_{e^-p} + (1 - Y_e) r_{e^+n}, \tag{5.15}$$

where $Y_e = X_p/(X_n + X_p)$, X_p and X_n are the proton and neutron mass fraction, respectively, and r_{e^-p} and r_{e^+n} are the electron and positron capture rates, respectively (Beloborodov 2003a). We have neglected the effect of neutrino absorptions on the evolution of Y_e in equation (5.15). Although absorptions are important at early times when the disk is optically thick, we are primarily concerned with the late-time value of Y_e, which does not depend sensitively on the neutrino irradiation (see §5.4.2).

As the disk evolves, the protons and neutrons eventually burn to form α-particles. At these times the disk is sufficiently cold that the positron and electron capture rates are negligible (i.e, $1/r_{e^-p} \gg t_{\rm visc}$) and Y_e has frozen-out. This fixes the difference between the free neutron and proton mass fractions

$$X_n - X_p = 1 - 2Y_e. \tag{5.16}$$

Since the rates for reactions that synthesize and destroy α-particles are all fast in comparison to the viscous time, we determine the composition using nuclear statistical equilibrium (NSE) between protons, neutron, and α-particles. This is expressed by the Saha relation (Shapiro & Teukolsky 1983)

$$X_p^2 X_n^2 = 1.57 \times 10^4 \; X_\alpha \rho_{10}^{-3} T_{10}^{9/2} \exp\left(-\frac{32.81}{T_{10}}\right). \tag{5.17}$$

NSE is a good assumption because the disk temperature is generally $\gtrsim 0.5$ MeV (see Fig. 5.2), except at very late times or for very low disk masses (e.g., the $M_{d,0} = 0.03 M_\odot$ case, for which we do not calculate the nuclear composition anyways). By combining equations (5.16) and (5.17) with mass conservation, $X_p + X_n + X_\alpha = 1$, we solve for all of the mass fractions at a given ρ, T, and Y_e.

5.4 Time-Evolving Solutions

We next present the results of integrating equations (5.6), (5.7), and (5.15) forward in time. For simplicity, we typically assume that $\dot{J} = 0$. A convenient property of our formalism is the ease with which these complications can be included (for example, we consider the effects of winds at the end of §4.1). The disk properties are determined by the initial conditions $M_{d,0}$, J_d, and $Y_{e,0}$, and by the viscosity α. For the majority of our study we set the initial $Y_{e,0} = 0.1$, which is characteristic of the inner neutron star crust (Haensel & Zdunik 1990a,b; Pethick & Ravenhall 1995). An additional important parameter is r_*, which is set by the spin of the central BH. In most of our calculations we take $r_* \simeq 2.3 r_g \simeq 1.02 \times 10^6$ cm, corresponding to the innermost stable circular orbit of a 3 $M_\odot$ BH with spin $a \simeq 0.9$; when calculating the properties of disk outflows in §5.5, however, we also consider the case of a nonrotating ($a = 0$) BH. We consider the general evolution of the disk in §5.4.1, and then focus on the composition in §5.4.2.

5.4.1 Disk Evolution and Energetics

At any given time, a ring model is in one of three phases: (1) early-time, optically thick to neutrinos and advectively dominated, (2) mid-time, optically thin to neutrinos and geometrically thin, and (3) late-time, radiatively-inefficient accretion flow (RIAF).[4] This is analogous to the different regions of steady-state, hyper-accreting accretion disks (see, e.g., Chen & Beloborodov 2007), but now the transitions occur with time instead of radius. The phases that a certain ring model samples during the course of its viscous expansion depends on $t_{\rm visc,0}$. A more compact disk (a shorter $t_{\rm visc,0}$) will exhibit all three phases, while larger disks may only exhibit phases (2) and (3), or even just (3).

We present a number of figures that are helpful in understanding these three phases and how they are affected by changing $M_{d,0}$. Figure 5.1 shows the radius

[4] An optically thick, geometrically thin stage occurs between stages (1) and (2); however, this phase is brief and is not dynamically very different from phase (2), so we do not consider it separately in our discussion.

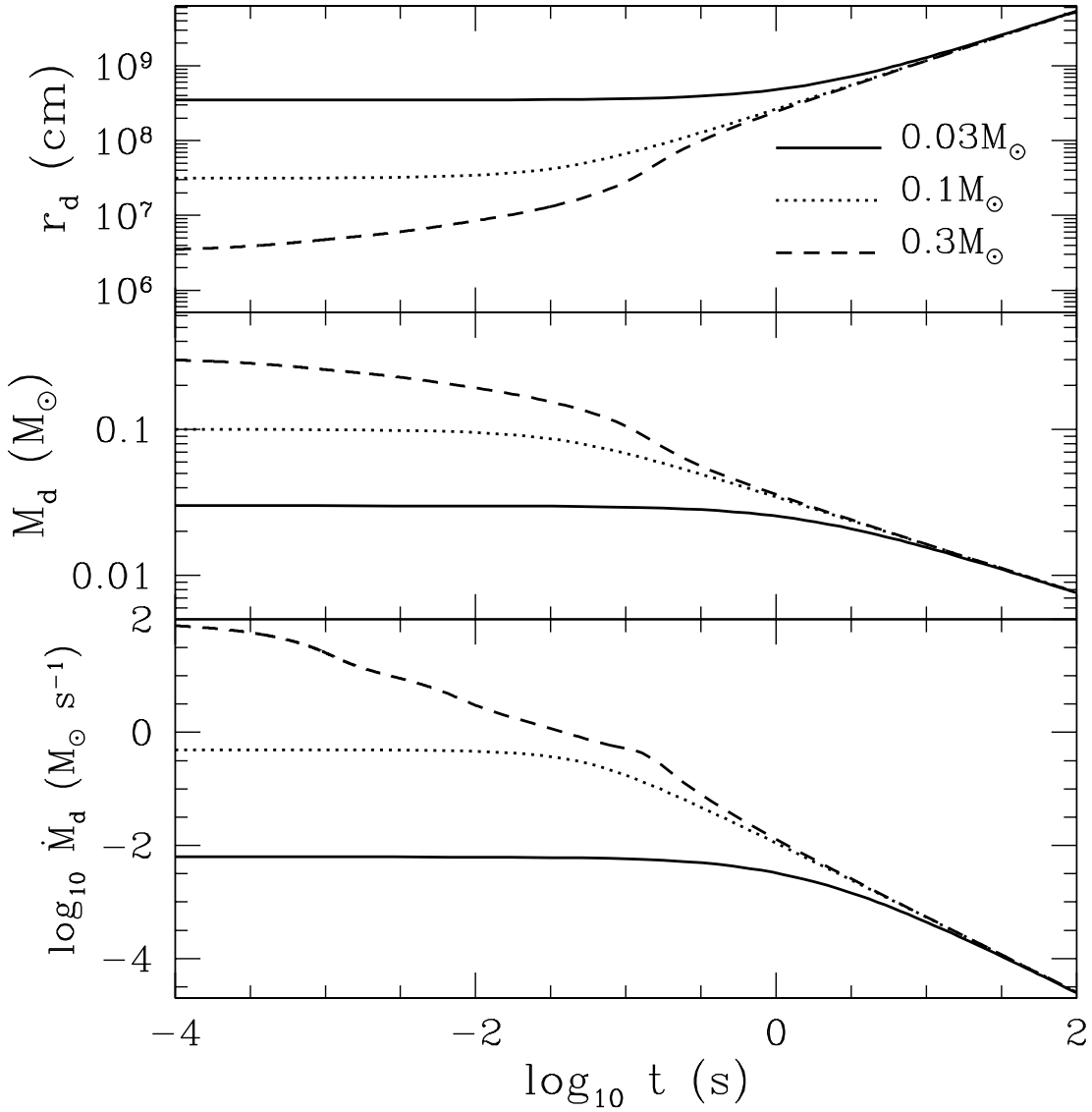

Figure 5.1: Example disk models showing the evolution of the disk radius, r_d, disk mass, M_d, and accretion rate, $\dot{M}_d$, as a function of time. We compare $M_{d,0} = 0.03$ (*solid lines*), 0.1 (*dotted lines*) and 0.3 $M_\odot$ (*dashed lines*) solutions; all use $J_{49} = 2$ and $\alpha = 0.1$. The inner radius is $r_* \simeq 2.3 r_g \simeq 1.02 \times 10^6$ cm (corresponding to a 3 $M_\odot$ BH with a spin of $a \simeq 0.9$).

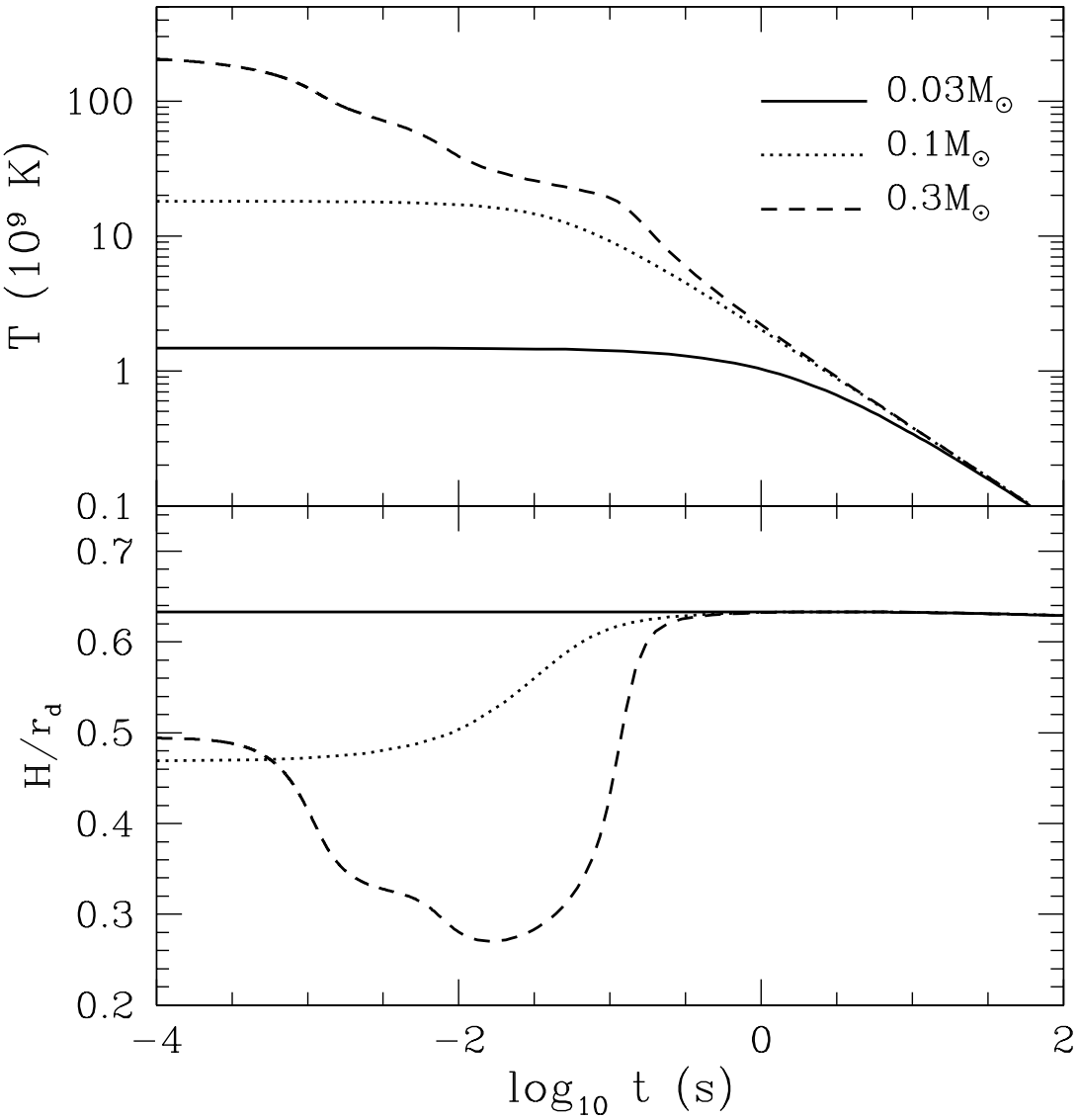

Figure 5.2: Comparison of the midplane temperatures and scaleheight for the three models from Fig. 1. In the lowest mass model, the ring is always advectively-dominated, thus H/r_d is constant.

r_d, mass M_d, and accretion rate $\dot{M}_d$ as a function of time, for $M_{d,0} = 0.3, 0.1$, and $0.03\,M_\odot$. Figure 5.2 compares the midplane temperature and scaleheight for these same models. Figures 5.3 and 5.4 show key results describing the energetics of the $M_{d,0} = 0.3$ and 0.1 $M_\odot$ solutions, respectively, while Figure 5.5 shows the different contributions to the total pressure in the disk as a function of time. Note that we fix the total angular momentum in these calculations ($J_{49} = 2$) and thus a larger $M_{d,0}$ corresponds to a smaller $r_{d,0}$ and a shorter $t_{\rm visc,0}$.

The first transition the disks make is from an optically thick, advective disk to a thin, neutrino-cooled disk; i.e., from phase (1) to (2). This is only exhibited by the $M_{d,0} = 0.3 M_\odot$ model and is seen most clearly at early times in Figure 5.2 when $H/r_d \simeq 0.5$ and in Figure 5.3 when $q_{\rm adv} \gg q_\nu^-$. Figure 5.5 shows that this phase is ion pressure (ideal gas) dominated. A simple estimate determines what initial disk mass is required for phase (1) to occur, i.e., for the initial disk to be optically thick and advective. The disk is advective for radii inside of which the neutrino diffusion time out of the disk exceeds the inflow time. Setting this radius equal to the initial radius of the disk (eq. [5.4]), we find that there is a critical disk mass below which the disk never experiences phase (1),

$$M_{d,\rm crit} \sim 0.2 \alpha_{0.1}^{-1/10} M_3^{-7/10} \left(\frac{J_{49}}{2}\right)^{9/10} \left(\frac{H}{0.5 r_d}\right)^{-3/5} M_\odot, \qquad (5.18)$$

where we have dropped scalings with f and A since they appear raised to the 1/10 power. This estimate is consistent with the fact that our $M_{d,1} = 0.1 M_\odot$ model is not advective at early times, as seen in Figures 5.2 and 5.4. In this case only phases (2) and (3) are seen, i.e., the disk is initially thin and neutrino cooled and later transitions to being advective.

Once the models reach the late-time, RIAF phase, or phase (3), they asymptote to self-similar solutions, independent of the initial disk mass. In this phase, the disk has $q_{\rm adv} > q_\nu^-$ and is radiation pressure dominated. We derive analytic self-similar solutions in Appendix B2 for this limit and show that $r_d \propto t^{2/3}$, $M_d \propto t^{-1/3}$ and $\dot{M}_d \propto t^{-4/3}$. The RIAF solution occurs external to an "ignition radius," which we estimate as the location where the pair capture cooling rate balances $\sim 1/2$ of

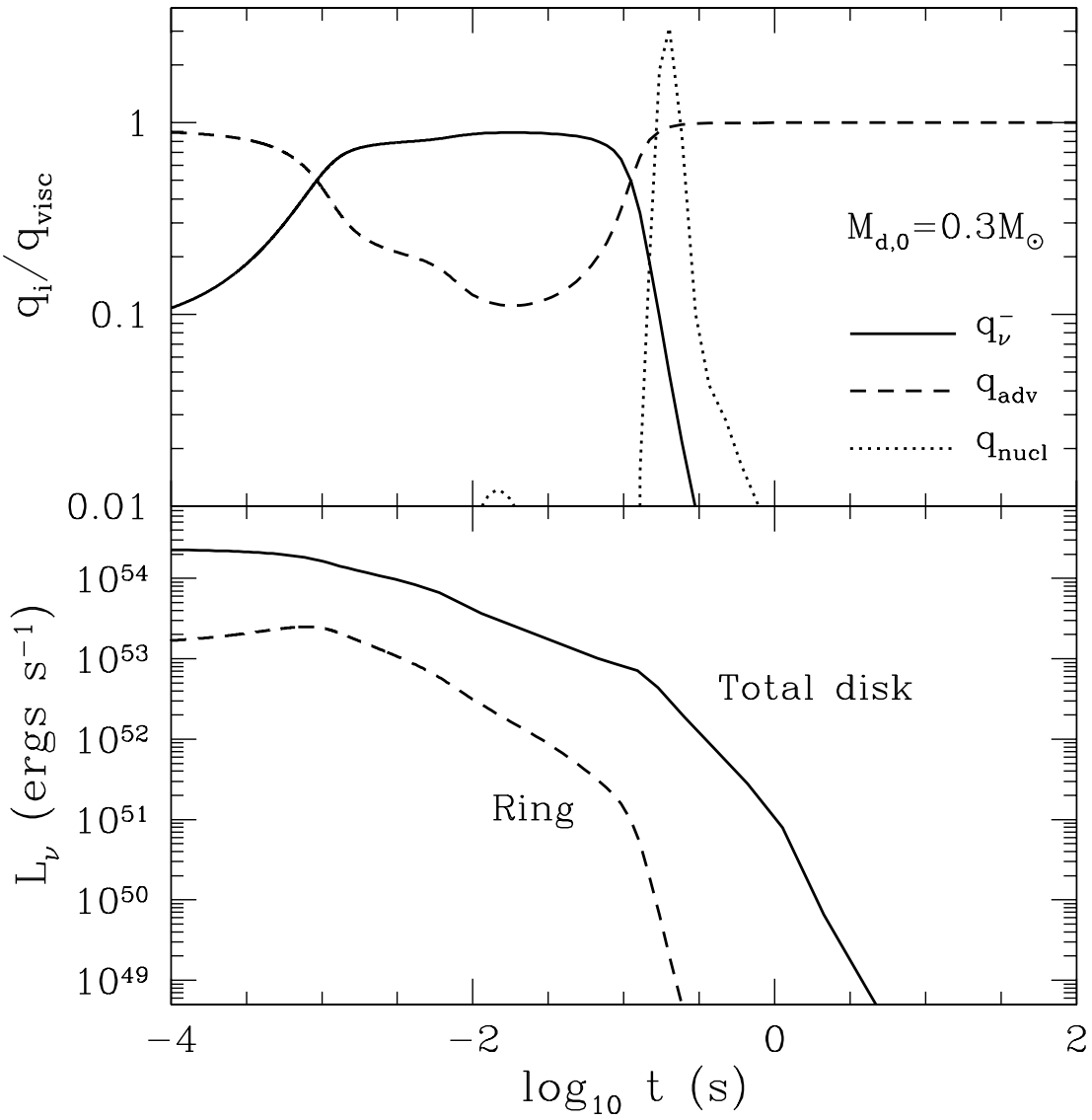

Figure 5.3: The cooling rates and neutrino luminosity for the $M_{d,0} = 0.3M_\odot$ model from Fig. 5.1. For the cooling rates we compare the neutrino (*solid line*) and advective (*dashed line*) rates, normalized to the viscous heating. The implied heating from the creation of α-particles is plotted as a dotted line, but is not accounted for in the disk evolution. The neutrino luminosities are from the entire disk (*solid line*) and the ring (*dashed line*). The former luminosity is estimated by integrating over a steady-state disk model at each time given $\dot{M}_d(t)$.

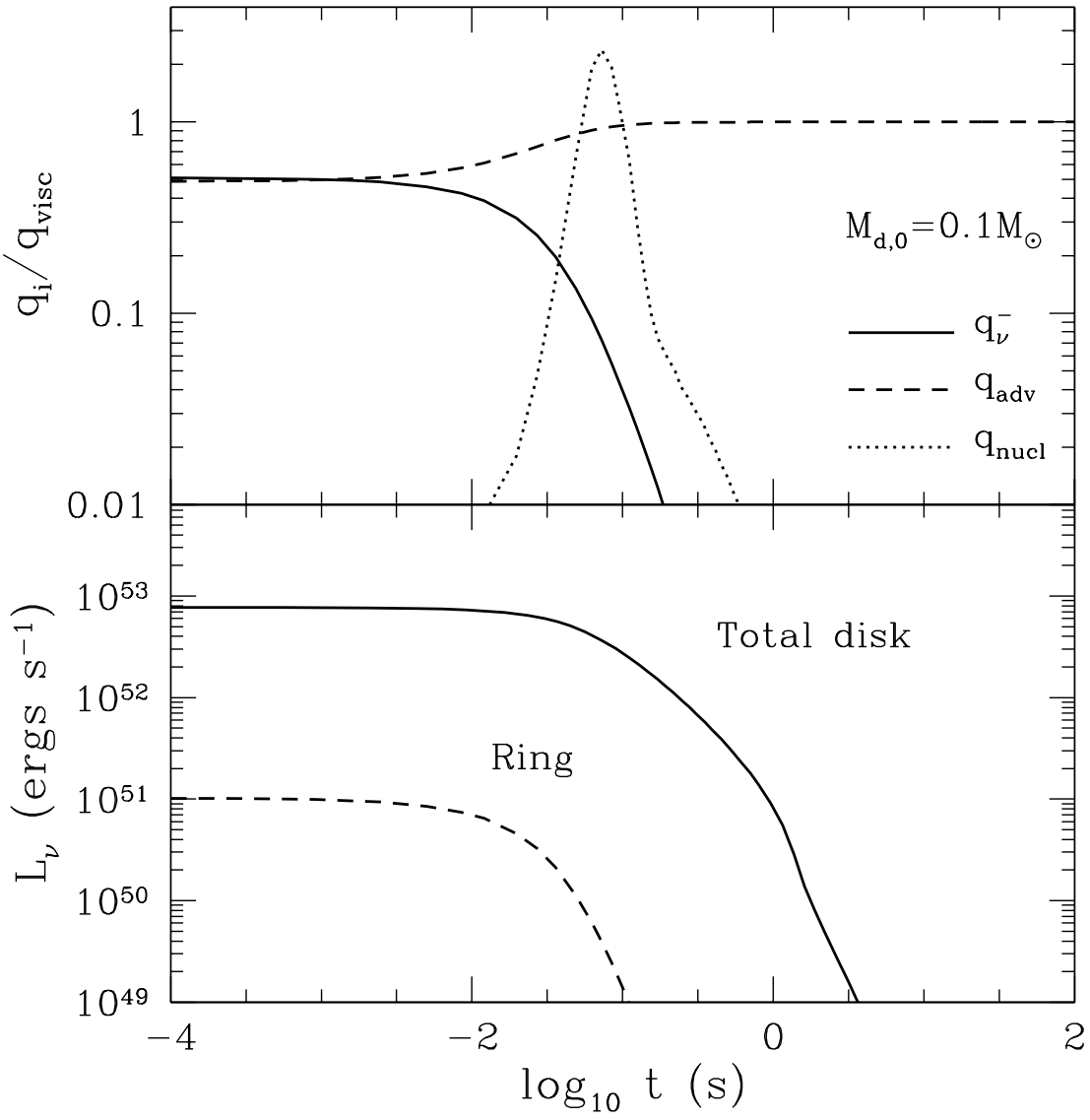

Figure 5.4: The same as Fig. 5.3, but for $M_{d,0} = 0.1M_\odot$.

the viscous heating for a thick disk,

$$r_{\rm ign} \simeq 3 \times 10^7 \alpha_{0.1}^{-2} M_3^{-3/5} \left(\frac{H/r_d}{0.4}\right)^{-14/5} \left(\frac{\dot{M}_d}{0.1 M_\odot {\rm s}^{-1}}\right)^{6/5} {\rm cm}, \tag{5.19}$$

where we have scaled H/r_d to ≈ 0.4, a value appropriate for the transition between the thin and thick disk regimes. We combine this with the analytic results for $r_d(t)$ and $\dot{M}_d(t)$ in the RIAF limit (eqs. [5.48] and [5.47])[5] to estimate the time when the disk transitions to being thick, which yields

$$t_{\rm thick} \sim 0.1 \alpha_{0.1}^{-23/17} M_3^{-13/17} \left(\frac{J_{49}}{2}\right)^{9/17} {\rm s}. \tag{5.20}$$

Equation (5.20) is only applicable if the disk is thin at early times. For sufficiently small initial disk masses, less than

$$M_{d,{\rm thick}} \sim 0.1 \alpha_{0.1}^{2/17} M_3^{-7/17} \left(\frac{J_{49}}{2}\right)^{14/17} M_\odot, \tag{5.21}$$

this is no longer true, and the disk is always a RIAF at its outer radius.

Figures 5.3 and 5.4 show that at approximately the same time as the disk transitions from being thin to thick, protons and neutrons are fused to He. Although the nuclear heating rate $q_{\rm nuc}$ is shown in Figures 5.3 and 5.4, this heating was not included in our time-dependent calculations so that we could obtain solutions at late times. The nuclear heating rate is sufficiently large, i.e, $q_{\rm nucl} \gtrsim q_{\rm visc}$, that the disk is not able to accommodate this added energy (it is already thick with $H \simeq r$ due to viscous heating alone). This probably implies that the burning contributes to driving a powerful wind (as described by Lee & Ramirez-Ruiz 2007).

However, such a wind already begins at this time by virtue of the disk being advective (as discussed in §5.5.2). In Appendix B3, we present analytic self-similar solutions for advective disks with mass loss and show that this significant mass-loss causes M_d and $\dot{M}_d$ to decline much more rapidly with time than is shown in Figure 5.1. This is shown explicitly in Figure 5.6, where we present disk models calculated using the mass and angular momentum-loss prescriptions described in

[5] We use these solutions rather than the thin-disk ones because the numerical results follow these more closely (Fig. 5.15).

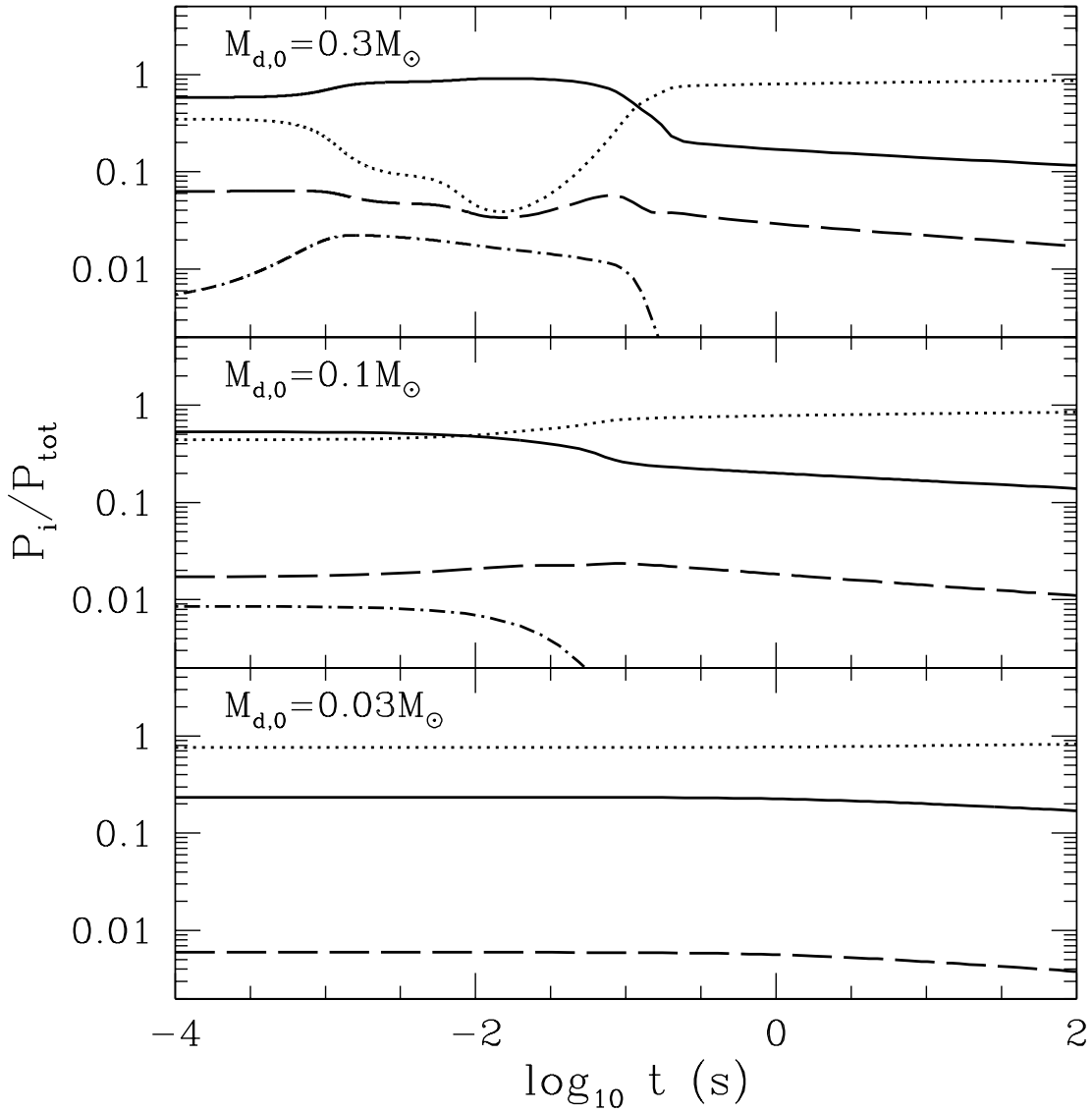

Figure 5.5: Pressure contributions for $M_{d,0} = 0.3M_\odot$ (*top panel*), $0.1M_\odot$ (*middle panel*) and $0.03M_\odot$ (*bottom panel*). The pressures are all normalized to the total pressure and include the ion pressure (*solid lines*), radiation pressure (*dotted lines*), degenerate electron pressure (*dashed line*), and neutrino pressure (*dot-dashed line*).

Appendix B3; such losses are assumed to occur only when the disk is thick, between $\sim \max(r_*, r_{\rm ign})$ and $\sim r_d$. Figure 5.6 compares time-dependent solutions with no wind (*solid line*), a wind with $p = 0.5$ (*dotted line*; see eq. [B8]), and a wind with $p = 1$ (*dashed line*).[6] The loss of angular momentum does not appreciably slow the radial expansion of the disk, but it does substantially accelerate the decline in the disk mass and accretion rate (see also eqs. [5.53] and [5.54]). If the models with winds are accurate, significant accretion is only likely to last for a few viscous times once the disk enters the late-time advective phase. Continued central engine activity at much later times could result from late-time infall of tidally stripped NS material (e.g., Lee & Ramirez-Ruiz 2007).

As an additional comparison, we present the effect of varying J_d in Figure 5.7. The main trend is that a higher J_d has a larger initial radius for a given M_d, and therefore a longer viscous time and smaller accretion rate. The late time behavior is more sensitive to J_d than the initial M_d, as predicted by the self-similar solutions, but it still does not affect the late time disk radius (see eq. [5.48]). We do not plot our results for different α since they are generally consistent with the analytic scalings above and in Appendix B.

5.4.2 Composition

The composition of the disk is important for determining the observational effects of any outflows. To this end, we plot the composition of our $M_{d,0} = 0.3\ M_\odot$, $J_{49} = 2$ disk as a function of time in the upper panel of Figure 5.8. In the bottom panel we plot the relevant timescales for setting the composition, namely the viscous timescale, $t_{\rm visc}$ (*solid line*), the neutronization timescale $t_n = 1/r_{e^-p}$ (*dotted line*), and the timescale for α-particle photodisintegration, $t_{\rm photo}$ (*dashed line*). At early times $t_n \ll t_{\rm visc}$, so that an equilibrium value of $Y_e \simeq 0.23$ is reached almost immediately. As the disk leaves the optically thick phase and becomes thinner, degeneracy pressure plays a larger role. This enhances neutron production, with a minimum $Y_e \simeq 0.05$. As the neutrino cooling subsides and the

[6] See Appendix B3 for the definition of p.

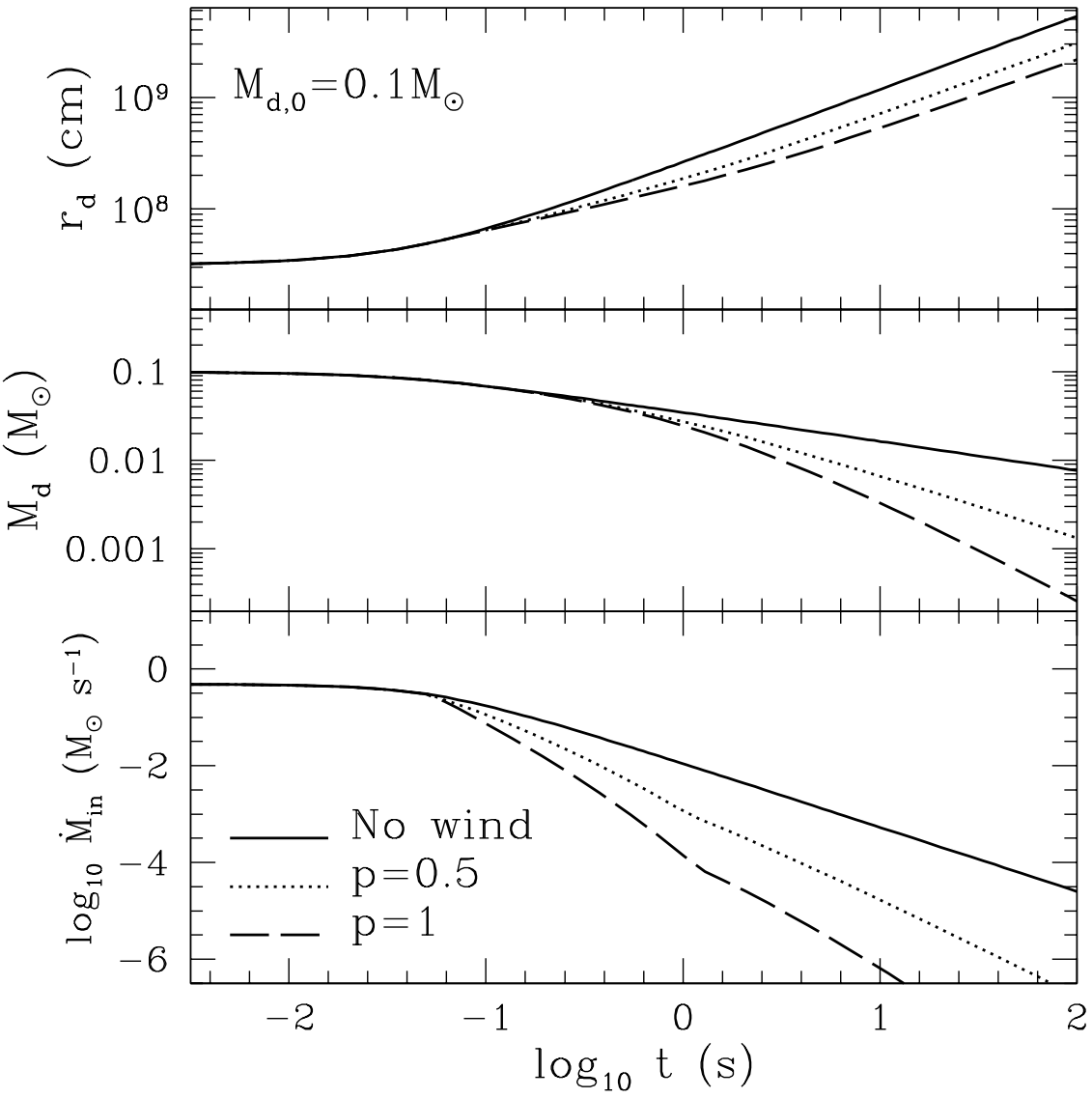

Figure 5.6: The radius r_d, disk mass M_d, and mass accretion rate reaching the central BH $\dot{M}_{\rm in}$ for different parameterizations of wind mass-loss during the advective phase. We initialize a disk with $M_{d,0} = 0.1M_\odot$ (and all other parameters fixed as in Fig. 5.1) and compare solutions with no wind (*solid line*), $p = 0.5$ (*dotted line*; see eq. [B8]), and $p = 1$ (*dashed line*).

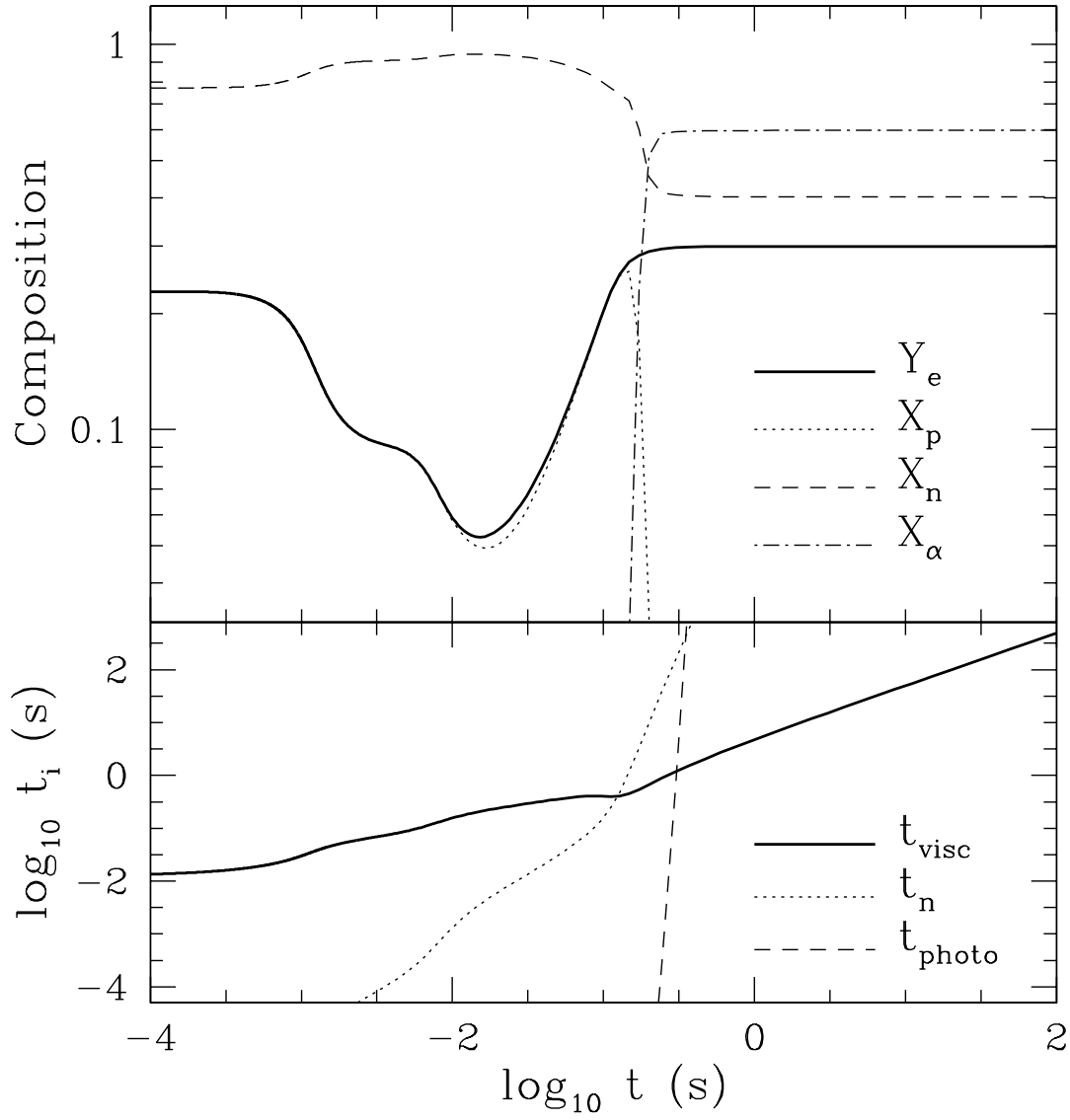

Figure 5.7: Similar to Fig. 5.1, but now taking the angular momentum to be $J_{49} = 2$ (*solid lines*), 4 (*dotted lines*), and 6 (*dashed lines*). All solutions take $M_{d,0} = 0.3M_\odot$ with all other variables the same as in Fig. 5.1.

disk becomes thick again, Y_e increases. Before Y_e can reach $\simeq 0.5$, it freezes-out at a value of $Y_e \simeq 0.3$ once $t_n > t_{\rm visc}$.

Besides the neutron abundance, Figure 5.8 also highlights the production of α-particles. Initially, the reactions needed to convert neutrons and protons to helium as well as photodisintegration of helium all happen on timescales much shorter than the disk evolution timescale (as an example, we plot the helium photodisintegration timescale in the bottom panel of Fig. 5.8), so that we can estimate the α-particle mass fraction using chemical balance (eq. [5.17]). Once the α-particle photodisintegration timescale becomes sufficiently long ($t_{\rm visc} < t_{\rm photo}$), chemical equilibrium no longer applies and $X_p = 0$, $X_n = 1 - 2Y_e \simeq 0.4$, and $X_\alpha = 2Y_e \simeq 0.6$.

Figure 5.9 shows how the late-time, frozen-out value of Y_e in the disk depends on the initial disk mass $M_{d,0}$ and radius $r_{d,0}$, for two different initial electron fractions, $Y_{e,0} = 0.1$ and $Y_{e,0} = 0.5$. The former is relevant for the disks created from NS-NS or BH-NS mergers (the focus of this paper), while a larger $Y_{e,0} \simeq 0.5$ is appropriate for disks created during the accretion-induced collapse of a white-dwarf to a neutron star (e.g., Woosley & Baron 1992; Dessart et al. 2006). Figure 5.9 shows that for sufficiently compact disks, the disk reaches a modestly neutron-rich composition, with $Y_e \simeq 0.3 - 0.4$, independent of the initial composition. This is because, as highlighted in Figure 5.8, the timescale to come into β-equilibrium is shorter than the viscous time. For disks with a small initial mass and/or a large initial radius (the lower right-hand corner of each panel), $t_n > t_{\rm visc}$ and the disk retains its initial composition (set by the tidally-disrupted progenitor and the subsequent dynamical stage of the merger). Finally, neutrino irradiation of the outer disk by the inner disk can increases the freeze-out electron fraction, but we estimate this changes the freeze-out value of Y_e by at most $\sim 20\%$.[7]

[7]Our calculations employ the pair-capture cooling prescription of DiMatteo et al. (2002), which assume $Y_e = 0.5$ and ultra-relativistic electrons; we find, however, that including the effects of degeneracy and arbitrary electron energies on the cooling changes the asymptotic electron fraction by at most a few percent.

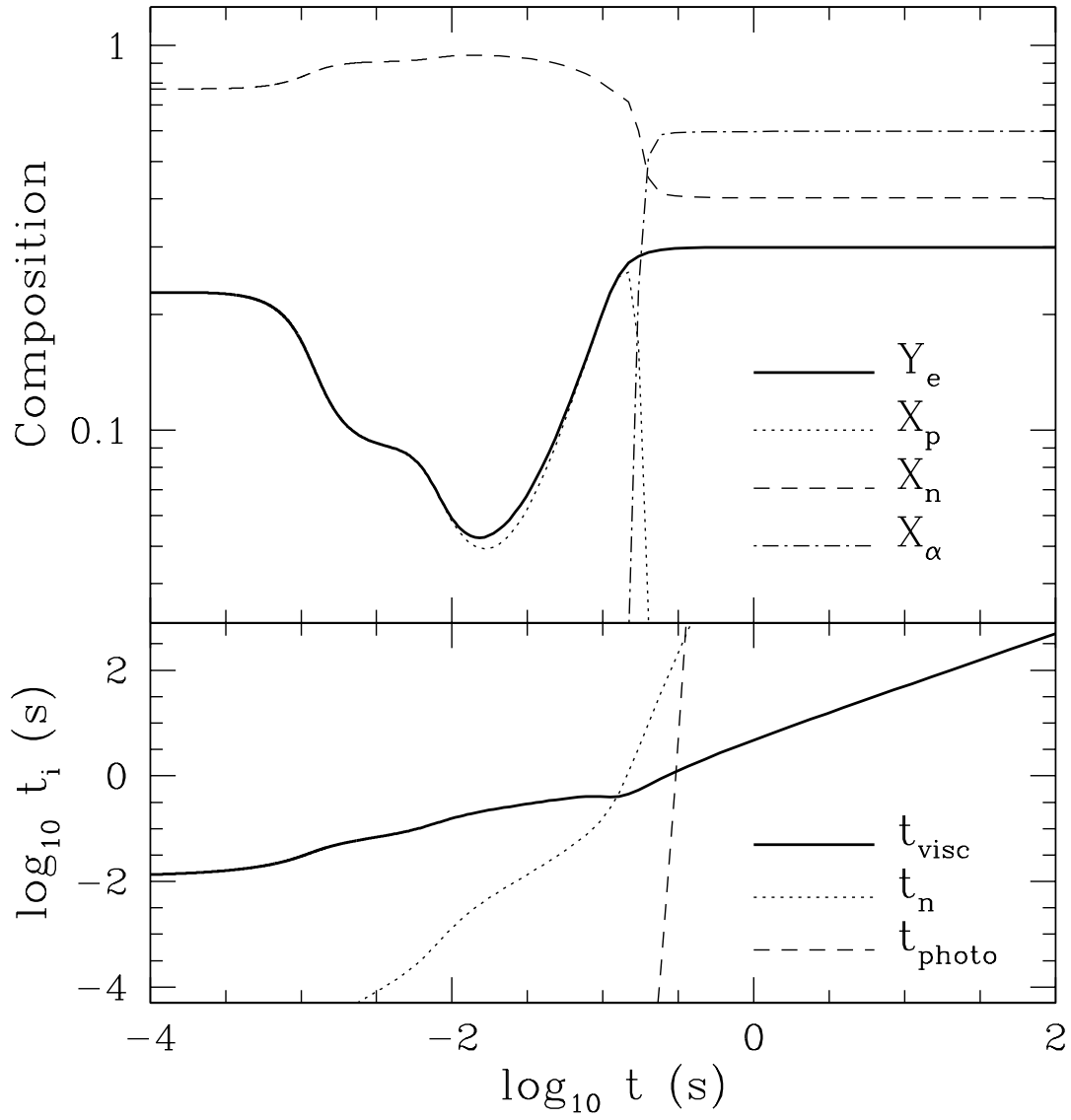

Figure 5.8: The composition and important reaction timescales as a function of time, for the $M_{d,0} = 0.3M_\odot$ model from Fig. 5.1. In the top panel we plot the electron fraction, Y_e and the mass fraction of protons, neutrons, and α-particles (*see inset key*). In the bottom panel we show the viscous time, $t_{\rm visc}$ (*thick, solid line*), the neutronization time, $t_n = 1/r_{e^-p}$ (*dotted line*), and the α-particle photodisintegration time, $t_{\rm photo}$ (*dashed line*).

5.5 Disk Winds

Having described the evolution of the accretion disk as a function of time, we now discuss the properties of outflows from these hyper-accreting disks. Winds driven from deep within the BH potential well could produce relativistic jets and power late-time central engine activity. Outflows driven from larger radii dominate the system's mass-loss and may power supernova-like optical transients through the decay of radioactive isotopes that are synthesized in the wind (Li & Paczyński 1998; Kulkarni 2005). In both cases, the mass-loss rate and nuclear composition are critical for determining the observable signature.

The type and character of the outflow depends on the disk's thermodynamic state and changes as it passes through the different stages of evolution described in the previous section. In §5.5.1 we discuss early times when winds are due to neutrino irradiation of the thin, efficiently neutrino-cooled portions of the disk. We then consider thermally driven winds during thick, radiatively-inefficient accretion in §5.5.2. This dominates the mass-loss at late times and blows away most of the remaining disk. In §5.5.3 we summarize the nuclear composition of the outflows during each phase. We predict an ejected ^{56}Ni mass of at most $\sim 10^{-3} M_\odot$ (§5.5.4). Its decay may power transient emission detectable following some short GRBs.

5.5.1 Neutrino-Heated Thin-Disk Winds

A wind with a mass-loss rate $\dot{M}_w$ driven from a thin disk at radius r must absorb a net power greater than $\dot{E}_b = GM\dot{M}_w/2r$ to become unbound from the central BH. In principle, $\dot{E}_b$ may be supplied by dissipation of the turbulence that produces the accretion shear stresses. "Viscous" heating of this kind only efficiently drives an outflow if a substantial fraction of the accretion power is dissipated in the disk's upper atmosphere, where the cooling timescale is long compared to the wind's outward advection timescale. However, local radiation MHD simulations to date suggest that very little energy dissipation occurs in the corona (e.g., Krolik et al. 2007). Instead, heating in the atmosphere above a thin, neutrino-cooled disk

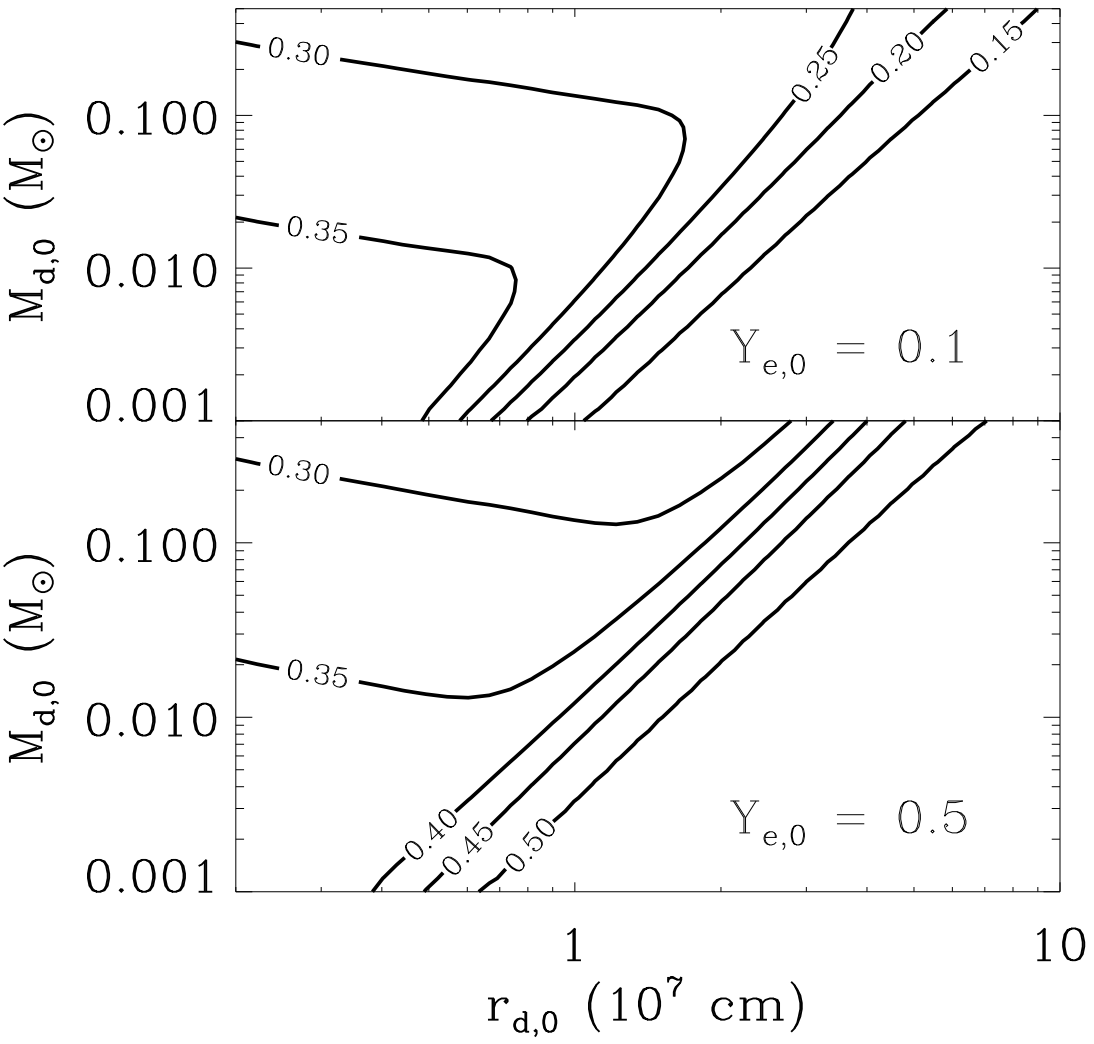

Figure 5.9: Contours of late-time electron fraction in the expanding disk as a function of initial disk mass $M_{d,0}$ and radius $r_{d,0}$, for two different initial compositions. Relatively compact disks come into β-equilibrium and reach an electron fraction independent of the initial Y_e, while low mass, more extended disks retain their initial composition. Figure 5.8 shows the evolution of Y_e with time for one particular disk solution.

is likely dominated by neutrino irradiation. We therefore focus on the neutrino-driven mass-loss rate, which sets a *minimum* $\dot{M}_w$, and which can be reliably estimated. Neutrino-driven outflows from hyper-accreting disks have also been studied in Chapter 4 and by Daigne & Mochkovitch (2002), Levinson (2006), and Barzilay & Levinson (2008); Dessart et al. (2008b) calculate the neutrino-driven mass-loss from the central NS following a NS-NS merger under the assumption that collapse to a BH is not prompt.

The neutrino-driven mass-loss rate is calculated by equating $\dot{E}_b$ to the total neutrino heating rate in the disk's atmosphere. For the radii and entropies that characterize the winds, heating via electron neutrino absorption on baryons ($p + \bar{\nu}_e \rightarrow n + e^+$ and $n + \nu_e \rightarrow p + e^-$) dominates other forms of neutrino heating (e.g., $\nu - \nu$ annihilation and $\nu - e^-$ scattering; see Qian & Woosley 1996; hereafter QW96). Since the neutrino absorption cross section, $\sigma_{\nu N} \simeq 5 \times 10^{-44} \langle \epsilon_\nu^2 \rangle$ MeV^{-2} cm^2, increases with neutrino energy, neutrinos radiated from near the inner radius r_* dominate. Assuming that the ν_e and $\bar{\nu}_e$ luminosities and spectra are approximately equal and can be approximated as originating from a point source at small radii, the neutrino heating rate through a surface density Σ at radius r is

$$q_\nu^+ = \frac{L_\nu \sigma_{\nu N} \Sigma}{4\pi m_N r^2} \simeq 2 \times 10^{39} L_{52} \langle \epsilon_{10}^2 \rangle \Sigma_{18} r_6^{-2} \, \mathrm{ergs\ s^{-1}\ cm^{-2}},$$

where $r = 10^6 r_6$ cm, $L_\nu = 10^{52} L_{52}$ ergs s^{-1}, $\langle \epsilon_\nu^2 \rangle = 100 \langle \epsilon_{10}^2 \rangle$ MeV^2, and $\Sigma = \Sigma_{18} 10^{18}$ g cm^{-2}. This expression assumes that the absorbing layer is optically thin, i.e., that $\tau_\nu \equiv \Sigma \sigma_{\nu N} / m_N \simeq 3 \Sigma_{18} \langle \epsilon_{10}^2 \rangle < 1$.

First, consider neutrino heating in comparison to viscous heating in the midplane. This ratio is largest when the disk is marginally optically thick ($\tau_\nu \simeq 1$), peaking at a value of

$$\left. \frac{q_\nu^+}{q_{\rm visc}} \right|_{\tau_\nu \simeq 1} \simeq 0.5 \left(\frac{\epsilon}{0.1} \right) \left(\frac{f}{1.6} \right) \left(\frac{A}{3.6} \right)^{3/5} \langle \epsilon_{10}^2 \rangle^{2/5} J_{49}^{2/5} M_3^{-6/5}, \qquad (5.23)$$

where $\epsilon \equiv L_\nu / \dot{M}_d c^2$ is the disk's radiative efficiency. Thus, although we neglected neutrino heating in §5.4, it may become somewhat important when $\tau_\nu \sim 1$ and should be included in a more detailed calculation.

We now consider a wind that emerges from the disk in the z-direction, parallel to the rotation axis. Away from the disk midplane, neutrino heating dominates over viscous heating, balancing cooling ($q_\nu^+ = q_\nu^-$) at a slightly lower temperature, $T_\nu \simeq 3.3 L_{52}^{1/6} \langle \epsilon_{10}^2 \rangle^{1/6} r_6^{-1/3}$MeV. Moving further out in the hydrostatic atmosphere, the temperature slowly decreases below T_ν. Due to the strong temperature dependence of the pair capture cooling rate ($q_\nu^- \propto T^6$), a "gain region" of net neutrino heating (i.e., $q_\nu^+ > q_\nu^-$) develops above a height $z_{\rm gain}$. This net heating drives an outflow.

The thermal power deposited in the upper disk atmosphere $\dot{E}_\nu$ is the specific heating rate q_ν^+/Σ (eq. [5.22]) multiplied by the mass of the atmosphere in the gain region $M_{\rm gain} \simeq 2\pi H(z_{\rm gain}) r^2 \rho(z_{\rm gain})$, where $H(z_{\rm gain})$ is the scale height near the base of the gain region. Although the midplane of a neutrino-cooled disk is generally dominated by nonrelativistic gas pressure (see Fig. 5.5), the gain region has a sufficiently low density that it is instead dominated by radiation pressure $P_{\rm rad} = (11/12) a T^4$. Its scale height is $H(z_{\rm gain}) \simeq (P_{\rm rad}/\rho g_{\rm z})|_{z_{\rm gain}}$, where $g_{\rm z}$ is the gravitational acceleration in the z-direction. Since $H(z_{\rm gain})$ is less than the midplane scale height H, $z_{\rm gain} \simeq$ H and $g_{\rm z} \simeq GMH/r^3$. The atmosphere in the gain region is roughly isothermal so we set $T(z_{\rm gain}) \approx T_\nu$. By combining these estimates and equating $\dot{E}_\nu$ with $\dot{E}_b$ we find that the neutrino-driven mass-loss rate from a thin disk is

$$\dot{M}_\nu|_{S^a \gg S_{\rm N}} \approx 10^{-6} L_{52}^{5/3} \langle \epsilon_{10}^2 \rangle^{5/3} r_6^{5/3} M_3^{-2} (H/r)^{-1} M_\odot {\rm s}^{-1}, \tag{5.24}$$

analogous to that derived by QW96 for proto-neutron star winds. The assumption that the atmosphere is radiation dominated is only valid if the asymptotic entropy in relativistic particles S^a exceeds that in nonrelativistic nucleons $S_{\rm N} \simeq 6 + \ln(T_{\rm MeV}^{3/2}/\rho_{10}) k_B$ baryon^{-1}, where $T = T_{\rm MeV}$ MeV. By dividing the energy gained by a nucleon in the wind $\simeq GMm_N/2r$ by the gain region temperature $T(z_{\rm gain})$, we estimate

$$S^a \simeq 60 L_{52}^{-1/6} \langle \epsilon_{10}^2 \rangle^{-1/6} r_6^{-2/3} M_3 \ k_{\rm B} \, {\rm baryon}^{-1} \tag{5.25}$$

as the asymptotic wind entropy.

Although equation (5.24) does not strictly hold when $S^a \sim S_{\rm N}$, QW96 show that $\dot{M}_\nu$ scales the same way with L_ν, $\langle\epsilon_\nu^2\rangle$, M, and r, but with a larger normalization of

$$\dot{M}_\nu|_{S^a\sim S_{\rm N}} \approx 10^{-5} L_{52}^{5/3}\langle\epsilon_{10}^2\rangle^{5/3} r_6^{5/3} M_3^{-2}(H/r)^{-1} M_\odot {\rm s}^{-1}. \quad (5.26)$$

The mass-loss rate is higher for low entropy winds because neutrino heating peaks further off the disk surface, which reduces the binding energy and gravitational acceleration of matter in the gain region. Using the numerical disk wind calculations described in Chapter 4 we have verified that equation (5.26) holds to within a factor $\simeq 2$ when $S^a \sim S_{\rm N}$.

In deriving equations (5.24) and (5.26), we have implicitly assumed that the timescale for neutrinos to heat matter in the gain region $t_{\rm heat} \equiv (U_{\rm th}\Sigma/\rho q_\nu^+)|_{z_{\rm gain}}$, where $U_{\rm th} \simeq 3P_{\rm rad}$ is the thermal energy density, is short compared to $t_{\rm visc}$, the timescale over which the disk properties appreciably change. Equating S^a (eq. [5.25]) to the entropy in relativistic particles $\propto T^3/\rho$, we find that

$$\rho(z_{\rm gain}) \simeq 10^8 r_6^{-1/3} L_{52}^{2/3}\langle\epsilon_{10}^2\rangle^{2/3} M_3^{-1} {\rm g\ cm^{-3}}. \quad (5.27)$$

Then, using equations (5.22) and (5.27), we have that[8]

$$t_{\rm heat} \simeq \left.\frac{3P_{\rm rad}}{\rho(q_\nu^+/\Sigma)}\right|_{z_{\rm gain}} \simeq 0.1\,{\rm s}\ L_{52}^{-1} r_6 \langle\epsilon_{10}^2\rangle^{-1} M_3 \quad (5.28)$$

For most of the disk solutions considered in this paper, we find that $t_{\rm heat} \lesssim t_{\rm visc}$ during the thin disk phase; thus, equations (5.24) and (5.26) are reasonably applicable near r_d.

Figure 5.10 compares the accretion rate $\dot{M}_d$ (*solid line*) with the neutrino-driven mass-loss rate $\dot{M}_\nu$. In order to determine L_ν and $\langle\epsilon_\nu^2\rangle$, we calculated steady-state disk models (e.g., Di Matteo et al. 2002) with the accretion rate set at each time according to our ring model with $J_{49} = 2$ and $M_d = 0.3 M_\odot$. We plot the neutrino-driven mass-loss rate $\dot{M}_\nu$ (eqs. [5.24] and [5.26]) at small (*dotted line*) and large (*short-dashed line*) radii. This shows that the mass-loss is dominated

[8]Equation (5.28) is also approximately equal to the outward advection timescale of the wind in the heating region.

by large radii where the majority of the mass lies, as expected since $\dot{M}_\nu \propto r^{5/3}$. The vertical dot-dashed line marks where the disk transitions to being thick (eq. [5.20]), after which neutrino-heating no longer dominates the wind mass-loss.

Outflows that are launched from small radii, near r_*, have the greatest potential to produce relativistic jets and to power high energy emission. But as we now argue, these neutrino-driven winds are too massive to become highly relativistic. Our calculation above focused on purely thermal, neutrino-driven winds, which accelerate matter to only a fraction of the escape speed (and thus are mildly relativistic). However, in the presence of a strong, large scale open poloidal magnetic field, a more powerful, magnetically-driven outflow is possible. Magnetocentrifugal support in the wind's hydrostatic atmosphere may further enhance mass-loss (e.g., Levinson 2006), but equation (5.24) still represents the *minimum* mass loading on field lines which thread a neutrino-cooled disk. Figure 5.10 shows that $\dot{M}_\nu(r_*) \sim 10^{-4} - 10^{-2} M_\odot$ s^{-1} during the thin disk phase. The luminosities of the prompt emission and late-time X-ray flares from short GRBs, however, do not typically exceed $L_\gamma \sim 10^{50}$ erg s^{-1} (and are often much lower; Nakar 2007). Thus, even assuming a modest radiative efficiency for the outflow of $\epsilon_w \sim 0.1$, the Lorentz factor Γ of a neutrino-heated disk wind must obey $\Gamma \simeq L_\gamma/[\epsilon_w \dot{M}_\nu(r_*)c^2] \lesssim 5$, which is inconsistent with existing compactness constraints on short GRBs (Nakar 2007). A more likely source for the relativistic outflows that power short GRBs and their late-time flares are nearly baryon-free field lines which thread the BH's event horizon (e.g., McKinney 2005). In addition, in §5.5.2 we argue that when the disk becomes advection dominated and neutrino irradiation effectively ceases, jet production may be more likely.

5.5.2 Radiatively-Inefficient Thick-Disk Winds

At late times ($t \sim t_{\rm thick}$; eq. [5.20]) the disk transitions from thin and neutrino-cooled to being advective. At this point a neutrino-driven outflow is unlikely to dominate the mass-loss, in part because the neutrino luminosity precipitously drops (Fig. 5.3 & 5.4). In addition, because RIAFs possess a positive Bernoulli

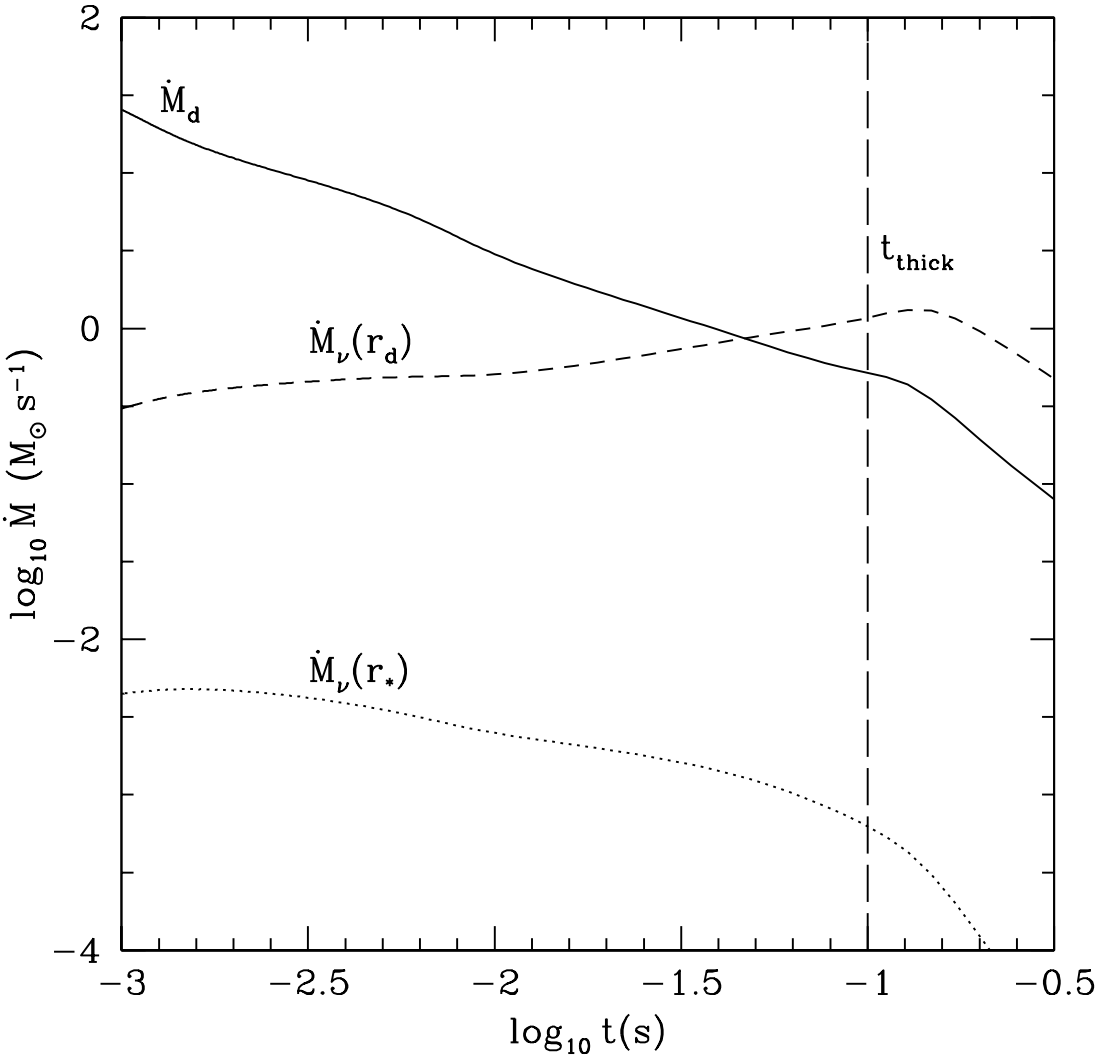

Figure 5.10: The accretion rate $\dot{M}_d$ (*solid line*) and neutrino-driven mass-loss rates $\dot{M}_\nu$ for our $J_{49} = 2$ and $M_{d,0} = 0.3 M_\odot$ model, focusing on the phase of thin, efficiently neutrino-cooled accretion. The neutrino-driven mass-loss rate $\dot{M}_\nu$ (interpolated between eqs. [5.24] and [5.26]) is shown at the inner disk radius ($r_* = 10^6$ cm; *dotted line*) and at the outer disk radius (near r_d, *short-dashed line*). The disk is advective to the right of the vertical line (eq. [5.20]), at which point the mass-loss will no longer be dominated by neutrino irradiation.

parameter, a powerful viscously-driven outflow is likely (Blandford & Begelman 1999; Stone & Pringle 2001; Proga & Begelman 2003).

In §5.4.1 we showed that the disk becomes radiatively inefficient external to an "ignition radius" $r_{\rm ign} \propto \dot{M}_d^{6/5}$ (eq. [5.19]). The outer disk, near r_d, thickens first (when $r_d \sim r_{\rm ign}$ at $t \sim t_{\rm thick}$) and radiatively inefficient conditions move inwards as $\dot{M}_d$ decreases. In the simplest picture, one might expect that the innermost radii become an RIAF only once $\dot{M}_d$ drops from its value at $t \sim t_{\rm thick}$ by an additional factor $\sim (r_*/r_d)^{5/6}$. In fact, the *entire* disk probably become radiatively inefficient on a timescale similar to $t_{\rm thick}$ if the accretion rate which reaches small radii abruptly decreases once the outer disk thickens (Fig. 5.6). Hence, at a time $t_{\rm thick}$, a significant portion of the accreting matter may be redirected into an outflow, with only a fraction $\sim (r_*/r_d)$ reaching small radii and accreting onto the BH (Stone & Pringle 2001).

X-ray binaries typically produce radio jets upon transitioning from their "high-soft" (radiatively efficient) to "low-hard" (radiatively inefficient) states (e.g., Remillard & McClintock 2006). In analogy, once the inner disk becomes an RIAF, conditions seem to favor the production of relativistic jets (see also Lazzati et al. 2008).[9]

Even if only a fraction (r_*/r_d) of the mass remaining when the disk thickens actually reaches the origin, the total energy supply available would be

$$E_{\rm jet} \equiv \epsilon_{\rm jet} M_d(t_{\rm thick}) c^2 \left(\frac{r_*}{r_d(t_{\rm thick})}\right)$$

$$\simeq 3 \times 10^{50} \left(\frac{\epsilon_{\rm jet}}{0.1}\right) \left(\frac{r_*}{10^6 {\rm cm}}\right) \alpha_{0.1}^{6/17} M_3^{-4/17} \left(\frac{J_{49}}{2}\right)^{8/17} {\rm ergs}, \quad (5.29)$$

where $\epsilon_{\rm jet}$ is the fraction of the accretion energy used to power a jet and we have estimated $M_d(t_{\rm thick})$ and $r_d(t_{\rm thick})$ using the self-similar thick disk solutions (eqs. [5.46] and [5.48], respectively). Equation (5.29) shows that the accretion energy available from near r_* following the RIAF transition is more than sufficient

[9] This is in stark contrast to jets powered by neutrino annihilation along the polar axis, which require a *high* radiative efficiency.

to power the late-time X-ray flares observed following some short GRBs. If this is the case, $t_{\rm thick}$ sets a characteristic timescale for late-time central engine activity. If $\alpha \lesssim 10^{-3}$, $t_{\rm thick}$ may be large enough to explain the ~ 30 s delay until flaring observed for some short GRBs (e.g., Berger et al. 2005; Villasenor et al. 2005). However, very late time energy injection, such as the *Chandra* flare observed two weeks after GRB050709 (Fox et al. 2005), appears to require an alternative explanation. In addition, given observational evidence for $\alpha \sim 0.1$ in a number of environments (King et al. 2007), it may be more natural to associate $E_{\rm jet}$ and $t_{\rm thick}$ with the energy and duration, respectively, of the short GRB itself, rather than the late-time central engine activity (see §5.6).

5.5.3 Outflow Nuclear Composition

The outflow nuclear composition has important consequences for the observable signature of compact object mergers. Nonrelativistic outflows are sufficiently dense to synthesize heavy isotopes (Pruet et al. 2004; Surman et al. 2006), which may power transient emission via radioactive decay. The isotopic yield depends on the speed, thermodynamic properties, and the asymptotic electron fraction Y_e^a in the outflow.[10] Although relativistic winds from the inner disk are unlikely to synthesize anything heavier than He (Lemoine 2002; Beloborodov 2003a), Y_e^a is important in this case as well. A neutron-rich outflow may alter the jet's dynamics and the prompt and afterglow emission from that of the standard GRB fireball model (e.g., Derishev et al. 1999; Beloborodov 2003b; Rossi et al. 2006).

Figure 5.11 delineates different regimes of outflow properties and composition (as given by Y_e^a) as a function of the wind launching radius r and accretion rate $\dot{M}_d$. We fix $\alpha = 0.1$ and $M = 3M_\odot$. The time-dependent evolution of the ring radius r_d is shown for a solution with $J_{49} = 2$ and $M_{d,0} = 0.3M_\odot$ (*solid line*). At each time a given steady-state disk profile can be read off of this plot as a horizontal line that extends from the far left and ends on r_d. Therefore, outflows

[10] The *asymptotic* electron fraction is germane because heavy nuclei primarily form after freeze-out from β-equilibrium.

from radii *interior* to r_d contribute to the disk's total nucleosynthetic yield.

The ignition radius $r_{\rm ign}$ (eq. [5.19]) is shown in Figure 5.11 with a short dashed line. For $r \gtrsim r_{\rm ign}$ the disk is an RIAF and marked in the figure as "Thick Disk." In this case, a viscously driven outflow dominates (§5.5.2). Since outflows from RIAFs escape the disk in roughly the accretion timescale, these winds retain the midplane electron fraction (Chapter 4), so that $Y_e^a \simeq Y_e^{\rm mid} \ll 0.5$ (because the disk itself freezes-out neutron-rich, as summarized in §5.4.2 and Fig. 5.9).

For $r \lesssim r_{\rm ign}$, the disk is efficiently neutrino-cooled and marked in Figure 5.11 as "Thin Disk." The absorption of neutrinos, which heats the outflow and unbinds it from the BH may also alter its nucleonic composition. This drives Y_e^a to a value set by the neutrino radiation field Y_e^ν, which in general is different from $Y_e^{\rm mid}$. A simple criterion was discussed in Chapter 4 for determining when $Y_e^a \simeq Y_e^\nu$. A typical nucleon in the accretion disk at radius r must absorb an energy $\simeq GMm_N/2r$ to become unbound from the BH, so that $N_\nu \simeq GMm_N/2r\langle\epsilon_\nu\rangle$ neutrinos must be absorbed per nucleon. If we take $N_\nu > Q \sim 2-3$, then a typical nucleon has changed its identity ($p \rightarrow n$ or $n \rightarrow p$) at least several times.

This implies that all purely neutrino-driven outflows from radii smaller than

$$r_\nu \equiv \frac{GMm_p}{2Q\langle\epsilon_\nu\rangle} \simeq 10^7 M_3 \langle\epsilon_{10}\rangle^{-1}(Q/2)^{-1}\,{\rm cm}, \tag{5.30}$$

where $\langle\epsilon_\nu\rangle \equiv 10\langle\epsilon_{10}\rangle$ MeV, achieve $Y_e^a \simeq Y_e^\nu$, independent of the disk's midplane composition.

We plot r_ν with $Q = 2$ as a dotted line in Figure 5.11, where $\langle\epsilon_\nu\rangle$ is calculated from $\dot{M}_d$ using our steady-state disk solutions (see §5.5.1). For $r \lesssim r_\nu$, any neutrino-driven outflow enters equilibrium with the neutrino radiation field (i.e., $Y_e^a \simeq Y_e^\nu$). For $r \gtrsim r_\nu$ the outflow approximately retains the midplane electron fraction (i.e., $Y_e^a \simeq Y_e^{\rm mid}$).

Although we have established the conditions under which Y_e^a is determined by neutrino absorptions, we must now address what sets Y_e^ν itself. If the rate of neutrino absorptions exceeds the rate of degenerate pair captures before the wind

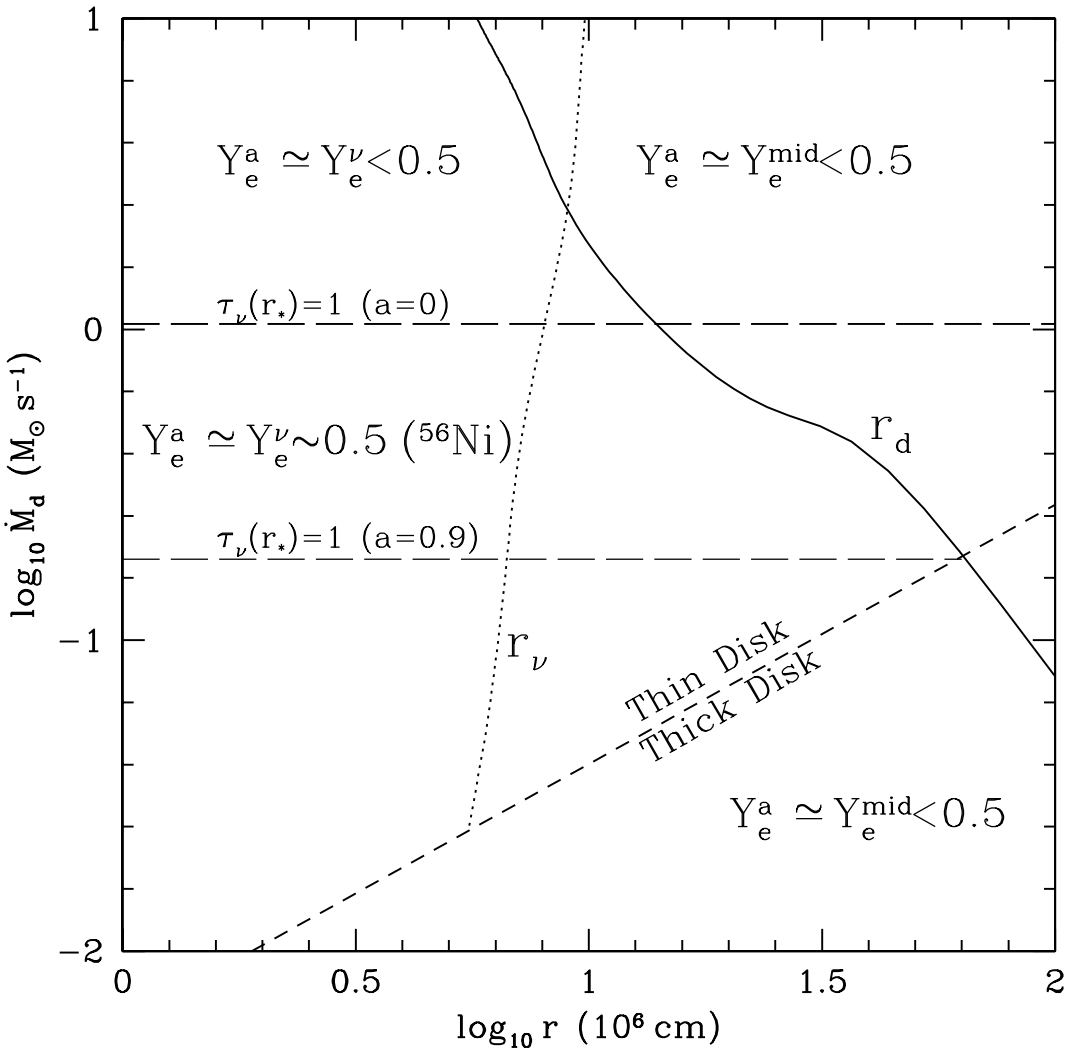

Figure 5.11: Asymptotic electron fraction Y_e^a for disk winds as a function of the wind launching radius r and accretion rate $\dot{M}_d$ (for $\alpha = 0.1$ and $M = 3M_\odot$). The solid line indicates the location of the ring radius r_d for our fiducial solution with $M_{d,0} = 0.3M_\odot$ and $J_{49} = 2$. The short dashed line is the "ignition" radius $r_{\rm ign}$ (eq. [5.19]). Exterior to this (marked "Thick Disk") the disk is advective with a viscously driven wind of composition $Y_e^a \simeq Y_e^{\rm mid} < 0.5$. Interior to $r_{\rm ign}$ (marked "Thin Disk") a neutrino-driven wind occurs. The dotted line shows $r = r_\nu$ with $Q = 2$ (eq. [5.30]) and determines where the neutrino absorptions necessary to unbind matter alter the wind composition, so that $Y_e^a \simeq Y_e^{\rm mid} < 0.5$ ($Y_e^a \simeq Y_e^\nu$) exterior (interior) to r_ν. The $\dot{M}_d$ above which $\tau(r_*) > 1$ is plotted for BH spins of $a = 0$ and $a = 0.9$. Above this line, the $\bar{\nu}_e$ and ν_e spectra differ and $Y_e^\nu < 0.5$, while below this their spectra are similar and $Y_e^\nu \simeq 0.5$. In the region where $r < r_{\rm ign}$, $\tau_\nu(r_*) < 1$, and $r < r_\nu$ (i.e., the middle/lower left-hand trapezoid), $Y_e^a \simeq Y_e^\nu \sim 0.5$; these conditions are favorable for ^{56}Ni production (see §5.5.4).

falls out of β-equilibrium, Y_e^ν is

$$Y_e^\nu \equiv \left(1 + \frac{L_{\bar{\nu}_e}}{L_{\nu_e}} \frac{\langle \epsilon_{\bar{\nu}_e} \rangle - 2\Delta + 1.2\Delta^2/\langle \epsilon_{\bar{\nu}_e} \rangle}{\langle \epsilon_{\nu_e} \rangle + 2\Delta + 1.2\Delta^2/\langle \epsilon_{\nu_e} \rangle}\right)^{-1}, \tag{5.31}$$

where $\Delta = 1.293$ MeV is the neutron-proton mass difference, and $L_{\nu_e}/L_{\bar{\nu}_e}$ and $\langle \epsilon_{\nu_e} \rangle / \langle \epsilon_{\bar{\nu}_e} \rangle$ are the mean $\nu_e/\bar{\nu}_e$ luminosities and energies, respectively, from a centrally-concentrated source (Qian et al. 1993; QW96). Equation (5.31) demonstrates that the ν_e and $\bar{\nu}_e$ spectra are crucial for setting Y_e^ν.

Since the disk's luminosity and temperature peak at just a few r_g, Y_e^ν is primarily determined by conditions at small radii. At early times, the accretion disk may be optically thick near r_* and so the ν_e and $\bar{\nu}_e$ spectra depend on the temperatures at ν_e and $\bar{\nu}_e$ neutrinospheres, respectively. Since there are more neutrons than protons in the disk, the optical depth to ν_e through the disk is higher than to $\bar{\nu}_e$; thus, the temperature at the $\bar{\nu}_e$ neutrinosphere is higher than at the ν_e neutrinosphere. This implies $L_{\bar{\nu}_e} \gg L_{\nu_e}$, $\langle \epsilon_{\bar{\nu}_e} \rangle \gg \langle \epsilon_{\nu_e} \rangle$, and thus $Y_e^\nu \ll 0.5$. Using 3-dimensional calculations of the merger of NSs with zero spin, Rosswog & Liebendörfer (2003) find that at ~ 15 ms following merger, $L_{\bar{\nu}_e} \simeq 3.5 L_{\nu_e}$, $\langle \epsilon_{\nu_e} \rangle \simeq 9$ MeV, and $\langle \epsilon_{\bar{\nu}_e} \rangle \simeq 15$ MeV, which implies $Y_e^\nu \simeq 0.21$, consistent with our arguments (see also Surman et al. 2008). We conclude that when the disk is optically-thick near r_*, a neutron-rich outflow is again the most likely outcome. The critical accretion rate at which $\tau_\nu(r_*) = 1$ is shown in Figure 5.11 with a long dashed line for both $a = 0$ and $a = 0.9$.

Once the disk becomes optically thin near r_*, the difference between the ν_e and $\bar{\nu}_e$ spectra is much less pronounced. This occurs because (1) the neutrinos and antineutrinos originate from regions with the same temperature; (2) any net lepton flux out of the disk must remain modest (i.e., $L_{\nu_e}/\langle \epsilon_{\nu_e} \rangle \simeq L_{\bar{\nu}_e}/\langle \epsilon_{\bar{\nu}_e} \rangle$); and (3) the difference between the e^- and e^+ capture cross sections for $kT \gg \Delta - m_e c^2$ is small. Taking $\langle \epsilon_{\nu_e} \rangle \sim \langle \epsilon_{\bar{\nu}_e} \rangle \gg \Delta$, equation (5.31) shows that $Y_e^\nu \simeq 0.5$, a value in the range required to produce ^{56}Ni (which we discuss further in §5.5.4). Indeed, Chapter 4 used the steady-state, optically-thin α-disk calculations of Chen & Beloborodov (2007; hereafter CB07) to calculate the neutrino radiation fields carefully, and showed that $Y_e^\nu \gtrsim 0.5$ over the majority of the disk (see their Fig. 1).

Although the precise spectra extracted from an α-disk calculation should be taken with caution, the conclusion that the ν_e and $\bar{\nu}_e$ spectra are similar for optically thin accretion (and $Y_e^\nu \simeq 0.5$) is probably robust.

Figure 5.11 illustrates that under most conditions the outflows from hyper-accreting disks are neutron-rich. Neutron-rich material ejected during the initial dynamical phase of compact object mergers has long been considered a promising source for producing Galactic r-process elements, whose precise astrophysical origin remains uncertain (Lattimer & Schramm 1974; see, however, Qian 2000). In addition, Surman et al. (2008) find that winds driven from the remnant accretion disk at early times (when it is optically thick; upper left quadrant of Fig. 5.11) are sufficiently neutron-rich to produce successful r-process. The outflows driven from the advective disk at late times, however, are unlikely to produce r-process elements, given their modest entropies and electron fractions of $Y_e \gtrsim 0.3$ (Figs. 5.8 and 5.9). Instead, this modest Y_e material will be synthesized to form intermediate mass neutron rich isotopes (Hartmann et al. 1985).

5.5.4 ^{56}Ni Production and Optical Transients

As summarized in Figure 5.11, most of the material in the outflow driven from a hyper-accreting disk will be neutron-rich. Nonrelativistic neutron-rich ejecta are difficult to detect because isotopes synthesized from low Y_e material are themselves very neutron-rich and typically possess very short half-lives, on the order of seconds (e.g., Freiburghaus et al. 1999). Thus, most of the radioactive energy is released at high optical depths and suffers severe adiabatic losses before the photons can diffusively escape. By contrast, ejecta with $Y_e^a \simeq 0.5$ are easier to detect because they can produce a significant quantity of ^{56}Ni (Hartmann et al. 1985), an isotope better suited to powering observable emission because its half-life $\simeq 6$ days is comparable to the timescale on which the outflow becomes optically thin. From Figure 5.11 we see that outflows in a modest range of parameter space (middle/lower-left trapezoid) are capable of synthesizing ^{56}Ni. One caveat to this conclusion is that it only applies if the winds are primarily neutrino driven. If the outflow is instead

magnetocentrifugally driven by a moderately strong open poloidal magnetic field (e.g., Levinson 2006; Xie et al. 2007), then $Y_e^a \ll 0.5$ can result, even if $Y_e^\nu \simeq 0.5$ (Chapter 4). In what follows we assume that the wind's are primarily neutrino driven.

Under this assumption, Figure 5.12 shows the total ^{56}Ni mass, $M_{\rm Ni} = (X_{\rm Ni}/0.4)M_{Y_e=0.5}$, produced in outflows from hyper-accreting disks as a function of the disk's initial mass $M_{d,0}$ and radius $r_{d,0}$, where $M_{Y_e=0.5}$ is the total mass-loss with $Y_e^a \simeq 0.5$ and $X_{\rm Ni}$ is the average ^{56}Ni mass fraction synthesized in the wind. We calculate $M_{Y_e=0.5}$ by integrating the neutrino-driven mass-loss (eqs. [5.24] and [5.26]) across the $Y_e^a \simeq 0.5$ region in Figure 5.11, using $r_d(t)$ and $\dot{M}_d(t)$ from the disk evolution calculations described in §5.4.

Pruet et al. (2004) present calculations of $X_{\rm Ni}$ which are parameterized in terms of the asymptotic entropy S^a, mass-loss rate $\dot{M}_w$, and asymptotic velocity v^a of an outflow with $Y_e^a \simeq 0.51$. The mass $M_{Y_e=0.5}$ is dominated by outflows from radii $\sim 3\times10^6 - 10^7$ cm when $\dot{M}_d \sim 0.1 - 1 M_\odot$ s^{-1} (corresponding to $L_{52} \sim$ few); equation (5.25) thus gives $S^a \sim 10 - 30 k_B$ baryon^{-1} for the ejecta with $Y_e^a \simeq 0.5$. Purely neutrino-driven winds achieve asymptotic velocities which are typically below the escape speed of the central object (e.g., Thompson et al. 2001); thus, the asymptotic kinetic energy is most likely dominated by energy released during the formation of heavy elements. Because ~ 8 MeV baryon^{-1} is released in producing Fe-peak elements, we estimate that $v^a \simeq 0.1 - 0.15$ c. Applying these wind parameters to Figure 3 of Pruet et al. (2004), we estimate that $X_{\rm Ni} \sim 0.2-0.5$, thereby justifying our scaling for $X_{\rm Ni}$ in Figure 5.12.

Figure 5.12 shows that for large initial disk masses ($M_{d,0} \gtrsim 0.1 M_\odot$), the ejected Ni mass, $\sim 3\times10^{-4} - 10^{-3} M_\odot$, can be appreciable. Disks with moderate initial radii $r_{d,0} \sim 10^7$ cm are optimal for producing ^{56}Ni because they are sufficiently large to contain the radius $r_\nu \sim 10^7$ cm and yet are sufficiently compact to have a large initial accretion rate, which maximizes the neutrino luminosity and thus the neutrino-driven mass-loss. Conveniently, initial disk parameters from many compact object merger simulations (see §5.2) are in the range required to produce $\sim 10^{-4} - 10^{-3} M_\odot$ of Ni.

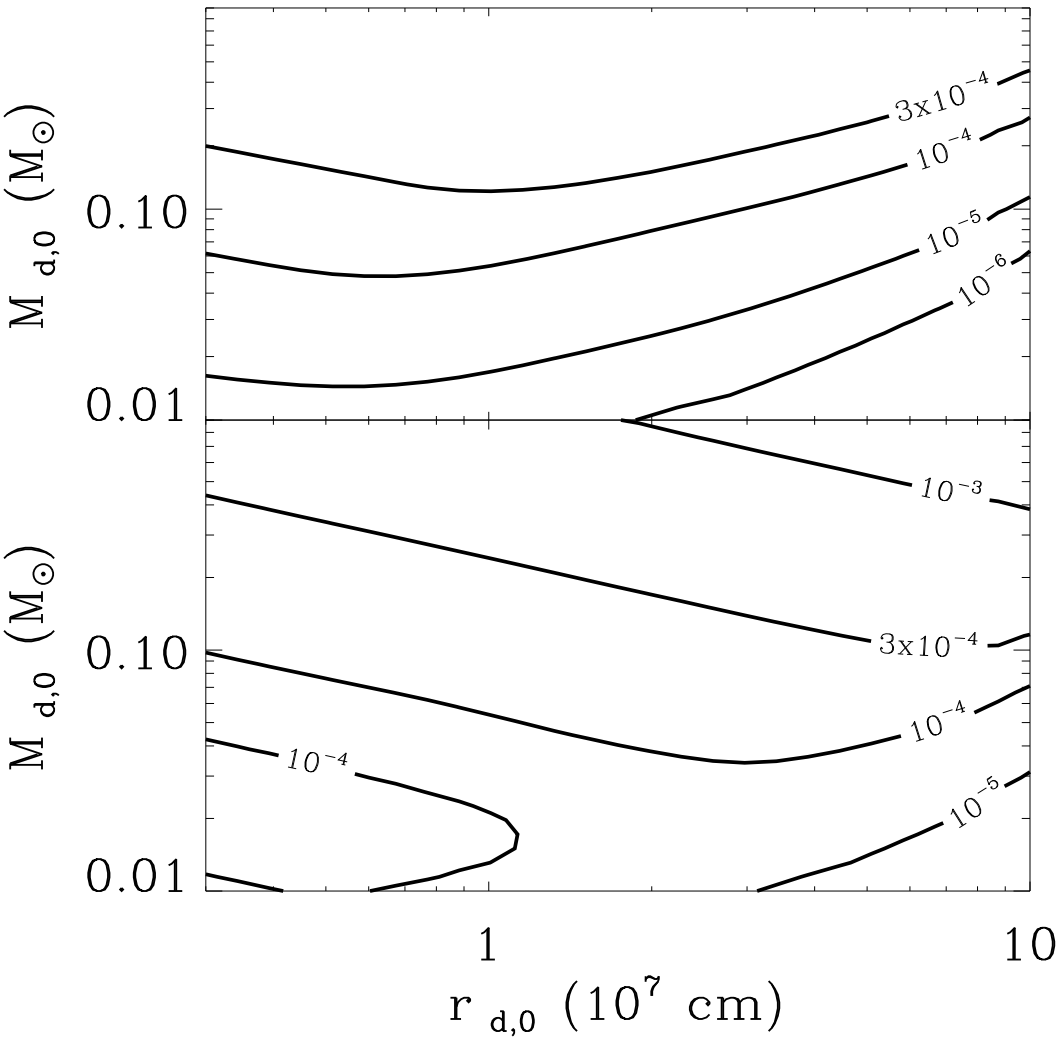

Figure 5.12: Contours of total ^{56}Ni mass $M_{\rm Ni} \equiv (X_{\rm Ni}/0.4) M_{Y_e=0.5}$ (in units of $M_\odot$) produced in the neutrino-driven outflows as a function of the initial disk mass $M_{d,0}$ and initial ring radius $r_{d,0}$, where $M_{Y_e=0.5}$ is the total mass-loss with $Y_e^a \simeq 0.5$ (based on the arguments in Fig. 5.11) and $X_{\rm Ni}$ is the average ^{56}Ni mass fraction synthesized in the wind. The upper and lower panels correspond to non-rotating ($a = 0$) and rapidly spinning ($a = 0.9$) BHs, respectively.

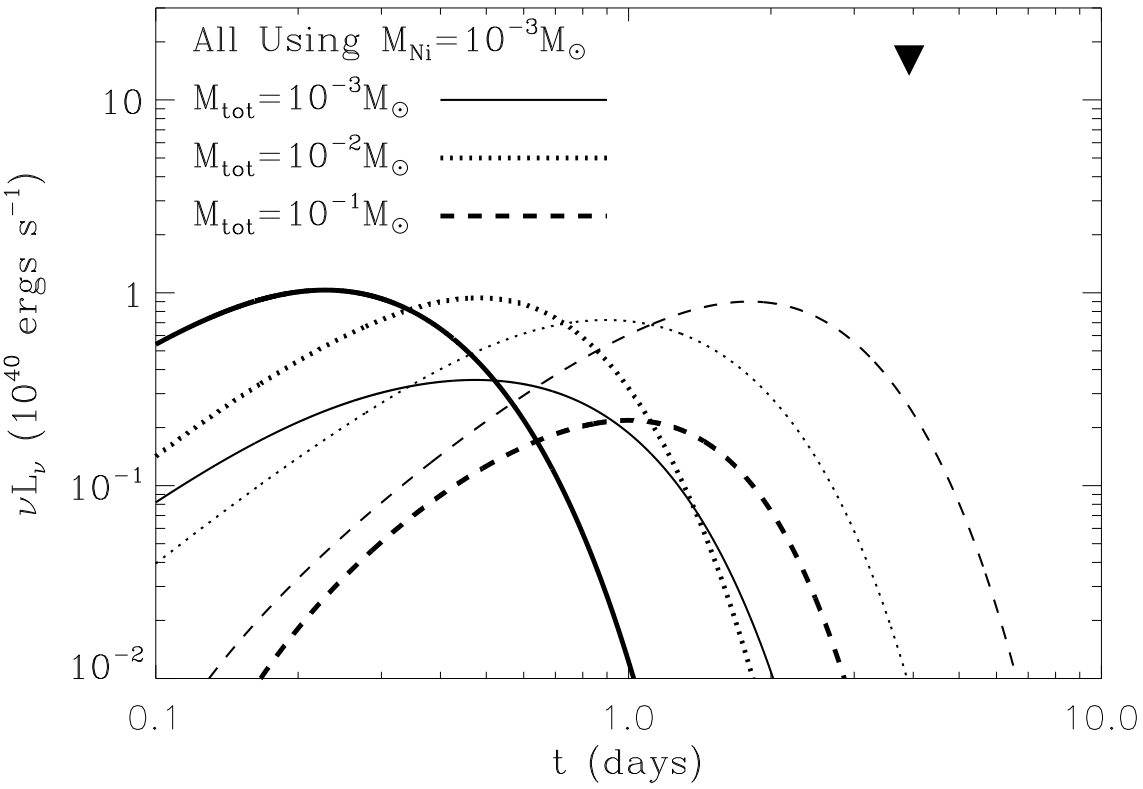

Figure 5.13: Luminosity of Ni decay-powered "macronovae" as a function of time since merger for Ni mass $M_{\rm Ni} = 10^{-3} M_\odot$ and ejecta velocity $v^a = 0.1$ c. Light curves are shown for three values of the total ejected mass $M_{\rm tot} = 10^{-3}$ (*solid line*), 10^{-2} (*dotted line*), and $10^{-1} M_\odot$ (*dashed line*). The luminosities in V and J-Band (0.44 and 1.26 μm, respectively) are shown with thick and thin lines, respectively. The V-band upper limit on emission following GRB050509B from Hjorth et al. (2005) is shown with a filled triangle.

The decay of $M_{\rm Ni} \sim 10^{-4} - 10^{-3} M_\odot$ can reheat the (adiabatically cooled) ejecta sufficiently to produce detectable transient emission. In order to explore this possibility, we calculate the light curves of ejecta heated by Ni decay ("macronovae") using the method of Kulkarni (2005). This simplified one-zone model accounts for the fraction of the gamma-rays produced by the Ni decay which are absorbed by the expanding material (Colgate et al. 1980) and assumes blackbody emission at the photosphere, neglecting Comptonization.

Figure 7.3 shows the V and J-band luminosities as a function of time since the merger for an outflow with Ni mass $M_{\rm Ni} = 10^{-3} M_\odot$ which is expanding at $v^a = 0.1$ c. The V-band light curve peaks earlier because the temperature at the photosphere decreases as the material expands. Somewhat after the peak in the light curves, recombination will decrease the opacity well below that considered here; thus our calculations are not quantitatively reliable at these times. The *total* mass $M_{\rm tot}$ ejected during the merger event, most of it neutron rich, is likely to be significantly larger than $M_{\rm Ni}$; this provides additional opacity for the Ni-rich material. To explore the effect of this additional material on the detectability of the Ni decay, the light curves in Figure 7.3 are shown for three values of $M_{\rm tot}$: $10^{-3} M_\odot$ (*solid line*), $10^{-2} M_\odot$ (*dotted line*), and $10^{-1} M_\odot$ (*dashed line*). As Figure 7.3 shows, larger $M_{\rm tot}$: (1) delays the time to peak emission ($t_{\rm peak}$ is roughly $\propto M_{\rm tot}^{1/2}$); (2) increases the total fluence of the event by trapping a higher fraction of the gamma-ray emission; and (3) increases the peak wavelength of the emission, pushing it into the near-IR for large $M_{\rm tot}$. We conclude that long wavelength ($\lambda \gtrsim \mu$m) observations at $t \sim 1$ day are the most promising for the detection of a Ni decay-powered macronova.

Hjorth et al. (2005) place an upper limit of $m_V > 27.5$ at $t = 3.9$ days on any emission associated with the short GRB 050509B (redshift $z \simeq 0.22$); we mark this constraint in Figure 7.3 with an arrow. For $M_{\rm tot} = 0.1 M_\odot$ this constrains the ejected Ni mass to be $M_{\rm Ni} \lesssim 10^{-2} M_\odot$ (see also Kulkarni 2005). As Figure 5.12 illustrates, compact object mergers are very unlikely to produce this much Ni, so the absence of a detection thus far is unsurprising.

5.6 Conclusion and Discussion

We have calculated the time-dependent evolution of accretion disks formed from compact mergers, and the properties of their outflows. Since most of the disk mass resides at large radii, we approximate the disk as a ring at a given radius and calculate the dynamics and composition of the ring as a function of time. This ring model is calibrated to correctly reproduces the Green's function solution for a viscously spreading ring with viscosity $\nu \propto r^{1/2}$ (appropriate for a thick disk; see Appendix A). With this simplified model, we have studied the full parameter space of remnant accretion disks (different initial masses, compositions, etc.) and can follow the viscous evolution for arbitrarily long timescales.

The energetics of the ring at a given time can be described by one of three models: (1) optically thick to neutrinos and advective, (2) optically thin to neutrinos and geometrically thin, and (3) optically thin to neutrinos and advective. A massive, compact disk (with a short initial viscous time $t_{\rm visc,0}$; eq. [5.5]) will exhibit all three of these accretion phases, evolving from (1) to (3) as a function of time (Figs. 5.1-5.4). Less massive disks, on the other hand, only pass through phases (2) and (3), or even just (3). Note that these phases refer to the energetics of the disk near the outer radius. At a given time, the disk may also undergo similar transitions as a function of radius; e.g., a disk that is advective at large radii will be neutrino cooled and geometrically thin inside the ignition radius $r_{\rm ign}$ (eq. [5.19]).

Neutrino-driven winds during the early-time optically thick and neutrino-cooled (thin disk) phases unbind so much mass that field lines connected to the disk cannot produce sufficiently relativistic material to power short-duration GRBs (§5.5.1 and Fig. 5.10). An alternative source for the relativistic material needed to produce short GRBs are nearly baryon-free magnetic field lines that thread the BH's event horizon (e.g., McKinney 2005). In addition, when the inner disk becomes advective ($\dot{M}_d \lesssim 0.07\,\alpha_{0.1}^{5/3}\,M_\odot\,s^{-1}$ for a = 0), conditions appear particularly suitable for the formation of relativistic jets (by analogy to X-ray binaries, which produce jets when making a similar transition; e.g., Remillard & McClintock

2006; see Lazatti et al. 2008 for a similar argument in the context of long-duration GRBs).

Once the disk has transitioned to a late-time advective phase (phase 3 above), the properties of the disk become well-described by self-similar solutions. Ignoring for the moment outflows from the disk, these solutions are $r_d \propto t^{2/3}$, $M_d \propto t^{-1/3}$, and $\dot{M}_d \propto t^{-4/3}$. Power-law variations in the disk properties are a generic feature of a viscously evolving disk that conserves total angular momentum. These scalings are not, however, likely to be applicable in practice because outflows during the advective phase unbind most of the remaining material (§5.4.1 & 5.5.2). Energy produced by fusion to He and heavier elements also contributes to driving an outflow (Figs. 5.3 & 5.4). Such outflows remove a significant fraction of the angular momentum of the disk. This leads to a much more rapid decrease in the disk mass and accretion rate at late times (Appendix B3 and Fig. 5.6). Significant accretion onto the central black hole will thus only last for a few viscous times after the onset of the advective phase.

At the outer edge of the disk, the transition from a neutrino-cooled thin disk to the late-time advective phase occurs at a time $t_{\rm thick} \sim 0.1\,\alpha_{0.1}^{-23/17}\,(J_{49}/2)^{9/17}$ s (eq. [5.20]). The rapid decrease in $\dot{M}_d$ after the onset of the advective phase implies that the inner disk becomes advective at a similar time (§5.5.2 and Fig. 5.6). Quantitatively, we find that for powerful winds with $p = 1$ (see eq. [5.49]), the inner disk becomes advective at $t \sim 0.2$, 5, and 100 sec, for $\alpha = 0.1, 0.01$, and 0.001, respectively (for our fiducial model with an initial mass of $0.1 M_\odot$ and an initial radius of $\simeq 3 \times 10^7$ cm). Thus, for $\alpha \sim 10^{-3}$, the timescale for the inner disk to become advective is comparable to the onset of observed flaring at ~ 30 sec in some short GRBs (e.g., Berger et al. 2005). Given the slow decline in disk mass with time before $t_{\rm thick}$, there is ample accretion energy available in the disk at this point to power the observed flaring. However, there is observational evidence for $\alpha \sim 0.1$ in a number of astrophysical disks (King et al. 2007); we thus doubt that $t_{\rm thick}$ is large enough to coincide with the onset of observed flaring. Instead $t_{\rm thick}$ is likely to be $\sim 0.1 - 1$ sec, comparable to the duration of the short GRB itself. In this case, the rapid decrease in the disk mass and accretion rate in the advective

phase imply that the remnant accretion disk alone does not contain sufficient mass at ~ 30 sec to power the observed late-time activity from short GRBs, nor is there any physical reason to expect a sudden change in the disk or jet properties at this time.

A more likely source of late-time flaring in compact object merger models is a continued inflow of mass at late times, such as is produced by the infalling tidal tail found in Lee & Ramirez-Ruiz's (2007) NS-NS merger simulations (see also Rosswog 2007). Similarly, the BH-NS merger simulations of Faber et al. (2006a,b) show that $\sim 0.03 M_\odot$ of material is ejected into highly eccentric orbits during the merger, which returns to the BH on a timescale $\gtrsim 1$ s. However, final conclusions regarding the quantity and ubiquity of late-time fall-back from NS-NS and BH-NS mergers must await full-GR simulations which include BH spin and realistic EOSs.

The second major focus of this paper has been on the composition of the accretion disk and its outflows as a function of time. For initial disk properties expected in compact object mergers (§5.2), the disk typically comes into β-equilibrium given the high temperatures and densities at small radii. As material spreads to larger radii, however, the composition of the disk freezes out before it becomes advective at late times; at freeze-out the disk is modestly neutron rich, with an electron fraction $Y_e \approx 0.3$ (§5.4.2 and Fig. 5.9). This neutron rich material – $\sim 10^{-2} M_\odot$ for typical initial disk parameters – is blown away once the disk enters the advective phase at $\sim t_{\rm thick}$. These outflows are particularly interesting given the low solar system abundance of material produced in nuclear statistical equilibrium at $Y_e \sim 0.3$ (Hartmann et al. 1985). In a separate paper, we will study this nucleosynthesis and its implications in more detail.

Although outflows from compact object merger accretion disks are neutron rich in most circumstances, neutrino-driven winds from radii $\simeq 10^6 - 10^7$ cm at accretion rates $\dot{M}_d \sim 0.03 - 1\, M_\odot\, {\rm s}^{-1}$ have electron fractions $Y_e \simeq 0.5$, precisely that required to synthesize significant amounts of ^{56}Ni (Fig. 5.11). We have calculated the total Ni mass ejected by compact object merger disks as a function of their initial mass and radius (§5.5.4 and Fig. 5.12). Disks with initial masses $\gtrsim 0.1 M_\odot$ can produce up to $\sim 10^{-3} M_\odot$ of ^{56}Ni. The radioactive decay of this Ni

as the outflow expands to large radii will produce an optical and infrared transient peaking $\sim 0.5 - 2$ days after the merger, with a peak flux of $\nu L_\nu \simeq 10^{40}$ ergs s^{-1} (Fig. 7.3). Because the Ni mass is likely to be a small fraction of the total mass of the ejecta (most of which is neutron rich), this transient is best detected at $\sim 1\,\mu$m. As Figure 7.3 shows, current observational limits on SN-like transients coincident with short GRBs are about a factor of ~ 10 above our predictions. However, somewhat deeper limits from a moderately closer burst could start to put interesting constraints on short GRB progenitors. It is also possible that the decay of some neutron-rich isotopes could heat the outflow and contribute to the late-time thermal emission (although most such isotopes have very short half-lives). This possibility should be investigated in future calculations using a nuclear reaction network.

Although we have focused on short GRBs throughout this paper, many of our results can be applied more broadly. For example, long-duration GRBs show late-time activity and flaring similar to that seen in short GRBs (e.g., Falcone et al. 2007). For the reasons described above, this activity is probably produced by a continued inflow of mass at late times (fallback from the stellar progenitor's envelope) rather than solely by the viscous evolution of the small-scale disk. As a final application of our results, we note that the accretion-induced collapse of a white dwarf to a neutron star (AIC) is expected to produce a compact disk of $\sim 0.1 - 0.5 M_\odot$ outside the newly formed neutron star's surface (Dessart et al. 2006). The calculations presented here describe the evolution of this remnant disk, with the one caveat that the composition of the disk in the AIC context may be strongly affected by neutrino irradiation from the newly-formed neutron star.

Acknowledgements

We thank Josh Bloom, Davide Lazzati, and Daniel Perley for useful conversations. A. L. P. is supported by the Theoretical Astrophysics Center at UC Berkeley. B. D. M. and E. Q. are supported in part by the David and Lucile Packard Foundation, NASA Grant NNG06GI68G, and a NASA GSRP Fellowship to B.D.M.

5.7 Appendix A: Calibration of the Ring Model

The surface density Σ of an axisymmetric disk in a Keplerian potential with constant total angular momentum evolves according to a diffusion equation (e.g., Frank et al. 2002):

$$\frac{\partial \Sigma}{\partial t} = \frac{3}{r}\frac{\partial}{\partial r}\left[r^{1/2}\frac{\partial}{\partial r}\left(\nu \Sigma r^{1/2}\right)\right], \tag{5.32}$$

where ν is the kinematic viscosity. Assuming that ν depends only on radius as a power law, viz: $\nu = \nu_0 (r/R_0)^n$, equation (6.10) is linear and, for an initial surface density distribution $\Sigma(r, t=0) = (M_0/2\pi R_0)\delta(r - R_0)$ which is narrowly peaked about the radius R_0, the solution (for $n < 2$) is given by

$$\Sigma(r,t) = \frac{M_0(1-n/2)}{\pi R_0^2 x^{(n+1/4)}\tau}\exp\left[\frac{-(1+x^{2-n})}{\tau}\right] I_{1/|4-2n|}\left[\frac{2x^{1-n/2}}{\tau}\right],$$

where M_0 is the initial disk mass, $x \equiv r/R_0$, $\tau \equiv t[12\nu_0(1-n/2)^2/R_0^2]$, and I_m is a modified Bessel function of order m. For small argument $y \ll 1$, $I_m(y)$ takes the asymptotic form $I_m \simeq (y/2)^m/\Gamma(m+1)$, where Γ is the Gamma function; thus, for late times or small radii such that $\tau \gg 2x^{1-n/2}$, equation (5.33) reduces to

$$\Sigma(r,t)|_{\tau \gg 2x^{1-n/2}} = \frac{M_0}{\pi R_0^2}\frac{(1-n/2)}{\Gamma[\frac{5-2n}{4-2n}]}\frac{1}{\tau^{\left(\frac{5-2n}{4-2n}\right)}x^n}\exp\left[\frac{-(1+x^{2-n})}{\tau}\right] \tag{5.34}$$

Most of the mass in the disk is located near the radius where the local mass $M_d \propto \Sigma r^2$ peaks; using equation (5.34), at late times this radius is found to be $r_{\rm peak} = R_0 \tau^{1/(2-n)}$. Hence, equation (5.34) becomes valid near $r_{\rm peak}$ for $\tau \gg 1$.

The constant A, which relates the total disk mass at late times from the exact solution of equation (6.10) to the mass defined by $\pi\Sigma(r_{\rm peak})r_{\rm peak}^2$, can be calculated from equation (5.34) to be

$$A(\tau \gg 1) \equiv \left.\frac{\int_0^\infty 2\pi\Sigma r dr}{\pi\Sigma(r_{\rm peak})r_{\rm peak}^2}\right|_{\tau\gg 1} = \frac{2e}{2-n} \tag{5.35}$$

Similarly, the constant B, which relates the total disk angular momentum at late times from the exact solution to that estimated by $\pi\Sigma r_{\rm peak}^2 (GMr_{\rm peak})^{1/2}$, is given by

$$B(\tau \gg 1) \equiv \left.\frac{\int_0^\infty 2\pi\Sigma r^{3/2} dr}{\pi\Sigma(r_{\rm peak})r_{\rm peak}^{5/2}}\right|_{\tau\gg 1} = \frac{2e}{2-n}\Gamma\left[\frac{5-2n}{4-2n}\right] \tag{5.36}$$

From mass continuity, the radial velocity is given by

$$v_r = \frac{-3}{\Sigma r^{1/2}} \frac{\partial}{\partial r} \left[\nu \Sigma r^{1/2} \right] = \frac{-3\nu_0}{R_0} \frac{1}{\Sigma x^{1/2}} \frac{\partial}{\partial x} \left[\Sigma x^{n+1/2} \right], \tag{5.37}$$

which, using equation (5.34), gives the accretion rate at small radii

$$\begin{aligned} \dot{M}_{\rm in} &= -2\pi \Sigma r v_r|_{\tau \gg 2x^{1-n/2}} \\ &= \frac{M_0}{R_0^2/\nu_0} \frac{3(1-n/2)}{\Gamma[(5-2n)/(4-2n)]} \exp[-1/\tau] \tau^{-\left(\frac{5-2n}{4-2n}\right)} \end{aligned} \tag{5.38}$$

Equation (5.38) is easily checked by noting that $\int_0^\infty \dot{M}_{\rm in} dt = M_0$, which shows that the entire initial disk eventually accretes onto the central object. In §5.3.1 we introduced the following prescription for evolving the disk mass:

$$\dot{M}_d = \frac{f M_d}{t_{\rm visc}}, \tag{5.39}$$

where, in terms of the viscosity prescription adopted above,
$t_{\rm visc} = r_d^2/\nu = t_{\rm visc,0}(r_d/R_0)^{2-n}$ and $t_{\rm visc,0} \equiv R_0^2/\nu_0$ is the initial viscous time. Assuming that the total disk angular momentum remains constant, $J \propto M_d r_d^{1/2} = M_0 R_0^{1/2}$, the solution to equation (5.39) is given by

$$M_d(t) = M_0 [1 + (4-2n) f (t/t_{\rm visc,0})]^{-1/(4-2n)} \tag{5.40}$$

In our evolutionary calculations we set f so that the accretion rate from the exact solution to equation (6.10) ($\dot{M}_{\rm in}$; eq. [5.38]) matches the solution to equation (5.39) at late times (i.e., in the self-similar limit). This requires

$$f = 3(1-n/2)\Gamma[(5-2n)/(4-2n)]^{4-2n} \tag{5.41}$$

For an advection-dominated disk, $\nu = \alpha c_s H \propto \Omega R^2 \propto r^{1/2}$; thus, $n = 1/2$, $f \simeq 1.602$, $A \simeq 3.62$, and $B \simeq 3.23$. For a neutrino-cooled, optically-thin disk which is dominated by gas pressure, $T \propto r^{-3/10}$ and $\nu \propto r^{6/5}$; thus, $n = 6/5$, $f \simeq 1.01$, $A \simeq 6.80$, and $B \simeq 6.09$.

In Figure 5.14 we show $\dot{M}_{\rm in}/\dot{M}_d$ as a function of $t/t_{\rm visc,0}$ for $n = 1/2$ in order to compare the disk evolution derived from the exact solution of equation (6.10)

to that calculated from our simplified model. Figure 5.14 also shows the ratio of the total disk mass $M_{\rm tot} \equiv \int_0^\infty 2\pi\Sigma r dr$ calculated from equation (5.33) to the disk mass M_d (eq. [5.40]) of the simplified model, as well as the ratio of $r_{\rm peak}$ (the radius where Σr^2 peaks, using eq. [5.33] for Σ) to the radius determined by angular momentum conservation: $r_d = R_0(M_d/M_0)^2$. Figure 5.14 shows that, although the accretion rate in the two models differ at very early times (the initially narrowly-concentrated ring takes a short period of time to spread to small radii), they approach one another to $\lesssim 20\%$ by $t \gtrsim 0.1 t_{\rm visc,0}$. Likewise, the disk mass and radii from the exact solution and simplified model are quite similar at all times.

The numerical values for A and B given in equations (5.35) and (5.36) and employed in our calculations apply only to the mass and angular momentum distribution in the disk at late times ($\tau \gg 1$). Initially, the disk is entirely concentrated at a single radius and $A(t=0) = B(t=0) = 1$; thus, $A(t)$ and $B(t)$ evolve significantly from early times until the disk enters the self-similar limit and so one might worry that the early-time description of the disk's evolution depends sensitively on the initial mass distribution. Our model only assumes, however, that the *ratio* $A(t)/B(t)$ remains constant, which is a good approximation. To illustrate this, Figure 5.14 shows $A(t)/B(t)$ calculated from the exact solution (eq. [5.33]) for $n = 1/2$. Note that $A(t)/B(t)$ increases from unity to its asymptotic value $A/B = \Gamma[(5-2n)/(4-2n)]$, which is $\simeq 1.12$ for $n = 1/2$.

5.8 Appendix B: Analytic Self-Similar Solutions

The late-time evolution of our disk calculations asymptote to power laws that are well approximated by analytic self-similar solutions. We derive these here to aid in interpreting our numerical results. Presentation is divided between neutrino-cooled, thin-disk solutions and late-time advective solutions. One could just as well derive analogous results for disks that are optically thick to neutrinos. We forgo this here since the initial viscous time is always sufficiently long that these solutions are never applicable to our numerical results. We conclude by presenting self-similar solutions for advective disks with substantial mass-loss, since these

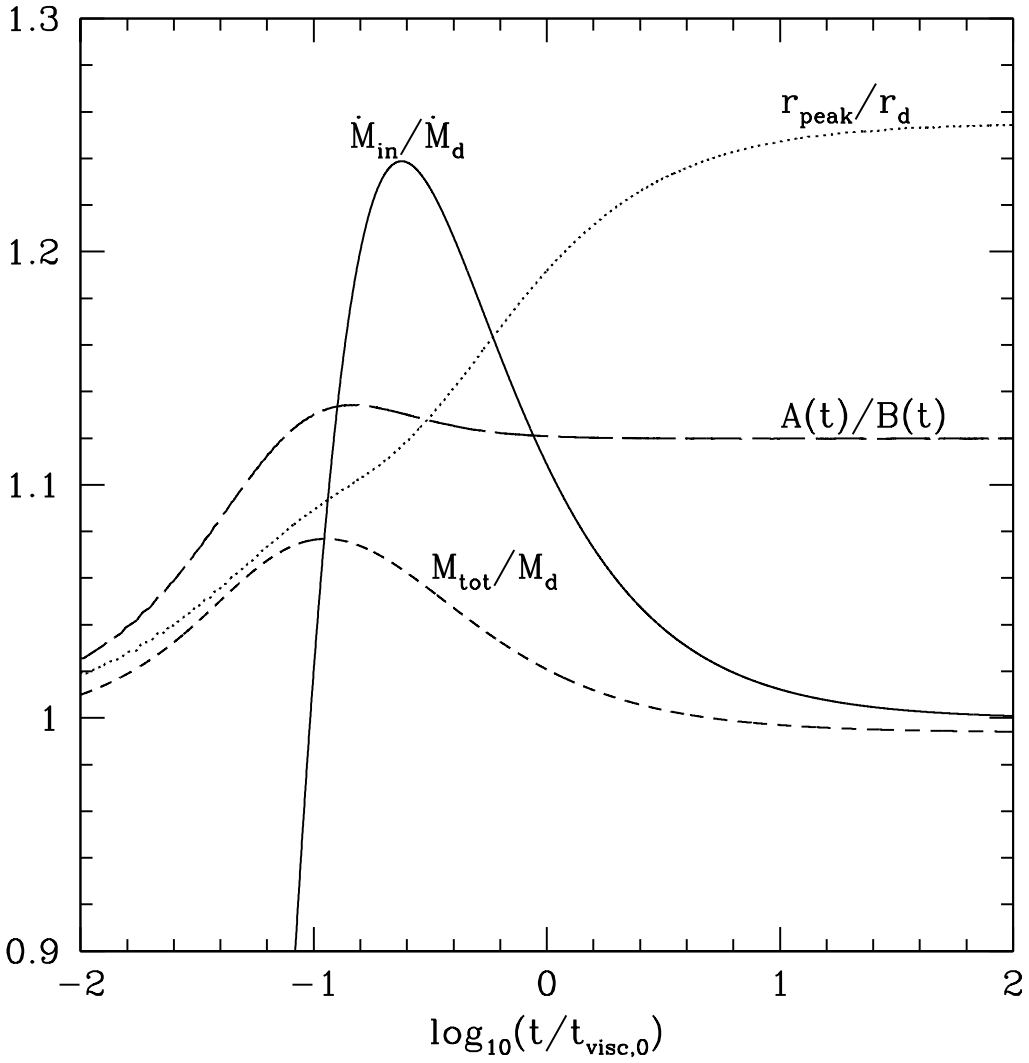

Figure 5.14: Comparison of the accretion rate (*solid*), disk mass (*short dashed*), and disk radius (where the local disk mass peaks; *dotted*) as calculated from our simplified ring model to that derived from the exact solution of the diffusion equation for a $\delta-$function initial mass distribution (eq. [5.33]); we assume $\nu \propto r^{1/2}$, as applies for a thick disk. The parameter $f \simeq 1.6$ (eq. [5.41]) adopted in our model is chosen to ensure that the accretion rates match at late times (i.e., $\dot{M}_{\rm in}/\dot{M}_d \rightarrow 1$). Also shown is the ratio $A(t)/B(t)$ (eqs. [5.35] and [5.36]), a measure of the relative distribution of mass and angular momentum, which asymptotes to $\Gamma[(5-2n)/(4-2n)] \simeq 1.12$ at late times.

differ significantly from the solutions without mass-loss.

5.8.1 Neutrino-Cooled, Thin-Disk Solutions

In the neutrino-cooled, thin-disk limit, the cooling is dominated by Urca, and the pressure is given by ideal gas. Combining local energy balance and continuity, $\dot{M}_d = fA\pi\nu\Sigma$, allows us to solve for the temperature and column density as functions of radius. We substitute these into the angular momentum equation, $B(GMr_d)^{1/2}\pi r_d^2\Sigma = J_d$, to solve for M_d as a function of $\dot{M}_d$ and J_d. We then assume the solutions have a self-similar form of $M_d \propto t^{-\beta}$, so that $\dot{M}_d = -dM_d/dt = \beta M_d/t$. In this way we solve for $\beta = 5/8$, $\dot{M}_d(t)$, and subsequently any other variable of interest. The results are

$$M_d = 1.3\times10^{-2} f_{1.6}^{-5/8}\left(\frac{A_{3.6}}{B_{3.2}}\right)\alpha_{0.1}^{-3/4}M_3^{-1/4}\left(\frac{J_{49}}{2}\right)t^{-5/8}M_\odot, \tag{5.42}$$

$$\dot{M}_d = 2.7\times10^{-2} f_{1.6}^{-5/8}\left(\frac{A_{3.6}}{B_{3.2}}\right)\alpha_{0.1}^{-3/4}M_3^{-1/4}\left(\frac{J_{49}}{2}\right)t^{-13/8}M_\odot\mathrm{s}^{-1} \tag{5.43}$$

and

$$r_d = 4.1\times10^{8} f_{1.6}^{5/4}\alpha_{0.1}^{3/2}M_3^{-1/2}t^{5/4}\mathrm{cm}. \tag{5.44}$$

where $f_{1.6} = f/1.6$, $A_{3.6} = A/3.6$, $B_{3.2} = B/3.2$, and t is measured in seconds, and the prefactors have been scaled to match our numerical results. The first thing to notice is that both M_d and $\dot{M}_d$ are rather insensitive to the choice of f as long as it is near unity, and A and B only appear as a ratio, which is also nearly unity. This provides confidence in using this parameterization, and these specific values for the corresponding parameters, when the disk is not well-described by $n = 1/2$. This analysis also demonstrates the relative dependence on α. In Figure 5.15 we compare these scaling (*dotted lines*) with the numerical calculations. This shows that these solutions are only applicable for a short time. At times when $t < t_{\rm visc}$ the evolution is much flatter and is dominated by initial conditions. At later times the disk becomes advective and the solutions of the next section apply.

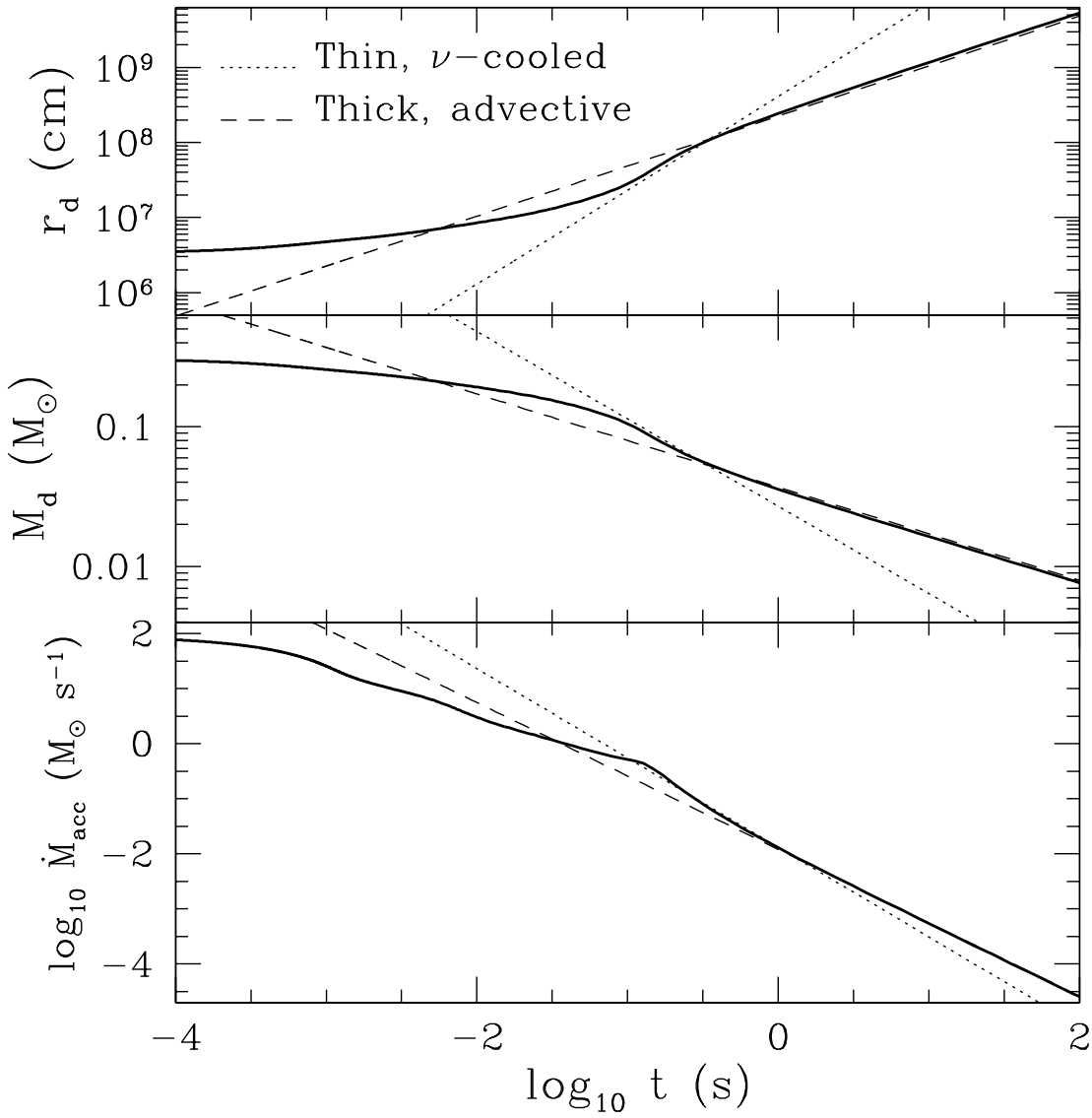

Figure 5.15: Comparison of the numerical disk solutions (*solid lines*) with the analytic solutions for the thin, neutrino-cooled (*dotted lines*) and thick, advective limits (*dashed lines*). The numerical solution is the $0.3M_\odot$ disk from Fig. 5.1.

5.8.2 Late-Time Advective Solutions

In this limit, self-similar solutions can be found in an analogous way. The viscous energy release is carried by advection with the internal energy dominated by relativistic particles, so that

$$\frac{9}{8fA\pi}\Omega^2\dot{M} = V_r\frac{H}{r}\frac{11}{6}aT^4. \tag{5.45}$$

Combining this with mass continuity, gives the column depth as a function of radius, $\Sigma(r) = (16/9A\pi\alpha)(\dot{M}/r^2\Omega)$. We then use this relation with $B(GMr_d)^{1/2}M_d = J_d$ and $\dot{M}_d = \beta M_d/t$, to find $\beta = 1/3$ and the self-similar solutions

$$M_d = 3.7\times10^{-2}\left(\frac{A_{3.6}}{B_{3.2}}\right)\alpha_{0.1}^{-1/3}M_3^{-2/3}\left(\frac{J_{49}}{2}\right)t^{-1/3}M_\odot, \tag{5.46}$$

$$\dot{M}_d = 1.2\times10^{-2}\left(\frac{A_{3.6}}{B_{3.2}}\right)\alpha_{0.1}^{-1/3}M_3^{-2/3}\left(\frac{J_{49}}{2}\right)t^{-4/3}M_\odot\mathrm{s}^{-1}, \tag{5.47}$$

and

$$r_d = 2.3\times10^8\alpha_{0.1}^{2/3}M_3^{1/3}t^{2/3}\mathrm{cm}. \tag{5.48}$$

These advective results are even more insensitive to A, B, and f than the thin-disk results. Equation (5.46)-(5.48) are plotted in Figure 5.15 as dashed lines. The numerical calculations follow these solutions very closely for times later than $t_{\rm thick}$ (given by eq. [5.20]).

Equations (5.46)-(5.48) can also be derived ignoring equation (5.45), but assuming that the scaleheight is fixed at $H/r \simeq 0.6$. This introduces the additional dependencies $M_d \propto (H/r)^{-2/3}$, $\dot{M}_d \propto (H/r)^{-2/3}$, and $r_d \propto (H/r)^{4/3}$, but gives nearly identical prefactors.

5.8.3 Advective Solutions with Mass-Loss

In §5.5.2 we described how advective disks are likely to lose a substantial fraction of their mass to viscously driven outflows. Because the outflow removes angular momentum as well – at least the specific angular momentum of the mass that is lost – the disk need not expand as rapidly to large radii. In addition, the disk mass and accretion rate decrease much more rapidly at late times than in the

self-similar solutions described in the previous subsection. To quantify this effect, we follow Blandford & Begelman (1999) and assume that only a fraction $\sim (r_*/r_d)^p$ of the available material is accreted onto the central BH. The remainder is lost to an outflow. Thus the outflow rate at any time is given by

$$\dot{M}_{\rm out} = \left(1 - \left[\frac{r_*}{r_d}\right]^p\right) \frac{fM_d}{t_{\rm visc}} \tag{5.49}$$

We further assume that the angular momentum-loss rate from the disk is given by

$$\dot{J} = -C\dot{M}_{\rm out} \left(GMr_d\right)^{1/2}. \tag{5.50}$$

where C is a constant that depends on the torque exerted by the outflowing mass on the remaining disk. If the outflow produces no net torque, an assumption that appears at least qualitatively consistent with the relatively small-scale magnetic fields seen in global MHD disk simulations (e.g., Stone & Pringle 2001), then the angular momentum-loss is only that due to the specific angular momentum of the outflow, and (Kumar, Narayan, & Johnson 2008)

$$C = \frac{2p}{2p+1}. \tag{5.51}$$

We solve equations (5.6), (5.7), (5.49), and (5.50), assuming $A/B = 1$ and $\nu \propto r^{1/2}$ (as appropriate for a thick disk). The solution depends on the relative magnitude of $1 - C$ and $C(r_*/r_d)^p$. For $C(r_*/r_d)^p \ll 1 - C$, which is true at nearly all times if equation (5.51) is applicable, then

$$r_d \simeq r_{d,0}\left[1 + 3f(1-C)\left(\frac{t}{t_{\rm visc,0}}\right)\right]^{2/3}, \tag{5.52}$$

$$M_d \simeq M_{d,0}\left[1 + 3f(1-C)\left(\frac{t}{t_{\rm visc,0}}\right)\right]^{-1/[3(1-C)]}, \tag{5.53}$$

and

$$\dot{M}_{\rm in} \simeq f\frac{M_{d,0}}{t_{\rm visc,0}}\left(\frac{r_*}{r_{d,0}}\right)^p \times$$

$$\left[1 + 3f(1-C)\left(\frac{t}{t_{\rm visc,0}}\right)\right]^{-[1+3(1+2p/3)(1-C)]/[3(1-C)]} \tag{5.54}$$

Note that if $p = C = 0$ (i.e., no mass or angular momentum-loss), then these self-similar solutions reduce to those of the previous subsection. However, for the case $p = 1$ consistent with a number of global advective disk simulations (e.g., Hawley & Balbus 2002), and in the absence of a net torque on the disk, $C = 2/3$ and these solutions correspond to $r_d \propto t^{2/3}$, $M_d \propto t^{-1}$, and $\dot{M}_{\rm in} \propto t^{-8/3}$ (see also Fig. 5.6). This shows that the disk mass and accretion rate decrease subsantially more rapidly in time than in the absence of an outflow, while the disk expands outward at roughly the same rate. If there is a net torque on the disk such that $C \simeq 1$, then equations (5.52)–(5.54) are not applicable. Instead, for $C(r_*/r_d)^p \gg 1 - C$, the solution is given by (for $p \neq 0$ and $t \gg t_{\rm visc,0}$)

$$r_d(t) \simeq \left[(3+2p) f r_*^p r_{d,0}^{1.5}\right]^{1/(1.5+p)} \left(\frac{t}{t_{\rm visc,0}}\right)^{1/(1.5+p)} \tag{5.55}$$

and

$$M_d(t) \simeq M_{d,0} \exp[-D(t/t_{\rm visc,0})^{p/(1.5+p)}] \tag{5.56}$$

where

$$D = \left(\frac{1.5+p}{p\,(3+2p)^{1.5/(1.5+p)}}\right) \left(\frac{f r_{d,0}^{1.5}}{[f r_*^p r_{d,0}^{1.5}]^{1.5/(1.5+p)}}\right). \tag{5.57}$$

For $p = 1$ and for $r_{d,0} \sim r_*$, these solutions become $r_d(t) \sim r_{d,0}(t/t_{\rm visc,0})^{2/5}$ and $M_d(t) \sim M_{d,0} \exp[-1.15(t/t_{\rm visc,0})^{2/5}]$. The radius of the disk thus increases significantly more slowly, and the mass of the disk decreases much more rapidly, than in the self-similar solutions without mass-loss.

The numerical solutions including mass-loss during the advective phase shown in Figure 5.6 assume that equation (5.51) is applicable and are indeed well-described by the self-similar solutions given in equations (5.52)-(5.54) at late times.

Chapter 6

Neutron-Rich Freeze-Out in Accretion Disks Formed From Compact Object Mergers

B. D. Metzger, A. L. Piro, E. Quataert (2009), MNRAS in press.[1]

Abstract

Accretion disks with masses $\sim 10^{-3} - 0.1 M_{\odot}$ are believed to form during the merger of a neutron star (NS) with another NS and the merger of a NS with a black hole (BH). Soon after their formation, such hyper-accreting disks cool efficiently by neutrino emission and their composition is driven neutron-rich by pair captures under degenerate conditions. However, as the disk viscously-spreads and its temperature drops, neutrino cooling is no longer able to offset viscous heating and the disk becomes advective. Analytic arguments and numerical simulations suggest that once this occurs, powerful winds likely drive away most of the disk's remaining mass. We calculate the thermal evolution and nuclear composition of viscously-spreading accretion disks formed from compact object mergers using one-dimensional height-integrated simulations. We show that freeze-out from weak

equilibrium necessarily accompanies the disk's late-time transition to an advective state. As a result, hyper-accreting disks generically freeze out neutron-rich (with electron fraction $Y_e \sim 0.2 - 0.4$), and their late-time outflows robustly synthesize rare neutron-rich isotopes. Using the measured abundances of these isotopes in our solar system, we constrain the compact object merger rate in the Milky Way to be $\lesssim 10^{-5}(M_{d,0}/0.1M_\odot)^{-1}$ yr^{-1}, where $M_{d,0}$ is the average initial mass of the accretion disk. Thus, either the NS-NS merger rate is at the low end of current estimates or the average disk mass produced during a typical merger is $\ll 0.1M_\odot$. Based on the results of current general relativistic merger simulations, the latter constraint suggests that prompt collapse to a BH is a more common outcome of NS-NS mergers than the formation of a transient hyper-massive NS. We also show that if most short duration gamma-ray bursts (GRBs) are produced by compact object mergers, their beaming fraction must exceed $f_b \approx 0.13(M_{d,0}/0.1M_\odot)$, corresponding to a jet half-opening angle $\gtrsim 30°(M_{d,0}/0.1M_\odot)^{1/2}$. This is consistent with other evidence that short duration GRB outflows are less collimated than those produced in long-duration GRBs.

6.1 Introduction

Massive, compact accretion disks are thought to form in a number of astrophysical events, including the merger of a black hole and a neutron star (BH-NS; Lattimer & Schramm 1974, 1976), the merger of a double NS binary (NS-NS; Eichler et al. 1989), the collapse of a rapidly-rotating stellar core (Woosley 1993), the accretion-induced collapse (AIC) of a white dwarf (WD) to a NS (Dessart et al. 2006, 2007), and the AIC of a NS to a BH (Vietri & Stella 1998, 1999). These disks are termed "hyper-accreting" due to their large accretion rates of up to several solar masses per second. Rapid accretion onto a BH following the collapse of a massive star is a popular model for the central engine of long-duration gamma-ray bursts (GRBs) (MacFadyen & Woosley 1999) due to their association with star forming regions and Type Ibc supernovae (SNe) (Woosley & Bloom 2006). Short-duration GRBs, on the other hand, originate from a more evolved

progenitor population (e.g., Berger et al. 2005) and may instead result from compact object (CO) mergers (e.g., Lee & Ramirez-Ruiz 2007), or the AIC of a WD (Chapter 3) or a NS (MacFadyen et al. 2005).

Hyper-accreting disks cool via neutrino emission when the accretion rate is sufficiently high ($\dot{M} \gtrsim 0.01-0.1 M_\odot$ s^{-1}; Popham et al. 1999). This allows the disk midplane to become dense and electron degenerate (Chen & Beloborodov 2007). Because positron captures ($e^+ + n \rightarrow p + \bar{\nu}_e$) are suppressed relative to electron captures ($e^- + p \rightarrow n + \nu_e$) under degenerate conditions, neutrino-cooled disks are driven neutron-rich (Pruet et al. 2003; Beloborodov 2003), i.e., to an electron fraction $Y_e \equiv n_{\rm p}/(n_{\rm p} + n_{\rm n}) < 0.5$, where $n_{\rm p}$ and $n_{\rm n}$ are the proton and neutron density, respectively.

If a portion of this neutron-rich material escapes the disk, several observable consequences may result (e.g., Derishev et al. 1999). In particular, although highly relativistic outflows are required to produce GRBs, slower outflows from larger radii in the disk are probably at least as common (e.g., Pruet et al. 2004). These dense outflows may synthesize heavy, neutron-rich isotopes as they expand away from the midplane and cool. Such outflows are difficult to detect directly because neutron-rich isotopes have short half-lives ($\sim$ seconds; Freiburghaus et al. 1999) and are thus unlikely to power a bright SN-like transient via their radioactive decay (although a dimmer, shorter-lived transient may be produced; Li & Paczynski 1998; Kulkarni 2005; Chapter 5).

Neutron-rich outflows can also be probed indirectly via their effect on the chemical evolution of the Galaxy. For instance, moderately neutron-rich outflows with $Y_e \approx 0.35-0.4$ produce isotopes (e.g., ^{79}Br and ^{78}Se) that are rare in our solar system (Hartmann et al. 1985; Woosley & Hoffman 1992). Hence, the measured abundances of these isotopes place stringent constraints on the rate at which low-Y_e material is ejected into the interstellar medium (ISM). In turn, if the amount of neutron-rich material ejected in a given event can be estimated, the true rate and beaming fraction (or jet opening angle) could in principle be constrained in models that associate these events with GRBs (e.g., Woosley & Baron 1992; Fryer et al. 1999). Constraints on the rate of CO mergers are particularly interesting

because they are the primary target for km-scale gravitational wave detectors such as LIGO and VIRGO, and rates derived from known merging systems (Kalogera et al. 2004; Kim et al. 2006) and population synthesis models (e.g., Belczynski et al. 2006) remain highly uncertain.

6.1.1 Summary of Previous Work

Most previous efforts to determine the composition of outflows from hyper-accreting disks have focused on winds driven by neutrino irradiation from the inner disk (Levinson 2006; Surman et al. 2006, 2008; Barzilay & Levinson 2007; Chapter 4), in analogy to those from proto-neutron stars following successful core-collapse SNe (e.g., Burrows, Hayes, & Fryxell 1995). However, the electron fraction at the base of neutrino-driven outflows is typically not preserved as matter accelerates to large radii because neutrino absorptions ($p + \bar{\nu}_e \rightarrow n + e^+$ and $n + \nu_e \rightarrow p + e^-$) drive Y_e to the equilibrium value

$$Y_e^\nu \approx [1 + (L_{\bar{\nu}_e}\langle\epsilon_{\bar{\nu}_e}\rangle / L_{\nu_e}\langle\epsilon_{\nu_e}\rangle)]^{-1} \tag{6.1}$$

given by the properties of the neutrino radiation field, where $L_{\nu_e}/L_{\bar{\nu}_e}$ and $\langle\epsilon_{\nu_e}\rangle/\langle\epsilon_{\bar{\nu}_e}\rangle$ are the mean $\nu_e/\bar{\nu}_e$ luminosities and energies, respectively, from the central NS or accretion disk (Qian et al. 1993). When the accretion rate is very high ($\dot{M} \gtrsim M_\odot$ s^{-1}) and the inner disk is optically thick to neutrinos, Y_e^ν can itself be $\ll 0.5$ because the $\bar{\nu}_e$'s originate from regions of higher temperature than the ν_e's (e.g., Surman et al. 2006). However, a disk with a fixed initial mass (such as is produced by a CO merger) spends very little time (if any) accreting at such a high rate; most neutrino-driven mass-loss from a viscously-spreading disk occurs at later times, when the entire disk is optically thin and $Y_e^\nu \sim 0.5$ (see Fig. 5.10). Thus, while early-time neutrino-driven outflows may produce modest amounts of r-process ejecta, their total yield in the context of CO mergers is probably insufficient to contribute appreciably to the Galactic abundance of neutron-rich isotopes (e.g., Surman et al. 2008). However, as we now discuss, later stages in the disk's evolution, when neutrino irradiation is relatively unimportant, are likely to eject even larger quantities of neutron-rich material.

In a recent paper (Chapter 5), we used a one-zone (or "ring") model to study the evolution of hyper-accreting disks. Guided by analytic work (Blandford & Begelman 1999) and numerical simulations (e.g., Stone & Pringle 2001; Hawley, Balbus, & Stone 2001; Hawley & Balbus 2002) which show that radiatively-inefficient accretion drives powerful outflows, we argued that the majority of the disk becomes unbound soon following the disk's transition to an advective state at late times. Since ejection occurs on approximately the dynamical timescale (which is faster than weak interactions at this stage), these "viscously-driven" outflows maintain the electron fraction of the disk midplane, unlike the neutrino-driven outflows at earlier times. Thus, in order to determine what isotopes are ultimately synthesized, the electron fraction in the disk must be known at late times when the disk becomes advective.

6.1.2 Outline of this Chapter

In this paper we determine the composition of late-time outflows from hyper-accreting disks by calculating the disk's midplane composition as the disk viscously-spreads and falls out of weak equilibrium. We concentrate in particular on BH accretion following a CO merger[2] (either NS-NS or NS-BH models), where a fixed initial disk mass is a reasonable approximation. In §6.2 we use a one-zone model similar to that in Chapter 5 to calculate $Y_e(t)$ for a wide variety of plausible initial disk masses and sizes. Although the one-zone model in §6.2 captures the basic evolution of hyper-accreting disks, the subsequent nucleosynthesis depends sensitively on the freeze-out electron fraction Y_e^f, and so a more detailed calculation is warranted. Furthermore, a one-zone model cannot, by construction, address the possibility that different annuli in the disk may freeze out with different values of Y_e^f. Therefore in §6.3 we present one-dimensional (1D), height-integrated calculations of the evolution of CO merger disks and their composition, and use them to determine the electron fraction mass distribution $M(Y_e^f)$ at late times. We find

[2]Although we center our discussion on accretion following CO mergers, most of our conclusions would apply equally to the AIC of a NS to a BH, which may produce a disk with similar initial properties (Shibata 2003; Shapiro 2004).

that under most conditions the majority of the mass freezes out neutron-rich with $Y_e^f \sim 0.2 - 0.4$. In §6.4 we summarize our results and use them to constrain the CO merger rate and the beaming fraction of short GRBs.

6.2 One Zone Model

In this section we present calculations of the electron fraction at freeze-out Y_e^f using a one-zone "ring" model similar to that presented in Chapter 5. The simplicity of this model allows us to efficiently explore a wide parameter space of initial disk mass $M_{d,0}$ and radius $r_{d,0}$, and it also provides a useful point of comparison for our 1D calculations in §6.3. The initial conditions and relevant equations are presented in §6.2.1. In §6.2.2 we present our results and show, using a simple analytic argument, that a moderately neutron-rich freeze-out (i.e., $Y_e^f \lesssim 0.5$) is generically expected, relatively independent of the details of how the disk viscously spreads.

6.2.1 Equations and Initial Conditions

Since the accretion disks produced during CO mergers are created from tidally disrupted NS material, we take the initial electron fraction to be $Y_e^0 = 0.1$, which is characteristic of the inner neutron star crust (e.g., Haensel & Zdunik 1990a,b; Pethick & Ravenhall 1995). In most of our calculations we take the BH mass to be $M_{\rm BH} = 3M_\odot$. The mass and radial profile of the remnant disks formed from CO mergers are uncertain theoretically because they depend on the unknown supranuclear-density equation of state and general relativistic effects, which are now being explored in merger simulations (e.g., Shibata & Taniguchi 2006). Disk masses $M_d \sim 10^{-3} - 0.3M_\odot$ with characteristic sizes $\sim 10^6 - 3 \times 10^7$ cm appear typical (e.g., Rasio et al. 2005; Oechslin & Janka 2006; Shibata & Taniguchi 2006).

The equations and assumptions employed in our one-zone model closely follow those in Chapter 5. To provide a brief summary, our calculation follows the thermal and viscous evolution of the disk radius $r_d(t)$ (the "ring") that contains

the majority of the mass, controls the accretion rate $\dot{M}$ onto the central object, and moves outwards as the disk accretes in order to conserve the total angular momentum $J \propto M_d r_d^{1/2}$. Our energy equation includes viscous heating and the dominant neutrino opacities. The model is calibrated so as to reproduce the exact δ-function solution to the viscous diffusion equation (eq. [6.10]) at late times. Although we refer the reader to Chapter 5 for details, we include here a brief discussion of changes and additions we have made and highlight the equations most important for this work.

The electron fraction is evolved using

$$\frac{dY_e}{dt} = (\lambda_{e^+n}+\lambda_{\nu_e n}) \left[1 - Y_e - \left(\frac{1-X_{\rm f}}{2}\right)\right] - (\lambda_{e^-p}+\lambda_{\bar{\nu}_e p}) \left[Y_e - \left(\frac{1-X_{\rm f}}{2}\right)\right], \quad (6.2)$$

where d/dt is a Lagrangian derivative, $\lambda_{e^-p}/\lambda_{e^+n}$ are the pair capture rates (see Beloborodov 2003, eqs. [6], [7]), $X_{\rm f}$ is the free nucleon mass fraction in nuclear statistical equilibrium (NSE) (from, e.g., Woosley & Baron 1992), and

$$\lambda_{\nu N} = \frac{L_\nu \sigma_{\nu N} X_N}{4\pi r_d^2 \langle\epsilon_\nu\rangle (1+\tau_{\nu N})} \approx 500 \frac{X_N L_{52} \langle\epsilon_{10}\rangle}{r_6^2 (1+\tau_{\nu N})}\ {\rm s}^{-1} \quad (6.3)$$

are the neutrino capture rates (e.g., Qian & Woosley 1996) due to irradiation from the inner accretion disk (see the discussion below). In equation (6.3), νN stands for either $\nu_e n$ or $\bar{\nu}_e p$, X_N is the corresponding proton or neutron mass fraction, $L_\nu \equiv L_{52} 10^{52}$ ergs s^{-1} is the neutrino luminosity, $\langle\epsilon_\nu\rangle \equiv 10\langle\epsilon_{10}\rangle$ MeV is the mean neutrino energy, and $\sigma_{\nu N} \simeq 9 \times 10^{-44} \langle\epsilon_\nu^2\rangle$ MeV^{-2}cm^2 is the neutrino capture cross section. The factor $(1 + \tau_{\nu N})$ accounts for the possibility that the absorbing annulus may become optically thick, where $\tau_{\nu N} \equiv \sigma_{\nu N} X_N \rho r_d / 2 m_p$ is the neutrino optical depth and ρ is the density; our calculation is fairly insensitive to this prescription for when $\tau_\nu > 1$, however, because τ_ν is generally $\ll 1$ at freeze-out. We neglect the proton-neutron mass difference $\Delta \approx 1.3$ MeV and the effects of electron degeneracy in calculating $\sigma_{\nu N}$ because the energies of the neutrinos that dominate the heating ($\langle\epsilon_\nu\rangle \sim 10$ MeV) greatly exceed Δ and the electron Fermi energy, respectively. We assume relativistic e^-/e^+ pairs when calculating the electron chemical potential; we have verified that this is a good approximation by checking that including the effects of arbitrary e^-/e^+ energies has no significant

effect on the value of Y_e^f. NSE is a generally a good assumption in calculating X_f because the entropy in the disk is sufficiently low that $\alpha-$particles form while the midplane temperature is still high ($T \gtrsim 0.5$ MeV).

The dominant process that sets Y_e during the thin disk phase is pair capture on free nuclei (e.g., Pruet et al. 2003). However, neutrino absorptions become important near freeze-out and must be included in a detailed calculation (see Fig. 6.2). The neutrino absorption rate $\lambda_{\nu N}$ is dominated by the high energy neutrinos that are radiated from the smallest radii in the disk. We calculate L_ν and $\langle \epsilon_\nu \rangle$ by extending our solutions down to the innermost stable orbit r_*, assuming that $\dot{M}$ is constant with radius interior to r_d. The neutrino flux is reasonably approximated as a "light bulb" at the origin in equation (6.3) because the neutrino capture rates only become comparable to the pair capture rates when the disk has spread to a radius that is much larger than that of the central BH.

Since neutrino captures only affect Y_e appreciably at times when the inner disk is optically thin to neutrinos, we assume that $L_{\nu_e} \approx L_{\bar{\nu}_e}$ and $\langle \epsilon_{\nu_e} \rangle \approx \langle \epsilon_{\bar{\nu}_e} \rangle$ (see the discussion in §5.5.3 for why this is a good approximation). Thus, the effect of neutrino captures is to drive Y_e towards $Y_e^\nu \approx 0.5$ (see eq. [6.1]). The effect of α-particle formation (i.e., $X_f \rightarrow 0$ in eq. [6.2]) would also be to drive $Y_e \rightarrow 0.5$ (the "alpha-effect"; e.g., Fuller & Meyer 1995); however, this effect is unimportant in our calculations because weak freeze-out generally precedes α-particle formation.

One difference relative to Chapter 5 is that here we take the viscous stress to be proportional to just the ion gas pressure $P_{\rm gas}$, as opposed to the total pressure $P_{\rm tot}$, which also includes radiation pressure from photons and e^-/e^+ pairs. In other words, we take the kinematic viscosity to be

$$\nu = \alpha P_{\rm gas}/\rho\Omega, \tag{6.4}$$

where α is a dimensionless constant and Ω is the Keplerian rotation rate. At early times in the evolution of the disk (in particular when it is neutrino-cooled), the disk is primarily supported by gas pressure and so using either $\nu \propto P_{\rm tot}$ or $\nu \propto P_{\rm gas}$ gives similar results. However, as the disk becomes thick at late times and Y_e freezes out, the disk becomes dominated by radiation pressure, with $P_{\rm tot}/P_{\rm gas} \sim 2-3$ during

freeze-out (see Fig. 6.2). The primary reason that we use $P_{\rm gas}$ instead of $P_{\rm tot}$ in equation (6.4) is to avoid the classic Lightman-Eardley (1974) viscous instability, which we otherwise find develops in our full 1D calculations described in §6.3. Because $P_{\rm tot}/P_{\rm gas}$ is modest ($\lesssim 3$) during the times that matter to our results, we choose $\alpha \sim 0.3$ and 0.03 as fiducial values for our calculations, to roughly bracket the value of $\alpha \sim 0.1$ motivated by a number of astrophysical observations (King et al. 2007). For typical disk parameters, we find that taking $\nu \propto P_{\rm gas}$ instead of $\nu \propto P_{\rm tot}$ in our one-zone models results in a modest ($\sim 20\%$) increase in the final electron fraction. This, together with our inclusion of neutrino absorptions in evolving Y_e, accounts for the fact that the final electron fractions Y_e^f presented here are somewhat larger than those presented in Figure 5.9.

As an improvement over Chapter 5, our calculation of the cooling rates due to e^-/e^+ captures on free nuclei now includes the effects of arbitrary electron energy and degeneracy. In addition, we include heating from the absorption of neutrinos that are radiated from the accretion disk at small radii (see eq. [6.14]). Finally, as in Chapter 5 we apply a "no torque" boundary condition at the inner radius $r_* = 10^6$ cm, which corresponds to the radius of the innermost stable orbit around a rapidly rotating Kerr BH ($a = 0.9$).

6.2.2 Results

Figure 6.1 shows contour plots of the freeze-out electron fraction Y_e^f as a function of the initial disk mass $M_{d,0}$ and radius $r_{d,0}$ using two different values of the viscosity, $\alpha = 0.03$ and 0.3.

The basic features of Figure 6.1 can be understood as follows. Sufficiently massive, compact disks (upper left corner of Fig. 6.1) come into pair capture-equilibrium and obtain an electron fraction that is relatively independent of the initial value $Y_e^0 = 0.1$, while low mass, more extended disks (lower right corner) retain their initial composition. As discussed below, a disk enters $\beta-$equilibrium if and only if it can cool efficiently via neutrino emission (see eq. [6.9]). By equating the radius where neutrino cooling balances $\sim 1/2$ of the viscous heating in a self-

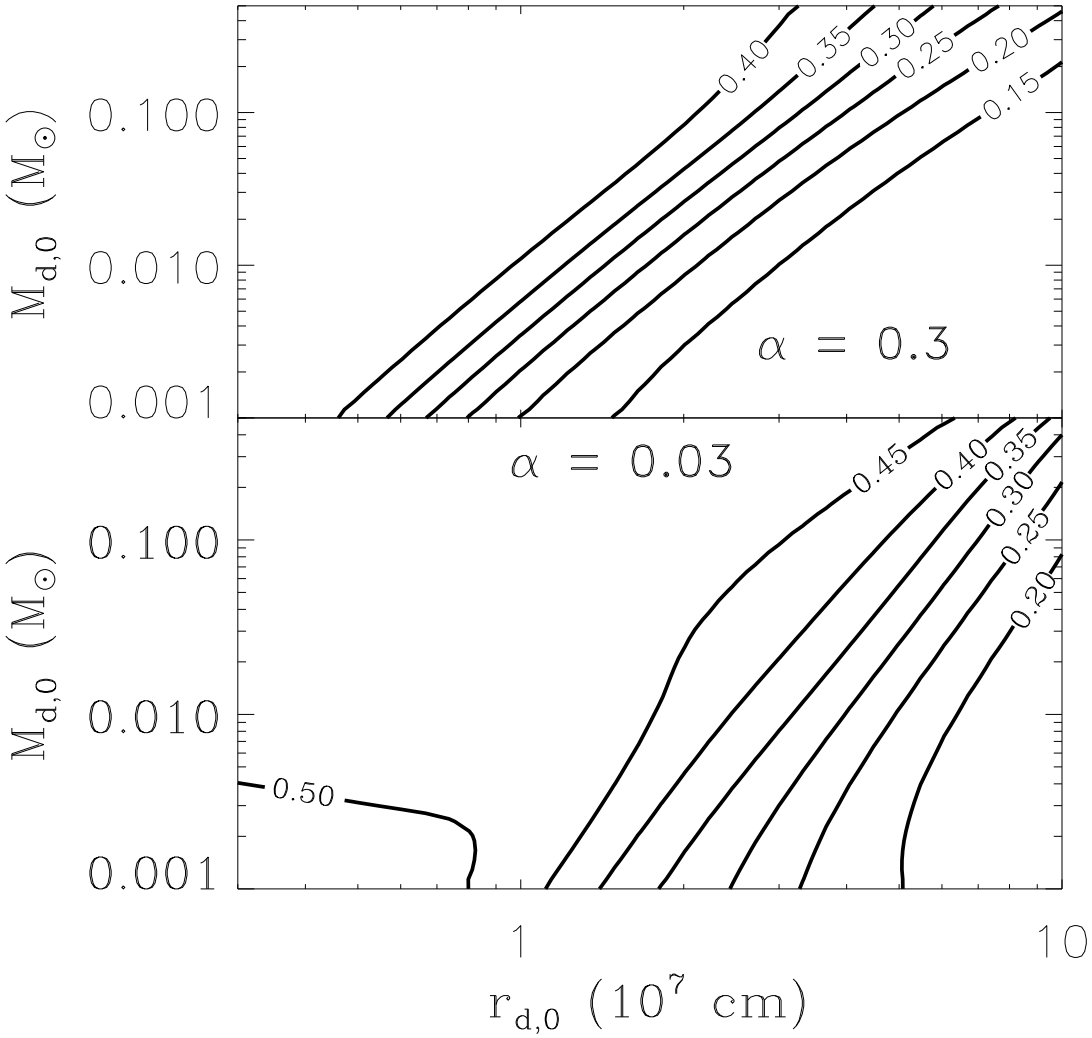

Figure 6.1: Contours of the final electron fraction Y_e^f following weak freeze-out in CO merger disks as a function of the initial disk mass $M_{d,0}$ and radius $r_{d,0}$ for two values of the viscosity, $\alpha = 0.3$ (*top*) and $\alpha = 0.03$ (*bottom*). The initial electron fraction in all models is taken to be $Y_e^0 = 0.1$.

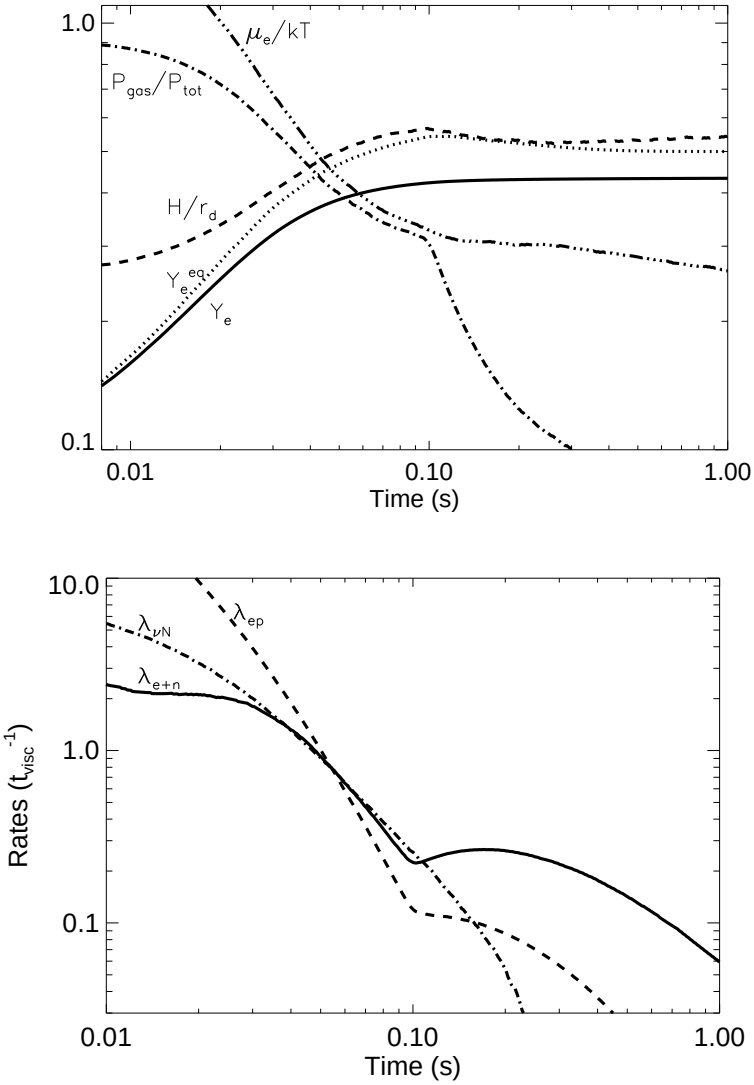

Figure 6.2: The process of weak freeze-out in our one-zone model of a viscously-spreading, hyper-accreting disk. The left panel shows the time evolution of the electron fraction Y_e (*solid line*), disk thickness H/r_d (*dashed line*), degeneracy parameter μ_e/kT (*triple-dot-dashed line*), and the ratio of gas to total pressure $P_{\rm gas}/P_{\rm tot}$ (*dot-dashed line*), calculated for $\alpha = 0.3$ and for a disk with initial mass $M_{d,0} = 0.1 M_\odot$ and radius $r_{d,0} = 3 \times 10^6$ cm. Also shown with a dotted line is the equilibrium electron fraction Y_e^{eq} obtained by setting the right hand side of equation (6.2) to zero. The right panel shows the rates of the weak interactions that modify $Y_e(t)$, normalized to the viscous timescale $t_{\rm visc}$. The electron, positron, and neutrino capture rates are denoted by λ_{ep}, λ_{e^+n}, and $\lambda_{\nu N}$, respectively. Note that Y_e freezes out of equilibrium at the same time that the disk becomes advective ($H/r_d \gtrsim 0.5$) and non-degenerate ($\mu_e \lesssim kT$). Since Y_e^{eq} rises to $\gtrsim 0.5$ as the disk becomes non-degenerate, the final composition is only moderately neutron-rich, with a final electron fraction $Y_e^f \simeq 0.43$.

similar solution for a thick disk, we estimate analytically that disks that satisfy

$$M_{d,0} \gtrsim 3 \times 10^{-3} \left(\frac{r_{d,0}}{10^7 \mathrm{cm}}\right)^{7/3} \left(\frac{\alpha}{0.1}\right)^{2/3} M_\odot \tag{6.5}$$

are sufficiently compact to become neutrino-cooled and neutron-rich at early stages in their evolution (see also eq. [5.19] and surrounding discussion). Equation (6.5) does a reasonable job of reproducing the parameter space in Figure 6.1 where Y_e^f differs significantly from its initial value. For instance, equation (6.5) shows that lower values of α allow less massive disks of a fixed size to enter β-equilibrium; this is consistent with the wider parameter space with $Y_e^f > Y_e^0 = 0.1$ at low α.

To illustrate the process of weak freeze-out explicitly, Figure 6.2 (*left panel*) shows the evolution of the electron fraction $Y_e(t)$ for a disk with $M_{d,0} = 0.1 M_\odot$ and $r_{d,0} = 3 \times 10^6$ cm. We also show the equilibrium electron fraction Y_e^{eq} (obtained by setting the right hand side of eq. [6.2] to zero), the ratio of the disk scaleheight to the radius H/r_d, the ratio of the gas pressure to the total pressure $P_{\rm gas}/P_{\rm tot}$, and the ratio of the electron chemical potential to the disk temperature μ_e/kT (i.e., the degeneracy parameter). Also shown for comparison in the right panel of Figure 6.2 are the weak interaction rates from equation (6.2), normalized to the viscous timescale $t_{\rm visc} \equiv \alpha^{-1}\Omega^{-1}(H/r_d)^{-2}$.

Figure 6.2 shows that at early times, when the disk is neutrino-cooled and $H/r_d \sim 1/3$, pair captures are rapid compared to the viscous timescale. Thus, the disk enters $\beta-$equilibrium with an electron fraction $Y_e \approx Y_e^{eq}$ that is $\ll 0.5$ because positron captures are suppressed relative to electron captures under the degenerate conditions ($\mu_e \gg kT$) in the midplane. At later times ($t \sim 0.1$ s) the disk thickens to $H/r_d \sim 0.5$ and becomes non-degenerate ($\mu_e \ll kT$) and radiation pressure-dominated. At this point $Y_e^{\rm eq}$ rises to $\gtrsim 0.5$ because positron captures under non-degenerate conditions now become energetically favored over electron captures due to the proton-neutron mass difference. Note, however, that as the disk thickens weak interactions become slow compared to the viscous timescale and Y_e freezes out at the value $Y_e^f \approx 0.43$. Although (non-local) neutrino absorptions are unimportant relative to electron captures at early times, their rate $\lambda_{\nu N}$ is comparable to the pair capture rates near freeze-out and must be included to

accurately determine Y_e^f.

Figure 6.1 shows that moderately neutron-rich freeze-out ($Y_e^f \sim 0.3 - 0.5$) is a common feature of accretion disks formed from CO mergers for a wide range of initial conditions. However, contrasting the disk's neutron-rich equilibrium state ($Y_e \simeq Y_e^{eq} \sim 0.1$) at early times with its final, non-degenerate state that actually favors a *proton-rich* composition in equilibrium (i.e., $Y_e^{eq} > 0.5$), it is *a priori* unclear why Y_e freezes out with a value $Y_e^f \sim 0.3-0.5$ between these two extremes.

To understand why this is the case, note that an approximate condition for weak freeze-out is that the pair capture timescale becomes longer than the viscous time $t_{\rm visc}$. Since the disk becomes non-degenerate around freeze-out, electron and positron captures occur at a similar rate (e.g., Qian & Woosley 1996)

$$\lambda_{eN} \approx 0.45 T_{\rm MeV}^5 \, {\rm s}^{-1}, \tag{6.6}$$

where $T \equiv T_{\rm MeV}{\rm MeV}$ and eN represents either $e^- p$ or $e^+ n$. The associated URCA cooling rate per nucleon is given by

$$\dot{Q}_{eN} = \langle \epsilon_\nu \rangle \lambda_{eN} \approx 2.3 T_{\rm MeV}^6 \, {\rm MeV \, s}^{-1}, \tag{6.7}$$

where $\langle \epsilon_\nu \rangle \approx 5.04 kT$ is the mean neutrino energy released per capture. The viscous heating rate per nucleon at $r \gg r_*$ is

$$\dot{Q}_{\rm visc} = \frac{9}{4} \nu \Omega^2 m_{\rm N} \approx \frac{9}{4} \alpha m_{\rm N} r^2 \Omega^3 \left(\frac{H}{r} \right)^2, \tag{6.8}$$

where $m_{\rm N}$ is the nucleon mass. If we assume that the disk is supported primarily by gas pressure[3] then the midplane temperature is $kT \approx m_{\rm N} r^2 \Omega^2 (H/r)^2$. Combining this with equations (6.6) – (6.8) we find that

$$\lambda_{eN} t_{\rm visc} = \frac{9}{4} \left(\frac{kT}{\langle \epsilon_\nu \rangle} \right) \left(\frac{H}{r} \right)^{-2} \left(\frac{\dot{Q}_{eN}}{\dot{Q}_{\rm visc}} \right) \simeq 1.8 \left(\frac{\dot{Q}_{eN}}{\dot{Q}_{\rm visc}} \right) \left(\frac{H/r}{0.5} \right)^{-2}. \tag{6.9}$$

Equation (6.9) shows that once neutrino cooling no longer offsets viscous heating (i.e., $\dot{Q}_{\rm visc} \gtrsim \dot{Q}_{eN}$) and the disk thickens to $H/r \sim 1$, weak freeze-out (i.e.,

[3] As discussed in §6.2.1 and shown in Figure 6.2, gas and radiation pressure are comparable at freeze-out; the assumption that gas pressure dominates is, however, sufficient for the purposes of a simple estimate.

$\lambda_{eN} t_{\rm visc} \lesssim 1$) necessarily results. Physically, this occurs because the disk is cooled by e^-/e^+ captures, the very same processes that largely control the evolution of Y_e (see Fig. 6.2). This conclusion is fairly robust because it applies at any radius and is independent of the value of α. Although the absorption of neutrinos from the central disk threatens to complicate this simple argument, the right panel of Figure 6.2 shows that the effect of absorptions is at most comparable to that of pair captures prior to freeze-out.

6.3 Height-Integrated Model

The results of §6.2 suggest that neutron-rich freeze-out is a common feature of viscously-spreading, hyper-accreting disks. However, the one-zone model makes a number of simplifying assumption that may affect the final electron fraction Y_e^f. In this section we present a 1D (height-integrated) model of a viscously-spreading disk that more precisely determines Y_e^f and its distribution with mass. In §6.3.1 we describe the initial conditions and relevant equations. Then we present our results in §6.3.2.

6.3.1 Equations and Initial Conditions

Our 1D calculation evolves the surface density Σ, midplane temperature T, and electron fraction Y_e as a function of radius r and time t using the 2N-RK3 (6th order space, 3rd order time) scheme described in Brandenburg (2001). We use a logarithmic radial grid that extends from just outside the inner edge of the disk at $r_* = 10^6$ cm, out to a radius that safely exceeds the outer edge of the disk at the final time step (typically $\approx 10^9$ cm).

The surface density is evolved according to the diffusion equation for an axisymmetric disk in a Newtonian 1/r gravitational potential (e.g., Frank et al. 2002):

$$\frac{\partial \Sigma}{\partial t} = \frac{3}{r}\frac{\partial}{\partial r}\left[r^{1/2} \frac{\partial}{\partial r}\left(\nu \Sigma r^{1/2} \right) \right], \tag{6.10}$$

where the viscosity ν is proportional to just the gas pressure (see eq. [6.4] and

surrounding discussion). The radial velocity v_r is not evolved explicitly but instead follows from equation (6.10) and mass continuity:

$$v_r = \frac{-3}{\Sigma r^{1/2}} \frac{\partial}{\partial r} \left(\nu \Sigma r^{1/2} \right). \tag{6.11}$$

We take the initial surface density of the disk to be

$$\Sigma(r, t = 0) \propto \left(\frac{r}{r_{d,0}} \right)^m \exp \left[-(2+m) \left(\frac{r}{r_{d,0}} \right) \right], \tag{6.12}$$

with the constant of proportionality set by requiring that the total disk mass equals $M_{d,0}$. Equation (6.12) concentrates the initial disk mass $\propto \Sigma r^2$ about the radius $r_{d,0}$, with larger values of the parameter m resulting in a more narrowly concentrated mass distribution. As discussed in §6.2.1, the precise mass distribution of disks produced from CO mergers is uncertain theoretically. In most of our calculations we take $m = 5$, although our results are relatively insensitive to m. Due to numerical issues that arise from the exponential drop-off of Σ at the outer edge of the disk, we impose an initial density floor that is sufficiently small that matter at the density floor contains a fraction $\lesssim 10^{-3}$ of the total disk mass at any time; we have verified that our results are insensitive to the level of this floor as long as it contains negligible mass. We have also performed calculations using a power-law density distribution that concentrates the disk's initial mass at small radii (e.g., $\Sigma \propto r^{-3}$); we find results that are similar to those obtained using equation (6.12) with $r_{d,0}$ taken near the disk's inner edge.

We calculate the scaleheight H by assuming hydrostatic equilibrium in the vertical direction, i.e., we take $H = c_s/\Omega$, where $c_s \equiv (P_{\rm tot}/\rho)^{1/2}$ is the isothermal sound speed. We evolve the midplane temperature using the equation for the specific entropy S, which is given by

$$T \frac{dS}{dt} = \dot{q}_{\rm visc} - \dot{q}_\nu^- + \dot{q}_\nu^+, \tag{6.13}$$

where $(d/dt) \equiv (\partial/\partial t) + v_r(\partial/\partial r)$, $\dot{q}_{\rm visc} = (9/4)\nu\Omega^2$ is the viscous heating rate, and $\dot{q}_\nu^-$ is the neutrino cooling rate, as given in Di Matteo et al. (2002) but modified to include the effects of arbitrary Y_e and electron degeneracy (e.g., Beloborodov

2003). The term

$$\dot{q}_\nu^+ = \lambda_{\bar{\nu}_e p}\langle\epsilon_{\bar{\nu}_e}\rangle\left[Y_e - \left(\frac{1-X_{\rm f}}{2}\right)\right] + \lambda_{\nu_e n}\langle\epsilon_{\nu_e}\rangle\left[1 - Y_e - \left(\frac{1-X_{\rm f}}{2}\right)\right] \qquad (6.14)$$

represents neutrino heating from the inner radii of the accretion disk, where $\lambda_{\nu_e n}$ and $\lambda_{\bar{\nu}_e p}$ are the neutrino capture rates given by equation (6.3). We not not include heating due to $\alpha-$particle formation because we are primarily interested in determining the final electron fraction, and $\alpha-$particles form only after the disk has fallen out of weak equilibrium.

The initial temperature profile is set by requiring that $H/r = 0.3$ at all radii. An initially thick disk is physically motivated by the fact that CO merger disks form dynamically hot; however, because the thermal time is short compared to the viscous time, the disk's evolution quickly becomes independent of the initial scaleheight anyways.

Finally, we evolve the electron fraction profile $Y_e(r)$ using equation (6.2), with $d/dt = \partial/\partial t + v_r\partial/\partial r$. To keep the required timesteps reasonable, we equate Y_e with its equilibrium value Y_e^{eq} when the weak interaction rates greatly exceed the local viscous rate $1/t_{\rm visc}$. As in §6.2, we take the initial electron fraction to be $Y_e^0 = 0.1$ at all radii.

The surface density across the ghost zones at the inner boundary is set to enforce a constant mass accretion rate $\dot{M} \propto \Sigma\nu$ at the value of $\dot{M}$ in the first active zone. We interpolate the temperature and electron fraction at the inner boundary. Unlike in the one-zone calculations in §6.2, we do not implement a no-torque boundary condition on the inner edge of the disk, in part because it leads to an unphysical temperature profile at small radii (in particular, $T \to 0$ as $r \to r_*$). Our results for Y_e^f are not sensitive to this boundary condition. We also interpolate all variables at the outer boundary, although this choice has no effect on our results because the outer boundary is not in causal contact with the inner flow. We have verified that our code conserves total mass $M_{\rm tot}$ and angular momentum J by checking that decreases in $M_{\rm tot}$ and J with time are compensated by their fluxes across the inner grid cell.

6.3.2 Results

Figures 6.3, 6.4, and 6.5 summarize our results for a disk with $\alpha = 0.3$, $M_{d,0} = 0.1 M_\odot$, and $r_{d,0} = 3 \times 10^6$ cm, which we take as our fiducial model. Figure 6.3 shows the local disk mass $\pi r^2 \Sigma$ (*top*) and the absolute value of the mass advection rate $\dot{M} \equiv 2\pi r \Sigma v_r$ (*bottom*) as a function of radius r at times $t = 0.01, 0.1$, and 1 s, with later times denoted by increasingly thinner lines; these epochs correspond to ~ 1, 10, and 100 times the initial viscous time at $r = r_{d,0}$.

Figure 6.3 shows that the disk spreads outwards in time, reaching $\sim 3 \times 10^8$ cm by $t \sim 1$ s. After a few viscous times, a constant inward accretion rate is established at small radii that roughly matches the *outward* mass advection rate of the bulk of the disk. The inner steady-state disk almost extends to the stagnation point where $v_r = 0$, which moves outwards with time.

Figure 6.4 shows radial profiles of the disk thickness H/r (*top*), the ratio of neutrino cooling $\dot{q}_{\rm cool} = \dot{q}_\nu^-$ to total heating $\dot{q}_{\rm heat} \equiv \dot{q}_{\rm visc} + \dot{q}_\nu^+$ (*middle*), and the midplane temperature (*bottom*). Figure 6.4 illustrates that at early times the bulk of the disk becomes efficiently cooled by neutrinos (i.e., $\dot{q}_{\rm cool} \approx \dot{q}_{\rm heat}$) and geometrically thin ($H/r \ll 1$). At later times, as the disk spreads and the temperature decreases, neutrinos are no long able to cool the majority of the mass efficiently (i.e., $\dot{q}_{\rm cool} \ll \dot{q}_{\rm heat}$) and H/r increases. As discussed in Chapter 5, the outer disk becomes thick first, and radiatively inefficient conditions move inwards as $\dot{M}$ decreases. This behavior can be seen explicitly in Figure 6.4 by comparing where H/r becomes large at early and late times. Note that the small "bump" in H/r corresponds to low-density material on the very outer edge of the disk which separates the density floor (where the thermal time is always much longer than the evolution timescale) from the bulk of the disk. This artifact of our initial conditions has no effect on our conclusions. Also note that at late times ($t = 1$ s) a range of radii around $r \simeq 40$ km has $q_{\rm cool} > q_{\rm heat}$. This region of net cooling radiates the thermal energy carried into the neutrino-cooled portion of the disk from the higher entropy advective disk at larger radii.

Figure 6.5 shows the evolution of the electron fraction Y_e (*solid line*) and its

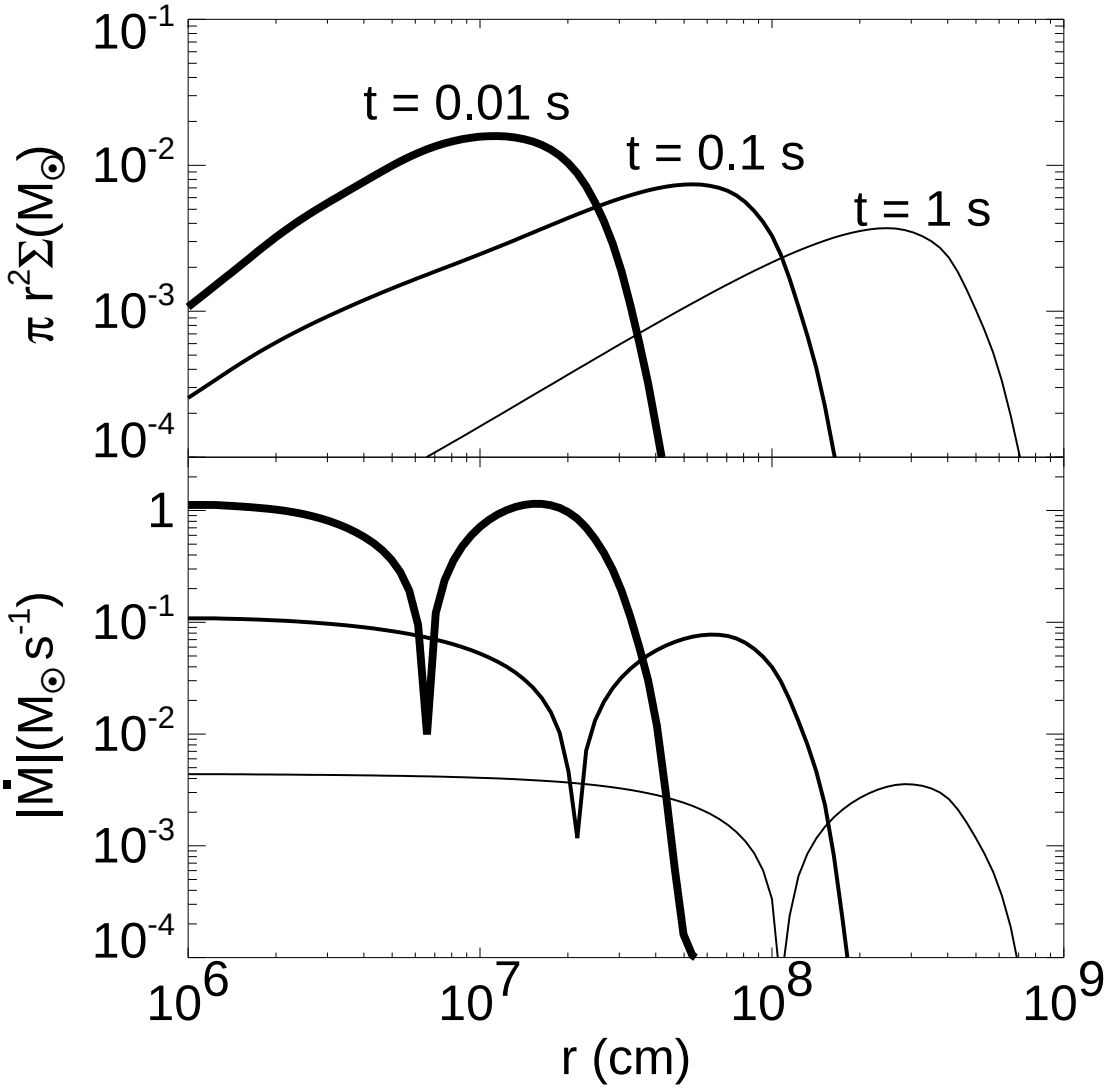

Figure 6.3: Local disk mass $\pi r^2\Sigma$ and the absolute value of the mass advection rate $\dot{M} \equiv 2\pi r v_r \Sigma$ as a function of radius. The model assumes $\alpha = 0.3$, $M_{d,0} = 0.1 M_\odot$ and $r_{d,0} = 3 \times 10^6$ cm (with $m = 5$ in eq. [6.12]). Solutions are shown at $t = 0.01, 0.1$, and 1 s, with later times denoted by increasingly thinner lines. The nodes in the lower panel occur at the stagnation point that separates matter accreting onto the BH ($\dot{M} < 0$) at small radii from the bulk of the disk that is spreading outwards ($\dot{M} > 0$).

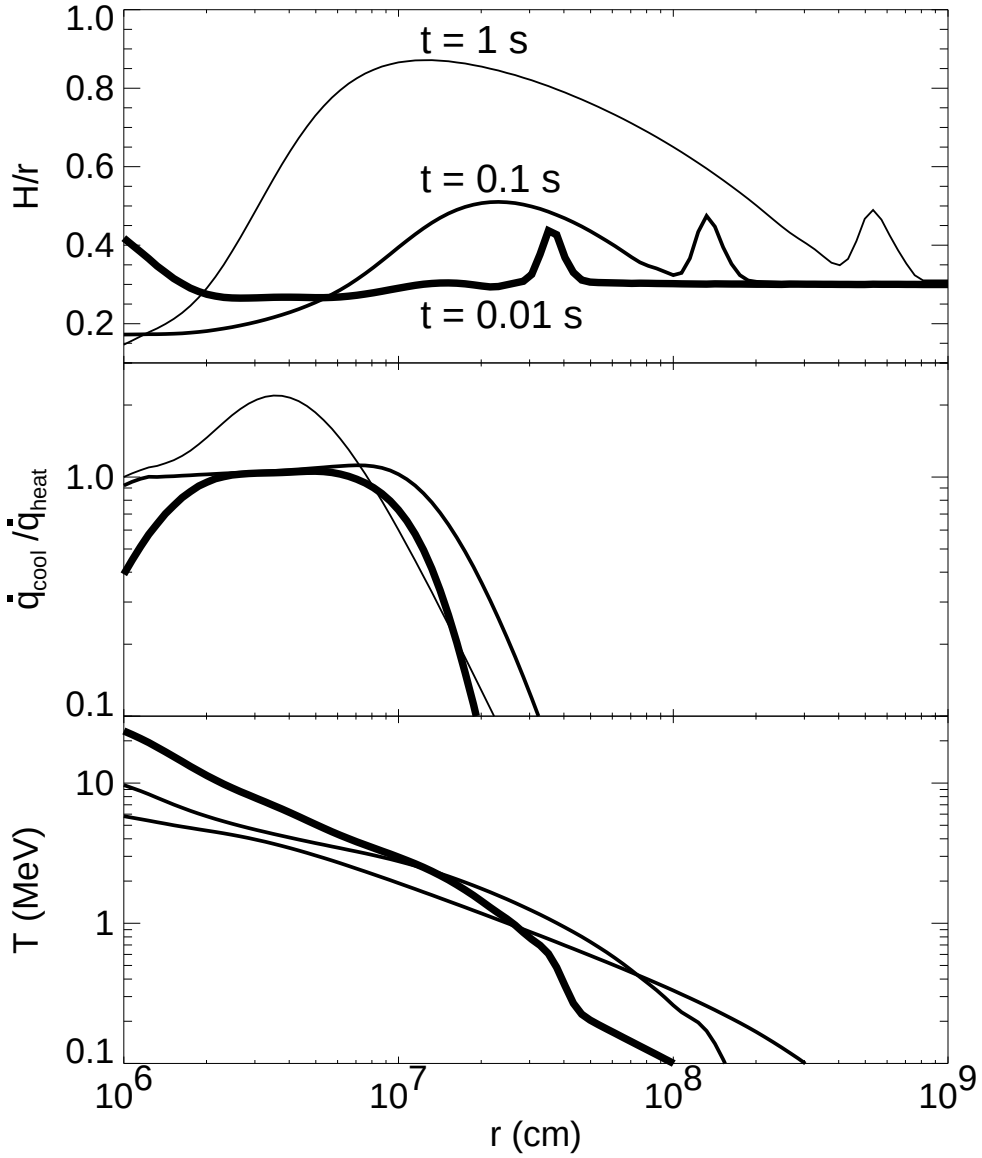

Figure 6.4: Scaleheight H/r, the ratio of neutrino cooling $\dot{q}_{\rm cool} = \dot{q}_\nu^-$ to total heating $\dot{q}_{\rm heat}$, and the midplane temperature T for the same model and times presented in Figure 6.3. The total heating $\dot{q}_{\rm heat} = \dot{q}_{\rm visc} + \dot{q}_\nu^+$ consists of viscous heating and neutrino irradiation from the accretion disk at small radii.

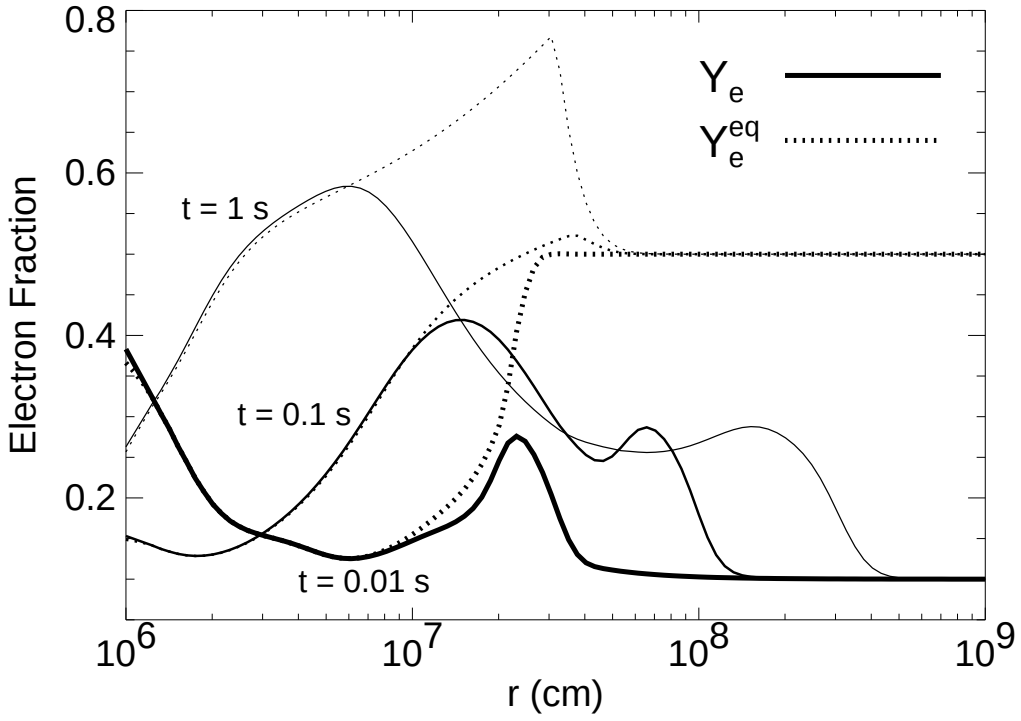

Figure 6.5: Electron fraction Y_e (*solid line*) and the equilibrium electron fraction Y_e^{eq} (*dotted line*) for the same model and times presented in Figures 6.3 and 6.4. At early times, the disk is in $\beta-$equilibrium, with $Y_e \approx Y_e^{eq} \ll 0.5$ at all radii that contain substantial mass. At later times, Y_e^{eq} rises as the disk becomes advective and non-degenerate, and Y_e freezes out with final values in the range $Y_e^f \sim 0.1 - 0.5$ (see Fig. 6.7).

equilibrium value Y_e^{eq} (*dotted line*). At very early times the entire disk is in weak equilibrium, with $Y_e = Y_e^{eq}$ at all radii that contain substantial mass.[4] However, as the disk spreads and thickens, the midplane becomes non-degenerate, which causes Y_e^{eq} to rise. As this occurs, weak interactions become slow compared to the timescale over which the disk evolves (for the same reasons discussed in §6.2.2), and Y_e begins to freeze-out of equilibrium as it lags behind the rising value of Y_e^{eq}. As with radiatively inefficient conditions, freeze-out begins at the outer edge of the disk and moves inwards with time. By the final time step the majority of the disk mass has frozen out, with values of Y_e^f that span the range $Y_e^f \sim 0.1 - 0.5$. This behavior is directly analagous to the freeze-out of the "ring" radius in the one-zone model (Fig. 6.2), but now occuring in each annulus of the disk.

In Figure 6.6 we quantify the global process by which the disk becomes advective and falls out of weak equilibrium by showing the time evolution of the total disk mass $M_{\rm tot}$, the total mass that is advective $M_{\rm tot}^{\rm adv}$, and the total mass that has fallen out of weak equilibrium $M_{\rm tot}^{\rm f}$. We define annuli that are advective and have fallen out of equilibrium as those that satisfy

$$\dot{q}_{\rm cool} \lesssim \dot{q}_{\rm heat}/2 \tag{6.15}$$

and

$$\lambda_{\rm max} \lesssim 3/t_{\rm visc}, \tag{6.16}$$

respectively, where $\lambda_{\rm max}$ is the maximum of the weak interaction rates in equation (6.2). Although the numerical prefactors used in equations (6.15) and (6.16) are somewhat arbitrary, our results are not sensitive to their precise values. Figure 6.6 shows that $M_{\rm tot}$ decreases with time as matter accretes onto the BH, with $M_{\rm tot} \propto t^{-1/3}$ at late times, as expected from the self-similar behavior of an advective disk with $H/r \sim$ constant (Chapter 5). After an initial viscous time, a comparable amount of material is advective and out of equilibrium; $M_{\rm tot}^{\rm adv}$ and $M_{\rm tot}^{f}$ remain fairly constant at $\sim 2 \times 10^{-2} M_\odot$ until the majority of the disk becomes advective and freezes out at late times.

[4] At radii larger than the extent of the disk, Y_e remains equal to its initial value at all times because these regions (which comprise the density floor) never enter equilibrium.

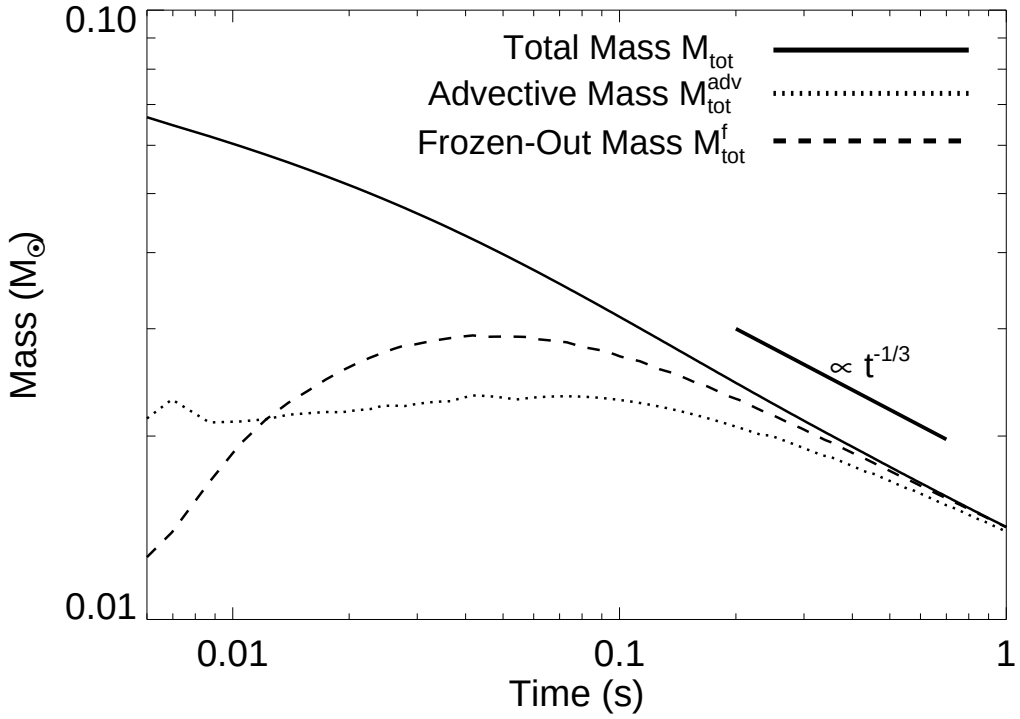

Figure 6.6: Time evolution of the total mass in the disk $M_{\rm tot}$, the total mass that has become advective because it cannot cool efficiently $M_{\rm tot}^{\rm adv}$ (as defined by eq. [6.15]), and the total mass that has fallen out of weak equilibrium $M_{\rm tot}^{f}$ (as defined by eq. [6.16]).

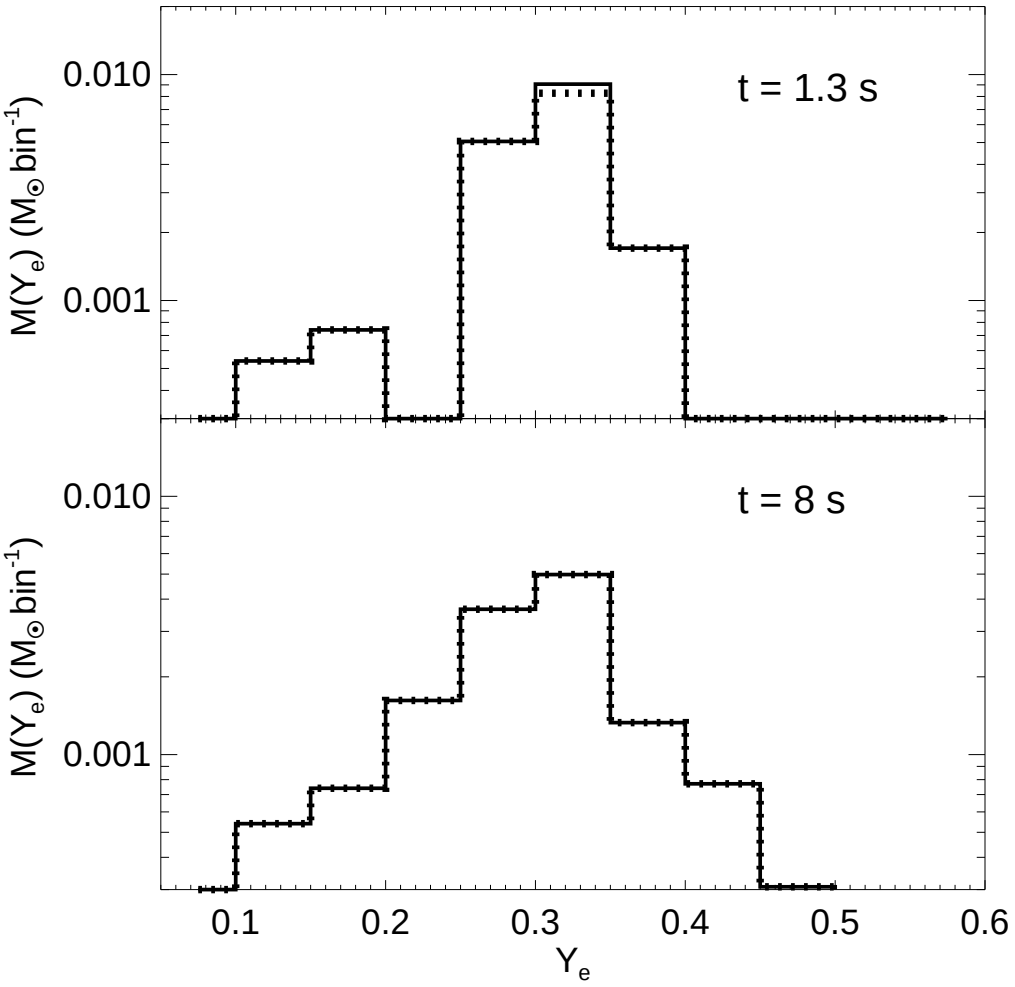

Figure 6.7: Amount of mass with a given electron fraction $M(Y_e)$ for the model with $M_{d,0} = 0.1M_\odot$, $r_{d,0} = 3\times10^6$ cm, and $\alpha = 0.3$. The solid and dotted lines include, respectively, mass that has become advective (eq. [6.15]) and that has fallen out of weak equilibrium (eq. [6.16]). The times $t = 0.03$ s and 0.3 s correspond to when the disk is 50% and 90% advective, respectively.

As discussed in §6.1, once a portion of the disk becomes advective, a viscously-driven outflow likely drives away a substantial portion of its mass (e.g., Blandford & Begelman 1999). In our calculations we have neglected the effects of such a mass sink on the evolution of the disk. Figure 6.6 shows that this approximation remains reasonable until $t \sim 0.03 - 0.1$ s because prior to this point the majority of the disk remains neutrino cooled. Mass- and angular momentum-loss to a wind leads to a more rapid decline in $\dot{M}$, which further speeds up the onset of the advective phase and weak freeze-out at smaller radii (Chapter 5).

In Figure 6.7 we show histograms of mass as a function of electron fraction $M(Y_e)$ at the times $t = 0.03$ s and $t = 0.3$ s. The solid and dashed lines are the matter that is advective and out of $\beta-$equilibrium, respectively (as defined by eqs. [6.15] and [6.16]). These distributions typically correspond to the same matter because annuli fall out of equilibrium as they become advective (see eq. [6.9]). We show the composition at these two particular times because they correspond to epochs when the disk has become $\approx 50\%$ and 90% advective, respectively (Fig. 6.6). Thus, these distributions likely represent typical values of the electron fraction in the viscously-driven outflows that dominate subsequent mass-loss from the disk.

It is useful to compare the results in Figure 6.7 with the one zone calculation from §6.2 for the same initial disk parameters (see Fig. 6.1). When the disk is 90% advective at $t = 0.3$ s, the height-integrated calculation finds a final electron fraction distribution centered around a mass-averaged value $\langle Y_e^f \rangle \approx 0.29$, which is somewhat lower than the value of $Y_e^f = 0.43$ given by the one-zone model. Indeed, in most of our calculations we find that Y_e^f calculated using the one zone model tends to slightly exceed $\langle Y_e^f \rangle$ obtained from the full 1D calculations.

In Figures 6.8 and 6.9 we show histograms similar to Figure 6.7, but for solutions calculated with a lower viscosity ($\alpha = 0.03$) and a lower initial mass ($M_{d,0} = 0.01 M_\odot$), respectively. The times chosen correspond to epochs when the disk is 50% and 90% advective. The mass-averaged electron fraction when the disk is 90% advective is $\langle Y_e^f \rangle \approx 0.3$ for both the lower α and lower $M_{d,0}$ models. The similarity in the distribution of Y_e^f for $\alpha = 0.3$ and $\alpha = 0.03$ in Figures 6.7 and 6.8 supports our argument that the freeze-out process is relatively independent of

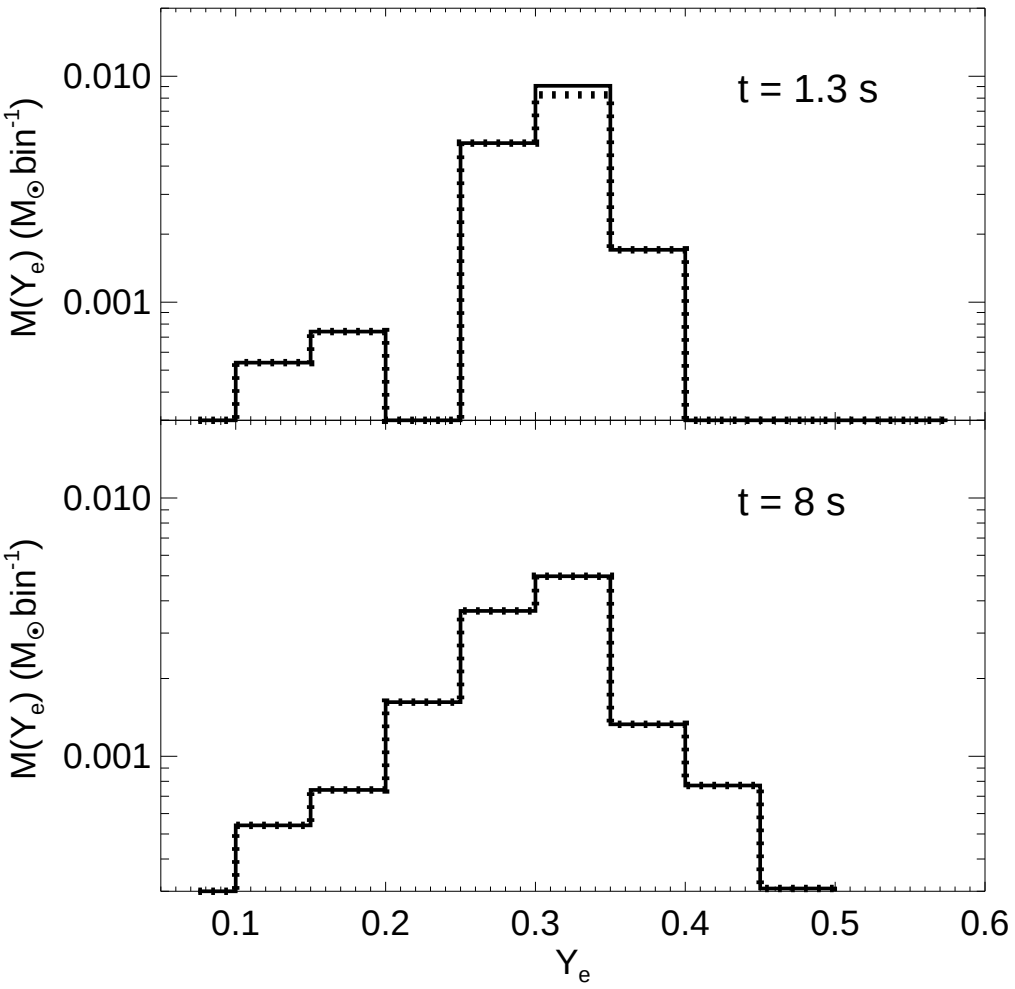

Figure 6.8: The same as Figure 6.7, but for $\alpha = 0.03$. The times shown, $t = 1.3$ s and 8 s correspond to when the disk is 50% and 90% advective, respectively.

the details of how the disk viscously spreads (see §6.2.2). The lower disk mass case (Fig. 6.9) is notable because a significant fraction of the disk's mass freezes out with $Y_e \lesssim 0.2$, and such low-Y_e material may produce third-peak r-process elements (Hoffman et al. 1997).

We have performed freeze-out calculations for a number of other disk parameters. In Table 6.1 we summarize our results for $\langle Y_e^f \rangle$ and the fraction $f_{\rm adv}$ of the initial disk mass that remains when the disk is 90% advective. Although different initial mass distributions and viscosities give somewhat different Y_e^f distributions, the neutron-rich freeze-out of $\sim 20 - 50\%$ of the disk's original mass is a generic property of the disks created during CO mergers.

6.4 Discussion

Accretion disks formed from CO mergers that are sufficiently massive and compact to satisfy equation (6.5) become neutrino-cooled, degenerate, and neutron-rich early in their evolution. Eventually, as the disk accretes and viscously spreads, neutrino cooling is no longer able to offset viscous heating and the disk becomes advective. At this point several important changes occur nearly simultaneously: the disk becomes geometrically thick ($H/r \sim 1$), radiation pressure-dominated, and non-degenerate at the same time that the equilibrium electron fraction Y_e^{eq} rises from $\ll 0.5$ to $\gtrsim 0.5$ and Y_e freezes out (Fig. 6.2; see also Beloborodov 2008). Weak freeze-out necessarily accompanies the disk's advective transition because e^-/e^+ captures are primarily responsible for both cooling the disk and setting its electron fraction (see eq. [6.9] of §6.2.2). Because Y_e^{eq} is rising as freeze-out occurs, moderately neutron-rich freeze-out with $Y_e^f \approx 0.2 - 0.4$ is a generic feature of accretion disks formed from CO mergers. Our calculations in §6.2 and §6.3 largely confirm this basic conclusion (see Table 6.1).

Neutron-rich freeze-out in hyper-accreting disks is usefully contrasted with the *proton−rich* freeze-out ($Y_e^f \simeq 0.88$) in the very early universe. Big bang nucleosynthesis (BBN) occurred on a timescale of minutes under non-degenerate and highly radiation-dominated conditions (entropy $S \sim 10^{10}\ k_B$ baryon^{-1}). By

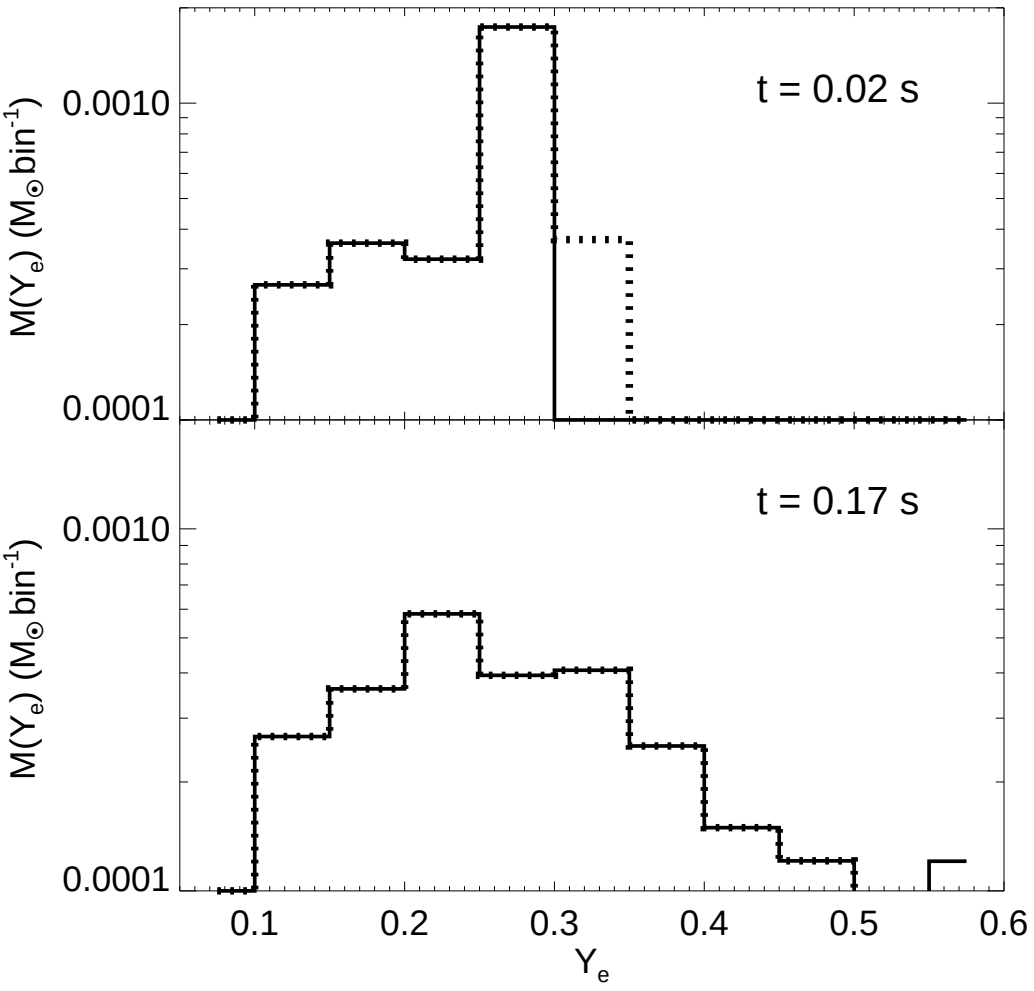

Figure 6.9: The same as Figure 6.7, but for $M_{d,0} = 0.01 M_{\odot}$.

Table 6.1 Properties of Freeze-Out in 1D Calculations

$M_{d,0}\,(M_\odot)$	$r_{d,0}\,(\mathrm{cm})$	α	$M_{\rm BH}\,(M_\odot)$	$\langle Y_e^f\rangle^{(a)}$	$f_{\rm adv}^{(b)}$
0.1	3×10^6	0.3	3	0.29	0.20
-	3×10^6	0.03	3	0.30	0.15
-	6×10^6	0.3	3	0.26	0.31
-	1.2×10^7	0.3	3	0.21	0.40
-	6×10^6	0.3	10	0.37	0.28
0.01	3×10^6	0.3	3	0.28	0.28
-	3×10^6	0.03	3	0.34	0.21
-	1.2×10^7	0.3	3	0.21	0.40
0.001	3×10^6	0.3	3	0.28	0.39
-	1.2×10^7	0.3	3	0.17	0.72

(a) Mass-averaged freeze-out electron fraction when the disk is 90% advective; (b) Fraction of the initial disk mass that remains when the disk is 90% advective.

contrast, hyper-accreting disks freeze-out on a timescale $\sim 0.1-1$ s (depending on α) under moderately degenerate conditions, and with comparable gas and radiation pressure, i.e., $S\sim 3-20\ k_B$ baryon^{-1}. Hyper-accreting disks freeze-out neutron-rich because they start in $\beta-$equilibrium under degenerate conditions, while the early universe never had $Y_e<0.5$ because degeneracy effects were never important.

A further important difference is in the production of heavy elements. Once the disk becomes advective and freezes out, a viscously-driven wind likely unbinds most of its remaining mass; as these outflows expand away from the midplane and cool, heavy elements will be formed. Due to the "deuterium bottleneck," BBN produced almost no elements heavier than He. By contrast, the late-time outflows from hyper-accreting disks possess modest entropies[5] and are thus generally in NSE when $\alpha-$particles form. Even an $\alpha-$rich freeze-out is unlikely (Hoffman & Woosley 1992) because, under dense (low entropy) neutron-rich conditions, α's burn efficiently via the reaction sequence ^{4}He(α n,γ)^{9}Be(α,n)^{12}C (Delano & Cameron 1971). As discussed further in §6.4.1, the abundances of the elements

[5]The entropy in the outflow is probably only a few k_B baryon^{-1} larger than in the disk midplane because only a fraction of the gravitational binding energy is required to drive an outflow (advective disks are only marginally bound).

synthesized are thus approximately determined by neutron-rich NSE (Hartmann et al. 1985).

It is also important to contrast the site of nucleosynthesis that we have introduced here with outflows driven from the disk by neutrino heating (e.g., Levinson 2006; Barzilay & Levison 2008; Chapter 4). Neutrino-driven outflows generally occur at early times or small radii, when the disk midplane is still in $\beta-$equilibrium and the irradiating neutrino flux is substantial. The outflow's final electron fraction in this case is set by an equilibrium with neutrino absorptions ($Y_e \approx Y_e^\nu$ in eq. [6.1]) and is not directly related to Y_e in the midplane (e.g., Surman & McLaughlin 2004). By contrast, the outflows considered here occur after the midplane itself has fallen out of weak equilibrium, and so the disk's electron fraction Y_e^f is retained by the outflow. While neutrino absorptions in the disk are somewhat important near freeze-out, at no point does the midplane electron fraction enter equilibrium with the neutrinos, as generically occurs in neutrino-driven outflows (Chapter 4). Instead, the outwardly-spreading disk provides a protective "cocoon" that transports low-Y_e material (kept neutron-rich by degenerate electron capture) away from the deneutronizing flux of neutrinos from the central disk. Furthermore, the viscously-driven outflows that we have focused on carry away a substantial fraction of the disk's initial mass; because neutrino-driven outflows likely eject less mass (Chapter 5), the total nucleosynthetic yield from CO mergers is probably dominated by the viscously-driven outflows at late times.

Finally, although we believe that the disk is largely unbound by viscous heating once it becomes advective (Blandford & Begelman 1999; Stone & Pringle 2001), if nothing else the energy released by $\alpha-$particle (or even heavier element) formation is sufficient to unbind the disk at late times (Lee & Ramirez-Ruiz 2007; Chapter 5). Since $\alpha-$particle formation occurs soon after the disk becomes advective, our conclusions would be qualitatively unchanged if nuclear (rather than viscous) energy powers the late-time outflow. In this case the formation of heavy elements would begin in the disk midplane, but the final nucleosynthetic yield would probably be similar.

6.4.1 Implications

As we have argued, moderate entropy, neutron-rich outflows appear to be a common property of accretion disks formed from CO mergers at late times. Although detailed calculations of the dynamics and nucleosynthesis in these outflows need to be performed, the late-time conditions in the disk favor the production of elements with abundances close to their NSE values at charged-particle reaction freeze-out. In particular, the entropies ($\sim 10\ k_B$ baryon^{-1}) and dynamical timescales ($\tau_{\rm dyn} \sim 0.01 - 0.1$ s) at freeze-out are similar to those explored in low entropy nucleosynthesis calculations by Woosley & Hoffman (1992). For example, in their model with $S \approx 29\ k_B$ baryon^{-1} and $\tau_{\rm dyn} \approx 0.1$ s, these authors find that all $\alpha-$particles reassemble into heavy nuclei for $Y_e \lesssim 0.45$, and that the final abundances closely resemble those of NSE (see the second column in their Table 2).

Neutron-rich NSE calculations were performed by Hartmann et al. (1985). For $Y_e \approx 0.35 - 0.40$, they find that the predominant isotopes created are ^{82}Se, ^{79}Br, and ^{78}Se (in order of decreasing Y_e; see their Fig. 3). The very low solar system abundances of these isotopes (total mass fraction $X_\odot \approx 3 \times 10^{-8}$) strongly constrains the rate of astrophysical events that produce material with $Y_e \approx 0.35 - 0.4$ in NSE: we estimate that the maximum allowed mass ejection of material with $Y_e \approx 0.35 - 0.4$ into the ISM is $\dot{M}_{\rm max} \approx (M_{\rm gal} X_\odot / t_{\rm gal}) \approx 1.5 \times 10^{-7} M_\odot$ yr^{-1}, where $t_{\rm gal} \approx 10^{10}$ yrs and $M_{\rm gal} \approx 5 \times 10^{10} M_\odot$ and are the age and baryonic mass of the Galaxy, respectively (Binney & Tremaine 1994). More neutron-rich material ($Y_e \lesssim 0.35$) will produce even heavier isotopes and, possibly, an r-process. Since these elements are also very rare, a similar constraint can be placed on the rate that very low-Y_e material is ejected into the ISM. For instance, isotopes near the second r-process peak ($A \sim 130$) have a typical solar mass abundance $X^r_\odot \sim 10^{-9}$ relative to hydrogen; therefore, if material ejected with $0.2 \lesssim Y_e \lesssim 0.35$ produced equal numbers of $N \sim 10$ r-process isotopes in this mass range, the constraint on the mass ejected would be $\dot{M}_{\rm max} \sim 5 \times 10^{-8} (N/10) M_\odot$ yr^{-1}, comparable to the rate for material with $Y_e \approx 0.35 - 0.4$ given above. In order to be conservative,

below we use the constraint $\dot{M}_{\rm max} \approx 1.5 \times 10^{-7} M_\odot$ yr^{-1} for all material ejected with $Y_e \lesssim 0.4$. However, a more precise determination of the isotopes produced by the ejection of moderate entropy material with $Y_e \approx 0.2 - 0.35$ would likely place even stronger constraints on the rate of CO mergers.

Based on Figures 6.7-6.9 and our one-zone calculations in §6.2 we find that a fraction $f_{\rm adv} \approx 0.2 - 0.5$ of the disk's initial mass remains when it becomes advective at late times (see Table 6.1), with a higher fraction for less massive, more extended disks. Of this material, we estimate that the majority of the mass will have $Y_e^f \lesssim 0.4$, when averaging over many events with different initial disk properties (see Figs. 6.7-6.9 and Table 6.1). Although ejecta from mergers that occur outside Galactic disk will not enrich the ISM, population synthesis studies estimate that for large spirals such as the Milky Way only a small fraction ($\lesssim 20\%$) of mergers occur in intergalactic space (Belczynski et al. 2006). Thus a fraction $\eta \approx 0.1 - 0.5$ of the disk's initial mass will both become unbound from the disk and pollute the ISM with rare neutron-rich isotopes. Hence, if the average mass of the disks formed from CO mergers is $\langle M_{d,0} \rangle$, their rate in the Milky Way cannot exceed

$$\dot{N}_{\rm max} \approx \frac{\dot{M}_{\rm max}}{\eta \langle M_{d,0} \rangle} \approx 10^{-5} \left(\frac{\eta}{0.2} \right)^{-1} \left(\frac{\langle M_{d,0} \rangle}{0.1 M_\odot} \right)^{-1} {\rm yr}^{-1}, \quad (6.17)$$

where we have normalized η to a typical value ~ 0.2.

Based on observed binary NS systems, Kalogera et al. (2004) find that the NS-NS merger rate in the Milky Way is between 1.7×10^{-5} and 2.9×10^{-4} yr^{-1} at 95% confidence. Population synthesis estimates (e.g., Belczynski et al. 2006) are consistent with this range but with larger uncertainties. Our constraint in equation (6.17) thus requires either NS-NS merger rates at the low end of current estimates, or a small average disk mass $\ll 0.1 M_\odot$.

Ultimately, equation (6.17) must be combined with GR simulations of the merger process that determine $M_{d,0}$ as a function of the total binary mass $M_{\rm tot} = M_1 + M_2$, the NS mass ratio $q = M_1/M_2 \leq 1$, and the NS equation of state (EOS). General relativistic merger simulations (Shibata et al. 2005; Shibata & Taniguchi 2006) find that when $M_{\rm tot}$ is above a critical value ($\gtrsim 2.6 M_\odot$, depending on the

EOS) the central object produced during the merger promptly collapses to a BH. In this case, $M_{d,0}$ decreases rapidly with increasing q (see Shibata & Taniguchi 2006, Fig. 13). For instance, when the double pulsar system PSR J0737-3039A/B (with $q \simeq 0.935$ and $M_{\rm tot} = 2.587 M_\odot$) merges in ≈ 100 Myr, current simulations predict that the disk will have a mass $\sim 10^{-3} - 10^{-2} M_\odot$ if BH formation is prompt (Shibata & Taniguchi 2006). This disk mass is reasonably consistent with our constraint in equation (6.17) and current NS-NS merger rate estimates. It is also consistent with the relatively low isotropic energies of short GRBs with measured redshifts ($\sim 10^{-5} - 10^{-3} M_\odot$ c^2; Nakar 2007).

On the other hand, simulations find that when $M_{\rm tot}$ is below the threshold for prompt collapse, a hypermassive NS supported by differential rotation is initially formed (Baumgarte et al. 2000). If this NS is able to transport angular momentum outwards, it will collapse to a BH on a longer timescale (≈ 100 ms; Shibata et al. 2006; Duez et al. 2006), producing a sizable disk ($\gtrsim 0.03 M_\odot$) whose mass is relatively independent of q (Oechslin & Janka 2006; Shibata et al. 2006). Since the disk masses formed after delayed collapse are comparable to those allowed by our constraint in equation (6.17) even for low $\dot{N} \sim 10^{-5}$ yr^{-1}, our results suggest that the formation of a long-lived hyper-massive NS is a rare outcome of NS-NS mergers.

Since there are no known BH-NS binaries, the BH-NS merger rate is even less certain. Bethe & Brown (1998) argue that BH-NS mergers could be substantially more common than NS-NS mergers, with Bethe et al. (2007) estimating a rate $\sim 10^4$ Gpc^{-3}yr^{-1}, corresponding to $\sim 10^{-3}$ yr^{-1} in the Milky Way. Our results rule out such a high rate unless $\langle M_{d,0} \rangle$ is less than $\sim 10^{-3} M_\odot$. A low average disk mass may be possible, however, because only systems for which the NS-BH mass ratio falls within a fairly narrow range may produce a sizable disk upon merging (e.g., Miller 2005).

The late-time nucleosynthesis in CO merger disks also places interesting constraints on the beaming fraction of short GRBs if most of these events truly result from CO mergers. Using the observed local short GRB rate of ≈ 10 Gpc^3 yr^{-1} (Nakar et al. 2006) and assuming that the merger rate is proportional to the blue

stellar luminosity (Phinney 1991), the short GRB rate in the Milky Way is estimated to be $\dot{N}_{\rm SGRB} \approx 10^{-6}$ yr^{-1} (Nakar 2007). Thus, if all mergers that produce disks also produce short GRBs, the beaming fraction must obey

$$f_b \gtrsim \frac{\dot{N}_{\rm SGRB}}{\dot{N}_{\rm max}} \approx 0.13 \left(\frac{\eta}{0.2}\right) \left(\frac{\langle M_{d,0} \rangle}{0.1 M_\odot}\right). \quad (6.18)$$

This constraint implies that the jet half-opening angle must exceed $\theta \sim (2 f_b)^{1/2} \sim 30^\circ (\eta/0.2)^{1/2} (M_{d,0}/0.1 M_\odot)^{1/2}$. This is consistent with other evidence that short GRBs may be less collimated than long GRBs (e.g., Grupe et al. 2006; Soderberg et al. 2006), which are instead inferred to have $0.002 \lesssim f_b \lesssim 0.01$ (Frail et al. 2001; Bloom et al. 2003; Guetta, Piran, & Waxman 2005). Note that equation (6.18) is probably a stronger constraint than equation (6.17) because only CO mergers that form sizable accretion disks are likely to produce GRBs in the first place.

In addition to material driven from the disk by late time winds, neutron-rich matter may be ejected *dynamically* during the merger process itself (e.g., Freiburghaus et al. 1999; Rosswog et al. 1999). Although the amount of material ejected in merger calculations depends sensitively on details such as the NS spin and equation of state (Rosswog et al. 1999), the rare isotopes synthesized by this highly neutron-rich ejecta may provide a constraint on the CO merger rate that is comparable to that from late-time outflows given by equation (6.17).

Our conclusion that accretion disks formed from CO mergers freeze-out neutron-rich is also consistent with the absence of SN-like longer wavelength transients coincident with these events. If CO merger disks froze out with $Y_e^f \gtrsim 0.5$ instead of $Y_e^f \lesssim 0.5$, their late-time outflows would efficiently synthesize ^{56}Ni (e.g., Seitenzahl et al. 2008), which could power an optical/infrared transient on $\sim$ day timescales following short-duration GRBs. Despite intensive searches, however, such transients have not yet been observed. For instance, early optical follow-up of the GRB 050509b (Hjorth et al. 2005) limited the amount of ^{56}Ni to $\lesssim 10^{-2} M_\odot$ (Kulkarni 2005; Bloom et al. 2006; Chapter 5), consistent with the modest amount of material with $Y_e^f \gtrsim 0.5$ that we find in Figures 6.7–6.9. Although we do not expect much ^{56}Ni to be produced in late-time outflows from CO merger disks, earlier neutrino-driven outflows may produce up to $\sim 10^{-3} M_\odot$ in Ni, which could power

a fainter optical or infrared transient (Chapter 5). In addition, outflows powered by fall-back accretion onto the BH at late times could power an X-ray transient on a timescale of days to weeks (Rossi & Begelman 2008).

Acknowledgements

We thank Todd Thompson and Stan Woosley for helpful conversations and useful information. A.L.P. is supported by the Theoretical Astrophysics Center at UC Berkeley. B.D.M. and E.Q. are supported in part by the David and Lucile Packard Foundation and a NASA GSRP Fellowship to B.D.M.

Chapter 7

Nickel-Rich Outflows From Accretion Disks Formed by the Accretion-Induced Collapse of White Dwarfs

B. D. Metzger, A. L. Piro, E. Quataert (2009), accepted to MNRAS.

Abstract

In several circumstances, electron captures can cause a white dwarf (WD) approaching the Chandrasekhar mass to collapse to a neutron star (NS) before a thermonuclear explosion ensues. It has generally been assumed that such an accretion-induced collapse (AIC) does not produce a detectable supernova (SN). If, however, the progenitor WD is rapidly rotating (as may be expected due to its prior accretion), a centrifugally-supported disk forms around the NS upon collapse. We calculate the subsequent evolution of this accretion disk and its nuclear composition using time-dependent height-integrated simulations with initial conditions taken from the AIC calculations of Dessart et al. (2006). Soon after its formation, the disk is cooled by neutrinos and its composition is driven neutron-rich (electron

fraction $Y_e \sim 0.1$) by electron captures. However, as the disk viscously spreads, it is irradiated by neutrinos from the central proto-NS, which dramatically alters its neutron-to-proton ratio. We find that electron neutrino captures increase Y_e to ~ 0.5 by the time that weak interactions in the disk freeze out. Because the disk becomes radiatively inefficient and begins forming α-particles soon after freeze-out, powerful winds blow away most of the remaining mass of the disk. These $Y_e \sim 0.5$ outflows synthesize up to a few times $10^{-2} M_\odot$ in ^{56}Ni. As a result, AIC may be accompanied by a radioactively-powered, SN-like transient that peaks on a timescale of ~ 1 day. Since few intermediate-mass elements are likely synthesized, these Nickel-rich explosions should be spectroscopically distinct from other SNe. The timescale, velocity, and composition of the AIC transient can be modified if the disk wind sweeps up a $\sim 0.1 M_\odot$ remnant disk created by a WD-WD merger; such an "enshrouded" AIC may account for sub-luminous, sub-Chandrasekhar Type I SNe. Optical transient surveys such as Pan-STARRs and the Palomar Transient Factory should detect a few AIC transients per year if their true rate is $\sim 10^{-2}$ of the Type Ia rate, and the Large Synoptic Survey Telescope (LSST) should detect several hundred per year. High cadence observations ($\lesssim 1$ day) are optimal for the detection and follow-up of these events.

7.1 Introduction

It is generally thought that when an accreting C-O white dwarf (WD) approaches the Chandrasekhar mass $M_{\rm Ch}$, the carbon ignites in its core, causing the WD to explode and produce a Type Ia supernova (SN). If, however, the composition of the WD is O-Ne instead of C-O, the outcome may be qualitatively different: electron captures on Ne nuclei will cause the WD to collapse to a neutron star (NS) before an explosion can ensue (Miyaji et al. 1980; Canal et al. 1990; Gutierrez et al. 2005; Poelarends et al. 2008). Such an accretion-induced collapse (AIC) may also occur for C-O WDs with large initial masses ($M > 1.1 M_\odot$) in systems with mass-transfer rates $\dot{M} \gtrsim 10^{-8} M_\odot$ yr^{-1} (Nomoto & Kondo 1991) or following the merger of two WDs in a binary if their total mass exceeds $M_{\rm ch}$ (e.g., Mochkovitch

& Livio 1989, 1990; Yoon et al. 2007). Indeed, spectroscopic surveys of WD-WD binaries (e.g., SPY; Napiwotzki et al. 2004) have discovered at least one system that will merge within a few Hubble times with a total mass tantalizingly close to $M_{\rm Ch}$ (Napiwotzki et al. 2002).

Despite its likely occurrence in nature, AIC has not yet been observationally identified, probably because it is less common and produces less ^{56}Ni than a normal SN (e.g., Woosley & Baron 1992). Identifying AIC or constraining its rate would, however, provide unique insights into the paths of degenerate binary evolution, the true progenitors of Type Ia SNe (e.g., Yungelson & Livio 1998), and the formation channels of globular cluster NSs (Grindlay 1987), low mass X-ray binaries (van den Heuvel 1984; Michel 1987), and millisecond pulsars (Grindlay & Bailyn 1988; Bailyn & Grindlay 1990). Identifying the optical signature of AIC is also important because these events may be a source of strong gravitational wave emission (Fryer et al. 2002; Ott 2008).

In this Letter we show how AIC may itself produce a SN-like transient which, although less luminous and shorter-lived than a typical SN, may nonetheless be detectable with upcoming optical transient surveys. Although little ^{56}Ni is ejected by the newly-formed proto-NS itself, we show that powerful winds from the accretion disks formed during AIC produce up to a few times $10^{-2}M_{\odot}$ in ^{56}Ni.

7.1.1 Nickel-Rich Winds from AIC Disks

Figure 7.1 summarizes the stages of AIC. Due to the accretion which proceeds the event, WDs that undergo AIC are probably rotating rapidly prior to collapse (Fig. 7.1A). As a result, a substantial fraction of the WD mass must be ejected into a disk during the collapse in order to conserve total angular momentum (Shapiro & Lightman 1976; Michel 1987). Dessart et al. (2006, 2007; hereafter D06,07) perform 2D axisymmetric AIC calculations, in which they find that a quasi-Keplerian accretion disk with mass $M_{\rm d,0} \sim 0.1 - 0.5M_{\odot}$ forms around the newly-formed proto-NS.

In Chapter 6 we studied the time-dependent evolution of accretion disks with

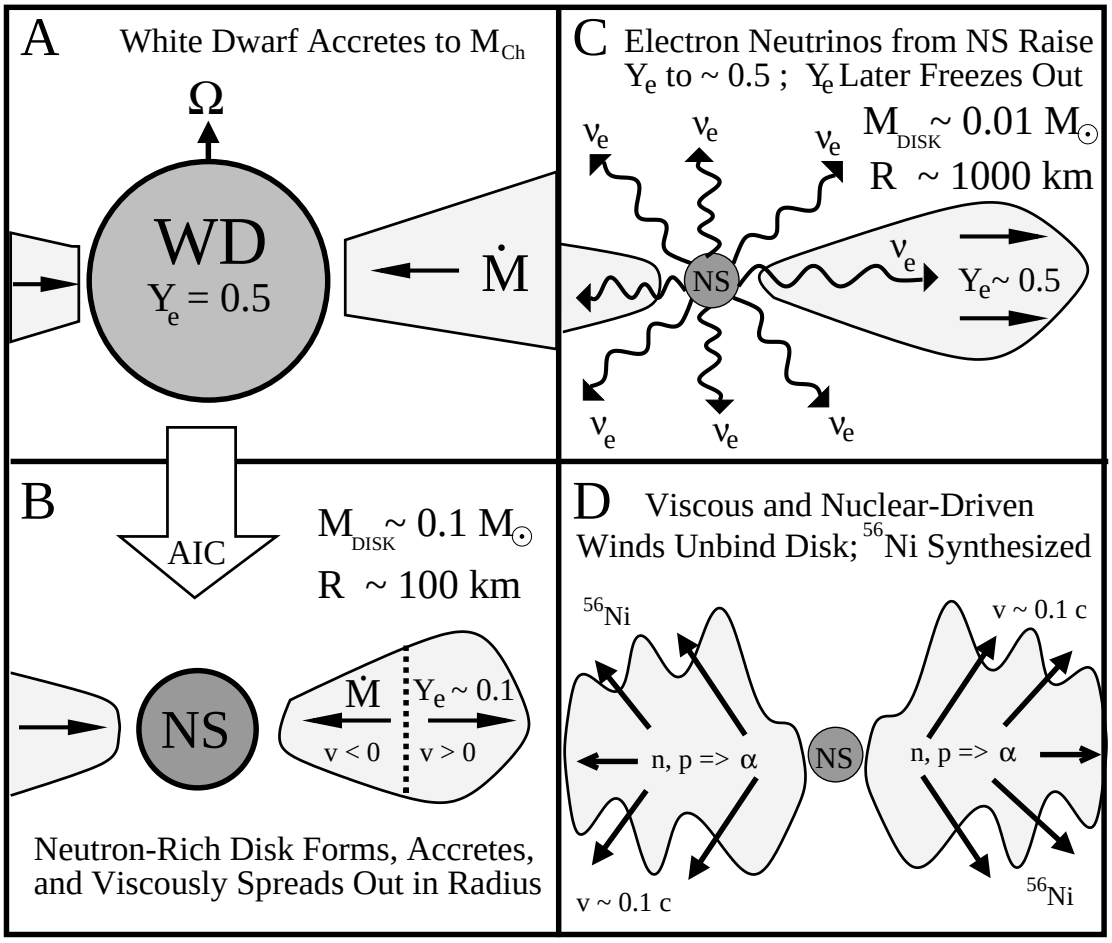

Figure 7.1: Stages in the accretion-induced collapse of a WD. (A) WD accretes up to near the Chandrasekhar mass ($M_{\rm Ch}$) from either a binary companion or following the disruption of another WD in a merger. Due to the accretion of angular momentum, the WD is rapidly rotating prior to collapse. (B) Electron captures cause the WD to collapse to a proto-NS surrounded by a compact accretion disk with a mass $\sim 0.1 M_\odot$ and a size ~ 100 km. Electron captures drive the composition neutron-rich (i.e., to an electron fraction $Y_e \sim 0.1$). As matter begins to accrete onto the proto-NS, the bulk of the disk spreads to larger radii. (C) As the disk spreads, the midplane is irradiated by neutrinos from the central proto-NS. Electron neutrinos are absorbed by neutrons, raising the electron fraction to $Y_e \sim 0.5$. (D) The electron fraction of the disk freezes out. Soon thereafter, powerful outflows blow the disk apart. As the ejecta expands adiabatically, material with $Y_e \gtrsim 0.5$ is efficiently synthesized into ^{56}Ni, the subsequent decay of which powers a SN-like optical transient.

similar initial properties that are formed from black hole (BH)-NS or NS-NS mergers. Many of these results also apply to proto-NS accretion following AIC. Although the disk is initially concentrated just outside the proto-NS surface, the bulk of the mass of the disk must spread to larger radii as matter accretes in order to conserve angular momentum. Early in their evolution, such "hyper-accreting" disks are neutrino-cooled and geometrically thin, and their composition is driven neutron-rich by an equilibrium between e^-/e^+ captures under degenerate conditions (e.g., Pruet et al. 2003; Fig. 7.1B): the electron fraction $Y_e \sim 0.1$, where $Y_e \equiv n_p/(n_p + n_n)$ and n_p/n_n are the proton/neutron number densities. As the disk viscously spreads and its temperature decreases, however, weak interactions eventually become slow compared to the evolution timescale of the disk and the value of Y_e freezes out.

Soon following freeze-out, neutrino cooling becomes inefficient and the disk becomes advective and geometrically thick (Chapters 5 and 6). Since advective disks are only marginally bound, powerful winds likely begin to unbind most of the remaining mass of the disk (Blandford & Begelman 1999), aided by the nuclear energy released as $\alpha-$particles begin to form (Lee & Ramirez-Ruiz 2007; Chapters 5 and 6). Because $\sim 20\%$ of the initial disk mass $M_{d,0}$ still remains when the disk becomes advective (or when $\alpha-$particles form), a robust consequence of disk formation during AIC is the ejection of up to a few times $10^{-2} M_\odot$. Since the ejecta are hot and dense, heavy isotopes are synthesized as they expand away from the midplane and cool. Because weak interactions are already slow by this point, which heavy isotopes are produced depends on Y_e in the disk at freeze-out.

In the case of BH accretion following BH-NS or NS-NS mergers, the disk freezes out neutron-rich with an electron fraction $Y_e \sim 0.2 - 0.4$ (Chapters 5 and 6). A crucial difference in the case of AIC, however, is the presence of the central proto-NS, which radiates a substantial flux of electron neutrinos as it de-leptonizes during the first few seconds following core bounce (e.g., Burrows & Lattimer 1986). This ν_e flux irradiates the disk, which acts to raise Y_e via absorptions on free neutrons ($\nu_e + n \rightarrow e^- + p$; Fig. 7.1C).

In §7.2 we present calculations of the evolution of the accretion disks formed

from AIC using time-dependent height-integrated simulations with initial conditions and neutrino irradiation taken from the AIC simulations of D06. We show that due to ν_e absorptions, a substantial fraction of the disk freezes out with $Y_e \gtrsim 0.5$. As a result, late time outflows from the disk primarily synthesize ^{56}Ni (Fig. 7.1D). We discuss the observational signature of these Ni-rich outflows in §7.3, and we conclude in §7.4 by evaluating the prospects for detecting AIC with upcoming optical transient surveys and as electromagnetic counterparts to gravitational wave sources.

7.2 AIC Accretion Disk Model

7.2.1 Methodology

The equations and assumptions employed here closely follow those in §6.3.1 for NS-NS or BH-NS mergers. To provide a brief summary, we evolve the surface density Σ, temperature T, and electron fraction Y_e as a function of radius r and time t using the 2N-RK3 scheme described in Brandenburg (2001). We employ an "α" prescription for the viscosity (Shakura & Sunyaev 1973), with the accretion stress proportional to the gas pressure. Our calculation includes all of the relevant neutrino cooling processes for both optically thin and optically thick disks (e.g., Di Matteo et al. 2002). We take the initial surface density $\Sigma(r, t = 0)$ from the Keplerian disk that forms soon after core bounce in the AIC calculations of D06. We focus on the $1.46 M_\odot$ WD model of D06, which collapses to form a $\approx 0.1 M_\odot$ disk that extends from the NS surface at ≈ 30 km out to several NS radii (see Fig. 5 of D06).

We evolve Y_e including both local e^-/e^+ pair captures ($e^- + p \rightarrow \nu_e + n$ and $e^+ + n \rightarrow \bar{\nu}_e + p$) and non-local neutrino absorptions ($\nu_e + n \rightarrow e^- + p$ and $\bar{\nu}_e + p \rightarrow e^+ + n$) due to irradiation from the central proto-NS. We approximate the neutrino flux from the proto-NS as arising from a "light bulb" at the origin because the neutrino capture rates only become important relative to the pair capture rates when the disk has spread to a radius which is much larger than that

of the central NS. We neglect the neutrino luminosity from the disk because it is small compared to the proto-NS luminosity. We assume that the initial electron fraction of the disk is $Y_e(r, t = 0) = 0.5$, i.e., that of the WD prior to collapse.

The neutrino absorption rates are proportional to $L_\nu \langle \epsilon_\nu \rangle$, where L_ν and $\langle \epsilon_\nu \rangle$ are the neutrino luminosities and mean energies, respectively, from the proto-NS. During the first $t \approx 1$ s following core bounce, we use $L_{\nu_e}, L_{\bar{\nu}_e}, \langle \epsilon_{\nu_e} \rangle$, and $\langle \epsilon_{\bar{\nu}_e} \rangle$ from D06 (specifically, their values in the equator; see their Fig. 9). The L_{ν_e} flux peaks at a very large value ($\gtrsim 10^{53}$ ergs s^{-1}) at early times, after the shock created at core bounce "breaks out" of the proto-NS's neutrinosphere. The flux at later times ($t \gtrsim 0.1$ s) is dominated by the cooling proto-NS, with L_{ν_e} remaining $\gtrsim L_{\bar{\nu}_e}$ as the proto-NS deleptonizes (Burrows & Lattimer 1986). Note that because $L_{\nu_e} \langle \epsilon_{\nu_e} \rangle > L_{\bar{\nu}_e} \langle \epsilon_{\bar{\nu}_e} \rangle$ during most of the first second following core bounce, the rate of ν_e captures exceeds the rate of $\bar{\nu}_e$ captures and the net effect of neutrino absorptions is to drive Y_e to a value $\gtrsim 0.5$ (Qian et al. 1993). This result is robust since shock break-out and deleptonization are generic features of NS formation (e.g., Burrows & Mazurek 1983); indeed, we find similar results using luminosities and mean energies from the rotating core-collapse simulations of Thompson, Quataert, & Burrows (2005).

When necessary, for $t \gtrsim 1$ s we take $L_\nu \propto t^{-1}$, motivated by the calculations of Pons et al. (1999), and assume $\langle \epsilon_\nu \rangle \propto L_\nu^{1/4} \propto t^{-1/4}$, as appropriate for a blackbody with a fixed radius. Although the neutrino luminosities and spectra at such late times are somewhat uncertain, we find that for $\alpha \gtrsim 0.01$ the disk evolves sufficiently rapidly that our results are relatively insensitive to the precise values of L_ν and $\langle \epsilon_\nu \rangle$ at late times.

7.2.2 Results

The viscous and thermal evolution of the accretion disks formed from AIC are very similar to those presented in Chapter 6 for NS-NS/NS-BH mergers; we refer the reader there for a detailed discussion of the overall evolution of the disk. The major qualitative difference between AIC and NS-NS/NS-BH merger disks is the

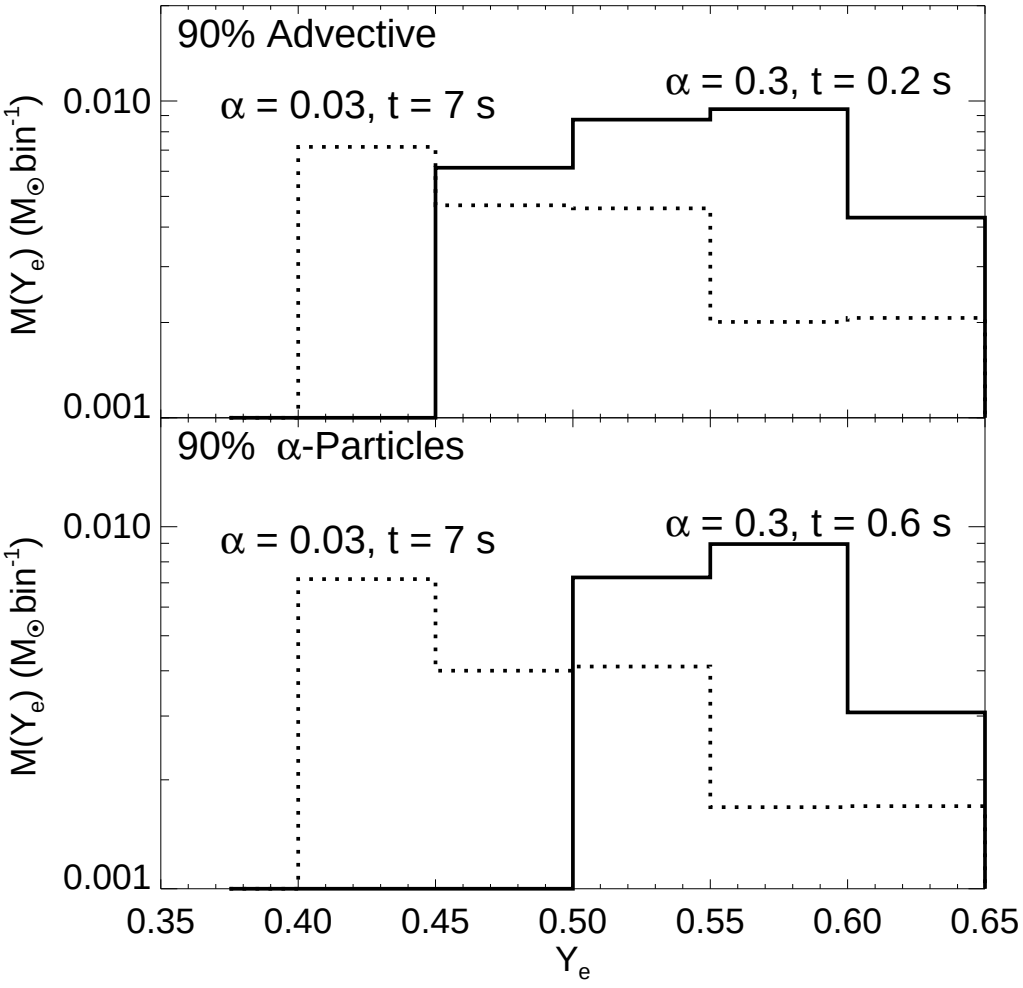

Figure 7.2: Amount of mass with a given electron fraction $M(Y_e)$ in the accretion disk formed from AIC for a model with an initial mass distribution and neutrino irradiation from the $1.46 M_\odot$ WD AIC simulation of D06. The top and bottom panels correspond to times when 90% of the mass of the disk is advective and has formed $\alpha-$particles, respectively. The solid and dashed lines show results for $\alpha = 0.3$ and $\alpha = 0.03$, respectively.

evolution of the electron fraction, so we focus on our results for Y_e below.

Figure 7.2 shows histograms of mass as a function of electron fraction $M(Y_e)$ for our fiducial model that employs an initial density profile and neutrino irradiation from the $1.46M_\odot$ WD model of D06. The solid and dashed lines show calculations performed with viscosity $\alpha = 0.3$ and $\alpha = 0.03$, respectively. The top panel shows $M(Y_e)$ when 90% of the mass of the disk has become advective, which corresponds to a time $t = 0.2(7)$ s for $\alpha = 0.3(0.03)$. Annuli in the disk are considered advective once the neutrino cooling rate becomes $\lesssim 1/2$ of the viscous heating rate. The bottom panel shows $M(Y_e)$ when 90% of the mass of the disk has fused into $\alpha-$particles, which corresponds to a time $t = (0.6)7$ s for $\alpha = 0.3(0.03)$. Although powerful outflows likely begin when the disk becomes advective (Blandford & Begelman 1999), thermonuclear disruption of the disk is assured once $\alpha-$particles form. This occurs because (1) the nuclear reactions that create (and destroy) deuterium (the building blocks of $\alpha-$particles) are still very fast compared to the evolution timescale of the disk (i.e., the disk is still in nuclear statistical equilibrium [NSE]) when the temperature drops sufficiently that the NSE $\alpha-$particle mass fraction becomes $\sim$ unity (e.g., Chen & Beloborodov 2007, eq. [13]); and (2) the energy released by forming $\alpha-$particles (~ 7 MeV per nucleon) exceeds the gravitational binding energy of the disk (see Chapters 5 and 6). Thus, the distributions in Figure 7.2 roughly bracket the distribution of Y_e in the outflows that carry away the remaining mass in the disk at late times.

Figure 7.2 shows that $\approx 0.02 - 0.03M_\odot$ (or $\approx 20 - 30\%$ of the initial disk mass) remains when the disk is largely advective. A comparable amount of mass remains when the disk forms $\alpha-$particles because this occurs at approximately the same time (Chapters 5 and 6; Beloborodov 2008). Although the bulk of the disk is initially driven neutron-rich by degenerate electron captures, Figure 7.2 shows that a large portion of the mass remaining at late times has $Y_e \gtrsim 0.5$. As discussed in §7.1.1, the disk composition is driven proton-rich by the powerful ν_e flux from the central proto-NS.

We have performed similar calculations for other disk parameters in order to study the sensitivity of our results to the initial properties of the disk (see

Table 7.1). For example, the disks found by D06,07 are fairly massive, but a less massive disk would result from a slower rotating WD. Thus, we have also performed calculations using the same initial density profile from D06, but normalizing the total initial disk mass to $M_{d,0} = 0.01 M_\odot$ instead of $0.1 M_\odot$. We have also calculated models with $\Sigma(r, t = 0)$, $L_\nu(t)$ and $\langle \epsilon_\nu \rangle(t)$ taken from the rapidly rotating, 1.92 $M_\odot$ WD model of D06, which formed a more massive initial disk ($M_{d,0} \approx 0.5 M_\odot$). In the high $M_{d,0}$ case we find that a significant fraction of the disk has exactly $Y_e = 0.5$ at freeze-out. This occurs because in this model $\alpha-$particle formation precedes weak freeze-out; thus, any excess free neutrons or protons are almost immediately captured into $\alpha-$particles (which have $Y_e = 0.5$) following a neutrino absorption (the "alpha-effect" of Fuller & Meyer 1995). We note, however, that torques within an accreting WD will probably prevent it from having sufficient differential rotation to support the large WD masses needed to form such a massive disk (Piro 2008); these models may still be achievable through the merger of two massive WDs.

In Table 7.1 we summarize our results for the total mass ($M_{\rm adv}$) and the total mass with $0.485 \lesssim Y_e \lesssim 0.6$ ($M_{\rm Ni}$) when the disk has become 90% advective. The latter is labeled $M_{\rm Ni}$ because a significant fraction of the mass ejected with Y_e in this range produces ^{56}Ni (see §7.3). In all cases, we find that a significant fraction ($\gtrsim 50\%$) of the mass remaining at late times has $Y_e \gtrsim 0.5$. Thus, under a variety of conditions, AIC leads to $\sim 10\%$ of the initial disk being ejected as moderately proton-rich material.

7.3 Optical Transients from AIC

In some ways, AIC can be considered a "failed" Type Ia SN because it does not produce $\sim 1 M_\odot$ of shock-heated ejecta. Indeed, the total ^{56}Ni mass ejected from the proto-NS is $\lesssim 10^{-3} M_\odot$ (e.g., Woosley & Baron 1992; D06,07; Chapter 4), rendering isolated NS birth practically invisible. In the presence of rotation, however, this failure is not complete. In §7.2 we showed that if an accretion disk forms around the proto-NS during collapse, a natural consequence of the subsequent evolution of the disk is that up to $\sim 10^{-2} M_\odot$ of material with $Y_e \gtrsim 0.5$

Table 7.1 Late-Time Mass and Composition of AIC Disks

$M_{d,0}^{(a)}$ ($M_\odot$)	Model$^{(b)}$	α	$M_{\rm adv}^{(c)}$ ($M_\odot$)	$M_{\rm Ni}^{(d)}$ ($M_\odot$)
0.1	$D06(1.46M_\odot$WD)	0.3	0.030	0.021
0.1	$D06(1.46M_\odot$WD)	0.03	0.021	8.9×10^{-3}
0.01	$D06(1.46M_\odot$WD)	0.3	4.3×10^{-3}	1.8×10^{-3}
0.5	$D06(1.92M_\odot$WD)	0.3	0.13	0.066
0.5	$D06(1.92M_\odot$WD)	0.03	0.11	0.051

(a) Initial disk mass; (b) Model used for the initial surface density $\Sigma(r, t = 0)$ and the proto-NS neutrino luminosities and energies; (c) Mass remaining when the disk is 90% advective; (d) Mass with $0.485 < Y_e < 0.6$ when the disk is 90% advective.

is ejected within a few seconds after core bounce.

When hyper-accreting disks become radiatively inefficient and begin forming $\alpha-$particles, gas and radiation pressure in the midplane are comparable and the entropy is $S \sim 10$ k$_B$ baryon^{-1}. Subsequent outflows from the disk are likely to possess a comparable entropy because heating that occurs as matter is unbound (e.g., due to $\alpha-$particle formation) is unlikely to deposit more than a few k$_B$ baryon^{-1} in additional entropy. A typical outflow speed is $v \sim 0.1 - 0.2$ c: this is approximately the escape speed from the disk when it becomes advective and a similar speed is attained from the ≈ 9 MeV baryon^{-1} released in producing Fe-peak elements.

Matter with $0.485 \lesssim Y_e \lesssim 0.6$ that begins in NSE at low entropy and expands adiabatically at mildly relativistic speeds is primarily synthesized into ^{56}Ni (e.g., Pruet et al. 2004) because ^{56}Ni is favored in NSE under proton-rich conditions (Seitenzahl et al. 2008). Our results in Figure 7.2 and Table 7.1 therefore imply that AIC outflows yield a typical Ni mass $M_{\rm Ni} \sim 10^{-2} M_\odot$ if the rotating $1.46M_\odot$-WD progenitors used in the calculations of D06,07 are representative. The decay of this Ni can reheat the (adiabatically cooled) ejecta sufficiently to produce detectable transient emission once the outflow expands sufficiently that photons can diffuse out (Arnett 1982).

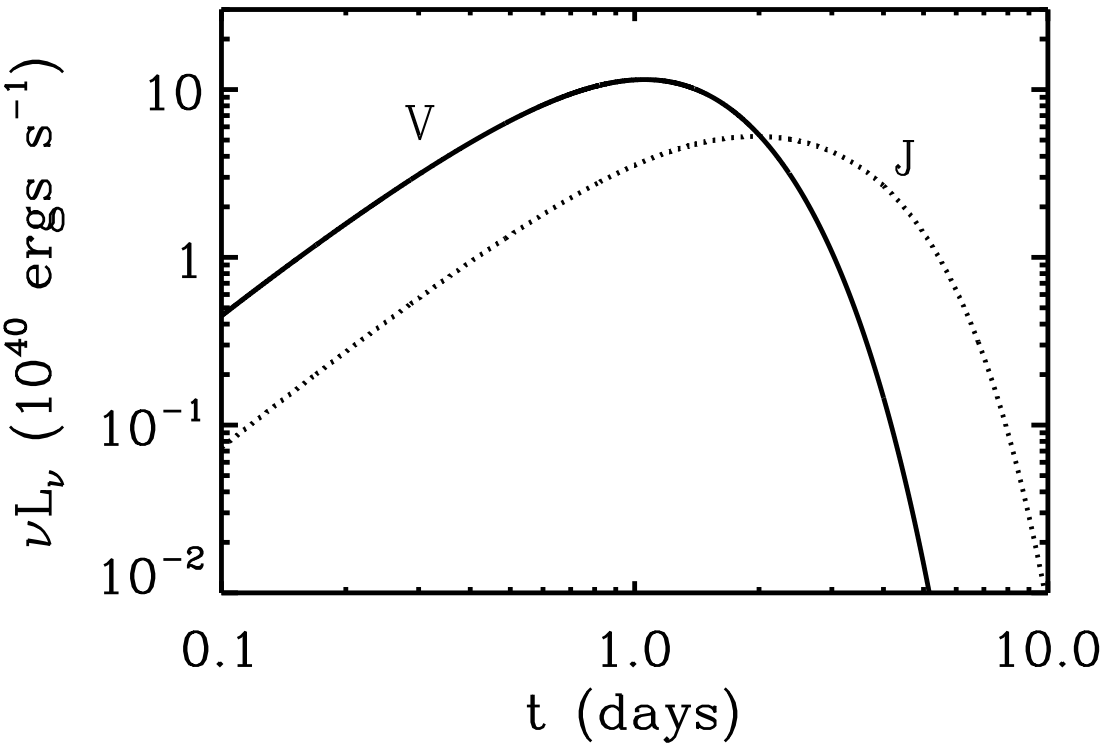

Figure 7.3: Luminosity of Ni decay-powered transient as a function of time for Ni mass $M_{\rm Ni} = 0.01 M_\odot$, total ejected mass $M_{\rm tot} = 0.02 M_\odot$, and ejecta velocity $v = 0.1$ c. The luminosities in V- and J-Band (0.44 and 1.26 μm, respectively) are shown with a solid and dashed line, respectively.

We explore this possibility by calculating the light curves of ejecta heated by Ni decay using the method of Kulkarni (2005) and Chapter 5. Figure 7.3 shows the V and J-band luminosities as a function of time since collapse for an outflow with Ni mass $M_{\rm Ni} = 10^{-2} M_\odot$ and total ejecta mass $M_{\rm tot} = 2 \times 10^{-2} M_\odot$ expanding at $v = 0.1$ c. The total luminosity peaks in the visual (V-band) on a ~ 1 day timescale, with $\nu L_\nu \sim 10^{41}$ ergs s^{-1}. The J-band light curve peaks somewhat later than V-band because the temperature at the photosphere decreases as the material expands. We discuss the likelihood of detecting such a transient with blind surveys in §7.4.

Although ^{56}Ni is likely to be the dominant isotope synthesized, other isotopes will also be produced in smaller abundances. For instance, under the conditions of interest $\sim 10\%$ of the ejected mass may remain in the form of $\alpha-$particles (Woosley & Hoffman 1992). Furthermore, our low-α calculations in Figure 7.2 indicate that some fraction of the material ejected may have $Y_e \lesssim 0.485$ (Fig. 7.2). In this case, freeze-out from NSE produces both stable (e.g., ^{58,60,62,64}Ni, ^{54,56,58}Fe) and radioactive (e.g., ^{66,68,70}Ni, ^{60,62,66}Zn) Fe-group elements instead of ^{56}Ni (Woosley & Hoffman 1992). Although this material will contribute to the opacity of the outflow ($M_{\rm tot}$ above), its additional contribution to the radioactive heating is unlikely to substantially alter the purely Ni-powered light curves in Figure 7.3.

7.4 Detection Prospects

Because AIC has never been observationally identified, its rate is uncertain. Binary population synthesis models predict galactic rates in the range $R_{\rm AIC} \sim 10^{-6} - 10^{-4}$ yr^{-1} (e.g., Yungelson & Livio 1998). The amount of highly neutron-rich material ejected per AIC can also be used to constrain the AIC rate (Hartmann et al. 1985; Fryer et al. 1999): if the $\sim 3 \times 10^{-3} M_\odot$ of ejected material with $Y_e \lesssim 0.4$ in the calculations of D06 is representative, $R_{\rm AIC}$ must be $\lesssim 10^{-4}$ yr^{-1} so as not to over-produce the abundances of neutron-rich isotopes in our solar system. If the proto-NS forms with a strong large-scale magnetic field $\sim 10^{15}$ G, then a much larger quantity $\sim 0.1 M_\odot$ of neutron-rich material is ejected by the

proto-NS's magneto-centrifugally driven wind (D07; Chapter 4) and the AIC rate is constrained to be even lower.

Assuming that the AIC rate is proportional to the blue stellar luminosity (Phinney 1991), a Galactic rate of $R_{\rm AIC} \equiv 10^{-4} R_{-4}$ yr^{-1} corresponds to a volumetric rate of $10^{-6} R_{-4}$ Mpc^{-3} yr^{-1}. For the $1.46 M_\odot$-WD model of D06, we predict that AIC produces an optical transient with a peak luminosity $\sim 10^{41}$ ergs s^{-1} (Fig. 7.3). This corresponds to a maximum detection distance of 650(410)[100] Mpc for a limiting magnitude of 25(24)[21]. Thus, the Pan-STARRs Medium Deep Survey (MDS; Kaiser et al. 2002), which covers ~ 84 deg^2 in g and r down to AB magnitude 25, will detect $\sim 2.4 R_{-4}$ yr^{-1}. The Palomar Transient Factory (PTF; Rau et al. 2008), which surveys ~ 8000 deg^2 to a limiting AB magnitude of 21, will detect $0.9 R_{-4}$ yr^{-1}. Thus, if $R_{\rm AIC} \sim 10^{-4}$ yr^{-1}, MDS and PTF should detect a few AIC events per year. Prospects for detection are much better with the Large Synoptic Survey Telescope (LSST; LSST collaboration 2007), which will image the entire sky down to a limiting magnitude ~ 24.5 every 3–4 nights and should detect AIC events at a rate $\sim 800 R_{-4}$ yr^{-1}. The short, few-day timescale of the transient requires observations with high cadence. Shallow, wider-area surveys such as PTF may be preferable because separating the transient from its host galaxy's light may be difficult for high redshift events.

The detectability of an optical transient is sensitive to whether there is sufficient mass in a remnant disk, which in turn depends on the angular momentum distribution of the WD progenitor. The very massive AIC progenitor from D06 ($1.92\ M_\odot$) is consistent with the large shear found by Yoon & Langer (2004, 2005), who studied angular momentum transport by Kelvin-Helmholtz instabilities during accretion. Piro (2008) argued, however, that large magnetic stresses impose nearly solid body rotation, which prevents the WD from reach a mass much over the (non-rotating) Chandrasekhar limit (this may also be the case for purely hydrodynamic instabilities; see Saio & Nomoto 2004). More work is needed to understand the possible progenitors of AIC, and the resulting implications for the accretion disk formed during collapse, taking into account the effects of magnetic stresses and compositional gradients on the redistribution of angular momentum

during accretion.

Other thermal transients are predicted to occur in nature on $\sim$ day timescales, such as ".Ia" SNe due to unstable thermonuclear He flashes from WD binaries (Bildsten et al. 2007). Although such events may originate from a similar stellar population and could be confused with AIC, a defining characteristic of AIC outflows is that most of the ejected material is processed through low entropy NSE. As a result, we expect few intermediate-mass elements to be produced (such as O, Ca, and Mg), although small amounts of He may be present. Thus, the Ni-rich explosions produced by AIC should be spectroscopically distinct from other types of SN identified to date.

The timescale, velocity, and composition of the AIC transient can be modified if significant amounts of WD material remain at large radii following AIC, either because the WD is still collapsing at late times or because some matter remains centrifugally supported in a remnant disk created by a super-$M_{\rm Ch}$ WD-WD merger (e.g., Yoon et al. 2007). In the later case, depending on the mass and composition of the WD binary, up to $\sim 0.1 M_\odot$ in C, O, Ne, or He could remain at a radius $R \sim 10^9$ cm. Once the Ni wind (with energy $\sim 10^{50}$ ergs) impacts this remnant material, it will (1) shock heat the material to a few times 10^9 K, which may synthesize intermediate mass elements (Woosley & Weaver 2002), but will not disassociate the Ni and will likely leave some unburned WD material; (2) slow the ejecta, by conservation of momentum, from $v \sim 0.1$ c to a few thousand km s^{-1}. A combination of slower ejecta and higher opacity would also lengthen the duration of the light curve by a factor of ~ 10 from that shown in Figure 7.3, making such an event easier to detect. Indeed, such an "enshrouded AIC" model represents a possible explanation for sub-luminous, sub-Chandrasekhar Type I SNe, such as 2008ha, which rose to its peak brightness in only ~ 10 days, possessed low line velocities ($\sim$ 2000 km s^{-1}), and was inferred to have $M_{\rm Ni} \approx 3 \times 10^{-3} M_\odot$ and $M_{\rm tot} \sim 0.15 M_\odot$ (Foley et al. 2009). We plan to study this possibility further, as well as explore the interaction between the disk wind and the outoing SN shock, in future work.

AIC may also be detectable with upcoming km-scale gravitational wave (GW)

detectors such as Advanced LIGO (Abramovici et al. 1992). If the collapse remains axisymmetric, the detection of AIC in GWs appears unlikely except within the Milky Way (D06,07; Dimmelmeier et al. 2008). However, if the progenitor WD is very rapidly rotating (as may result following a WD-WD merger), the ratio of rotational to gravitational energy of the proto-NS upon collapse may be sufficiently large for the growth of nonaxisymmetric instabilities, which would greatly increase the GW signal and detection prospects (Fryer et al. 2002; Ott 2008). Indeed, D06 find that their their 1.92 $M_{\odot}$-WD model rotates sufficiently rapidly to trigger a dynamically unstable spiral mode upon collapse (Ott et al. 2005). We note that our calculations predict that large Ni yields will accompany the massive disks that form from such rapidly rotating progenitors (e.g., we find $M_{\rm Ni} \approx 0.07 M_{\odot}$ for D06's $1.92 M_{\odot}$ model; see Table 7.1). Thus, events accompanied by GW emission that is detectable to extragalactic distances will likely produce a somewhat brighter SN transient than our fiducial example in Figure 7.3. More generally, the brightness of the optical emission from AIC directly traces the importance of rotation during the collapse.

Acknowledgements

We thank Luc Dessart for providing his AIC calculations. We also thank Todd Thompson for helpful conversations and for providing the neutrino luminosity and spectral evolution from his rotating core-collapse supernova calculations. A. L. P. is supported by the Theoretical Astrophysics Center at UC Berkeley. B. D. M and E. Q. were supported in part by the David and Lucile Packard Foundation, NASA grant NNG05GO22H, and the NSF-DOE Grant PHY-0812811.

Bibliography

IceCube Collaboration: R. Abbasi 2009, arXiv:0902.0131

Abdo, A. A., et al. 2009, "Fermi Observations of High-Energy Gamma-Ray Emission from GRB 080916C" , accepted to Science, Feb. 11 2009

Abramovici, A., et al. 1992, Science, 256, 325

Aharonian, F., et al. 2007, ApJ, 664, L71

Akiyama, S., Wheeler, J. C., Meier, D. L., & Lichtenstadt, I. 2003, ApJ, 584, 954

Arnett, W. D. 1982, ApJ, 253, 785

Arons, J., & Scharlemann, E. T. 1979, ApJ, 231, 854

Atteia, J.-L., et al. 1987, ApJS, 64, 305

Bahcall, J. N., & Mészáros, P. 2000, Physical Review Letters, 85, 1362

Bailyn, C. D., & Grindlay, J. E. 1990, ApJ, 353, 159

Balbus, S. A., & Hawley, J. F. 1998, Reviews of Modern Physics, 70, 1

Barkana, R., & Loeb, A. 2001, Phys. Rep., 349, 125

Barthelmy, S. D., et al. 2005, Nature, 438, 994

Barthelmy, S., et al. 2005, GRB Coordinates Network, 3385, 1

Barzilay, Y., & Levinson, A. 2008, New Astronomy, 13, 386

Baumgarte, T. W., Shapiro, S. L., & Shibata, M. 2000, ApJ, 528, L29

Begelman, M. C., & Li, Z.-Y. 1992, ApJ, 397, 187

Belcher, J. W., & MacGregor, K. B. 1976, ApJ, 210, 498

Belczynski, K., Perna, R., Bulik, T., Kalogera, V., Ivanova, N., & Lamb, D. Q. 2006, ApJ, 648, 1110

Bell, A. R. 2004, MNRAS, 353, 550

Beloborodov, A. M. 2003a, ApJ, 588, 931 ($B03a$)

Beloborodov, A. M. 2003b, ApJ, 585, L19

Beloborodov, A. M. 2008, American Institute of Physics Conference Series, 1054, 51

Berger, E., et al. 2003, Nature, 426, 154

Berger, E., Kulkarni, S. R., & Frail, D. A. 2003, ApJ, 590, 379

Berger, E., et al. 2005, Nature, 438, 988

Bethe, H. A., & Brown, G. E. 1998, ApJ, 506, 780

Bethe, H. A., Brown, G. E., & Lee, C.-H. 2007, Physics Reports, 442, 5

Bethe, H. A., & Wilson, J. R. 1985, ApJ, 295, 14

Bildsten, L. & Cutler, C. 1992, ApJ, 400, 175

Bildsten, L., Shen, K. J., Weinberg, N. N., & Nelemans, G. 2007, ApJ, 662, L95

Binney, J., & Tremaine, S. 1994, "Galactic Dynamics" (Second Edition), Princeton University Press

Blackman, E. G., & Yi, I. 1998, ApJ, 498, L31

Blaes, O. M., Davis, S. W., Hirose, S., Krolik, J. H., & Stone, J. M. 2006b, ApJ, 645, 1402

Blaes, O. 2007, ArXiv Astrophysics e-prints, arXiv:astro-ph/0703589

Blandford, R. D. 2002, Lighthouses of the Universe: The Most Luminous Celestial Objects and Their Use for Cosmology, 381

Blandford, R. D., & Begelman, M. C. 1999, MNRAS, 303, L1

Blandford, R. D., & McKee, C. F. 1976, Physics of Fluids, 19, 1130

Blandford, R. D., & Payne, D. G. 1982, MNRAS, 199, 883

Blinnikov, S. I., Novikov, I. D., Perevodchikova, T. V., & Polnarev, A. G. 1984, Soviet Astronomy Letters, 10, 177

Blondin, J. M., Mezzacappa, A., & DeMarino, C. 2003, ApJ, 584, 971

Bloom, J. S., et al. 1999, ApJ, 518, L1

Bloom, J. S., Frail, D. A., & Kulkarni, S. R. 2003, ApJ, 594, 674

Bloom, J. S., Butler, N. R., & Perley, D. A. 2008, American Institute of Physics Conference Series, 1000, 11

Bloom, J. B., et al. 2005, Bulletin of the American Astronomical Society, 37, 793

Bloom, J. S., et al. 2006, ApJ, 638, 354

Bloom, J. S., & Prochaska, J. X. 2006, Gamma-Ray Bursts in the Swift Era, 836, 473

Brandenburg, A. 2003, in Advances in Nonlinear Dynamos: The Fluid Mechanics of Astrophysics & Geophysics, Vol 9, ed. A. Ferriz-Mas & M. Nunez (London, New York: Taylor & Francis), 269

Bruenn, S. W., De Nisco, K. R., & Mezzacappa, A. 2001, ApJ, 560, 326

Bucciantini, N., Thompson, T. A., Arons, J., Quataert, E., & Del Zanna, L. 2006, MNRAS, 368, 1717

Bucciantini, N., Quataert, E., Arons, J., Metzger, B. D., & Thompson, T. A. 2007, MNRAS, 380, 1541

Bucciantini, N., Quataert, E., Arons, J., Metzger, B. D., & Thompson, T. A. 2008, MNRAS, 383, L25

Bucciantini, N., Quataert, E., Metzger, B. D., Thompson, T. A., Arons, J., & Del Zanna, L. 2009, arXiv:0901.3801

Bulik, T., Sikora, M., & Moderski, R. 2002, ArXiv Astrophysics e-prints, arXiv:astro-ph/0209339

Buras, R., Rampp, M., Janka, H.-T., & Kifonidis, K. 2003, Physical Review Letters, 90, 241101

Buras, R., Rampp, M., Janka, H.-T., & Kifonidis, K. 2006, A&A, 447, 1049

Burrows, A., Hayes, J., & Fryxell, B.A. 1995, ApJ, 450, 830

Burrows, A., & Lattimer, J. M. 1986, ApJ, 307, 178

Burrows, A., & Mazurek, T. L. 1983, Nature, 301, 315

Burrows, A., Livne, E., Dessart, L., Ott, C. D., & Murphy, J. 2006, ApJ, 640, 878

Burrows, A., Livne, E., Dessart, L., Ott, C. D., & Murphy, J. 2006, New Astronomy Review, 50, 487

Burrows, A., & Mazurek, T. J. 1982, ApJ, 259, 330

Burrows, D. N., et al. 2005, Science, 309, 1833

Butler, N. R., & Kocevski, D. 2007, ApJ, 663, 407

Campana, S., et al. 2006, A&A, 454, 113

Canal, R., Isern, J., & Labay, J. 1990, ARAA, 28, 183

Chang, P., Spitkovsky, A., & Arons, J. 2008, ApJ, 674, 378

Cardall, C. Y., & Fuller, G. M. 1997, ApJ, 486, L111

Cavallo, G., & Rees, M. J. 1978, MNRAS, 183, 359

Chen, W.-X., & Beloborodov, A. M. 2007, ApJ, 657, 383

Chevalier, R. A. 1989, ApJ, 346, 847

Colgate, S. A., Petschek, A. G., & Kriese, J. T. 1980, ApJ, 237, L81

Contopoulos, J. 1994, ApJ, 432, 508

Contopoulos, I., Kazanas, D., & Fendt, C. 1999, ApJ, 511, 351

Cook, G. B., Shapiro, S. L., & Teukolsky, S. A. 1994, ApJ, 424, 823

Costa, E., et al. 1997, Nature, 387, 783

Couch, S. M., Milosavljević, M., & Nakar, E. 2008, ApJ, 688, 462

Cowan, J. J., et al. 2005, ApJ, 627, 238

Cranmer, S. R., & van Ballegooijen, A. A. 2005, ApJS, 156, 265

Dai, Z. G., et al. 2006, Science, 311, 1127

Daigne, F., & Mochkovitch, R. 2002, A&A, 388, 189 ($DM02$)

Delano, M. D., & Cameron, A. G. W. 1971, Astrophys. Space Sci. , 10, 203

Della Valle, M., et al. 2006, ArXiv Astrophysics e-prints, arXiv:astro-ph/0608322

Del Zanna, L., Volpi, D., Amato, E., & Bucciantini, N. 2006, A&A, 453, 621

Derishev, E. V., Kocharovsky, V. V., & Kocharovsky, V. V. 1999, ApJ, 521, 640

Dermer, C. D., & Atoyan, A. 2006, New Journal of Physics, 8, 122

Dessart, L., Burrows, A., Ott, C. D., Livne, E., Yoon, S.-Y., & Langer, N. 2006, ApJ, 644, 1063

Dessart, L., et al. 2007, ApJ, 669, 585 (D07)

Dessart, L., Burrows, A., Livne, E., & Ott, C. D. 2008, ApJ, 673, L43

Di Matteo, T., Perna, R., & Narayan, R. 2002, ApJ, 579, 706

Dimmelmeier, H., Ott, C. D., Marek, A., & Janka, H.-T. 2008, Phys. Rev. D, 78, 064056

Drenkhahn, G., & Spruit, H. C. 2002, A&A, 391, 1141

Duan, H., & Qian, Y.-Z. 2004, Phys. Rev. D, 69, 123004

Duez, M. D., Liu, Y. T., Shapiro, S. L., Shibata, M., & Stephens, B. C. 2006, Phys. Rev. D, 73, 104015

Duez, M. D., Liu, Y. T., Shapiro, S. L., & Stephens, B. C. 2004, Phys. Rev. D, 69, 104030

Duncan, R. C., Shapiro, S. L., & Wasserman, I. 1986, ApJ, 309, 141

Duncan, R. C., & Thompson, C. 1992, ApJ, 392, L9

Eichler, D., & Levinson, A. 1999, ApJ, 521, L117

Eichler, D., Livio, M., Piran, T., & Schramm, D. N. 1989, Nature, 340, 126

Faber, J. A., et al. 2006a, Phys. Rev. D, 73, 4012

Faber, J. A., et al. 2006b, ApJ, 641, L93

Falcone, A. D., et al. 2007, ApJ, 671, 1921

Fan, Y. Z., & Wei, D. M. 2004, ApJ, 615, L69

Fan, Y. Z., Zhang, B., & Wei, D. M. 2005, ApJ, 628, L25

Fender, R., et al. 2004, Nature, 427, 222

Ferrero, P., et al. 2007, AJ, 134, 2118

Fishbone, L. G. 1973, ApJ, 185, 43

Fishman, G. J., & Meegan, C. A. 1995, ARA&A, 33, 415

Foley, R. J., et al. 2009, arXiv:0902.2794

Fox, D. B., et al. 2005, Nature, 437, 845

Frail, D. A., Kulkarni, S. R., Nicastro, L., Feroci, M., & Taylor, G. B. 1997, Nature, 389, 261

Frail, D. A., et al. 2001, ApJ, 562, L55

Frank, J., King, A. R., & Raine, D. J. 2002, Accretion Power in Astrophysics (3rd ed.; Cambridge: Cambridge Univ. Press)

Freiburghaus, C., Rosswog, S., & Thielemann, F.-K. 1999, ApJ, 525, L121

Fruchter, A. S., et al. 2006, Nature, 441, 463

Fryer, C., Benz, W., Herant, M., & Colgate, S. A. 1999, ApJ, 516, 892

Fryer, C. L., & Heger, A. 2000, ApJ, 541, 1033

Fryer, C. L., Holz, D. E., & Hughes, S. A. 2002, ApJ, 565, 430

Fryer, C. L., Woosley, S. E., Herant, M., & Davies, M. B. 1999b, ApJ, 520, 650

Fuller, G. M., & Meyer, B. S. 1995, ApJ, 453, 792

Fuller, G. M., & Qian, Y.-Z. 1996, Nucl. Phys. A, 606, 167

Fynbo, J.P.U., et al. 2006, preprint (astro-ph/0608313)

Galama, T. J., et al. 1998, Nature, 395, 670

Gal-Yam, A., et al. 2006, Nature, 444, 1053

Gao, W.-H., & Fan, Y.-Z. 2006, ChJAA, 6, 513

Gehrels, N. et al, 2005, Nature, 437, 851

Gehrels, N., et al. 2006, Nature, 444, 1044

Genet, F., Daigne, F., & Mochkovitch, R. 2007, MNRAS, 381, 732

Ghirlanda, G., Nava, L., Ghisellini, G., Celotti, A., & Firmani, C. 2009, arXiv:0902.0983

Ghosh, P., & Lamb, F. K. 1978, ApJ, 223, L83

Giannios, D., & Spruit, H. C. 2005, A&A, 430, 1

Giannios, D. 2007, ArXiv e-prints, 704, arXiv:0704.1659

Goodman, J. 1986, ApJ, 308, L47

Goodman, J., & MacFadyen, A. I. 2007, arXiv:0706.1818

Granot, J., & Kumar, P. 2006, MNRAS, 366, L13

Grindlay, J. E. 1987, The Origin and Evolution of Neutron Stars, 125, 173

Grindlay, J. E., & Bailyn, C. D. 1988, Nature, 336, 48

Grupe, D., Burrows, D. N., Patel, S. K., Kouveliotou, C., Zhang, B., Mészáros, P., Wijers, R. A. M., & Gehrels, N. 2006, ApJ, 653, 462

Gruzinov, A., 2005, Physical Review Letters, 94

Guetta, D., Piran, T., & Waxman, E. 2005, ApJ, 619, 412

Gutiérrez, J., Canal, R., & García-Berro, E. 2005, A&A, 435, 231

Haensel, P., & Zdunik, J. L. 1990a, A&A, 227, 431

Haensel, P., & Zdunik, J. L. 1990b, A&A, 229, 117

Hartmann, D., Woosley, S. E., & El Eid, M. F. 1985, ApJ, 297,

Hawley, J. F., & Balbus, S. A. 2002, ApJ, 573, 738

Hawley, J. F., Balbus, S. A., & Stone, J. M. 2001, ApJ, 554, L49

Hawley, J. F., Gammie, C. F., & Balbus, S. A. 1995, ApJ, 440, 742

Herant, M., Benz, W., Hix, W. R., Fryer, C. L., & Colgate, S. A. 1994, ApJ, 435, 339

Hillebrandt, W., Wolff, R. G., & Nomoto, K. 1984, A&A, 133, 175

Hirose, S., Krolik, J. H., & Stone, J. M. 2006, ApJ, 640, 901

Hjorth, J., et al. 2003, Nature, 423, 847

Hjorth, J., et al. 2005, ApJ, 630, L117

Hoffman, R. D., Woosley, S. E., & Qian, Y.-Z. 1997, ApJ, 482, 951

Hughes, S. A. 2003, Annals of Physics, 303, 142

Hughes, S. A., & Holz, D. E. 2003, Classical and Quantum Gravity, 20, 65

Hurley, K., et al. 1994, Nature, 372, 652

Iwamoto, K., et al. 1998, Nature, 395, 672

Janiuk, A., Perna, R., DiMatteo, T., & Czerny, B. 2004, MNRAS, 355, 950

Janka, H.-T., Eberl, T., Ruffert, M., & Fryer, C. L. 1999, ApJ, 527, L39

Janka, H.-T., & Mueller, E. 1995, ApJ, 448, L109

Kaiser, N. et al. 2002 Proc. of the SPIE, 4836, 154

Kalogera, V., et al. 2004, ApJ, 601, L179

Kaspi, V. M., & Helfand, D. J. 2002, Neutron Stars in Supernova Remnants, 271, 3

Katz, J. I. 1997, ApJ, 490, 633

Kennel, C. F., & Coroniti, F. V. 1984, ApJ, 283, 694

Kim, C., Kalogera, V., & Lorimer, D. R. 2006, ArXiv Astrophysics e-prints, arXiv:astro-ph/0608280

King, A. R., Pringle, J. E., & Wickramasinghe, D. T. 2001, MNRAS, 320, L45

King, A. R., et al. 2005, ApJ, 630, L113

King, A. R., Pringle, J. E., & Livio, M. 2007, MNRAS, 376, 1740

Klebesadel, R. W., Strong, I. B., & Olson, R. A. 1973, ApJ, 182, L85

Kluźniak, W. & Lee, W. H. 1998, ApJ, 494, L53

Kluźniak, W., & Ruderman, M. 1998, ApJ, 505, L113

Kochanek, C. S., & Piran, T. 1993, ApJ, 417, L17

Kohri, K. & Mineshige, S. 2002,ApJ, 577, 311

Komissarov, S. S., & Barkov, M. V. 2007, MNRAS, 382, 1029

Kopal, Z. 1959, Close Binary Systems (London: Chapman & Hall)

Kouveliotou, C., Meegan, C. A., Fishman, G. J., Bhat, N. P., Briggs, M. S., Koshut, T. M., Paciesas, W. S., & Pendleton, G. N. 1993, ApJ, 413, L101

Kouveliotou, C., et al. 1994, Nature, 368, 125

Kouveliotou, C., et al. 1998, Nature, 393, 235

Krolik, J. H., Hirose, S., & Blaes, O. 2007, ApJ, 664, 1045

Kulkarni, S. R. 2005, ArXiv Astrophysics e-prints, arXiv:astro-ph/0510256

Kulkarni, S. R., et al. 1999, Nature, 398, 389

Kumar, P., & Narayan, R. 2008, arXiv:0812.0021

Kumar, P., Narayan, R., & Johnson, J. L. 2008, MNRAS, 388, 1729

Kumar, P., & McMahon, E. 2008, MNRAS, 384, 33

LSST Collaboration, LSST Science Case.
http://www.lsst.org/Science/lsst_baseline.shtml

Langer, N., Cantiello, M., Yoon, S.-C., Hunter, I., Brott, I., Lennon, D., de Mink, S., & Verheijdt, M. 2008, IAU Symposium, 250, 167

Lai, D., Rasio, F. A., & Shapiro, S. L. 1994, ApJ, 423, 344

Lai, D., & Qian, Y.-Z. 1998, ApJ, 505, 844

La Parola, V., et al. 2006, A&A, 454, 753

Lamers, H., & Cassinelli, J. P. 1999, Introduction to Stellar Winds (Cambridge: Cambridge University Press)

Lattimer, J. M., & Schramm, D. N. 1974, ApJ, 192, L145

Lattimer, J. M., & Schramm, D. N. 1976, ApJ, 210, 549

Lazzati, D., Ramirez-Ruiz, E., & Ghisellini, G. 2001, A&A, 379, L39

Lazzati, D., & Perna, R. 2007, MNRAS, 375, L46

Lazzati, D., Perna, R., & Begelman, M. C. 2008, MNRAS, 388, L15

Lee, W. H. & Kluźniak, W. 1995, Acta Astron., 45, 705

Lee, W. H. & Kluźniak, W. 1998, ApJ, 526, 178

Lee, W. H. & Kluźniak, W. 1999, MNRAS, 308, 780

Lee, W. H., Ramirez-Ruiz, E., & Page, D. 2004, ApJ, 608, L5

Lee, W. H., Ramirez-Ruiz, E., & Page, D. 2005, ApJ, 632, 421 ($L05$)

Lee, W. & Ramirez-Ruiz, E. 2007, New J. Phys., 9, 17

Lemoine, M. 2002, A&A, 390, L31

Levan, A. J., et al. 2006, MNRAS, 368, L1

Levinson, A. 2006, ApJ, 648, 510

Levinson, A., & Eichler, D. 1993, ApJ, 418, 386

Levinson, A., & Eichler, D. 2003, ApJ, 594, L19 ($LE03$)

Li, L.-X., & Paczyński, B. 1998, ApJ, 507, L59

Li, Z.-Y., Chiueh, T., & Begelman, M. C. 1992, ApJ, 394, 459

Lightman, A. P., & Eardley, D. M. 1974, ApJ, 187, L1

Lithwick, Y., & Sari, R. 2001, ApJ, 555, 540

Lyne, A. G., et al. 1998, MNRAS, 295, 743

Lyutikov, M., & Blackman, E. G. 2001, MNRAS, 321, 177

Lyutikov, M., & Blandford, R. 2003, arXiv:astro-ph/0312347

MacFadyen, A. I., & Woosley, S. E. 1999, ApJ, 524, 262

MacFadyen, A. I., Ramirez-Ruiz, E., & Zhang, W. 2005, ArXiv Astrophysics e-prints, arXiv:astro-ph/0510192

MacGregor, K. B., & Pizzo, V. J. 1983, ApJ, 267, 340

Malesani, D., et al. 2007, A&A, 473, 77

Manchester, R. N. 2004, Science, 304, 542

Mangano, V., et al. 2007, A&A, 470, 105

Mazets, E. P., et al. 1981, Ap&SS, 80, 3

McKinney, J. C. 2005, ArXiv Astrophysics e-prints, arXiv:astro-ph/0506368

McKinney, J. C. 2006, MNRAS, 368, L30

McQuinn, M., et al. 2009, arXiv:0902.3442

Meegan, C. A., Fishman, G. J., Wilson, R. B., Horack, J. M., Brock, M. N., Paciesas, W. S., Pendleton, G. N., & Kouveliotou, C. 1992, Nature, 355, 143

Mestel, L., & Spruit, H. C. 1987, MNRAS, 226, 57

Mestel, L. 1968, MNRAS, 138, 359

Mészáros, P., & Rees, M. J. 2000, ApJ, 541, L5

Meszaros, P., & Rees, M. J. 1993, ApJ, 405, 278

Metzger, M. R., Djorgovski, S. G., Kulkarni, S. R., Steidel, C. C., Adelberger, K. L., Frail, D. A., Costa, E., & Frontera, F. 1997, Nature, 387, 878

Meyer, B. S., Mathews, G. J., Howard, W. M., Woosley, S. E., & Hoffman, R. D. 1992, ApJ, 399, 656

Meyer, B. S., & Brown, J. S. 1997, ApJS, 112, 199

Meyer, B. S. 2002, Physical Review Letters, 89, 231101

Michel, F. C. 1969, ApJ, 158, 727

Michel, F. C. 1987, Nature, 329, 310

Miller, M. C. 2005, ApJ, 626, L41

Migliari, S., & Fender, R. P. 2006, MNRAS, 366, 79

Miyaji, S., Nomoto, K., Yokoi, K., & Sugimoto, D. 1980, PASJ, 32, 303

Mochkovitch, R., & Livio, M. 1989, A&A, 209, 111

Mochkovitch, R., & Livio, M. 1990, A&A, 236, 378

Montanari, E., et al. 2005, ApJ, 625, L17

Morrison, I. A., Baumgarte, T. W., & Shapiro, S. L. 2004, ApJ, 610, 941

Muno, M. P., et al. 2006, ApJ, 636, L41

Nakamura, T., Umeda, H., Iwamoto, K., Nomoto, K., Hashimoto, M.-a., Hix, W. R., & Thielemann, F.-K. 2001, ApJ, 555, 880

Nakar, E., Gal-Yam, A., & Fox, D. B. 2006, ApJ, 650, 281

Nakar, E. 2007, PhR, 442, 166

Nagataki, S., & Kohri, K. 2001, PASJ, 53, 547

Napiwotzki, R., et al. 2002, A&A, 386, 957

Napiwotzki, R., et al. 2004, Spectroscopically and Spatially Resolving the Components of the Close Binary Stars, 318, 402

Narayan, R., & Kumar, P. 2009, MNRAS, L193

Narayan, R., Paczynski, B., & Piran, T. 1992, ApJ, 395, L83

Narayan, R., Piran, T., & Kumar, P. 2001, ApJ, 557, 949

Narayan, R., Piran, T., & Shemi, A. 1991, ApJ, 379, L17

Narayan, R., & Yi, I. 1994, ApJ, 428, L13

Nissanke, S., Hughes, S. A., Holz, D. E., Dalal, N., & Sievers, J. L. 2009, arXiv:0904.1017

Nomoto, K., & Kondo, Y. 1991, ApJ, 367, L19

Nomoto, K., Miyaji, S., Sugimoto, D., & Yokoi, K. 1979, BAAS, 11, 725

Nomoto, K., Tanaka, M., Tominaga, N., Maeda, K., & Mazzali, P. A. 2007, arXiv:0707.2219

Norris, J. P., & Bonnell, J. T. 2006, ApJ, 643, 266

Nousek, J. A., et al. 2006, ApJ, 642, 389

Oechslin, R., & Janka, H.-Th. 2006, MNRAS, 368, 1489

Ofek, E. O., et al. 2007, ApJ, 662, 1129

Otsuki, K., Tagoshi, H., Kajino, T., & Wanajo, S.-y. 2000, ApJ, 533, 424

Ott, C. D. 2008, arXiv:0809.0695

Ott, C. D., Ou, S., Tohline, J. E., & Burrows, A. 2005, ApJ, 625, L119

Paczyński, B. 1986, ApJ, 308, L43

Paczyński, B. 1991, Acta Astronomica, 41, 257

Paczyński, B. 1998, ApJ, 494, L45

Paczyński, B. 2001, Acta Astronomica, 51, 1

Paczyński, B., & Piran, T. 1992, ApJ, 395, L83

Perley, D. A., et al. 2008, arXiv:0811.1044

Perna, R., Armitage, P. J., & Zhang, B. 2005, ApJ, 636, L29

Pethick, C. J., & Ravenhall, D. G. 1995, Annu. Rev. Nucl. Part. Sci., 45, 429

Phinney, E. S. 1991, ApJ, 380, L17

Pian, E., et al. 2006, Nature, 442, 1011

Piran, T. 2005, Nuovo Cimento C Geophysics Space Physics C, 28, 373

Piran, T. 2005, Reviews of Modern Physics, 76, 1143

Piro, A. L. 2008, ApJ, 679, 616

Piro, A. L. & Pfahl, E. 2007, ApJ, 658, 1173

Podsiadlowski, P., Mazzali, P. A., Nomoto, K., Lazzati, D., & Cappellaro, E. 2004, ApJ, 607, L17

Poelarends, A. J. T., Herwig, F., Langer, N., & Heger, A. 2008, ApJ, 675, 614

Pons, J. A., Reddy, S., Prakash, M., Lattimer, J. M., & Miralles, J. A. 1999, ApJ, 513, 780

Popham, R., Woosley, S. E., & Fryer, C. 1999, ApJ, 518, 356

Price, D. J., & Rosswog, S. 2006, Science, 312, 719

Prochaska, J. X., Chen, H.-W., Dessauges-Zavadsky, M., & Bloom, J. S. 2007, ApJ, 666, 267

Proga, D., & Begelman, M. C. 2003, ApJ, 592, 767

Proga, D., MacFadyen, A. I., Armitage, P. J., & Begelman, M. C. 2003, ApJ, 599, L5

Proga, D. & Zhang, B. 2006, MNRAS, 370, L61

Pruet, J., & Dalal, N. 2002, ApJ, 573, 770

Pruet, J., Fuller, G. M., & Cardall, C. Y. 2001, ApJ, 561, 957

Pruet, J., Guiles, S., & Fuller, G. M. 2002, ApJ, 580, 368

Pruet, J., Thompson, T. A., & Hoffman, R. D. 2004, ApJ, 606, 1006 ($P04$)

Pruet, J., Woosley, S. E., & Hoffman, R. D. 2003, ApJ, 586, 1254

Qian, Y.-Z. 2000, ApJ, 534, L67

Qian, Y.-Z., Fuller, G. M., Mathews, G. J., Mayle, R. W., Wilson, J. R., & Woosley, S. E. 1993, Physical Review Letters, 71, 1965

Qian, Y.-Z., & Wasserburg, G. J. 2007, PhR, 442, 237

Qian, Y.-Z., Vogel, P., & Wasserburg, G. J. 1998, ApJ, 494, 285

Qian, Y.-Z., & Woosley, S. E. 1996, ApJ, 471, 331

Rasio, F. A., et al. 2005, Proc. JGRG14 Yukawa Institute for Theoretical Physics (preprint astro-ph/0503007)

Rasio, F. A., & Shapiro, S. L. 1994, ApJ, 432, 242

Rau, A., et al. 2008, http://www.weizmann.ac.il/home/galyam/PTF/Rau-paper.pdf

Razzaque, S., & Mészáros, P. 2006a, ApJ, 650, 998

Razzaque, S., & Mészáros, P. 2006b, Journal of Cosmology and Astro-Particle Physics, 6, 6

Rees, M. J., & Mészáros, P. 1992, MNRAS, 258, 41P

Rees, M. J., & Meszaros, P. 1994, ApJ, 430, L93

Remillard, R. A., & McClintock, J. E. 2006, ARA&A, 44, 49

Rhoads, J. E. 1997, ApJ, 487, L1

Rhoads, J. E. 1999, ApJ, 525, 737

Rossi, E. M., & Begelman, M. C. 2008, arXiv:0808.1284

Rossi, E. M., Beloborodov, A. M., & Rees, M. J. 2006, MNRAS, 369, 1797

Rosswog, S. 2007, MNRAS, 376, L48

Rosswog, S., & Liebendörfer, M. 2003, MNRAS, 342, 673

Rosswog, S., Liebendörfer, M., Thielemann, F.-K., Davies, M. B., Benz, W., & Piran, T. 1999, A&A, 341, 499

Rosswog, S., & Ramirez-Ruiz, E. 2002, MNRAS, 336, L7

Rosswog, S., Ramirez-Ruiz, E., & Davies, M. B. 2003, MNRAS, 345, 1077

Rosswog, S., Speith, R., & Wynn, G. A., 2004, MNRAS, 351, 1121

Ruderman, M. 1975, New York Academy Sciences Annals, 262, 164

Ruffert, M., & Janka, H.-Th. 1999, A&A, 344, 573

Ruffert, M., & Janka, H.-Th. 2001, A&A, 380, 544

Ruffert, M., Janka, H.-Th., & Schäfer, G. 1996, A&A, 311, 532

Ruffert, M., Janka, H.-T., Takahashi, K., & Schaefer, G. 1997, A&A, 319, 122

Salmonson, J. D., & Wilson, J. R. 1999, ApJ, 517, 859

Saio, H., & Nomoto, K. 2004, ApJ, 615, 444

Sari, R., & Piran, T. 1997, ApJ, 485, 270

Sari, R., Piran, T., & Narayan, R. 1998, ApJ, 497, L17

Sasaqui, T., Otsuki, K., Kajino, T., & Mathews, G. J. 2006, ApJ, 645, 1345

Sawyer, R. F. 2003, Phys. Rev. D, 68, 063001

Schatzman, E. 1962, Annales d'Astrophysique, 25, 18

Scheck, L., Kifonidis, K., Janka, H.-T., Mueller, E. 2006, A&A, 457, 963

Seitenzahl, I. R., Timmes, F. X., Marin-Laflèche, A., Brown, E., Magkotsios, G., & Truran, J. 2008, ArXiv e-prints, 808, arXiv:0808.2033

Setiawan, S., Ruffert, M., & Janka, H.-Th. 2004, MNRAS, 352, 753

Setiawan, S., Ruffert, M., & Janka, H.-Th. 2006, A&A, 458, 553

Shakura, N. I., & Sunyaev, R. A. 1973, A&A, 24, 337

Shapiro, S. L. 2004, ApJ, 610, 913

Shapiro, S. L., & Teukolsky, S. A. 1983, Black Holes, White Dwarfs, and Neutron Stars: The Physics of Compact Objects (New York: Wiley)

Shemi, A., & Piran, T. 1990, ApJ, 365, L55

Shibata, M. 2003, ApJ, 595, 992

Shibata, M., Liu, Y. T., Shapiro, S. L., & Stephens, B. C. 2006, Phys. Rev. D, 74, 104026

Shibata, M., Taniguchi, K., & Uryū, K. 2005, Phys. Rev. D, 71, 084021

Shibata, M. & Taniguchi, K. 2006, Phys. Rev. D, 73, 064027

Sironi, L., & Goodman, J. 2007, ApJ, 671, 1858

Smith, N., & Owocki, S. P. 2006, ApJ, 645, L45

Sneden, C., Cowan, J. J., & Gallino, R. 2008, ARA&A, 46, 241

Soderberg, A. M. 2006, American Institute of Physics Conference Series, 836, 380

Soderberg, A. M., et al. 2006, ApJ, 650, 261

Soderberg, A. M., Nakar, E., Berger, E., & Kulkarni, S. R. 2006, ApJ, 638, 930

Spitkovsky, A. 2006, ApJ, 648, L51

Spitkovsky, A. 2008, ApJ, 673, L39

Spitkovsky, A. 2008, ApJ, 682, L5

Spruit, H. C., & Uzdensky, D. A. 2005, ApJ, 629, 960

Stanek, K. Z., et al. 2003, ApJ, 591, L17

Stella, L., Dall'Osso, S., Israel, G. L., & Vecchio, A. 2005, ApJ, 634, L165

Stone, J. M., & Pringle, J. E. 2001, MNRAS, 322, 461

Strumia, A., & Vissani, F. 2003, Physics Letters B, 564, 42

Sumiyoshi, K., Suzuki, H., Otsuki, K., Terasawa, M., & Yamada, S. 2000, PASJ, 52, 601

Surman, R., & McLaughlin, G. C. 2004, ApJ, 603, 611

Surman, R., & McLaughlin, G. C. 2005, ApJ, 618,

Surman, R., McLaughlin, G. C., & Hix, W. R. 2006, ApJ, 643, 1057

Surman, R., McLaughlin, G. C., Ruffert, M., Janka, H.-T., & Hix, W. R. 2008, ApJ, 679, L117

Suzuki, T. K., & Nagataki, S. 2005, ApJ, 628, 914

Taylor, G. B., Frail, D. A., Berger, E., & Kulkarni, S. R. 2004, ApJ, 609, L1

Tanvir, N. R., et al. 2005, Nature, 438, 991

Totani, T., & Panaitescu, A. 2002, ApJ, 576, 120

Thompson, C. 1994, MNRAS, 270, 480

Thompson, C. 2006, ApJ, 651, 333

Thompson, C., & Duncan, R. C. 1993, ApJ, 408, 194

Thompson, C. 1994, MNRAS, 270, 480

Thompson, T. A., Burrows, A., & Meyer, B. S. 2001, ApJ, 562, 887

Thompson, T. A. 2003, ApJ, 585, L33

————. 2003b, in Core Collapse of Massive Stars, edt. C. Fryer (Dordrecht: Kluwer), 175

Thompson, T. A., Chang, P., & Quataert, E. 2004, ApJ, 611, 380

Thompson, T. A. 2005, Nuovo Cimento C Geophysics Space Physics C, 28, 583

Thompson, T. A., Quataert, E., & Burrows, A. 2005, ApJ, 620, 861

Troja, E., King, A. R., O'Brien, P. T., Lyons, N., & Cusumano, G. 2008, MNRAS, 385, L10

Turner, N. J. 2004, ApJ, 605, L45

Uhm, Z. L., & Beloborodov, A. M. 2007, ApJ, 665, L93

Uryū, K., & Eriguchi, Y. 1999, MNRAS, 303, 329

Usov, V. V. 1992, Nature, 357, 472

Usov, V. V., & Chibisov, G. V. 1975, Soviet Astronomy, 19, 115

Uzdensky, D. A., & MacFadyen, A. I. 2005, Bulletin of the American Astronomical Society, 37, 1188

Uzdensky, D. A., & MacFadyen, A. I. 2006, ApJ, 647, 1192

van den Heuvel, E. P. J. 1984, Journal of Astrophysics and Astronomy, 5, 209

van Paradijs, J., Taam, R. E., & van den Heuvel, E. P. J. 1995, A&A, 299, L41

van Paradijs, J., et al. 1997, Nature, 386, 686

Vestrand, W. T., et al. 2006, Nature, 442, 172

Vietri, M. 1995, ApJ, 453, 883

Vietri, M., & Stella, L. 1998, ApJ, 507, L45

Vietri, M., & Stella, L. 1999, ApJ, 527, L43

Villain, L., Pons, J. A., Cerdá-Durán, P., & Gourgoulhon, E. 2004, A&A, 418, 283

Villasenor, J. S., et al. 2005, Nature, 437, 855

Vink, J., & Kuiper, L. 2006, MNRAS, L45

Vlahakis, N., Peng, F., Konigl, A. 2003, ApJ, 594, L23

Vranesevic, N., et al. 2004, ApJ, 617, L139

Wanajo, S., Kajino, T., Mathews, G. J., & Otsuki, K. 2001, ApJ, 554, 578

Wang, L., Baade, D., Höflich, P., & Wheeler, J. C. 2003, ApJ, 592, 457

Wang, L., Howell, D. A., Höflich, P., & Wheeler, J. C. 2001, ApJ, 550, 1030

Wasserburg, G. J., Busso, M., & Gallino, R. 1996, ApJ, 466, L109

Waxman, E. 1995, ApJ, 452, L1

Waxman, E., & Bahcall, J. N. 2000, ApJ, 541, 707

Weber, E. J., & Davis, L. J. 1967, ApJ, 148, 217

Wheeler, J. C., Yi, I., Höflich, P., & Wang, L. 2000, ApJ, 537, 810

Woods, P. M., & Thompson, C. 2004, ArXiv Astrophysics e-prints, arXiv:astro-ph/0406133

Woods, P. M., & Thompson, C. 2006, Compact stellar X-ray sources, 547

Woosley, S. E. 1993, ApJ, 405, 273

Woosley, S. E., & Baron, E. 1992, ApJ, 391, 228

Woosley, S. E., & Bloom, J. S. 2006, Annual Rev. of A&A, 44, 507

Woosley, S. E., Eastman, R. G., & Schmidt, B. P. 1999, ApJ, 516, 788

Woosley, S. E., & Hoffman, R. D. 1992, ApJ, 395, 202

Woosley, S. E., & Weaver, T. A. 1995, ApJS, 101, 181

Woosley, S. E., Wilson, J. R., Mathews, G. J., Hoffman, R. D., & Meyer, B. S. 1994, ApJ, 433, 229

Xie, Y., Huang, C.-Y., & Lei, W.-H. 2007, Chinese Journal of Astronomy and Astrophysics, 7, 685

Yoon, S.-C., & Langer, N. 2004, A&A, 419, 623

Yoon, S.-C., & Langer, N. 2005, A&A, 435, 967

Yoon, S.-C., Podsiadlowski, P., & Rosswog, S. 2007, MNRAS, 380, 933

Yüksel, H., Kistler, M. D., Beacom, J. F., & Hopkins, A. M. 2008, ApJ, 683, L5

Yungelson, L., & Livio, M. 1998, ApJ, 497, 168

Zhang, B. 2007, Advances in Space Research, 40, 1186

Zhang, B., et al. 2007, ApJ, 655, L25

Zhang, B., et al. 2007, ApJ, 655, 989

Zhang, B., & Kobayashi, S. 2005, ApJ, 628, 315

Zhang, B., & Mészáros, P. 2002, ApJ, 581, 1236

Zhang, B., & Mészáros, P. 2004, International Journal of Modern Physics A, 19, 2385